



University
of Glasgow

Nasti, Umberto (2020) *Emerging materials for superconducting nanowire photon counting arrays*. PhD thesis.

<http://theses.gla.ac.uk/81517/>

Copyright and moral rights for this work are retained by the author

A copy can be downloaded for personal non-commercial research or study, without prior permission or charge

This work cannot be reproduced or quoted extensively from without first obtaining permission in writing from the author

The content must not be changed in any way or sold commercially in any format or medium without the formal permission of the author

When referring to this work, full bibliographic details including the author, title, awarding institution and date of the thesis must be given

Enlighten: Theses

<https://theses.gla.ac.uk/>
research-enlighten@glasgow.ac.uk

University of Glasgow



James Watt School of Engineering
Division of Electronics and Nanoscale Engineering

A thesis presented for the degree of Doctor of Philosophy

Emerging materials for superconducting nanowire photon counting arrays

Supervisors:

Prof. Robert Hadfield

Dr. Alessandro Casaburi

Student:

Umberto Nasti

November 2019

Abstract

Superconducting nanowire single-photon detectors (SNSPDs) are the leading technology for low noise, high efficiency infrared single-photon detection. The basic SNSPD consists of a nanowire patterned in an ultrathin superconducting thin film, which is cooled below its critical temperature and biased close to its critical current. The absorption of a single-photon creates a resistive region, triggering a fast output voltage pulse which can be readily amplified and registered. The excellent performance of SNSPDs at near infrared and telecommunications wavelengths has led to their adoption in important applications such as quantum secure communications, single-photon spectroscopy and single-photon LIDAR. A clear challenge for the SNSPD community is to extend the spectral range of SNSPDs into the mid infrared, and to improve material uniformity to enable the realization of large area arrays for multimode or free space coupling. The aim of this work is to evaluate potential materials for next generation mid-infrared SNSPD arrays. In this work, thin films of polycrystalline NbN and amorphous MoSi have been optimized to test the uniformity of a multipixel array configuration composed of 8 nanowire meander structures covering $10\ \mu\text{m} \times 10\ \mu\text{m}$ area, 100 nm width and 50% filling factor. The 8-pixels SNSPD arrays have been patterned on 8 nm thickness NbN grown on high resistivity silicon (HR Si) substrate at room temperature and at 800 °C exhibiting respectively 4.4 K and 7.3 K as mean critical temperature across the pixels. The 8-pixels SNSPD array patterned on 8 nm thickness MoSi cooling the HR Si substrate to $-180\ \text{°C}$ has exhibited a mean critical temperature of 3.2 K across the pixels. Optical properties have been measured by an attenuated 1550 nm laser diode source delivered by single mode optical fibre at a controlled distance from the chip in order to broadly illuminate the array. The optical properties have been studied only for the 8 nm thickness NbN SNSPD array grown at room temperature has demonstrated uniform optical properties across pixels exhibiting similar saturation of the internal efficiency over a large bias, similar dark count rate and similar timing jitter (about 137 ps) across pixels. In the single photon regime at 1550 nm, pixels 4 and 6 of the 8 nm thick NbN SNSPD array exhibit 28.4% and 4.7% pixel detection efficiency as measured at the bias current 95% of their respective critical current at 2.2 K.

*Physics does not consist only of atomic research,
science does not consist only of physics,
and life does not consist only of science.
The aim of atomic research is to fit our empirical knowledge
concerning it into our other thinking.*

Erwin Schrödinger (1887-1961)

Table of Contents

Abstract	i
List of Tables	v
List of Figures	xviii
List of Publications by the Candidate	xix
Acknowledgement	xxi
Author's Declaration	xxii
Glossary	xxiii
Physics Constants (SI unit)	xxiii
Physics Symbols (SI unit)	xxiii
Maxwell's Equations (CGS unit)	xxiii
Acronyms	xxiv
1 Introduction	1
1.1 Motivation	2
1.2 Thesis Outline	2
2 Background	4
2.1 Photon Counting: Current Technology and Emerging Applications . .	4
2.1.1 Photomultiplier Tube	6
2.1.2 Single-Photon Avalanche Photodiode	7
2.1.3 Superconducting Detectors	8
2.2 Superconductivity: theoretical introduction	9
2.2.1 The Two-Fluid Model	10
2.2.2 The BCS Theory	13
2.2.3 Non-Equilibrium Superconductivity	15
2.3 The Hot-Spot Model	18
2.4 System Detection Efficiency	21
2.4.1 Optical Coupling Efficiency	21
2.4.2 Absorptance	24
2.4.3 Intrinsic Detection Efficiency	27
2.5 Dark Count Rate	28
2.6 Timing Jitter	28
2.7 Dead Time	29
2.8 Multi-Pixel SNSPD review	30

3	Experimental methods	33
3.1	Sputtering basics	33
3.1.1	DC/RF Sputtering	36
3.1.2	Magnetron Sputtering	38
3.1.3	Reactive Sputtering	40
3.2	The Magnetron Sputtering Equipment	43
3.3	Lithography	48
3.3.1	Photolithography	50
3.3.2	Electron Beam Lithography	52
3.4	Reactive Ion etching	55
3.5	Cryogenic systems	57
3.5.1	The Gifford-McMahon (GM) cycle	58
3.5.2	The Pulse Tube Refrigerator (PTR)	71
4	Thin Film Characterization	75
4.1	Selection and preparation of substrates	75
4.2	NbN thin film optimisation	76
4.3	MoSi thin film optimisation	79
4.4	Superconducting properties of patterned thin film test structures	81
5	SNSPD Array Characterization	87
5.1	Design and Fabrication	87
5.2	Sample Mount and Fibre Alignment	90
5.2.1	Zephyrator mount and alignment	90
5.2.2	Rankinator mount and alignment	98
5.3	Low Temperature Electrical and Optical Characterization	101
5.3.1	NbN Array	101
5.3.2	MoSi Array	118
6	Conclusions	123
6.1	Discussion	123
6.2	Outlook	129
	Bibliography	131

List of Tables

1	Author's contributions to the work. All elements are works of the author, excepted where stated in the text.	xxii
3.1	List and properties of targets installed in the Plassys VI as of October 2019	45
3.2	Dry Etch recipe used to realize SNSPD array and microbridges structure.	57
4.1	Lattice type of NbN, NbTiN, MgO, sapphire and Si at 300 K.	75
4.2	Critical temperature of 8nm-thick NbN and MoSi films grown at different temperature before and after the photolithography.	85
4.3	Intrinsic superconducting properties of 8 nm thickness NbN and MoSi microbridges deposited on silicon substrate: critical temperature T_c , critical current density at 0 K $J_c(0K)$, resistivity at 20 K $\rho(20K)$, sheet resistance at 20 K	85
4.4	Critical temperature, energy gap, and the inductance per square of 8nm-thick NbN and MoSi growth on pure silicon substrates at different temperatures. Inductance per square values are calculated from eq.(4.2).	86
5.1	Table of power attenuations, relative incident photon per pulse on pixels and relative photon rate per second calculated by eq.5.13 and eq.15.14. The laser wavelength is $\lambda = 1550nm$, pulsed with $\nu_{laser} = 1MHz$ and power P is calculated by equation (5.3) assuming $P_0 = 9.5\mu W$	110
5.2	Kinetic inductance and critical current of each pixel of the 8-pixels NbN SNSPD array.	116
5.3	Timing jitter of each pixel of the 8-pixels NbN SNSPD array measured at 60 dB.	117
5.4	Summary of the prototype SNSPD array properties: timing jitter, kinetic inductance, critical current, critical temperature, and pixel detection efficiency (PDE) measured when the pixel is biased 95% of its critical current.	118
5.5	Critical current at 400 mK and critical temperature of each of pixel of the 8-pixels MoSi SNSPD array.	121
6.1	Properties of NbN and MoSi useful for the fabrication of SNSPDs.	124
6.2	Critical temperature of 8-pixels SNSPD array made on 8 nm thickness NbN grown on HR Si at room temperature and at 800 °C and made on 8nm thickness MoSi grown on HR Si at -180 °C.	125

6.3	Critical temperature of 8nm-thick NbN and MoSi films grown at different temperature before and after the SNSPD fabrication.	125
6.4	Critical current of 8-pixels SNSPD array made on 8 nm thickness NbN grown on HR Si at room temperature and at 800 °C measured at 2.2 K and made on 8nm thickness MoSi grown on HR Si at −180 °C measured at 400 mK.	126

List of Figures

2.1	Diagram of the sensitivity of modern single photon detectors made via semiconductor materials (PMTs and SPADs) and via superconducting materials. The sensitivity of superconducting detectors can in principle extend to the microwave range.	5
2.2	SNSPD metrics: a) The detection efficiency (DE): three incident photons generate voltage pulses signalling the detection of a photon. The middle photon does not produce a voltage pulse indicating that the DE is less than 100%. b) The dark count rate (DCR): voltage pulses are dark signals as they are not caused by incident photons. The red voltage pulse is triggered by the detection of a photon. The black voltage pulse is a dark count as it is not caused by an incident photon. c) The timing jitter (TJ): each of the incident photons produces a voltage pulse which signals the detection of the photon. Each voltage pulse produced does not start at exactly the same time after the absorption of an incident photon. This uncertainty between the time the photon is incident on the detector and the voltage pulse starting is the timing jitter (green arrow). d) The dead time (DT). Three of the incident photons produce voltage pulses which signal the detection of each photon. One photon (middle) is incident while a voltage pulse is still present meaning that it can not be detected. This is because the single-photon detector is in a state where an incident photon will not produce a voltage pulse. The time which the single-photon detector is in the state that an incident photon will not produce a voltage pulse is the detector dead time[38].	5
2.3	Diagram of a photomultiplier tube. When a photon hits the photocathode, a photo-electron is generated and accelerated by the electric field generated between the photocathode and the anode. The photoelectron hits a series of dynodes generating secondary electrons amplifying the signal.	6
2.4	Diagram of a single photon avalanche photodiode. It consists of a p-n junction and a multiplication region. When a photon hits the junction, an electron-hole pair is generated and accelerated by the electric field generated between the junction generating a signal. . . .	7
2.5	Superconducting detectors. a) Superconducting Tunnel Junction[56]. b) Transition Edge Sensor[57]. c) Microwave Kinetic Inductance Detector[58].	8
2.6	Plot of the resistance against the temperature of a solid mercury wire immersed in liquid helium in Onnes measurement in 1911[23].	9

2.7	Difference between a perfect conductor (left) and a superconductor (right) in presence of an external magnetic field.	10
2.8	Penetration of an external magnetic field B_0 inside a superconductor.	11
2.9	Plot of the distribution of n_s density near the surface of the superconductor[64].	12
2.10	Phase diagram H-T for a) Type I superconductors and b) Type II superconductors.	12
2.11	a) Diagram of a Cooper pair: two electrons interact via phonons of the lattice. b) Feynman diagram of a Cooper pair: two electrons e^- interact between them exchanging a phonon γ	13
2.12	Energy spectrum of a) Normal metal at $T = 0$ K. All electrons condense at lower energetic level under the Fermi level respecting Pauli's law. b) Superconductor at $T = 0$ K. All electrons are bound in a bosonic system called Cooper pair, so they can condense at the ground level.	14
2.13	Plot of the equation (2.9) showing the superconducting energy gap Δ as a function of temperature T	14
2.14	Schematic representation of the the two-temperature (2-T) model as a heat flow diagram[60].	16
2.15	The Rothwarf-Taylor model: schematics of carrier dynamics in the superconducting state under optical excitation[77]. a) After the absorption of an incident photon $\hbar\omega > 2\Delta$ Cooper pairs are broken generating free interacting electrons. b) Electrons interact with phonons of the lattice generating Cooper pairs by 2Δ phonons emission. c) 2Δ phonon can break Cooper pair generating new electrons that interact with phonons creating Cooper pairs by low energy phonons emission. d) Low energy phonons are expelled from the material restoring superconducting state.	17
2.16	A sketch of the normal-core hot-spot model to describe the detection mechanism of SNSPDs[79].	18
2.17	A sketch of the refined hot spot model to describe the detection mechanism of SNSPDs.[79].	19
2.18	The process of single-photon detection in according to the hot-spot model[4]. i) The superconducting device is cooled below its T_c and biased just below its critical current I_c . ii) An incident photon $h\nu > 2\Delta$ generates a normal core. iii) and iv) the normal core diffuses along the width of the device generating a resistive state. v) and vi) the normal core loses energy restoring the superconductivity in the device.	20
2.19	Diagram of the free optical coupling. The Gaussian model is used to describe how the laser beam is incident on the device placed from the SMF a distance z . The beam width $w(z)$ is calculated by equation (2.22).	22
2.20	Cross section of the fibre-to-detector assembly[87]. (a) Single-mode fibre terminated in a stainless steel and zirconia ferrule inserted into (b) a zirconia alignment sleeve (outlined for clarity). The completed detector and substrate (c) has wiring along a silicon "tongue" (d) that extends out the zirconia sleeve (e) and is wirebonded to pins (f) separated by an insulator that allow electrical connection to the electrical set-up.	24

2.21	Development of nanowire geometries[91]. In order to increase the active area (red circle), SNSPD nanowire design evolved from a straight wire to meanders covering square areas. An SNSPD array structure can be used to achieve a much larger active area.	25
2.22	Optical absorption of 5 nm thickness NbN, NbTiN, MoSi and TiN grown via magnetron sputtering process. The sputtering equipment used to fabricate these film (the Plassys VI) is described in the section 3.2. Variable angle spectroscopic ellipsometry (VASE) was employed to measure the optical properties of the materials[100].	25
2.23	Simplified sketch of distribution of the current in a 180° bend in a nanowire. The local increase of the current density over the value of critical current density leads to hotspot formation in the vicinity of the inner corner (red region) in bend disrupts the homogeneous flow (blue region) of the transport current[100].	27
2.24	a) Equivalent circuit of a SNSPD. b) Example of the output voltage pulse of the SNSPD.	29
2.25	The superconducting nanowire avalanche photodetector (SNAP) concept. Schematic of a) equivalent circuit and b) design geometry of a SNAP. Each detector can be shown with an inductor in series with a resistance. A detection event in either of detectors in the avalanche region, highlighted with red dashed rectangle, can excite neighbouring detectors causing the whole array to switch. The large change in the current is summed up and converted into a large voltage pulse by the help of the inductor L_0	30
2.26	a) Circuit diagram of a 3-PND, comprising 3 superconducting nanowire connected in parallel. Each nanowire is connected to a series resistor R_0 to minimize leakage current. b) Circuit diagram of a 2-SND, comprising 2 superconducting nanowire connected in series. Each nanowire is connected to a parallel resistor R_0	31
3.1	Diagram of the Sputtering Process.	33
3.2	IV-Characteristics of a DC discharge[136]. The DC discharge is initiated by Townsend's avalanche. The range of the Townsend discharge is almost flat. This originates from the fact that a small increase in voltage leads to a higher electron multiplication in the gap, producing more electrons and ions, giving more secondary emission at the cathode, leading to even more electrons in the gap and a further multiplication of charges. This means that for a small increase in voltage, the current rises considerably. When it is self-sustaining, the gas begins to glow intensively. The mode most often used in thin-film technology is the abnormal glow. In the high-current regime the plasma shows an electrical breakdown (arc).	35
3.3	Schematic diagram of the plasma potential distribution of a DC and an RF discharge. The RF discharge has a relatively low plasma impedance (high negative glow) at a constant discharge power compared to the DC discharge[137].	36

3.4	Scheme of magnetron sputtering process. The magnetic field (green lines) traps secondary electrons (blue) in the discharge for a longer duration, increasing the probability of ionising argon (magenta) during their travel from cathode (target) to anode (substrate).	38
3.5	Schematic representation of the plasma confinement observed in conventional and unbalanced magnetrons[142].	39
3.6	IV characteristic of the plasma during a reactive sputtering in the voltage stabilization condition[151].	41
3.7	IV characteristic of the plasma during a reactive sputtering in the current stabilization condition[151].	42
3.8	Plassys VI DC/RF Magnetron sputter deposition system installed in the JWNC (upper). CAD drawing of the sputtering tool (lower). . . .	43
3.9	a) Scheme of the MAK sputtering gun (Meivac, USA) installed in the main chamber of the sputtering tool. b) Extremity of the MAK gun where the target is placed. c) The target is bonded to a Cu backing plate with a magnetic keeper attached. d) The bonding is made by a silver paste[153].	44
3.10	Diagram of the confocal configuration installed in the Plassys VI. The guns are oriented upwards at 15° to the vertical axis, whereas the substrate holder is on axis facing downwards. The substrate holder is placed at 100 mm from targets to get the most uniform film growth over a large area.	45
3.11	A heater tape is attached to the main chamber in order to bake-out the walls of the main chamber.	46
3.12	Load lock attached to the main chamber of the sputtering tool. The transfer arm (left) is used to move the sample from the load lock (right) into the main chamber (not show)	47
3.13	The substrate carrier. It has an adaptor mount to install 6 inches (152.4 mm) diameter wafers or eventually substrates diced in 10 mm × 10 mm or 15 mm × 15 mm squares. The Molybdenum adaptor is used when substrates need to be heated, the Al one when substrates needs to be cooled.	48
3.14	The fundamentals of lithography scheme process: the sample is deposited onto a substrate after the sputtering process. The sample is then covered by a polymeric substance called resist sensitive to the high energy irradiation. The geometry of the pattern desired is designed on the mask placed between the sample and the irradiation source. After the exposure, the sample is developed and if the resist is positive the part of the part exposed are removed. If the resist is negative the part unexposed are removed.	49
3.15	Thickness of main types S1800 positive photoresist as function of the speed of the spin coating. This graph is taken from S1800 microposit datasheet[154].	50
3.16	a)Mask Aligner MA6 manufactured by SÜSS MICROTEC SE installed in the JWNC[155]. b) Power source of the exposure lamp, in this case a 350 W UV365 mercury arc discharge lamp. c) Vacuum chuck where the photomask is placed.	51

3.17	a) Vistec VB6 UHR EWF electron beam lithography equipment installed in the JWNC. b) Schematic illustrating the main principles of EBL system operation.	52
3.18	Interaction volume of e-beam exposure. As the primary electrons penetrate the resist and enter in the substrate, some of them undergo large-angle scattering events, leading to backscattering, in which these electrons return back to the resist in places far from the spot where the primary beam entered. The forward scattering arises from electron-electron interactions, which deflect the primary electrons by a typically small angle, thus statistically broadening the e-beam in the resist (and further in the substrate)	53
3.19	a)Diagram of a standard configuration for a reactive ion etch (RIE) chamber. b) Oxford Plasmalab 80 Plus Plasma Etcher installed in the JWNC. The tool is equipped by an interferometer to monitor to monitor the etch depth.	55
3.20	RIE process scheme of silicon in CF_4 plasma. Ions CF_3^+ follow the electric field direction while radicals F move randomly by Brownian motion.	56
3.21	Schematic of Gifford McMahon refrigeration cycle[165].	59
3.22	a) Gold-plated cooper circular disc filled by pogo pin holders. Each holder is made by Tufnol. b) Sample holder for eight 15 mm x 15 mm square samples. c) Samples are connected to pins by contact. On each holder is attached a calibrated temperature sensor silicon diode model DT-670. On the sample holder is installed a $1\text{ k}\Omega$ resistor to act as heater of the system.	60
3.23	a) Thermal anchoring in the Ekinator. b) Ekinator electrical set-up. The set-up is built in a metallic box to prevent electrical noise pickup. Pogo pins and the heater are connected via Fischer connectors from the cryosystem to the interface GEN8PRMX and BNC connectors. The interface is connected to a PC via the interface Labjack U6 by USB port.	61
3.24	Ekinator electric set-up scheme. a) External pogo pins are connected to the voltage source across a relay onto the interface GEN8PRMx and a load resistor. Pins in the middle are connected to the voltmeter to measure the voltage drop. The bias current is given by the voltage drop across the load resistor measured by a voltmeter. b) The heater is connected to the PID controller across an amplifier (gain x10). The voltage across the heater is monitored by a multimeter in parallel to the amplifier.	62
3.25	SRS SIM900 Mainframe. From the left: SIM922 Diode Temperature Monitor, isolated voltage source SIM928, two digital voltmeter SIM970, SIM960 PID controller.	62
3.26	a) Gold-plated aluminium radiation shield machined in the workshop of School of Engineering Department of the University of Glasgow. b) Ekinator sealed by a vaccum can and connected to a turbopump (Adixen).	63

3.27	a) R-T characteristic of 8nm-thick NbN growth on HR Si substrate heated at 800 °C and patterned in a 2 μm x 200 μm microbridge. In this work, the critical temperature is taken in the middle point of the resistive transition. b) I-V characteristic at 2.1 K of 8 nm-thick NbN growth at 800 °C on HR Si and patterned in a 2 μm x 200 μm microbridge. The critical current $I_c(2.1K) = \pm 144.3\mu\text{A}$	64
3.28	Cryocooler temperature when the heater is biased via PID. The PID internal setpoint is amplified by the P200 amplifier and the cryostat temperature grows for Joule heating. To stabilize the PID output, the instrument has been configured as follows: P = 1.6, I = 1.5E-1, D=0.1E-5 to stabilize the output signal. The PID output (amplified) is monitored by a Keithley 200 multimeter.	65
3.29	(a) Zephyrator second stage (4 K). The sample holder is mounted on a stand-off-stage attached to the 4 K stage of the cryocooler. The stage is then covered by an Al thermal shield. (b) Complete image of the Zephyrator with the vacuum can. The black box attached is the feed-through of optical fibres. (c) Zephyrator electronic set-up. From the top: the TCSPC module for timing jitter measurement, the metallic box connected to the VNA for kinetic inductance measurement, the universal counter for the count rate and the mainframe SIM900 where there are installed the temperature monitor, the voltage source connected to the sample across a load resistor and a quad voltmeter. All these instrument are connected to a PC desktop and controlled via Python codes.	66
3.30	Optical set-up. All the instruments required for an optical measurement are collected in an instrumentation rack. From the top: the femtosecond mode-locked fibre Kphotonics CNT-1550-TK laser used for timing jitter measurement, oscilloscope Agilent Technologies 54845A, 8 GHz bandwidth, 1550nm laser diode source, two attenuators, a waveform generator connected to the laser source to generate pulsed laser of 5MHz frequency. Next to the drawer there is a manual polarizer. The laser power output is measured by a digital power meter. Optical fibres are checked by a FS200 fibre inspection scope (Thorlabs) before to be connected to instrument.	67
3.31	Electrical scheme for the SNSPD kinetic inductance measurement.	68
3.32	Electrical scheme for the SNSPD optical characterization.	69
3.33	Electrical scheme for the SNSPD timing jitter measurement.	70
3.34	Schematic of Pulse Tube Refrigerator operation cycle.	71

3.35	a) Picture of the sorption pumps installed in the Rankinator. b) Schematic of sorption pumps. Charcoals (black) are installed before the 4 K stage. Pump heaters (red) are biased (turned on) when the PTR reaches 40 K to ensure a major desorption of the He gas. When they are on, He gas flows into tubes (grey) to coldheads. Active Gas-Gap Heat Switches (AGHSs) (purple) dissipate heat into the ^4He and into the film burner to condense ^4He liquid (below 1 K). ^3He inside the tube is then liquefied since the tube is connected thermally to the film burner that is below 1 K. Under these conditions, the ^3He coldhead can reach a base temperature of 400 mK. Si diodes thermometers (blue) are connected on the pump heaters, heat switches and on ^4He coldhead. On ^3He coldhead is installed a RuO_2 thermometer diode (dark red).	72
3.36	Sorption pump micro-pin wiring diagram. The hermetic seal is not placed on the outer can, but inside a T-piece outside the can. This creates the extra room needed for more wiring seals[168]. Wiring are then connected to a homemade breakout box connected to Keithley current supplies, Lakeshore 224 temperature monitor and SIM921 resistance bridge.	73
3.37	a) The confocal microscope is mounted on a stack of 4 attocubes: one to move the microscope both in the X and Y direction and the other two to move respectively the microscope along the length (X), the width (Y). The Z-stepper motor need to focus the optical fibre (SMF28) on the sample. b) Scheme of the confocal microscope. c) Attocube ANC300 piezo motion controller to control three attocubes.	74
4.1	NbN critical temperature T_c versus nitrogen pressure on the total sputtering pressure expressed in percentage. NbN are grown on HR Si substrates at room temperature via DC magnetron sputtering process. The sputtering process has been run for 20 minutes to ensure the growth of large thickness film (roughly more than 100 nm). For a given total pressure P_{tot} , a maximum in the T_c can be found by varying the proportion of N_2 . This value increases with the total sputtering pressure till a maximum value. In this case the maximum value (14.6 K) corresponds to 1.7 mTorr total pressure with 10.6% nitrogen.	77
4.2	a) ICON AFM equipment installed in JWNC cleanroom. b) 1D profile plot of a NbN thin film growth on HR Si substrate and marked with a pen marker to enable a step to created by a primitive lift off procedure. The edge bump is an artifact caused by the AFM when the scanning needle jumps from a low area to a high area (the scanning direction here is from the right to the left). The measure has been made on a range of 5 μm on the lateral position. Data have been extracted from the software Nanoscope Analysis as .txt file then plotted and translated to 0 by the software OriginPro. The vertical distance represents the thickness measured. The value measured is about 9.5 nm \pm 0.01 fitting between the two levels.	77

4.3	RT characteristic of two NbN 8nm-thick films deposited on HR Si at room temperature and heated at 800 °C. The critical temperature is choose in the middle of the resistive transition. The critical temperature is enhanced and the width of the superconducting transition is decreased due to substrate heating. These data have been measured with the Ekinator (section 3.5.2).	78
4.4	RT characteristic of three unpatterned MoSi of different thickness. The insert table shows the approximate values of the thickness measured by the Icon AFM equipment.	80
4.5	RT characteristic of two MoSi 8nm-thick films deposited on HR Si at room temperature and cooled at −180 °C. The film growth on the cooled substrate shows a slight increase of the critical temperature. These data have been measured with the Ekinator (section3.5.2) . . .	80
4.6	Layout of the 2 μm x 200 μm microbridge designed for the 4-point probe characterization(section 3.5.1). External pads (I^+ and I^-) are connected to the voltage source adding a load resistor in series. Internal pads (V^+ and V^-) are connected to a voltmeter	81
4.7	Images of 8nm-thickness NbN microbridge 2 μm x 200 μm before the dry etch (a) and after the dry etch (b) taken by the Nikon Eclipse optical microscope installed in the JWNC. The microbridge is connected to four large pads. The outer pads are for passing bias current whilst the voltage drop is measured across the central pair.	82
4.8	Critical current density versus temperature for 2 μm x 200 μm NbN, 5 μm x 200 μm MoSi (growth cooling substrate) and 10 μm x 200 μm MoSi (growth at room temperature). All films are 8nm thickness. Experimental data are fitted using a Chi-squared nonlinear fit with the equation of BCS theory (2.12) to extract the critical current density at 0 K ($J_c(0)$) and the critical temperature T_c	82
4.9	RT characteristic of two 2 μm x 200 μm NbN test structures grown at room temperature (magenta) and heating the substrate at 800 °C (black), 5 μm x 200 μm MoSi (grown cooling substrate to −180 °C) and 10 μm x 200 μm MoSi (grown at room temperature). All films are 8nm-thick.	83
4.10	a) RT characteristic of 2 μm x 200 μm microbridge NbN grown at room temperature on a HR Si substrate. b) The system superconductor/substrate can be considered like two resistors R_1 and R_2 in parallel. Since their resistance is similar, at room temperature the resistance of NbN is affected by substrate resistance and the result is a lower value expected.	84

5.6	Set-up for the fibre alignment. a) The system is composed of a microscope integrated by a NIR InGaAs camera. A halogen lamp is needed to flood illuminate the sample. b) The sample mount is attached in the X-Y stage from the backside. c) Alignment of the optical fibre as observed by the NIR InGaAs camera. To cover entirely the area of the 8-pixels structure, the power output of a 1550 nm laser diode has been stabilized at 10 μ W.	91
5.7	Optical coherence tomography set-up used to measure the distance d between the device and the fibre ferrule. In this work, the distance d is measured when the system is cooled down.	92
5.8	a) Average power fibre interference spectrum and its b) Fast Fourier Transform (FFT) processed result obtained by a Matlab program. The separation distance between the chip surface and the fibre ferrule is approximately 178 μ m when the device is cooled to 2.2 K.	93
5.9	Graphical representation of eq.5.2 for the optical fibre SMF28, showing the initial beam width, $w_0 = 5.25\mu m$ and the Rayleigh length, $z_0 = 54.8\mu m$, for light with $\lambda = 1.55\mu m$	94
5.10	Map of the normalized intensity distribution of the coupling efficiency along the 8-pixels structure when the device is 178 μ m far from the optical fibre. In this map, the intensity has been calculated only in the region of pixels, while external region are considered zero intensity. The position of pixels is fixed as designed in the .gds file[Fig.5.1]. Assuming precise alignment of the fibre axis on the centre of the SNSPD array structure, when the fibre is 178 μ m far from the device, the beam covers mainly pixels in the middle (1, 2, 5 and 6).	95
5.11	Upper: image of the .gds file representing the 8-pixels structure composed by 8 meander structure $10\mu m \times 10\mu m$ dimensions. By the software is possible to estimate coordinates of each point of the structure. In this case the origin ($x = y = 0$) is settled in the middle of the rectangle. Down: in this configuration, coordinates of the pixel 1 are respectively $x_1 = -1$, $x_2 = -12$, $y_1 = -3$ and $y_2 = 14$. These coordinates are taken from the beginning to the end of the meander structure (the black region is the nanowire). Coordinates of other pixels have been taken in the same way.	96
5.12	Calculated ratio of optical power plotted as a function of vertical distance z between the end of the fibre to the device.	97
5.13	a) Sample mount made to be attached under the microscope under ^3He coldhead of the Rankinator	98
5.14	Cross section of the microscope lens set-up. Laser beam comes out from the optical fibre(right hand side), it is collimated by a Geltech 352280-C lens (focus length $F = 18.40$ mm, numerical aperture $NA = 0.15$) and then focused by a Geltech 352330-C lens ($F = 3.10$ mm, $NA = 0.68$). Both these lenses come with an anti-reflection coating (AR) designed for 1050 nm to 1700 nm as reported in their datasheet (Thorlabs website). From Sparrow's criterion, at 1550 nm wavelength, the expected beam waist in at the focus is 1.19 μ m. In the Rankinator setup with vibration damping, the best measured spot side is 2.3 μ m (left hand side).	98

5.15	Sparrow criterion. Using the focusing lens with $NA = 0.68$, the minimum resolvable FWHM for 1550nm light is $1.19 \mu\text{m}$, but internal vibrations of the cryosystem generate a spot size of about $2.3 \mu\text{m}$ [168].	99
5.16	Experimental set-up to build a reflection map of the device under test in the Rankinator at 5 K to avoid heating of piezoelectric motors.	100
5.17	Coupling efficiency into $10\mu\text{m} \times 10\mu\text{m}$ SNSPD device plotted as a function of distance between the fibre end and the device in the Rankinator cryostat. The coupling efficiency is calculated by equation(5.7).	100
5.18	IV characteristic at 2.2 K of the pixel 1 of the SNSPD array structure made via 8nm-thick NbN grown on a HR Si substrate at room temperature. Due to the large normal state resistance, the current across the superconducting nanowire drops when it switches into the resistive state. Large normal state resistance produces large Joule heating generating hysteresis in the plot (red circle).	101
5.19	Histogram of critical currents measured at 2.2 K of 8 nm thickness NbN SNSPD 8-pixels array grown heating HR Si substrate to 800°C .	102
5.20	Normalised resistance versus temperature of odd numbered pixels of the 8nm thickness NbN SNSPD array grown heating HR Si substrate at 800°C . The resistance of pixels is normalized respect to normal resistance R_n measured at 10 K.	103
5.21	Histogram and table of critical currents measured at 2.2 K of all 8-pixels SNSPD array made via 8nm-thick NbN grown on Si substrate at room temperature (RT). The mean value of critical current and the discrepancy for this system are respectively $J_c^{mean} = 7.925 \mu\text{A}$ and $\sigma = 1.0912 \mu\text{A}$.	104
5.22	RT characteristic of the 8-pixels NbN SNSPD array grown at room temperature. The mean critical temperature is $T_c^{mean} = 4.44 \text{ K}$ and the standard deviation is $\sigma = 0.23 \text{ K}$. Large discrepancies of normal resistances (in particular of pixel 2) can be associated with the proximity effect of the e-beam lithography process that can affect dimensions of pixels.	104
5.23	Amplified dark signal as measured by the oscilloscope at 2.2 K of the pixel 1 of the SNSPD array structure on 8nm-thick NbN grown on silicon substrate at room temperature. The total gain is 56 dB (amplifier-chain RF Bay Inc. LNA-580 23 dB gain and LNA-1000 33 dB). The pixel 1 is biased near its critical current ($8 \mu\text{A}$). The red line represents the trigger (100 mV) of the oscilloscope(8 GHz bandwidth). The peak of the amplified signal is about 127 mV.	105
5.24	Enlargement plot of the dark signal (no amplified). The red line is the fitting equation 5.10. The rest time extracted from the fit is about $\tau = 9\text{ns}$ Negative voltages (below 0 V) is because the amplifier chain has a poor low frequency response (10 - 580 MHz for LNA-580 and 10 - 1000 MHz for LNA-1000). The amplifier chain acts as a high pass filter.	106
5.25	Dark count rate against bias current measured at 2.2 K of the 8-pixels SNSPD array structure on 8nm-thick NbN grown at room temperature.	107

5.26	Normalized photon count rate against bias current (normalized to the critical current) of pixel 1. The photon count rate is higher when the device is illuminated in TE mode, that means that the absorption of the device increase when the incident light is TE polarized.	108
5.27	Photon count rate at different attenuation measured at 2.2 K of pixel 1 of the SNSPD array structure on 8nm-thick NbN grown on HR Si at room temperature. Bias current is normalized to the respective critical current ($I_c = 8\mu A$). The attenuation starts from 11 μW at 0 dB attenuation (10^7 photons per pulse) to 69 dB (10 photons per pulse).	108
5.28	Photon count rate at 2.2 K for 8-pixel SNSPD array based on 8 nm thick NbN deposited on HR silicon at room temperature. Bias current is normalized to their respective critical current[Fig.5.21]. High photon flux, incident optical power 11 μW , 1550 nm wavelength, repetition frequency 1 MHz.	110
5.29	Photon count rate at 2.2 K for the 8-pixels NbN SNSPD array structure. Bias current is normalized to their respective critical currents. Laser is attenuated to 50 dB corresponding to 860 photons per pulse from the end of the fibre tip.	111
5.30	Photon count rate at 2.2 K for the 8-pixels NbN SNSPD array structure. Bias current is normalized to their respective critical currents. Laser is attenuated to 70 dB corresponding to 8.6 photons per pulse from the end of the fibre tip.	112
5.31	Pixel detection efficiency (PDE) in a) linear scale and b) logarithmic scale of each pixels using equation (5.16). Laser beam is attenuated to 70 dB to bring the 8-pixels structure in the single photon regime[Table 5.1]. Bias current is normalized to their respective critical currents.	113
5.32	Optical coupling efficiency as function of vertical distance z between the end of the fibre to the device. The simulation has been made assuming the middle of the pixel 4 as the centre of the laser beam. Other pixels are discarded because they were not connected during the second cooldown.	114
5.33	Plot of the kinetic inductance of pixel measured by the VNA at 2.2 K. The critical current of the pixel is reduced to the expected value ($8 \mu A$) due of the electrical noise of the electrical set-up built for the kinetic inductance. The kinetic inductance at 0 μA is about 1 μH	115
5.34	Timing jitter of the pixel 5 measured attenuating the laser beam at 60 dB. The plot is taken from the software HydraHarp. The FWHM of the Gaussian curve is calculated automatically by the software. The FWHM is 140 ps.	117

5.35	IV characteristic at 400 mK of the pixel 1 of the SNSPD array structure made via 8nm-thick MoSi. The y-axis is the bias current settled by the DC current source (the instrument is controlled by a Python code) and the x-axis is the voltage drop of the device. The pixels is biased between $\pm 1\mu A$. The device enter into the resistive state when $I_c = 0.74\mu A$. When the device is biased in the negative region $I_c = -0.7\mu A$. This offset is due to the electrical noise of the instrument since it does no work with battery as the voltage source SIM928.	119
5.36	Histogram of critical currents measured at 400 mK of 8 nm thickness MoSi SNSPD 8-pixels array. Pixel 6 and 7 are respectively an open and a short circuit.	119
5.37	a) Resistance versus temperature measurement characteristic of 6 pixels of the 8nm thickness MoSi SNSPD array. Only pixel 1, 2, 4 and 5 exhibits similar curve shape while pixel 3 and 8 exhibit a comparable resistive state, but large spread of critical temperature. b) RT characteristic of pixels 1, 2, 4 and 5. Their critical temperature is 4 K	120
5.38	Dark signal of pixel 4 of 8 nm thickness MoSi grown cooling the substrate to $-180^\circ C$ (red). The peak of this dark signal is 107 mV for the MoSi. The dark signal of MoSi device appears in absence of bias. This effect is due to thermal effect of BeCu coax cables to connect the device to the room temperature electric set-up causing a voltage offset.	121
5.39	Dark Count Rate of pixels 2 and 4 of 8nm MoSi SNSPD array. Dark rate is present even when pixels are not biased due due to thermal effect of coaxial cables that connect pixels to the room temperature instrument.	122
6.1	SEM images of the SNSPD array realized via 8 nm thickness NbN. The system is composed of 8 pixels embedded in a $50\ \Omega$ CPW. Ground is common and each pixel is biased independently.	123
6.2	a) OFHC copper cap for optical coupling. b) Complete sample mount with optical coupling and c) its scheme. The fibre ferrule is inserted in the middle of the cap and kept hold by a clamp screwed on the top. The distance of the fibre from the device (Z-axis) is controlled by the use of thin steel shims.	128

List of Publications by the Candidate

Journal

U. Nasti, L. Parlato, M. Ejrnaes, R. Cristiano, T. Taino, H. Myoren, R. Sobolewski, and G. Pepe, “Thermal fluctuations in superconductor/ferromagnet nanostripes”, Physical Review B 92, 014501 (2015).

L. Parlato, U. Nasti, M. Ejrnaes, R. Cristiano, H. Myoren, Roman Sobolewski and G. Pepe, “Dark counts in superconducting single-photon NbN/NiCu detectors”, Proc. of SPIE Vol. 9504 950404-1, (2015).

L. Parlato, M. Ejrnaes, U. Nasti, R. Arpaia, T. Taino, T. Bauch, H. Myoren, Roman Sobolewski, F. Tafuri, F. Lombardi, R. Cristiano, and G. Pepe, “Investigation of dark counts in innovative materials for superconducting nanostripe single-photon detector applications”, Proc. of SPIE Vol. 10229 102290I-1, (2017).

A. Banerjee, R. M. Heath, D. Morozov, D. Hemakumara, U. Nasti, I. Thayne and R. H. Hadfield, “Optical properties of refractory metal based thin films”, Optical Materials Express 2072, Vol. 9, No. 8 (2018).

Conferences

U. Nasti, L. Parlato, M. Ejrnaes, R. Cristiano, T. Taino, H. Myoren, R. Sobolewski, and G. Pepe, Thermal fluctuations in superconductor/ferromagnetic nanostripes, Superconductors-based sensors and quantum technologies Workshop, Moscow State Pedagogical University, Moscow, Russia, April 2016 (Oral Presentation).

U. Nasti, D. Morozov, G. Taylor, A. Banerjee, R. M. Heath, A. Casaburi and R. H. Hadfield, Characterization of emerging materials for large area superconducting nanowire single-photon detector arrays, Applied Superconductivity Conference 2018, Washington State Convention Center, Seattle, Washington, USA, November 2018 (Poster).

U. Nasti, D. Morozov, G. Taylor, A. Banerjee, R. M. Heath, A. Casaburi and R. H. Hadfield, Thin film optimization for superconducting nanowire single-photon detector array, 14th European Conference on Applied Superconductivity, Scottish Exhibition Centre, Glasgow, United Kingdom, 1st-5th September 2019 (Poster).

U. Nasti, D. Morozov, G. Taylor, A. Banerjee, R. M. Heath, A. Casaburi and R. H. Hadfield, Emerging materials for superconducting nanowire photon counting arrays, Superconducting Quantum Devices 2019 Workshop, James Watt School of Engineering, James Watt South Building, University of Glasgow, Glasgow, United Kingdom, 5th-6th September 2019 (Oral Presentation).

Acknowledgement

First and foremost, I would like to thank my supervisor Prof. Robert Hadfield, to give me the opportunity to join his research group as PhD student. I am really grateful for his help especially at the beginning of my PhD, guidance and supervision throughout the duration of my PhD studies during these four years.

I would like to acknowledge the European Research Council for the funding that has supported me throughout my work.

I would like to show my gratitude to my second supervisor Dr. Alessandro Casaburi, for his support and advices.

A special thanks to Dr. Archan Banerjee who showed me how to manage the sputtering equipment making me able to realize superconducting thin films for my research, to Dr. Kleanthis Erotokritou and Dr. Dmitry Morozov for their great friendship, support and training in the labs and a special thanks to Dr. Andrea Pizzone for his precious help to introduce me in the group.

I thank my fellow lab mates Jon Collins, Koran Jackson, Gregor Taylor and Konstantinos Tsimvrakidis, for the stimulating discussions and for all the fun we had in the lab and in the office.

Many thanks also to the postdoc members of quantum sensors group who were present throughout this journey, thanks to Dr. Robert Heath, Dr. Jharna Paul and Dr. Gavin Orchin.

It has been a real pleasure to be part of the James Watt Nanofabrication Centre (JWNC). Especially, thanks to Mr. David Gourlay and Mr. Jon Humphreys for their support in the maintenance of the sputtering equipment, to Mrs Helen McLelland for her training in the use of scanning electron microscopes (SEMs) essential for device inspection and to Mr. Michael Duffy for his assistance during dry etch processes.

Author's Declaration

I, UMBERTO NASTI, declare that, except where explicit reference is made to the contribution of others, this thesis is the result of my own work and has not been submitted for any other degree at the University of Glasgow or any other institution. For the avoidance of ambiguity, a full breakdown of my personal contribution is stated in Table 1

Table 1: Author's contributions to the work. All elements are works of the author, excepted where stated in the text.

Chapter	Personal Contribution
1	Text
2	Text; graphics
3	Text; graphics; Ekinator upgrade: installation of the heater, changing of pogo-pins, re-wiring of the system, new electrical set-up box, installation of calibrated thermometers, PID configuration.
4	Text; graphics; graph data; NbN and MoSi sputtering recepies; Icon AFM, photomask, photolithography process
5	Text; graphics; graph data; SNSPD array CAD design with the aid of Dr. Dmitry Morozov, e-beam lithography with advice from of Dr. Dmitry Morozov and Dr. Jharna Paul, OCT measurement with the aid of Dr. Gavin Orchin, device characterization, optical nano-mapping with the aid of Dr. Dmitry Morozov and Dr. Gavin Orchin
6	Text

Glossary

Physical Constants (SI unit)

c	Speed of Light	3×10^8	m/s
h	Planck's constant	6.63×10^{-34}	J s
k_B	Boltzmann Constant	1.38×10^{-23}	J/K
e	Electron Charge	1.6×10^{-19}	C
m_e	Electron Mass	9.11×10^{-31}	kg
ξ_0	Free Space Electric Constant Permittivity	8.85×10^{-12}	C ² /Nm ²
μ_0	Free Space Magnetic Constant Permeability	1.26×10^{-6}	kg m/s ² A ²

Physical Symbols (SI units)

ρ	Density	kg/m ³
n	Charge Carrier Density	1/m ³
\mathbf{E}	Electrical Field	V/m
\mathbf{B}	Magnetic Field Flux Density	kg/s ² A
\mathbf{H}	Magnetic Field Strength	A/m
\mathbf{J}	Current Density	A/m ²
\mathbf{v}_F	Fermi Velocity	m/s
E_g	Semiconductor Energy Gap	eV*
Δ	Superconducting Energy Gap	eV*
ξ_0	Coherence Length	m
λ_L	London Penetration Length	m

Maxwell's Equations (CGS units)

$$\nabla \cdot \mathbf{E} = 4\pi\rho \qquad \nabla \times \mathbf{E} = -\frac{1}{c} \frac{\partial \mathbf{B}}{\partial t}$$

$$\nabla \cdot \mathbf{B} = 0 \qquad \nabla \times \mathbf{B} = -\frac{4\pi}{c} \mathbf{J} + \frac{1}{c} \frac{\partial \mathbf{E}}{\partial t}$$

*Energy Gaps are expressed in CGS units.

Acronyms

2-T Model	Two Temperature Model
ABS	Absorptance
AGHS	Active Gas-Gap Heat Switch
AFM	Atomic Force Microscope
ALD	Atomic Layer Deposition
ARC	Anti-Reflection Coating
BCS Theory	Bardeen-Cooper-Schrieffer Theory
BKT Transition	Berezinskii–Kosterlitz–Thouless Transition
CGS	Gaussian Unit System (Centimetre-Gram-Second)
CPW	Coplanar Waveguide
DBR	Distributed Bragg Reflector
DC	Direct Current
DCR	Dark Count Rate
DE	Detection Efficiency
DT	Dead Time
EBL	Electron Beam Lithography
FFT	Fast Fourier Transform
FWHM	Full Width Half Maximum
FDM	Frequency-Division Multiplexing
GM	Gifford-McMahon
HR	High Resistivity
IDE	Internal Detection Efficiency
IMA	Interantional Advanced Materials
IPA	Iso-Propyl Alcohol
KJLC	Kurt J. Lesker Company Ltd
LIDAR	Light Detection and Ranging
LNA	Low Noise Amplifier
MIBK	Methyl Isobutyl Ketone
MKID	Microwave Kinetic Inductance Detector
MMS	Materials Microelectronics and Services
NA	Numerical Aperture
OCE	Optical Coupling Efficiency
OCT	Optical Coherence Tomography
OFHC	Oxygen-Free High Thermal Conductivity
OPO	Optical Parametric Oscillator
PCB	Printed Circuit Board
PID	Proportional Integral Derivative
PMT	PhotoMultiplier Tube
PTR	Pulse Tube Refrigerator
QOC	Quantum Optical Communication
QPs	Quasi-Particles

R-T Model	Rothwarf-Taylor Model
RF	Radio Frequency
RIE	Reactive-Ion Etching
RRR	Residual Resistance Ratio
SEM	Scanning Electron Microscope
SDE	System Detection Efficiency
SI	International System of Units (Metre-Kilogram-Second)
SMF	Single Mode Fibre
SNAP	Superconducting Nanowire Avalanche Photodetectors
SNSPD	Superconducting Nanowire Single Photon Detector
SPAD	Single Photon Avalanche Diode
SPD	Single Photon Detector
STJ	Superconducting Tunnel Junction
TCSPC	Time-Correlated Single-Photon Counting
TE	Transverse Electric
TES	Superconducting Transition Edge Sensors
TJ	Timing Jitter
TM	Transverse Magnetic
VNA	Vector Network Analyzer
VRU	Variable Resolution Unit

Chapter 1

Introduction

The detection of single quanta of electromagnetic radiation (single photons) has been motivated by applications such as medical imaging and diagnosis, chemical analysis, astronomy and communication. Quantum technologies for information processing promise unparalleled information processing and secure telecommunications capabilities. Modern single photon detectors like the PhotoMultiplier Tube (PMT) or the Single Photon Avalanche PhotoDiode Detector (SPAD) are still widely used in many photon-counting applications. In 2001, Gol'tsman realized a detector via thin film NbN superconductor patterned into a nanowire via electron beam lithography. This device demonstrated a single photon sensitivity to 810 nm wavelength photons with excellent timing resolution[1]. In general a Superconducting Nanowire Single Photon Detector (SNSPD) is a device that works at liquid helium temperature (about 4 K) and is current-biased just below the superconducting critical current. When a photon is detected by the device, this generates a series of non-equilibrium effects that generate a resistive state along the width the device causing a voltage drop. The microscopic physical mechanism in the nanowire after absorbing an incident photon is explained by the so called hot-spot model[2, 3] and it will be discussed in detail in the next chapter. Since the first considerations, this type of detector has stimulated ambitious research by many groups across the world[4]. SNSPDs gain from an extremely wide spectral sensitivity from the X-ray[5] to the mid-infrared regime[6]. It is even used for neutron measurements and other elementary particles[7]. A very low dark count rate[8] and non-comparable low time jitter values down to 3 ps[9] make them interesting for time-correlated single-photon counting (TCSPC) measurements[10]. This intensive research effort has led highly competitive detector parameters, making them suitable for many applications in optics, communication and imaging[4, 11]. Up to now, much research has been done to optimize the detection parameters like detection efficiency, dark count rate, recovery time and jitter times[11]. Many single-photon detector technologies have been implemented in array formats, including Geiger-mode avalanche photodiode[12, 13], microchannel plates[14, 15], and transition edge sensors[16, 17]. Linear arrays can be used to extract spectral information using a diffraction grating or prism, and two-dimensional arrays are often used to extract spatial information while maintaining the temporal information and single-photon sensitivity that the individual single photon detectors provide. Alternatively, by spreading a single optical mode across multiple single-photon detectors, photon-number-resolution[18, 19] and higher counting rates[19] can be achieved.

1.1 Motivation

One of the challenges in the fabrication of SNSPD arrays is the choice of the superconducting material. This choice is based on two factors: by the optical properties of the material at telecommunications wavelength (1550 nm) or in general in the infrared range and by the uniformity of the superconducting properties of the materials. Uniformity becomes relevant especially for the fabrication of large area arrays. The standard material used for SNSPD fabrication is polycrystalline NbN, chosen mainly for its high critical temperature for very thin films[20] but its crystalline structure makes this material susceptible to constrictions over large area limiting the active area of the SNSPD to a maximum of $63\ \mu\text{m} \times 63\ \mu\text{m}$ [21]. However, amorphous materials such as MoSi are also desirable for the fabrication of SNSPDs due to their lack of a well-defined crystal structure and they can be easily deposited on any substrate without a particular lattice matching allowing high degree of homogeneity and uniformity over large areas[22]. The aim of this research is focused on testing the uniformity of multipixel SNSPD array fabricated via NbN and MoSi thin films in terms of their superconducting properties and of their optical properties at telecommunications wavelength.

1.2 Thesis Outline

The thesis is structured as follows:

- **Chapter 2: Background**

In this chapter the theoretical background behind SNSPDs is explained. Firstly, the chapter introduces a brief section about the current state-of-the-art in photon counting technologies. Then follows a discussion of superconductivity phenomena, explaining concepts such as the critical temperature and energy gap. In the next section, the microscopic effects inside the superconductor after absorption of the photon are explained and the hot-spot model, is introduced. SNSPD metrics such as quantum efficiency, dark counts, timing jitter and dead time are presented, highlighting recent improvement in each one of these characteristics. In conclusion, the chapter presents an overview of the SNSPD multipixel array configuration and recent developments.

- **Chapter 3: Experimental Methods**

This Chapter explains experimental methods for SNSPD array fabrication and testing. The process of fabrication of a SNSPD follows three steps: deposition on a substrate, lithography and reactive-ion etching to define the geometry. After fabrication, the device needs to be installed in a cryostat and cooled below its critical temperature to be characterized both electrically and optically. The next section of this chapter is then dedicated to the equipment used for the fabrication and test of SNSPD arrays realized for this thesis. Each experimental method is introduced by a brief theoretical introduction of the process.

- **Chapter 4: Thin Film Characterization**

Before realizing SNSPD arrays, it is necessary to get information about superconducting properties of thin films made via sputtering. In this chapter describes the optimization of the critical temperature of bulk (over 100 nm thickness) NbN varying the concentration of nitrogen over the total sputtering pressure. Once that the highest critical temperature is achieved, this becomes the starting point to fabricate 8-nm thick NbN. Since MoSi has been made using an alloy target, some films with different thickness have been sputtered to determine the sputtering rate to realize the 8-nm thickness MoSi. The chapter concludes with the discussion of the experimental data of the superconducting properties of 8-nm thickness NbN and MoSi.

- **Chapter 5: SNSPD Array Characterization** This chapter highlights electrical and optical performance of SNSPDs arrays realized in 8-nm thickness NbN and MoSi thin films. First, the prototype 8-pixels layout is introduced. Each pixel is a meander structure that covers $10\ \mu\text{m} \times 10\ \mu\text{m}$ area, with a nanowire width of 100 nm. Following will be described the process of optical alignment of the device (sample mount and optical set-up). The Gaussian beam model is used to simulate the light beam when it leaves the optical fibre to the device to achieve information about the optical coupling efficiency. Devices are then characterized electrically to measure the critical temperature and the critical current of each pixels and optically to study the single photon response under illumination at 1550 nm wavelength of each pixel.

- **Chapter 6: Conclusions**

In the final chapter, results of the previous chapter are discussed and overall conclusions of the work will be presented concluding with an outlook on future research directions.

Chapter 2

Background

This chapter introduces the theoretical concepts and background underpinning superconducting nanowire single-photon detectors (SNSPDs). Firstly, an introduction to photon counting is presented, introducing the main classes of photon counting detectors based on semiconductor and superconducting materials. Then a discussion of superconducting phenomena is given, explaining the established theories of superconductivity and introducing concepts of Cooper pairs and gap energy. To macroscopic models are then discussed two main microscopic models to explain the interaction between an incident photon and a superconductor and the hotspot model to explain the photon detection mechanism in SNSPDs is described. Strategies for optimising detection efficiency, minimizing dark counts, timing jitter and dead time in SNSPDs are discussed. The chapter concludes with an overview of the evolution of SNSPD geometry from single nanowires to array configurations plus the challenges of fabrication and implementation of scalable electronic readout.

2.1 Photon Counting: Current Technology and Emerging Applications

Single photon detectors (SPD) are an important enabling technology for many emerging photonic applications including quantum optical communications (QOC). Since information packets are stored in single photons as predicted by the Planck-Einstein relation[36, 37]:

$$E = h\nu = \frac{hc}{\lambda} \quad (2.1)$$

these devices are able to count millions of photons per second, determine at what instant the photon arrived and able to distinguish if the signal detected is a photon from the source. SPD sensitivity depends strongly on the material used to fabricate the detector. SPD made of semiconductor material such as photomultiplier tubes (PMTs) or single photon avalanche diodes (SPADs) perform well across the visible wavelength range but in the infrared their sensitivity drops steeply because the photon energy is comparable to the semiconductor energy gap (of order one electronvolt [eV]). Detectors made of superconducting material with a characteristic superconducting energy gap of order meV (section 2.2.2) can in principle operate as photon counters as far as the microwave range[Fig.2.1].

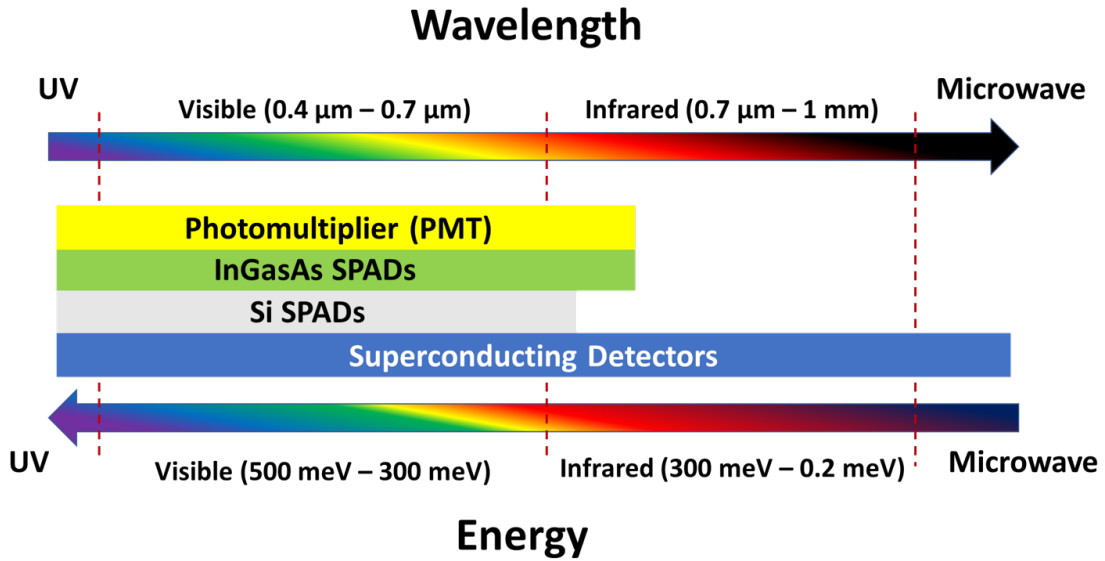


Figure 2.1: Diagram of the sensitivity of modern single photon detectors made via semiconductor materials (PMTs and SPADs) and via superconducting materials. The sensitivity of superconducting detectors can in principle extend to the microwave range.

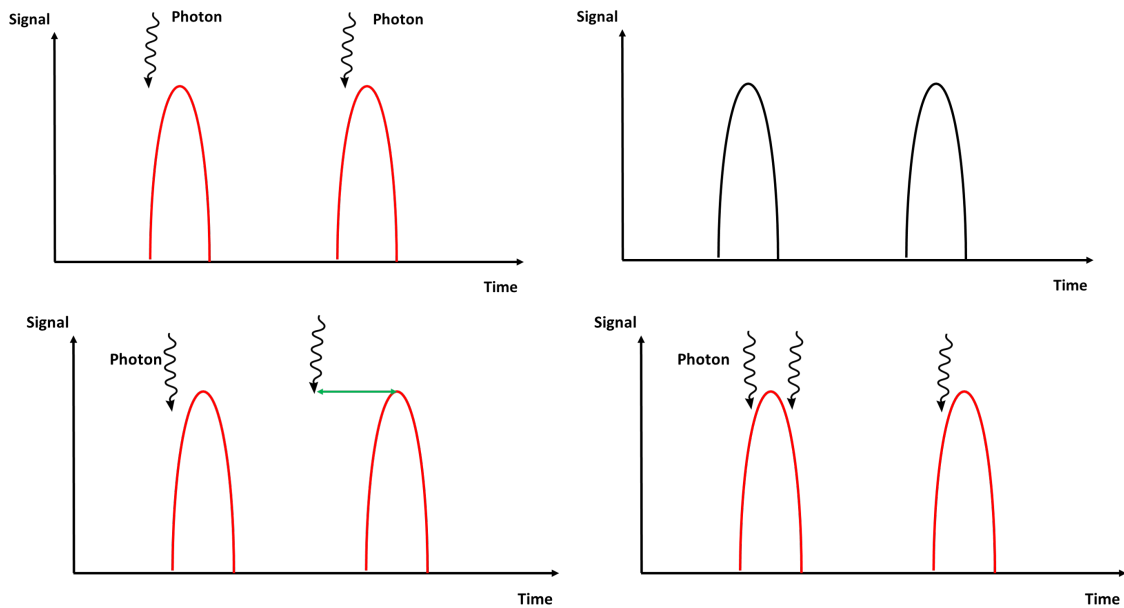


Figure 2.2: SNSPD metrics: a) The detection efficiency (DE): three incident photons generate voltage pulses signalling the detection of a photon. The middle photon does not produce a voltage pulse indicating that the DE is less than 100%. b) The dark count rate (DCR): voltage pulses are dark signals as they are not caused by incident photons. The red voltage pulse is triggered by the detection of a photon. The black voltage pulse is a dark count as it is not caused by an incident photon. c) The timing jitter (TJ): each of the incident photons produces a voltage pulse which signals the detection of the photon. Each voltage pulse produced does not start at exactly the same time after the absorption of an incident photon. This uncertainty between the time the photon is incident on the detector and the voltage pulse starting is the timing jitter (green arrow). d) The dead time (DT). Three of the incident photons produce voltage pulses which signal the detection of each photon. One photon (middle) is incident while a voltage pulse is still present meaning that it can not be detected. This is because the single-photon detector is in a state where an incident photon will not produce a voltage pulse. The time which the single-photon detector is in the state that an incident photon will not produce a voltage pulse is the detector dead time[38].

The most crucial performance metric of a SPD is the probability of registering a count event after incidence of a photon on the detector. This metric, which is called detection efficiency DE depends on optical properties of the film, detector geometry and energy of incident photons. Stray light and electrical noise can also potentially mimic the optical signal. These false detection events are called dark counts, usually quantified in terms of a dark count rate (DCR). The timing uncertainty between the arrival of the photon at the SPD (which can be known extremely precisely with modern optical sources) and the generation of the output pulse from the SPD, may set the timing resolution. This is known as the timing jitter (TJ) of the SPD. In addition, a SPD has a finite recovery time before it is ready to detect a subsequent photon. This parameter is defined as the dead time (DT) of the detector. This sets a limit on the theoretical maximum count rate of the SNSPD (which in practice may be limited by other factors, such as the readout electronics). The [Fig.2.2] illustrates the key metrics of SPDs described before.

2.1.1 Photomultiplier Tube

The first SPD ever invented is the photomultiplier tube (PMT) introduced for the first time in the 1950s[39, 40]. PMTs are based on the photoelectric effect: a photon generates an electron at the cathode, which is accelerated inside a vacuum tube by biased metal plates known as dynodes. The electron current is amplified every time it hits the dynodes by secondary electron emission and it is measured at the anode[Fig.2.3]. The main reason PMTs are still used in some applications is that they are macroscopic devices with large collection area (about 10 cm diameter). In the range of visible light, PMTs have a maximum efficiency of 40% at 500 nm wavelength, a dark count rate of about 100 Hz and a timing jitter of 300 ps[41]. The sensing part of the PMT known as the photocathode is typically made of semiconductor materials, so for use at 1550 nm wavelength, PMT has to be operated at low temperature reaching a maximum value of 2% detection efficiency at 200 K[41, 42].

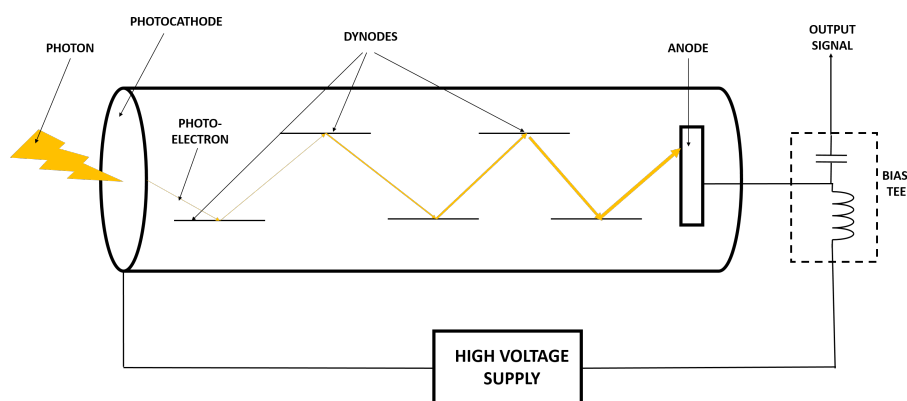


Figure 2.3: Diagram of a photomultiplier tube. When a photon hits the photocathode, a photo-electron is generated and accelerated by the electric field generated between the photocathode and the anode. The photoelectron hits a series of dynodes generating secondary electrons amplifying the signal.

2.1.2 Single-Photon Avalanche Photodiode

The single-photon avalanche photodiode (SPAD) is the other main type of single-photon detector based on semiconductor materials. These detectors are based on a p-n junction structure. A p-n junction[43] is an interface between two types of semiconductor materials (p-type and n-type) inside a single crystal of semiconductor: the p-type (positive) side that is characterized by a reduced number of electrons exceeding holes while the n-type (negative) side contains an excess of electrons. These sides are created by doping[43] for example by ion implantation, diffusion of dopants, or by epitaxy (growing a layer of crystal doped with one type of dopant (for example p) on top of a layer of crystal doped with another type of dopant (for example n)). The photodiode works when the p-n junction is reverse biased. In this condition, the p-type side is connected to the negative terminal of a bias source, while the n-type side is connected to the positive one[Fig.2.4]. In this configuration the junction behaves as an insulator[43]. When a photon interacts with the junction, it creates an electron-hole pair and is then accelerated in the junction by the bias voltage across the junctions generating an output signal. Like PMTs, SPADs have to be operated at low temperature. Silicon SPADs at 250 K are able to detect single photons with an efficiency of 65% at 650 nm wavelength, a noise level of 25 Hz, and a timing jitter of 400 ps[42]. The energy gap of Si limits photon counting sensitivity to around 950 nm wavelength. At 1550 nm (the main telecommunications wavelength) indium gallium arsenide (InGaAs) SPADs have been developed since it has an energy gap of 0.7 eV. This detector at 210 K showed 20% efficiency at 1550 nm[44] and at 125 K showed 38% efficiency at 1310nm[45].

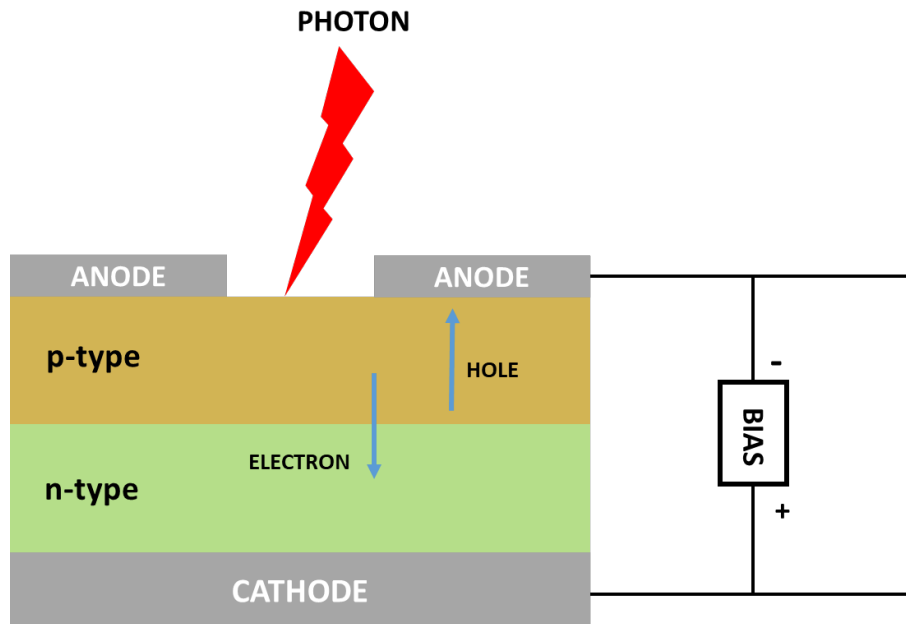


Figure 2.4: Diagram of a single photon avalanche photodiode. It consists of a p-n junction and a multiplication region. When a photon hits the junction, an electron-hole pair is generated and accelerated by the electric field generated between the junction generating a signal.

2.1.3 Superconducting Detectors

Superconducting detectors were realized to overcome limits of PMTs and SPADs in the infrared range.

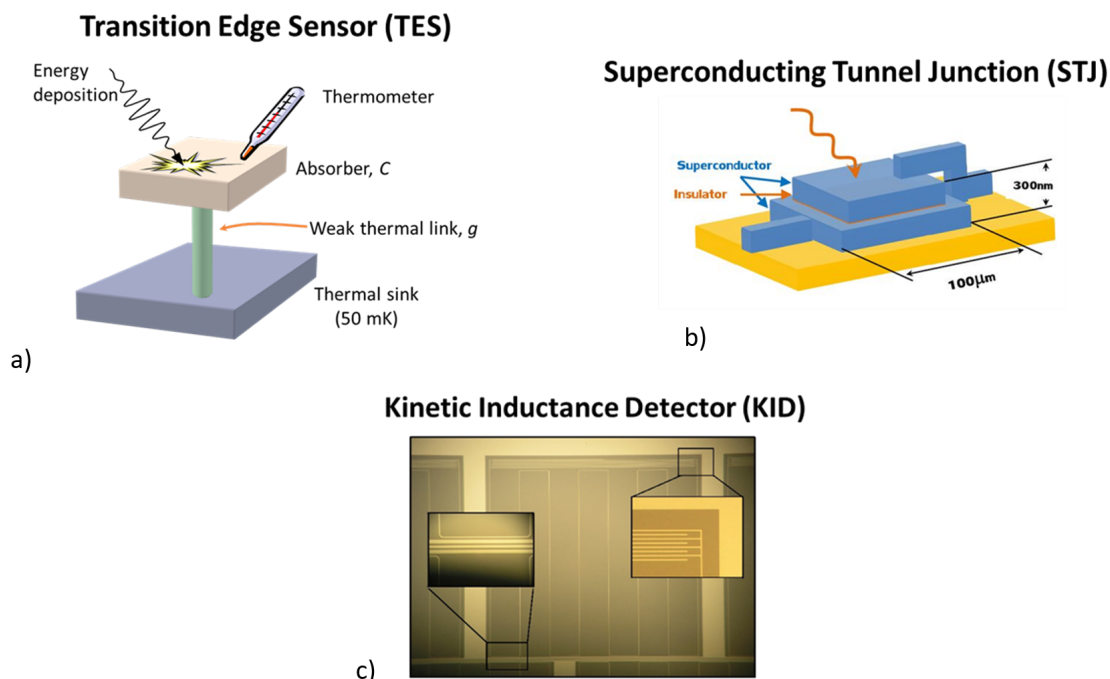


Figure 2.5: Superconducting detectors. a) Superconducting Tunnel Junction[56]. b) Transition Edge Sensor[57]. c) Microwave Kinetic Inductance Detector[58].

The superconducting transition-edge sensor (TES)[Fig.2.5 a)] was introduced in 1940s[46]. This technology uses the sharp change in resistance at the superconducting transition of a thin film. When a superconducting film is kept at a temperature close to the transition point, a single photon is able to trigger a large change in the resistance of the film. By monitoring the resistance, we can thus detect single photons. The probability of detecting a single photon at 1550 nm wavelength is as high as 95%[56]. On the other hand, TESs require about 1 microsecond to reset to detection condition and have a timing jitter of 100 ns[47]. Another type of superconducting detector is the Superconducting Tunnel Junction[Fig.2.5 b)] (STJ). It consist of two superconductors separated by a very thin layer of insulating material. The incident photon generates a current across two superconductors via quasiparticle tunnelling. This allows STJs to be used as photon-counting detectors with intrinsic energy resolution over a wide energy band from the X-ray band to the near infrared[48, 49]. The Microwave Kinetic Inductance Detector[Fig.2.5 c)] (MKID) is another type of superconducting photon detector first developed by scientists at the California Institute of Technology and the Jet Propulsion Laboratory in 2003[50]. The generation of quasi-particles after the absorption of the photon change the kinetic inductance of the superconductor. This inductance is combined with a capacitor to form a microwave resonator whose resonant frequency changes with the absorption of photons.

This resonator-based readout is useful for developing large-format detector arrays, as each detector can be addressed by a single microwave tone and many detectors can be measured using a single broadband microwave channel, a technique known as frequency-division multiplexing[51, 52]. MKIDs are being developed for a range of astronomy applications[53, 55]. Usually, TESs, STJ and MKIDs are made of superconducting materials with low transition temperature, such as tungsten (W), aluminium (Al) and titanium nitride (TiN). Thus, these detectors require expensive cryostats to be operated below 1 K making them less appropriate for commercial use. Since their discovery in 2001, SNSPDs are the most promising technology for high speed optical communications in the single photon regime. SNSPDs can be fabricated with several types of superconducting materials as NbN, NbTiN that can work at 4 K, so they do not require lower temperatures. Alternative superconducting materials are amorphous such as MoSi and WSi. Actually, the best SNSPD has been fabricated with a WSi amorphous superconductor achieving 93% quantum efficiency at 1550 nm at 2 K[59].

2.2 Superconductivity: theoretical introduction

The phenomenon of superconductivity was discovered in 1911 by Heike Kamerlingh Onnes[23]. He found that immersing a solid wire of mercury in liquid helium its DC resistance dropped to zero below 4.2 K[Fig.2.6].

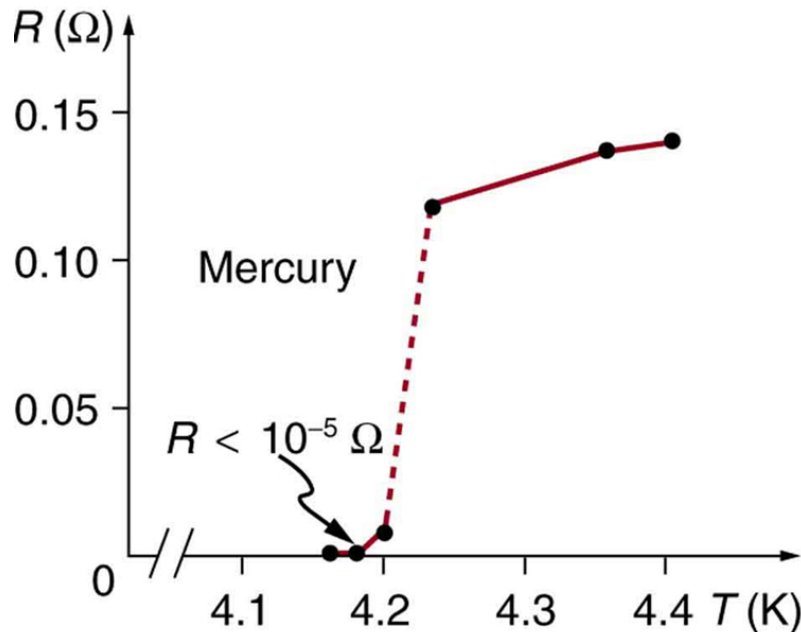


Figure 2.6: Plot of the resistance against the temperature of a solid mercury wire immersed in liquid helium in Onnes measurement in 1911[23].

This effect was interpreted as a phase transition, taking place at a critical temperature T_c . Below this temperature, the mercury passed from a normal resistive state to a state characterized by a null resistance. In 1933, Walther Meissner and Robert Ochsenfeld showed that apart from perfect conductivity with zero resistance, there was a further characteristic property of superconducting materials[61].

They observed that when a magnetic field was applied to a superconducting material it expelled the external field[Fig.2.7].

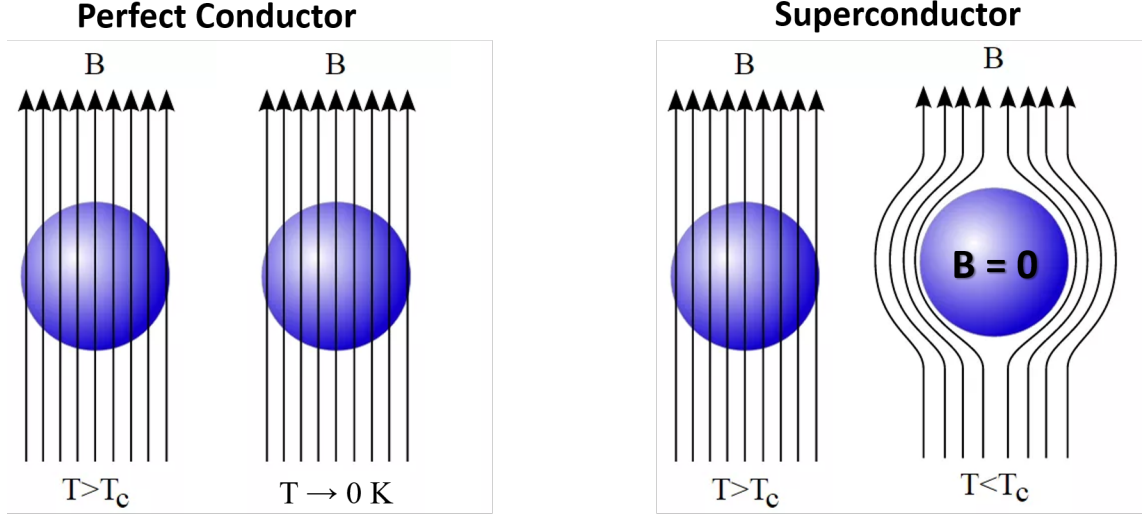


Figure 2.7: Difference between a perfect conductor (left) and a superconductor (right) in presence of an external magnetic field.

This is the property that distinguishes a superconductor from a perfect conductor: at low temperature, a perfect conductor does not expel the magnetic field applied. This means that the magnetic field in a perfect conductor must be constant: if it is null at room temperature it will be null at low temperatures, if the magnetic field is not null at room temperature it will not be expelled at low temperature.

2.2.1 The Two-Fluid Model

A first phenomenological theory to explain the effects of the superconductivity was developed by the brothers Fritz and Heinz London in 1935[62]. This theory is known as the two-fluid model. In this model, electrons in a superconductor are viewed as two fluids: one fluid consists of normal electrons and these behave in exactly the same way as the free electrons in a normal metal. When they are accelerated by an electric field, they are frequently scattered by impurities and defects in the ion lattice and by thermal vibrations of the lattice of the metal generating the electric resistance of Ohm's law. The second fluid consists of superelectrons n_s density that move in a frictionless state. In presence of an electric field \mathbf{E} then the motion equation of superelectrons is:

$$\frac{\partial \mathbf{j}_s}{\partial t} = \frac{e^2 n_s}{m} \mathbf{E} \quad (2.2)$$

where e and m are respectively the charge and the mass of electron, $\mathbf{j}_s = n_s e \mathbf{v}$ is the supercurrent density where \mathbf{v} is the velocity of electrons. The equation (2.2) represents the first London equation. Substituting this equation into Faraday's law of induction

$$\nabla \times \mathbf{E} = -\frac{1}{c} \frac{\partial \mathbf{B}}{\partial t} \quad (2.3)$$

the result is the following:

$$\frac{\partial}{\partial t} \left(\nabla \times \mathbf{j}_s + \frac{n_s e^2}{mc} \mathbf{B} \right) = 0 \quad (2.4)$$

To satisfy the Meissner effect the flux inside the superconductor must be zero so:

$$\nabla \times \mathbf{j}_s + \frac{n_s e^2}{mc} \mathbf{B} = 0 \quad (2.5)$$

Using the Maxwell equation $\nabla \times \mathbf{B} = -\mu_0 \mathbf{j}_s$, the mathematical relation $\nabla \times \nabla = \nabla \cdot \nabla - \nabla^2$ and $\nabla \cdot \mathbf{B} = 0$, the second London equation is obtained:

$$\nabla^2 \mathbf{B} - \frac{1}{\lambda_L^2} \mathbf{B} = 0 \quad (2.6)$$

where the parameter

$$\lambda_L = \sqrt{\frac{m}{\mu_0 n_s e^2}} \quad (2.7)$$

is defined as the London penetration depth and it characterizes the distance to which a magnetic field penetrates into a superconductor[Fig.2.8].

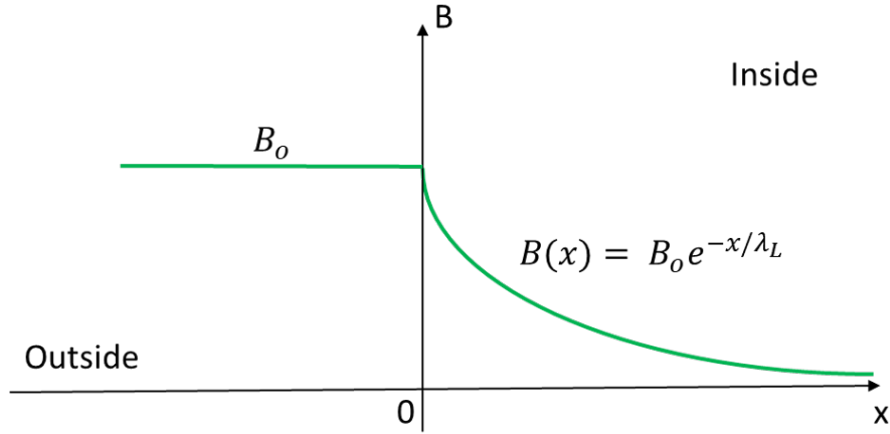


Figure 2.8: Penetration of an external magnetic field B_0 inside a superconductor.

The London equations (2.2) and (2.6) are local equations (i.e. they relate the current density j_s to the magnetic field \mathbf{B} at the same point), and hence define the superconducting properties as such. However, early discrepancies between experimental estimations of λ_L for certain conventional superconductors, led Pippard in 1950 to introduce non-local effects into the London equations[63]. Spatial changes of quantities such as the superconducting density n_s in a superconductor may only occur on a finite length scale, the coherence length ξ_o , and not over arbitrarily small distances. That is to say, whenever n_s is varying in space its value may change significantly over distances of order ξ_o . Thus the coherence length defines the intrinsic non locality of the superconducting state. Using the uncertainty principle, Pippard estimated the coherence length to be:

$$\xi_o = \hbar \frac{v_F}{\Delta} \quad (2.8)$$

where v_F is the Fermi velocity and Δ is defined as the energy gap of the superconductor. In other words, the superconducting densities n_s cannot remain uniform near a surface[Fig.2.9]. The length it takes for n_s to drop from full value to zero is the coherence length ξ_o .

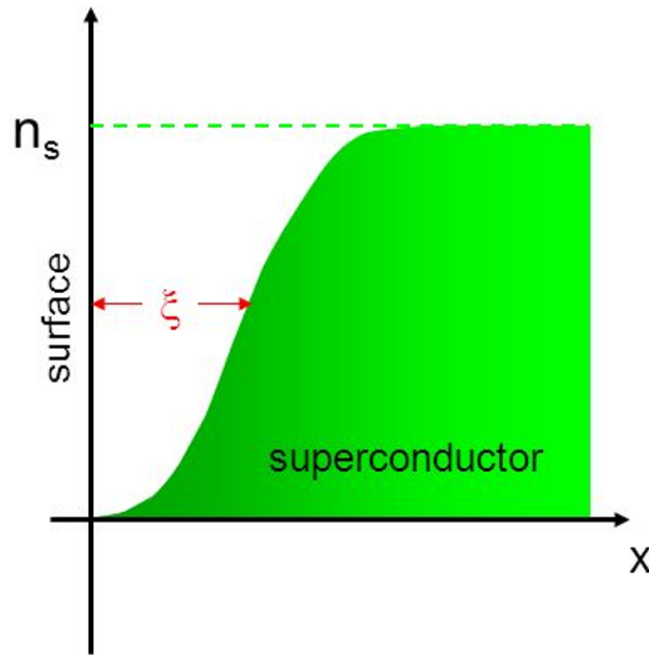


Figure 2.9: Plot of the distribution of n_s density near the surface of the superconductor[64].

The relation between the coherence length ξ_o and the penetration length λ_L defines two kinds of superconductors named respectively Type I and Type II. Type I superconductors have $\xi_o > \lambda_L$ and one critical magnetic field where the Meissner effect is null. Type II superconductors have $\xi_o < \lambda_L$, so their magnetic behaviour is different with respect to the type I. These superconductors have two critical magnetic fields: the lower critical field $H_{C1}(T)$ under which the material is superconducting, and the upper critical field $H_{C2}(T)$ above which the material is a normal conductor [Fig.2.10].

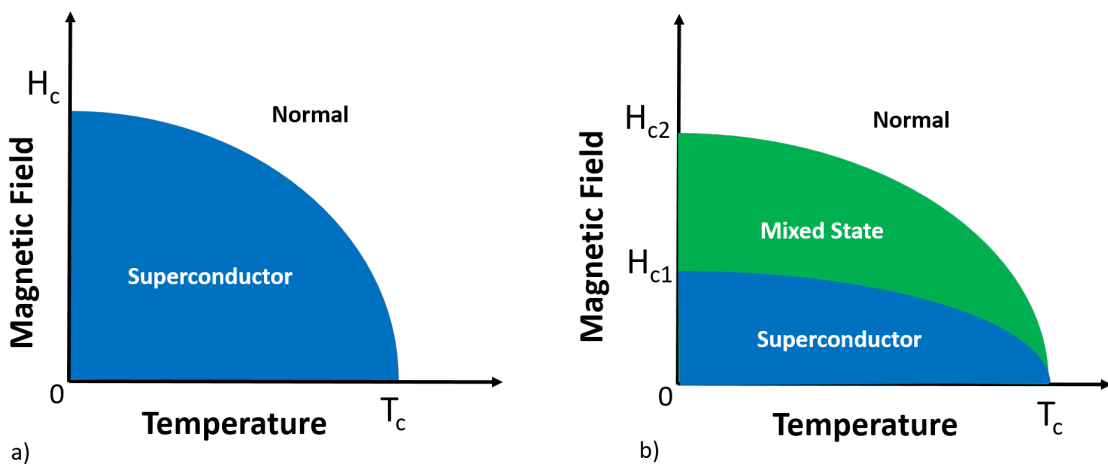


Figure 2.10: Phase diagram H-T for a) Type I superconductors and b) Type II superconductors.

Within these two bounds, the material is in a mixed state characterized by an incomplete Meissner effect: magnetic field lines partially penetrate into the material and produce vortices of current with a conductive normal core[65]. Through the coherence length ξ_o it is possible to classify the dimensionality of a superconductor. Usually when the thickness t of a superconductor is less than ξ_o , then the system can be considered two dimensional. In comparison, a one dimensional superconductor has both thickness and the width less than the coherence length.

2.2.2 The BCS Theory

In 1957, J. Bardeen, L. N. Cooper and J. R. Schrieffer proposed the famous microscopic theory of superconductivity, the BCS theory[66], which explained the phenomena in metallic superconductors. The BCS theory is based on the concept that electrons with opposite spins and momenta in the superconducting state are paired with each other by exchanging a virtual particle, i.e. phonon arising from lattice vibrations[67]. An electron in a metal normally behaves as a free particle. The electron is repelled from other electrons due to their negative charge, but it also attracts the positive ions that make up the rigid lattice of the metal. At room temperature, electrons carry an electrical current through the metal. The resistance of the metal is caused by collisions and scattering as electrons move through the vibrating lattice of metal atoms. As the metal is cooled, the lattice vibrations are reduced. A moving electron attracts nearby atoms, which create a positively charged region that can attract another nearby electron. This attraction distorts the ion lattice, moving the ions slightly toward the electron, increasing the positive charge density of the lattice in the vicinity. This positive charge can attract other electrons. At long distances, this attraction between electrons due to the displaced ions can overcome the electron repulsion due to their negative charge, and cause them to pair up. The rigorous quantum mechanical explanation shows that the effect is due to electron-phonon interactions, with the phonon being the collective motion of the positively-charged lattice[Fig.2.11].

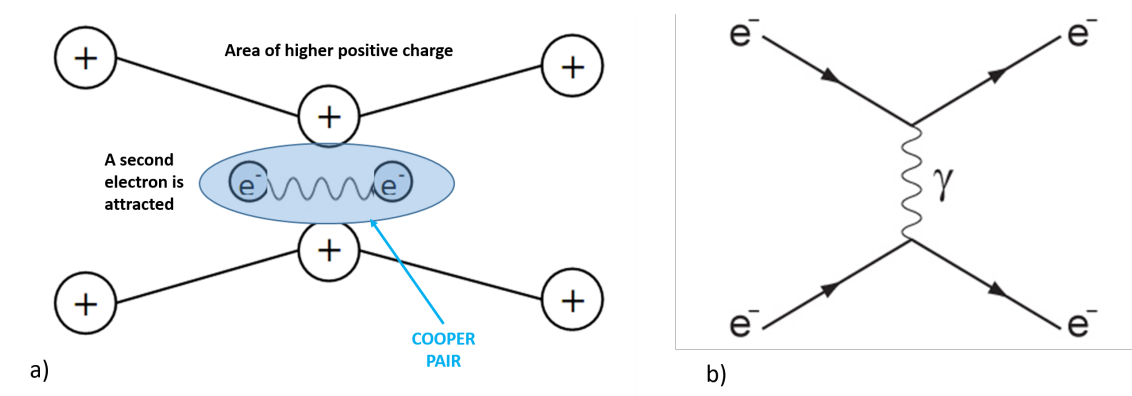


Figure 2.11: a) Diagram of a Cooper pair: two electrons interact via phonons of the lattice. b) Feynman diagram of a Cooper pair: two electrons e^- interact between them exchanging a phonon γ .

The pairs of electrons are called Cooper pairs, after L. N. Cooper who first introduced this idea[68].

Cooling the metal near 0 K, the number of Cooper pairs increase condensing to the ground state and an energy gap 2Δ appears in the energy spectrum[Fig.2.12].

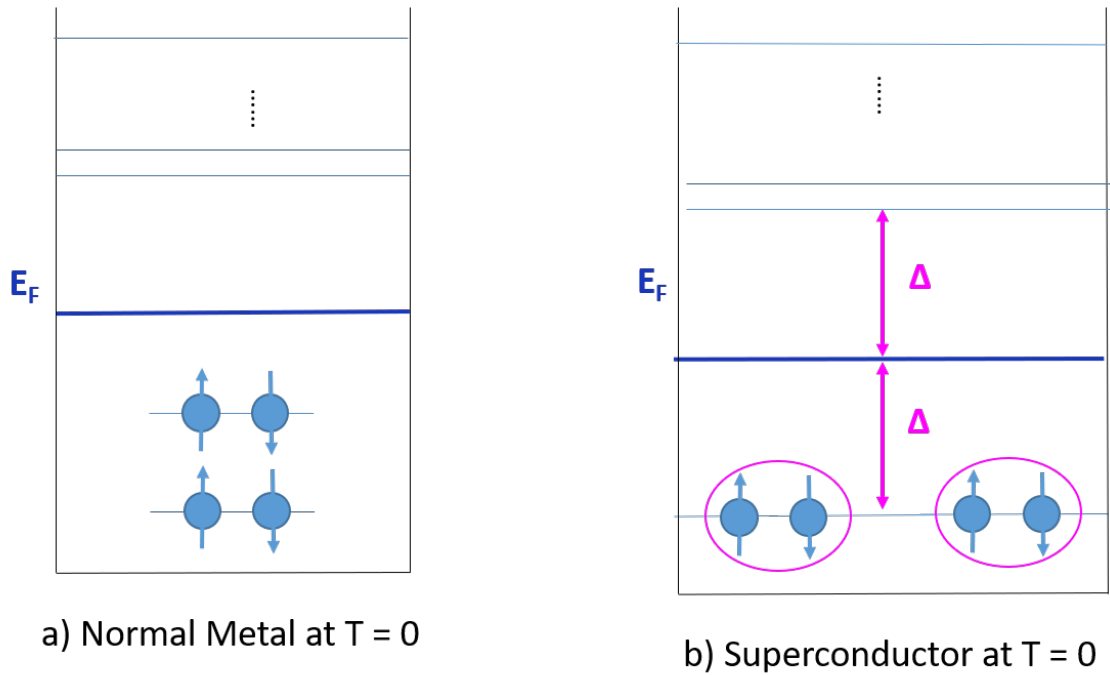


Figure 2.12: Energy spectrum of a) Normal metal at $T = 0$ K. All electrons condense at lower energetic level under the Fermi level respecting Pauli's law. b) Superconductor at $T = 0$ K. All electrons are bound in a bosonic system called Cooper pair, so they can condense at the ground level.

To break a Cooper pair, the minimum energy required is 2Δ . The energy gap depends on temperature according to the following equation[69] plotted in [Fig.2.13]

$$2\Delta = 3.5k_B T_c \left[1 - \frac{T}{T_c} \right]^{1/2} = 2\Delta(0) \left[1 - \frac{T}{T_c} \right]^{1/2} \quad (2.9)$$

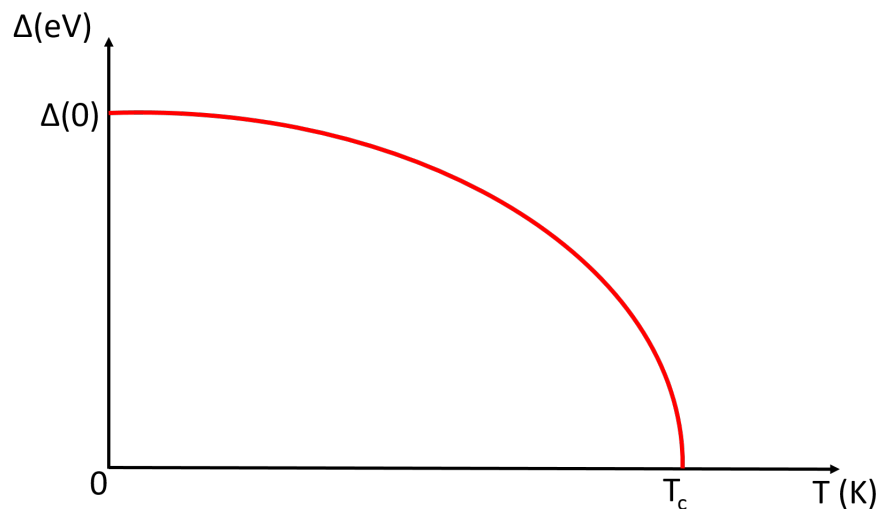


Figure 2.13: Plot of the equation (2.9) showing the superconducting energy gap Δ as a function of temperature T .

If there a minimum energy, then there is also a minimum velocity below which Cooper pairs move without excitations. For the superconductor[69]:

$$v_c = \frac{2\Delta}{2\hbar k_F} \quad (2.10)$$

where k_F is the Fermi momentum[70]. This defines the critical current

$$j_c = env_c = \Delta \frac{ne}{\hbar k_F} \quad (2.11)$$

Combining the equation (2.9) with (2.11):

$$j_c = j_c(0) \left[1 - \frac{T}{T_c}\right]^{1/2} \quad (2.12)$$

In summary, the formation of the superconducting state is a second order phase transition (no heat exchange involved) where electrons of opposite spin can interact forming Cooper pairs that condense to the ground state generating an energy gap 2Δ in the spectrum. The absence of excitation is explained by the absence of resistance in the material. Assuming the condensate of Cooper pairs as a supercurrent, it generates a magnetic field that acts as screening from external magnetic field.

2.2.3 Non-Equilibrium Superconductivity

The equilibrium state of a superconductor can be destroyed by a photon with energy $\hbar\omega \geq 2\Delta$ resulting in excitations referred to as quasiparticle (QP) excitations. Meanwhile, two QPs can readily recombine to form a Cooper pair and emit a phonon with energy of 2Δ . Understanding nonequilibrium QP dynamics in superconductors exposed to external excitations is very important for the superconducting theory and applications. The nonequilibrium QP dynamics can be studied using an optical-pulse excitation of current-biased samples (typically in the form of microbridges) and then measuring an induced transient voltage signal. These, so-called photoimpedance studies, allow for direct verification of applicability of given materials and device structures for photodetectors. Until now there is not a complete theory of nonequilibrium superconductivity. The interaction between a photon and Cooper pairs can be best described by two simple phenomenological approaches: the two-temperature (2-T) model[73] and the Rothwarf-Taylor (R-T) model[74].

The Two-Temperature Model

The two-temperature model is generally used to describe normal state photoexcitation, and it is suitable for describing the superconducting state when the temperature is near T_c , and the thermal-equilibrium QP density is dominant. In this model, the superconductor is a thin film on a substrate carrying a constant current. The system is cooled at the bath temperature T_b very close to T_c . Electrons and phonons are described in terms of their energy distributions and assign two different temperatures T_e and T_{ph} to the electron and phonon subsystems respectively. When a laser pulse is incident on the superconductor, photon energy is absorbed in the electron subsystem. The radiation thermalizes first within the electron subsystem via electron-electron ($e - e$) interaction.

Next, the electrons relax by interacting with phonons via electron-phonon ($e-ph$) interaction. Finally, the excess energy is removed from the sample with phonons escaping to the substrate[Fig.2.14].

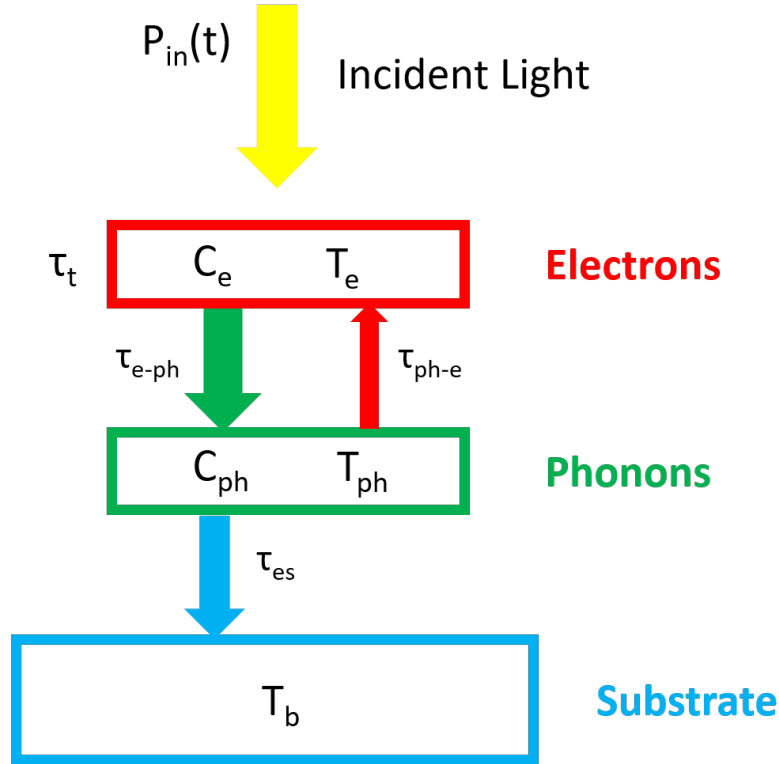


Figure 2.14: Schematic representation of the the two-temperature (2-T) model as a heat flow diagram[60].

Assuming that electrons and phonons are in their respective local equilibria, the balance between the subsystems is governed by the coupled differential equations[75, 76]:

$$C_e \frac{dT_e}{dt} = \frac{\alpha P_{in}(t)}{V} - \frac{C_e}{\tau_{e-ph}} (T_e - T_{ph}) \quad (2.13)$$

$$C_{ph} \frac{dT_{ph}}{dt} = \frac{C_e}{\tau_{e-ph}} (T_e - T_{ph}) - \frac{C_{ph}}{\tau_{es}} (T_{ph} - T_b) \quad (2.14)$$

where C_e and C_{ph} are the electron and phonon specific heats, α is the radiation absorption coefficient, V is the volume of the superconductor and T_b is the substrate temperature, $P_{in}(t)$ is the incident optical power of the laser while τ_{e-ph} and τ_{es} are respectively the characteristic times for electron-phonon ($e-ph$) relaxation and the time of escape (es) of phonons to the substrate. The change of the electron temperature incurred by the absorbed radiation power can be measured by the change of voltage due to a change of the temperature dependent resistance of the sample

$$\Delta V = I \left[\left(\frac{dR}{dT} \right) \Delta T_e \right] \quad (2.15)$$

where I is the bias current and R is the resistance of the sample. The thermalization time τ_t in the 2-T model is determined by the width of the laser pulse, while the fall time is governed by τ_{e-ph} .

The 2-T model has been used to investigate the thermal properties of a superconducting NbN single photon detector providing an estimate of the ratio of electron and phonon heat capacities and suggest that the thermal resistance is dominated by the process of phonon escape from the NbN film into the substrate[76].

The Rothwarf-Taylor Model

The RT model introduced in 1967 is most applicable for describing the superconducting state's carrier dynamics when the temperature is maintained well below T_c . At such temperatures, most of electrons in a superconductor near the Fermi surface are combined into Cooper pairs and occupy the ground state. The superconducting ground state is separated from the QPs energy levels by a superconducting energy gap 2Δ . The R-T phenomenology describes the dynamics of excited QPs n_q and phonons N_ω , which have enough energy to break Cooper pairs. When a photon $\hbar\omega > 2\Delta$ is incident on the superconductor it breaks Cooper pairs creating highly excited, hot electrons. Subsequently, these electrons loose their energy via $e - e$ scattering, followed by $e - ph$ interaction. Next, electrons recombine back to form Cooper pairs via emission of the so-called 2Δ -phonons, i.e., phonons with the energy of at least 2Δ . These phonons can break other Cooper pairs and form new excitations. These processes continue until all phonons reach equilibrium either via anharmonic decay to low-energy phonons, or by escaping out of the region of interest[Fig.2.15].

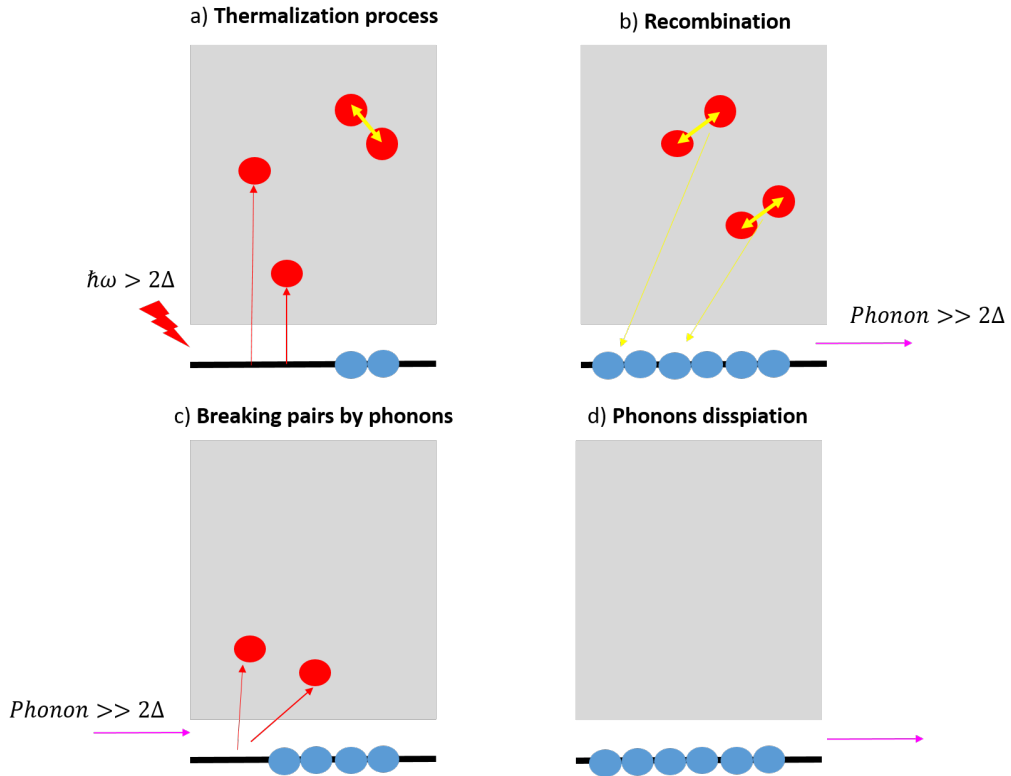


Figure 2.15: The Rothwarf-Taylor model: schematics of carrier dynamics in the superconducting state under optical excitation[77]. a) After the absorption of an incident photon $\hbar\omega > 2\Delta$ Cooper pairs are broken generating free interacting electrons. b) Electrons interact with phonons of the lattice generating Cooper pairs by 2Δ phonons emission. c) 2Δ phonon can break Cooper pair generating new electrons that interact with phonons creating Cooper pairs by low energy phonons emission. d) Low energy phonons are expelled from the material restoring superconducting state.

The process can be modeled quantitatively by the two coupled, time-dependent nonlinear differential RT equations[77]:

$$\frac{dn_q}{dt} = I(t) - Rn_q^2 + \frac{2}{\tau_B}N_\omega \quad (2.16)$$

$$\frac{dN_\omega}{dt} = \frac{Rn_q^2}{2} - \beta N_\omega - (N_\omega - N_{\omega T})\tau_{es}^{-1} \quad (2.17)$$

where n_q and N_ω , as we mentioned before, are QP and 2Δ -phonon concentrations respectively, R and β are QP recombination and pair-breaking rates respectively, τ_B and τ_{es} are respectively the phonon pair breaking and the phonon escape time, $N_{\omega T}$ is the thermal equilibrium concentration of 2Δ -phonons, and $I(t)$ is the excitation pulse.

2.3 The Hot-Spot Model

The hot-spot model is the standard phenomenological model to describe the detection mechanism of an SNSPD[78]. The elementary structure of an SNSPD is a nanowire with a nominal width of 100nm made from a thin layer of a superconductor (typically less than 10nm). An SNSPD is operated by applying a bias current I_B close to the critical current I_C . An absorbed photon in the nanowire excites an electron with high energy. Due to subsequent thermalization of excited electron, quasiparticles are generated in a cascading process. The quasiparticles diffuse in a cloud of growing diameter. The normal core can be formed in the centre of a cloud if superconductivity is locally suppressed. In order to redistribute the transport current in the nanowire, the diameter of the normal conducting core formed should be not smaller than the coherence length ξ . Then the transport current flows around the resistive core[Fig.2.16]. This should provide an increase of current density into the sidewalks. When the diameter of the hot-spot is big enough, the superconductivity is suppressed through the cross-section of the nanowire by reaching the critical value of the current density in the sidewalks.

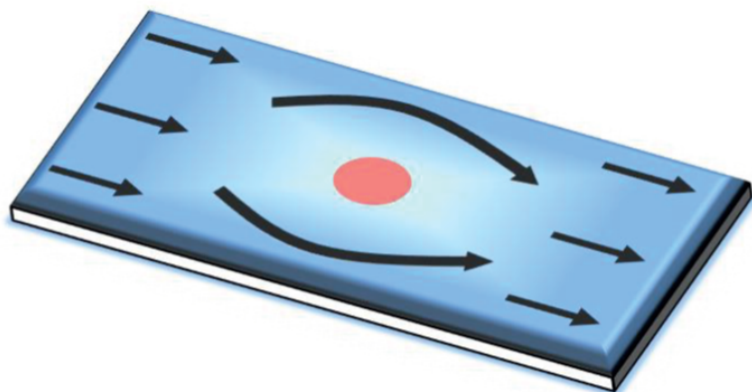


Figure 2.16: A sketch of the normal-core hot-spot model to describe the detection mechanism of SNSPDs[79].

This model is essentially based on an area argument: each unit of energy contributes to making the hot-spot larger, which serves to increase the diameter of the obstacle that the current must overcome. Since the system is 2D, the energy-current relation is quadratic:

$$I_{det} = I_c(1 - \gamma\sqrt{E}) \quad (2.18)$$

where γ is the material and device dependent proportionality factor while E is the energy of the absorbed photon. This model was then refined in 2005 by Semenov[80, 3] considering the spatial distribution of Cooper pairs after the photon excitation. Instead of the normal core of the hot spot, the number of Cooper pairs are considered within a section defined by the coherence length[3]. In this region the superconductivity is not totally destroyed and a reduced number of Cooper pairs can still carry the current. Once the critical velocity of Cooper pairs is achieved, they break up causing the nanowire to become resistive[Fig.2.17].

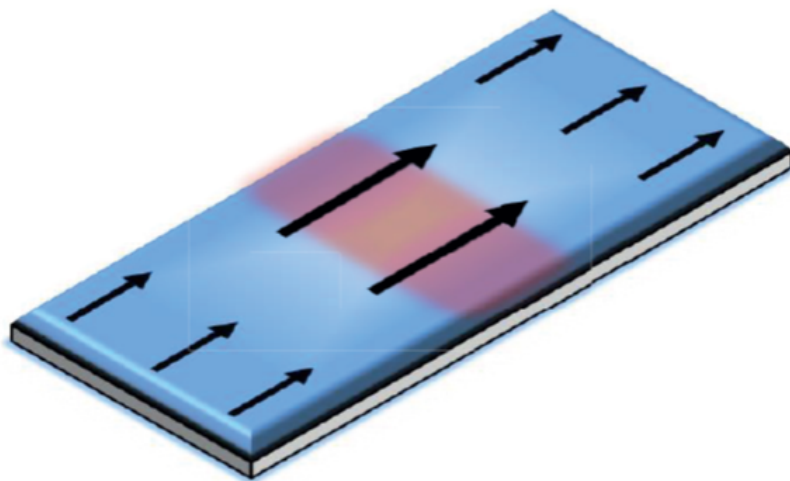


Figure 2.17: A sketch of the refined hot spot model to describe the detection mechanism of SNSPDs.[79].

Since the current carrying capacity is proportional to the total number of remaining Cooper pairs, the expression for the current-energy relation presented as:

$$I_{det} = I_c(1 - \gamma E) \quad (2.19)$$

Through these models it is possible to understand the concept of detection of an SNSPD: an incident photon of energy $h\nu > 2\Delta$ creates a local normal region in the superconducting device. This region is a concentration of quasiparticles of energy greater than energy gap 2Δ , so they tend to destroy the nearest Cooper pairs increasing the normal region along the width of the device generating a resistive state.

Since the device is cooled below its critical temperature T_c , quasiparticles lose their energy interacting with the phonons of the lattice combining in Cooper pairs restoring the superconducting state[Fig.2.18].

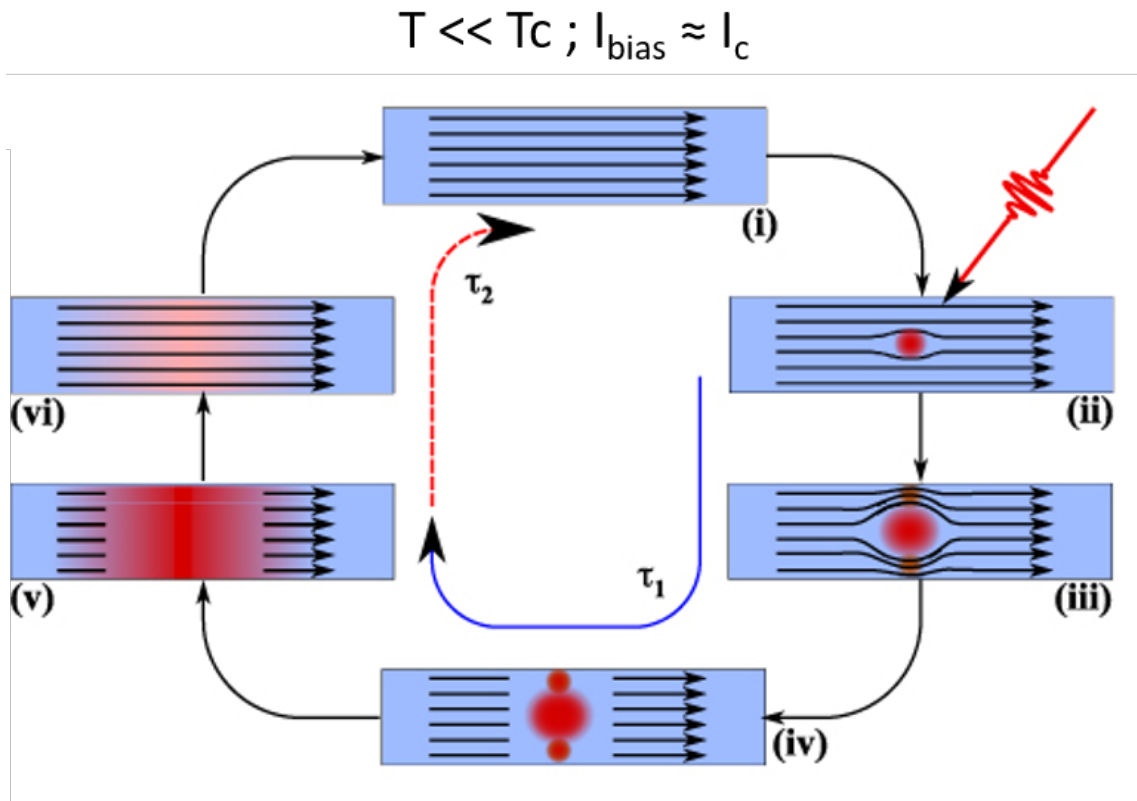


Figure 2.18: The process of single-photon detection in according to the hot-spot model[4]. i) The superconducting device is cooled below its T_c and biased just below its critical current I_c . ii) An incident photon $h\nu > 2\Delta$ generates a normal core. iii) and iv) the normal core diffuses along the width of the device generating a resistive state. v) and vi) the normal core loses energy restoring the superconductivity in the device.

2.4 System Detection Efficiency

A basic definition of the detection efficiency of a detector considers the ratio between the number of counted photons divided by the number of incoming photons. The best possible case is to achieve a DE of unity (100%), meaning all incident photons are detected but for a real detector, not all of the incident photons on a single-photon detector are necessarily detected. Together with the quality of the optical coupling in the experimental setup, the detection efficiency defines the general characteristic of any setup named a system detection efficiency (SDE). Thus, SDE can be presented as a product of three general efficiencies:

$$SDE = OCE \times DE = OCE \times IDE \times ABS \quad (2.20)$$

where *OCE* is defined by the optical coupling efficiency that describes the losses due to photons absorbed or scattered within the experimental environment before reaching the detector. *IDE* is the intrinsic detection efficiency, which is determined by the intrinsic photon-detection mechanism of the superconductor. At last, the absorptance *ABS* represents the absorption of the optical power in a material. The combination of absorption efficiency and intrinsic detection efficiency is the detection efficiency DE which was introduced above.

2.4.1 Optical Coupling Efficiency

The coupling efficiency describes the fraction of the input light that is incident on the active area of the detector. This parameter depends by the input of the incident light. The input to the detector system is typically a single-mode optical fibre (SMF), so the loss mechanisms include optical losses in this fibre and any lenses (due to absorption in the optics or the finite size of the optics) and light incident outside the active area of the detector (due to misalignment, vibrations, or the tails of the optical beam). The approach most often taken to efficiently couple light to an SNSPD is to place a single-mode optical fibre in close proximity or contact with the surface of the detector[82, 83]. In this configuration, the optical coupling efficiency is calculated via the Gaussian model of the laser beam[Fig.2.19]. A gaussian beam is determined by two properties: its central intensity at the beam waist I_0 and by the radius of the beam $w(z)$. The intensity distribution is given as[84]

$$I(x, y, z) = I_0 \left(\frac{w_0}{w(z)} \right)^2 \exp\left(-\frac{2(x^2 + y^2)}{w(z)^2} \right) \quad (2.21)$$

where z is the position along the optical axis, $x^2 + y^2$ is the distance perpendicular to z (expressed in cartesian coordinates) and $w(z)$ is the beam width[Fig.5.9] gives as

$$w(z) = w_0 \sqrt{1 + \left(\frac{z}{z_0} \right)^2} \quad z_0 = \frac{\pi w_0^2}{\lambda} \quad (2.22)$$

where w_0 is the beam width at at Rayleigh length z_0 .

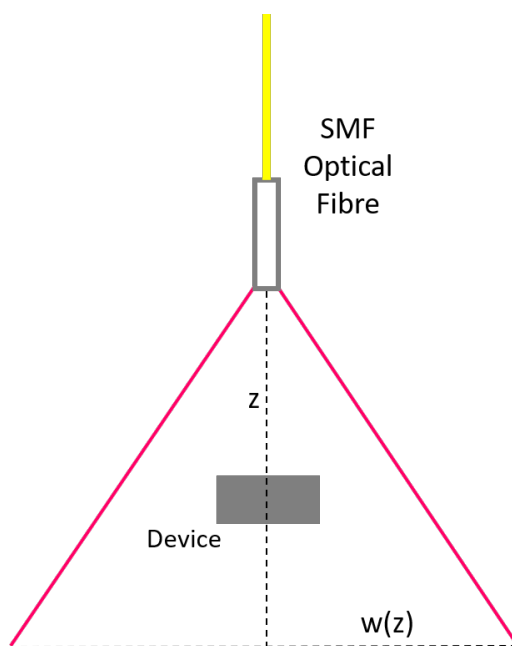


Figure 2.19: Diagram of the free optical coupling. The Gaussian model is used to describe how the laser beam is incident on the device placed from the SMF a distance z . The beam width $w(z)$ is calculated by equation (2.22).

Integrating the equation (2.21) over the area A of the detector we can obtain the power

$$P(z) = \int dAI(x, y, z) = I_0 \left(\frac{w_0}{w(z)} \right)^2 \int_{x_1}^{x_2} dx \int_{y_1}^{y_2} dy e^{-\frac{2(x^2+y^2)}{w(z)^2}} \quad (2.23)$$

Since the integral is Gaussian, we can also use the error function[191]

$$\operatorname{erf} \left[\frac{\sqrt{2}}{w(z)} x \right]_{x_1}^{x_2} = \frac{2\sqrt{2}}{\sqrt{\pi}w(z)} \int_{x_1}^{x_2} dx e^{-a^2x^2} \quad (2.24)$$

and write the equation (2.23) as:

$$P(z) = I_0 \frac{\pi w_0^2}{8} \left[\operatorname{erf} \left(\frac{\sqrt{2}}{w(z)} x \right) \right]_{x_1}^{x_2} \left[\operatorname{erf} \left(\frac{\sqrt{2}}{w(z)} y \right) \right]_{y_1}^{y_2} \quad (2.25)$$

To calculate the total power P_0 in the beam, we have to integrate over the whole area:

$$P_0 = I_0 \frac{\pi w_0^2}{8} \left[\operatorname{erf} \left(\frac{\sqrt{2}}{w(z)} x \right) \right]_{-\infty}^{\infty} \left[\operatorname{erf} \left(\frac{\sqrt{2}}{w(z)} y \right) \right]_{-\infty}^{\infty} = I_0 \frac{\pi w_0^2}{2} \quad (2.26)$$

The coupling efficiency η_{coup} of a detector can be expressed[85] as the ratio between the power $P(z)$ hitting the detector with the total power P_0 .

$$\eta_{coup}(z) = \frac{P(z)}{P_0} = \frac{1}{4} \left[\operatorname{erf} \left(\frac{\sqrt{2}}{w(z)} x \right) \right]_{x_1}^{x_2} \left[\operatorname{erf} \left(\frac{\sqrt{2}}{w(z)} y \right) \right]_{y_1}^{y_2} \quad (2.27)$$

The equation (2.27) is the coupling efficiency dependent by the distance z of the optical fibre from the detector. Furthermore, misalignment can often be a problem, particularly in cases when the detector diameter and the mode-field diameter in the fibre are both about 10 μm . A second approach that overcomes the drawbacks of direct fibre coupling is to use a lens assembly on the end of a fibre, which can be positioned at cryogenic temperatures[86]. The lens assembly can refocus the light at a working distance longer than the substrate thickness, allowing the light to be coupled through the substrate and thereby permitting the use of a cavity structure fabricated on top of the detector. The lens assembly can also be designed to focus the light to a spot size smaller than the mode-field diameter of the fibre, permitting a very high fraction of the light to be coupled onto the detector. Finally, having control over the position of the lens assembly at cryogenic temperatures allows it to be actively aligned to the detector using the detector count rate as feedback. Although this approach is more complex and can be more susceptible to vibrations, depending on the design of the positioning mechanism, its potential for consistently low coupling loss and compatibility with cavity-integrated detectors makes it better for achieving the highest possible detection efficiencies. A recent approach is to place the detector in the middle of silicon disc defined by deep etching through the silicon wafer. Then the disc is installed in a zirconia alignment sleeve, where is placed a standard SMF[Fig.2.20]. This type of fibre coupling is called self-alignment[87].

Self-alignment is ensured by the precise dimensions of the Si disc, fibre ferrule and ceramic alignment sleeve. The use of zirconia ceramic ferrules and sleeves is standard in the telecommunications industry and results in sub-micrometre centre-to-centre lateral alignment between opposing ferrules.

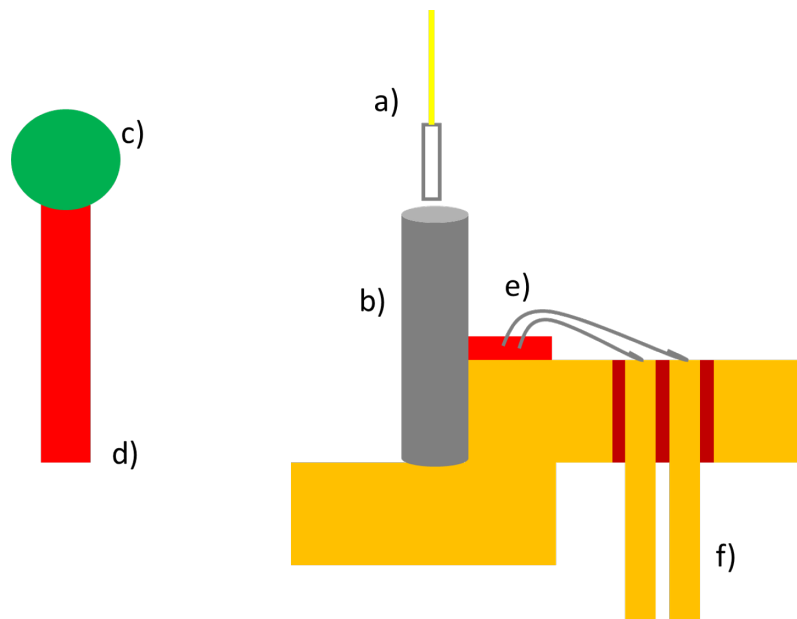


Figure 2.20: Cross section of the fibre-to-detector assembly[87]. (a) Single-mode fibre terminated in a stainless steel and zirconia ferrule inserted into (b) a zirconia alignment sleeve (outlined for clarity). The completed detector and substrate (c) has wiring along a silicon “tongue” (d) that extends out the zirconia sleeve (e) and is wirebonded to pins (f) separated by an insulator that allow electrical connection to the electrical set-up.

2.4.2 Absorptance

The absorptance is the absorption efficiency which determines the probability of absorption of the incident photons into detector active area. This parameter depends by the geometry of the detector. In order to fabricate a detector with a reasonable active area, nanowire geometries have evolved from a single straight wire to much longer wires in meander designs covering square[88, 89] and circular areas[90]. The extension to an array structure enhances the active area of the SNSPD[Fig.2.21]. The production of larger meanders is limited by the increased occurrence of imperfections in the wire during fabrication. They are referred to as constrictions and have a lower critical current density relative to the rest of the wire. This reduces the maximum bias current that can be applied, which lowers the detection efficiency[94] and results in a spatially non-uniform response[95]. Recent measurements reported that the absorptance of SNSPDs changed with the filling factor (defined as the line width divided the ratio between the nanowire and the gap in between the meander structure) and optical polarization[92, 93] measuring an efficiency of 21% for light polarized parallel to the nanowires with a filling factor of 50%.

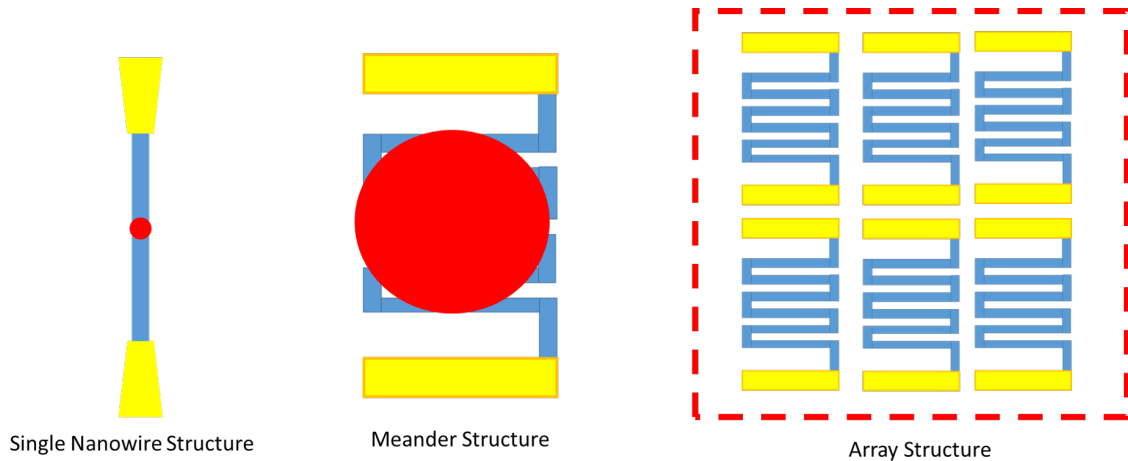


Figure 2.21: Development of nanowire geometries[91]. In order to increase the active area (red circle), SNSPD nanowire design evolved from a straight wire to meanders covering square areas. An SNSPD array structure can be used to achieve a much larger active area.

Approaches to increasing device area include the development of grids of parallel nanowires and arrays of shorter nanowires[96, 97]. Additionally, major improvements in system detection efficiency have been achieved by using optical cavities and anti-reflection coatings to increase the photon absorption efficiency[98, 99]. The efficiency ABS depends also on the optical properties of the material used to fabricate the detector. Recent studies conducted by our group investigating the optical properties of NbN, NbTiN, TiN and MoSi have demonstrated that MoSi and TiN thin films exhibit high value of optical absorption at 1550 nm and above that of than NbN and NbTiN[100].

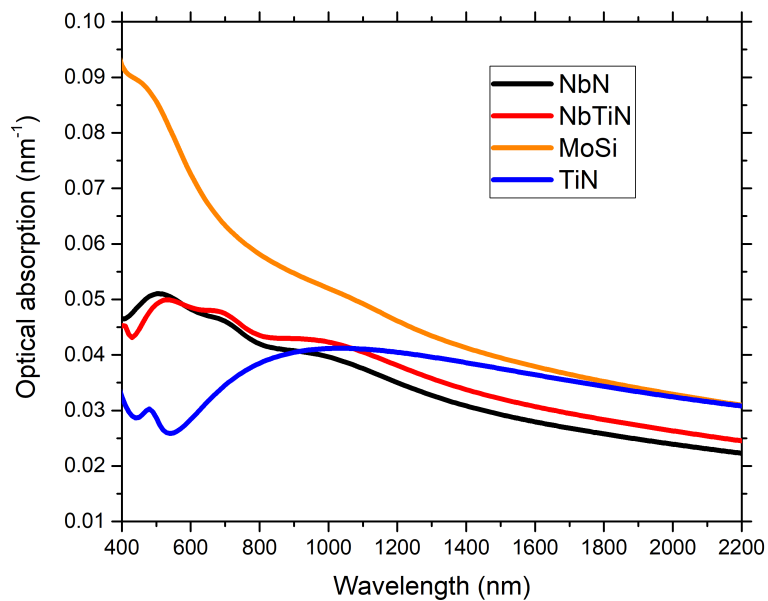


Figure 2.22: Optical absorption of 5 nm thickness NbN, NbTiN, MoSi and TiN grown via magnetron sputtering process. The sputtering equipment used to fabricate these film (the Plassys VI) is described in the section 3.2. Variable angle spectroscopic ellipsometry (VASE) was employed to measure the optical properties of the materials[100].

Another way to increase the absorption spectral bandwidth of a SNSPD is to realize multiple-layer superconducting nanowires on metallic mirrors with insulating space layers of different thickness. This structure is known as supercontinuum SNSPD[101] for example a supercontinuum SNSPD made by 6.5-nm-thick NbN divided in two layers divided by 3-nm-thick SiO₂ and using Al as metal mirror separated from the SNSPD by 190-nm-thick SiO₂, exhibits detection efficiencies greater than 60% from 950 to 1650 nm. The absorptance depends also by the polarization of the incident light. A study has demonstrated that a SNSPD exhibits a high absorptance when it is illuminated by transverse electric (TE) polarized light (the electric field is parallel to the superconducting nanowire)[102, 92, 103]. Simulating that 4 nm thickness NbN patterned in a meander structure of 100 nm width and 50% filling factor is illuminated with 1550 nm wavelength with an electrical field of 1 V/m, the distribution of the electric field amplitude of the TE incident light result uniform inside and outside the device with an amplitude of about 0.8 V/m. Simulating the illumination of the same device by transverse magnetic (TM) polarized light (the electric field is perpendicular to the superconducting nanowire), the distribution of the electric field amplitude is not uniform, but it results high at the external borders of the device, while inside the device the centre reaches a value of 0.4 V/m that decrease along internal borders of the device[102]. To overcome this problem with the TM polarization, a SNSPD is usually embedded in thick wrapping layer composed of dielectric material with a high permittivity ϵ (for example $\epsilon = 12$ for Si at 1550 nm[102]). A SNSPD embedded in an optical microcavity made of Si, SiO₂ as substrate ($\epsilon = 2.1$ for Si at 1550 nm[103]) and Au as reflection layer has demonstrated to be insensitive to the polarization achieving an absorptance of about 96% at 1550nm both with TE and TM polarization (difference less than 0.5%)[102]. An expression commonly used to estimate the absorptance of thin metal films[104] is:

$$ABS = \frac{4Z_0 R_{sheet}}{(Z_0 + (n + 1)R_{sheet})^2} \quad (2.28)$$

where $Z_0 = \sqrt{\mu_0/\epsilon_0} = 376.73\Omega$ is impedance of vacuum, R_{sheet} is the sheet resistance of thin metal film and n the refractory index of the film.

2.4.3 Intrinsic Detection Efficiency

The intrinsic detection efficiency quantifies the portion of absorbed photons which produce electrical detection pulses. This factor is strongly dependent on the energy gap of the superconductor. As mentioned in previous sections, a high energy gap is critical to achieving a high internal detection efficiency, particularly at long wavelength[105] (lower energy photons). From the equation (2.9), the internal detection efficiency increases in superconductor with a low critical temperature. Irradiating a superconductor by He ion irradiation it is possible to decrease its superconducting properties like the energy gap and the critical temperature. Irradiating 8 nm NbN by He ion fluence of $5 \cdot 10^{15} \text{ cm}^{-2}$, a recent study[106] has achieved a system detection efficiency of 92% at 2.2 K for 1550 nm. This process is used after the fabrication of the device (after the dry etch process) and the use of He ions prevents any etching effect onto the device. Besides, the internal efficiency depends also on the critical current of the superconductor[107]. Defects or constrictions in the nanowires limit the range of detection efficiency which can be achieved[94]. These defects, known as constrictions, have been studied calculating the critical currents in thin superconducting strips with some geometries as sharp right-angle turns or 180°turnarounds[108]. Results show that current crowding near bends of the current path reducing the experimental critical current[Fig.2.23]. The reduction factor of the critical current due to a bend in the nanowire depends on the angle of the bend, the wire width w , and the radius of the bend r_b .

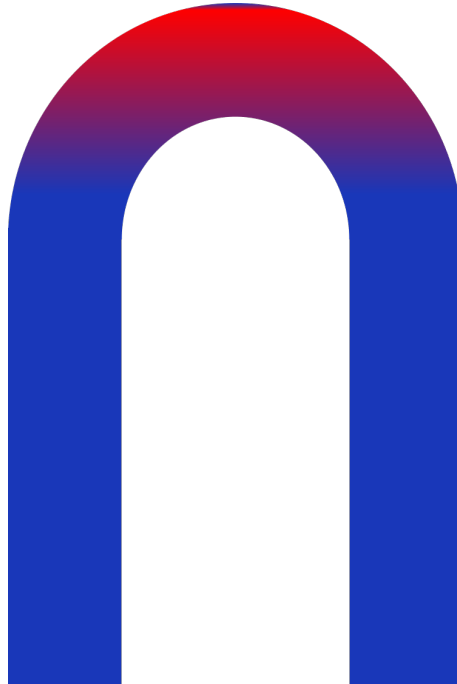


Figure 2.23: Simplified sketch of distribution of the current in a 180° bend in a nanowire. The local increase of the current density over the value of critical current density leads to hotspot formation in the vicinity of the inner corner (red region) in bend disrupts the homogeneous flow (blue region) of the transport current[100].

2.5 Dark Count Rate

Dark counts are detection events without absorption of any photons. In SNSPDs, these false signals are generated by formation of resistive regions similar to those discussed in photodetection events; resulting in a false detection which can not be distinguished from photon detection events. Dark count sets a limit on photon counting applications where the source is very weak. This is because the information can be lost in the presence of high background dark count rate. The origin of dark counts in biased superconducting nanowires is still under debate. Some research found the main reason of the dark count in the thermal fluctuations of low dimensional system. For a superconductor, these fluctuations are described in terms of the depairing of vortex-antivortex pairs[109, 110]. In 2D superconductors, it is known that a phase transition called the Berezinskii-Kosterlitz-Thouless (BKT) transition[111, 112] can occur at the temperature slightly below the critical temperature T_c defining a new critical temperature called T_{BKT} . Below T_{BKT} , bound vortex-antivortex pairs (VAPs) with no net flux exist, while in a temperature range between T_{BKT} , and T_c , there are free vortices due to thermal unbinding of the VAPs. Even below T_{BKT} , the application of bias current in the superconducting nanowire exerts a Lorentz force that acts in opposite directions for the vortex and antivortex of a VAP. The bias current can finally overcome the binding energy of the VAP and break the pair into single vortices. Crossing of the unbound vortices in the nanowire perpendicular to the current may trigger the superconducting to normal transition generating an output signal. Spontaneous nucleation of a single vortex near the edge of the strip and its motion across to the opposite edge[113] might release sufficient energy for the formation of a resistive belt across the wire. Hybrid superconductor/ferromagnet (S/F) bilayers[114] have been fabricated to reduce the motion of VAPs in the SNSPDs. The presence of a weak ferromagnetic overlayer significantly influences both the superconducting properties as the enhancement of the critical current and of the optical properties[115, 116]. In a fully proximitized, hybrid S/F nanostructures, such as NbN/NiCu (NiCu alloy is a weak ferromagnet), has been discovered also a considerable reduction of the dark count rate and a significant increase of the photoresponse signal proportional to the enhancement of the critical current density[117].

2.6 Timing Jitter

Ideally, a SNSPD produces an electrical signal in the same instant when the device detects the incident photon. In a real experiment, voltage pulses produced do not start at exactly the same time after the absorption of the photon. This delay between the absorption of the photon and the electrical response of the device is defined timing jitter. As random variable, the jitter has a Gaussian distribution and the time jitter represents the FWHM of the Gaussian curve. This parameter represents the temporal resolution of SNSPD. The timing jitter may stem for example from the random position on the device where the photon is absorbed or how the hotspot is formed and the thermalization of quasiparticles. Therefore, it might depend on the geometry and dimensions as well as the material of the detector. Recently a NbN SNSPD demonstrated a timing jitter below 3 ps for visible wavelengths and below 5 ps at 1550 nm[118].

2.7 Dead Time

In single photon detectors, after each photon detection event, the detector needs to be reset, gaining the ability to respond for the next photon detection. This reset time is known as dead time. For a SNSPD, the dead time includes two parts. The first is the interval during which superconductivity is interrupted and the detector is blind to the absorption of any other photon. The second part is the time interval during which the detector is superconducting and recovering its steady state current, to be able to efficiently register the arrival of the next photon. The dead time is governed by the inductive time constant of the circuit, which is imposed by the kinetic inductance of the superconducting film due to the inertia of the Cooper pairs in the superconducting state[94]. A simple but elegant phenomenological model[Fig.2.24] can be used to simulate the measurable output voltage pulse from an SNSPD biased at I_b . The inductance L_k represents the superconducting state while $R(t)$ is the normal state generated by the photon.

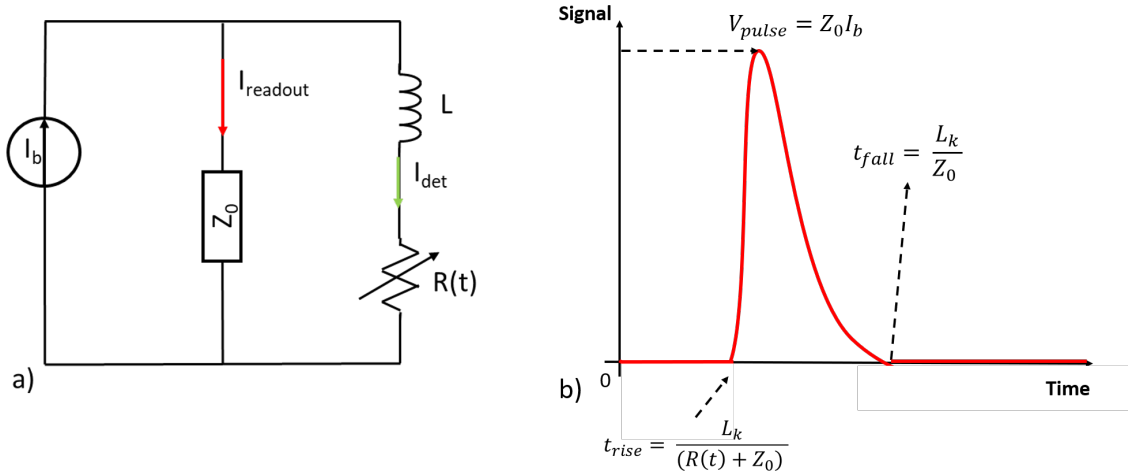


Figure 2.24: a) Equivalent circuit of a SNSPD. b) Example of the output voltage pulse of the SNSPD.

The impedance of the readout electronics is represented by a load resistor Z_0 (typically 50Ω) connected in parallel to the SNSPD. When the detector is in the superconducting state, $R(t) = 0$. When a photon is absorbed, the normal domain is nucleated, giving the wire a resistance $R(t)$ generating a voltage pulse $V_{\text{pulse}} = I_b Z_0$ by rise time:

$$\tau_1 = \frac{L_k}{R(t) + Z_0} \quad (2.29)$$

After the absorption, the pulse decays with a time constant

$$\tau_2 = \frac{L_k}{Z_0} \quad (2.30)$$

As the equation suggests, for a specific type of read-out circuitry, the reset time depends on the kinetic inductance of the SNSPD. This represents a crucial problem for the fabrication of large area SNSPD since that means even to increase the kinetic inductance of the superconductor and thus maximize reset time of the detector.

2.8 Multi-Pixel SNSPD review

One of the first prototypes of a multi-pixel SNSPD was presented in 2007[119]. The electrical scheme is based on the concept of the avalanche detector known as superconducting nanowire avalanche photodetectors (SNAPs). In this structure N SNSPDs are connected in parallel[Fig.2.25].

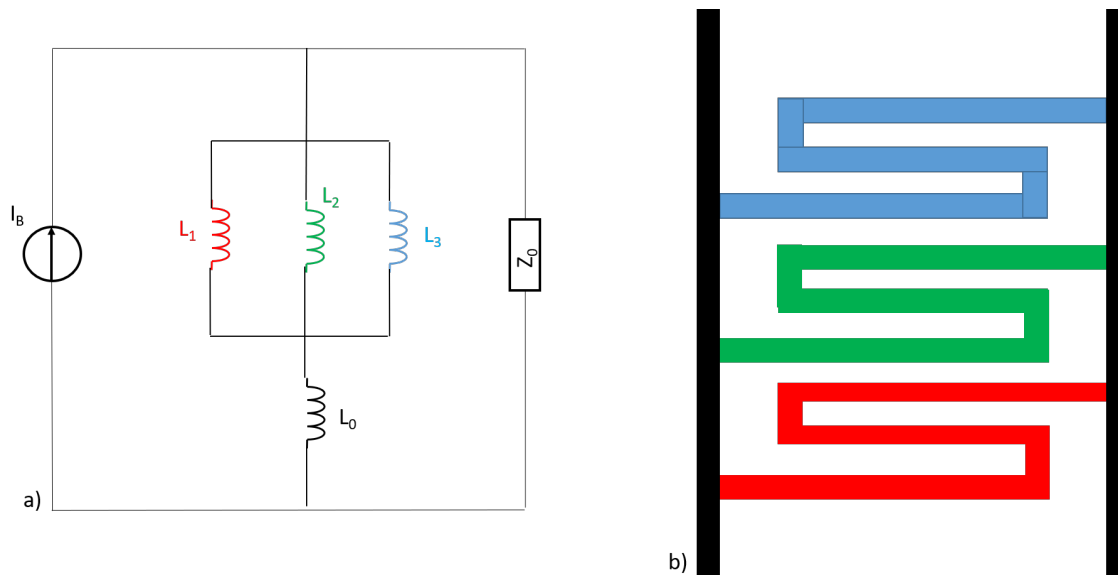


Figure 2.25: The superconducting nanowire avalanche photodetector (SNAP) concept. Schematic of a) equivalent circuit and b) design geometry of a SNAP. Each detector can be shown with an inductor in series with a resistance. A detection event in either of detectors in the avalanche region, highlighted with red dashed rectangle, can excite neighbouring detectors causing the whole array to switch. The large change in the current is summed up and converted into a large voltage pulse by the help of the inductor L_0 .

When a detector absorbs the photon, it goes through a current-assisted phase transition to the normal state. Integrating an extra inductor L_0 in series, the current will be forced to flow through the other parallel wires. Since the bias current is close to the critical current value of each wire, the extra current forces a transition of all the parallel wires with a cascade mechanism. When all the wires have switched, the detector becomes highly resistive and the total bias current redistributes to the external load Z_0 . The resulting signal is N times larger and N times faster compared to a meandered SNSPD. This method found application in situations where the signals are very weak, but they are not able to count incident photons. A configuration capable of photon counting is Parallel Nanowire Detector(PND)[120]. In this configuration, SNSPDs are connected in parallel to a voltage source[Fig.2.26] and unlike the avalanche array, in this case detection in one SNSPD does not cause cascade switching of the other detectors. Each element acts as a single-photon detector and their responses can be read either separately or together in the output. The PND is a good counting detector[120, 121], but has a drawback of current redistribution problems due to its parallel design. The bias current from the firing elements is partially redirected to the unfiring elements generating false photon detections and consequently limits the dynamic range[120]. To solve this problem, a Serial Nanowire Detector (SND) has been introduced[122, 123].

In this configuration, superconducting nanowire are connected in series and each nanowire is shunted with a parallel resistor R_0 [Fig.2.26].

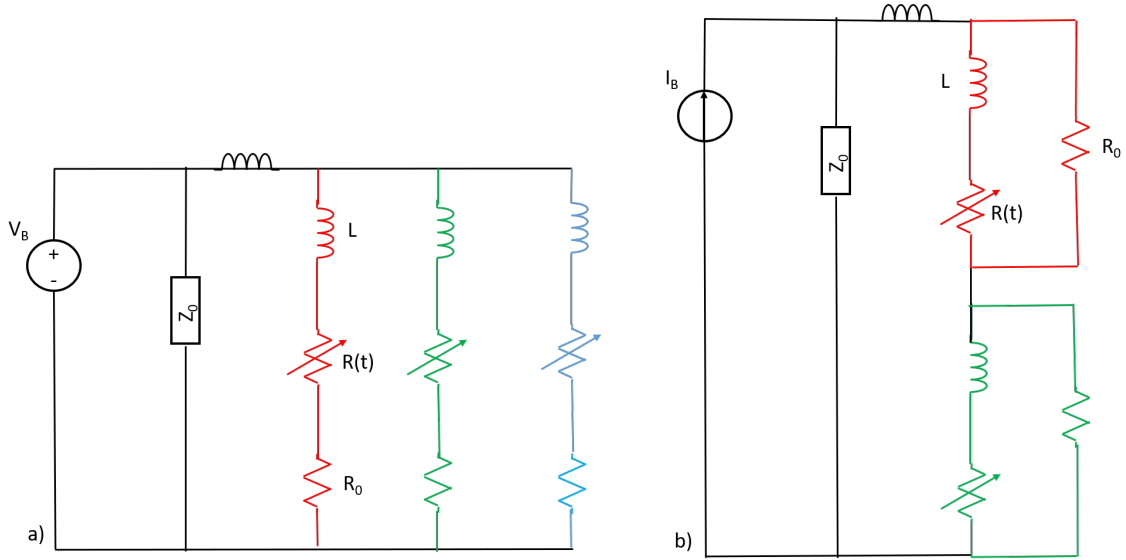


Figure 2.26: a) Circuit diagram of a 3-PND, comprising 3 superconducting nanowire connected in parallel. Each nanowire is connected to a series resistor R_0 to minimize leakage current. b) Circuit diagram of a 2-SND, comprising 2 superconducting nanowire connected in series. Each nanowire is connected to a parallel resistor R_0 .

In the steady state, all nanowires are biased at the same bias current. When hot-spot event occurs in a nanowire, this one shows a drop voltage $V \sim I_B \cdot R_0$. The total voltage across the SND is proportional to the number of photon detected. This configuration has been used by the Institute of Photonics and Nanotechnology in Rome for a 24-pixels SNSPDs able to discriminate 0-25 photon levels and a jitter of 116 ps[124]. One crucial point of the operation of a multi-pixel SNSPD is its electrical readout. The presence of a large number of pixels increase the number of high-frequency coaxial cables causing a significant increase of thermal load in the cooling system. An example is the row/column readout (also known as crosswire readout) and it is based on summing the signals from all nodes in a given row or column, resulting in an output channel per row and column of the array. This technique has proved that the number of readout cables can be reduced to $2N$ for an $N \times N$ array format[35, 125] but the realization of a large spatial array of over 1,000 pixels remains challenging due to the thermal issue associated with the signal readout. For this reason a cryogenic signal-processing technique based on a single flux quantum (SFQ) circuit has been proposed[126]. SFQs circuits are superconductor digital circuits composed of superconductor loops with Josephson junctions (JJs) as their switching devices. The binary information in the SFQ circuits is represented by quantized flux in a superconductor loop, allowing low-power operation with a clock frequency up to tens of GHz[127]. Since their operation temperature is identical to the SNSPD operation conditions, SFQ represents good candidate for SNSPDs readout demonstrating a lower timing jitter compared with the conventional method using readout circuit[128]. Recently, a 64 channel encoder based on SFQ circuits combined with a 64 pixel NbTiN SNSPD array has been demonstrated for high timing resolution readout operation[127] making it a good candidate for real-time imaging applications.

Another type of readout to apply to SNSPD arrays is to embed the single pixel SNSPD into a lumped-element resonator[130]. This microwave structure is known as Radio-Frequency Superconducting Nanowire Single Photon Detector (RF-SNSPD). As the MKID, this detector can be multiplexed in the frequency domain. In contrast to the MKID, this detector can operate in the single-photon regime. To enable the single photon detection, the RF-SNSPD is driven by a microwave current with the amplitude close to the critical current of the nanowire. Thus, the operation regime is highly nonlinear, which enables single-photon detection. This model has been used as readout of an array structure of 16-pixel of NbN[131] resulting in a maximum detection efficiency of less than 10%. The fabrication of large area SNSPD arrays is limited even by the uniformity of the material. For example, NbN is a good candidate for its high critical temperature, but its polycrystalline form depends strongly on the substrate. Thus it is difficult to produce a uniform, high quality film over large area due to factors such as crystal orientation and lattice defects[94]. Due their amorphous nature, superconducting materials like MoSi or WSi can be grown onto any substrate without a particular orientation. This ensures the production of a high-quality uniform film over large area. Recently, a 64-pixel 320 μm diameter array of WSi has exhibited an efficiency of 40% at 1550nm[129]. Other advantages of amorphous superconducting materials is their low superconducting energy gap. While polycrystalline NbN presents an energy gap $2\Delta = 5\text{meV}$ [35], the gap of amorphous MoSi is about $2\Delta = 2.3\text{meV}$ [35], this means that MoSi looks more sensitive than NbN to interact with infrared photons. In addition, MoSi exhibits a large absorptance than NbN in the range of telecommunication wavelength[100] and for this reason this material does not require necessarily to be installed in an optical microcavity. Another crucial point in the realization of multipixels SNSPD is in the fabrication process. During these process, superconducting properties can be affected decreasing seriously the performance of SNSPD. The fabrication optimization is thus required to increase the performance of SNSPDs.

Chapter 3

Experimental methods

This chapter explains the experimental methods used in this thesis. The steps in the fabrication process for deposition of superconducting thin films, SNSPD devices and arrays are explained in detail. Experimental techniques for electrical and optical characterization of thin film samples and devices at low temperatures are then described. Each process used in this work is introduced by a brief theoretical background.

3.1 Sputtering basics

The first step of the SNSPD fabrication is the process of film growth on a substrate. A standard technique for thin film growth is known as sputtering[132] and it consists of removing atoms from the surface of the target material by an ionized gas called a plasma. When the surface of the target is bombarded with high velocity positive ions, it is possible to cause the ejection of surface atoms. The ejected atoms can be made to condense on the substrate at an optimal distance from the target to form a continuous thin film[Fig.3.1].

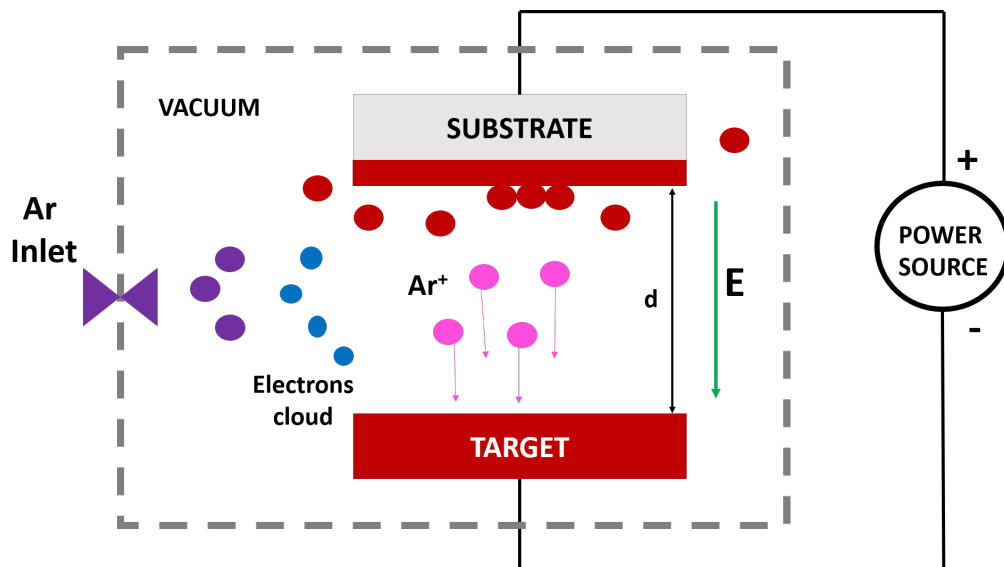


Figure 3.1: Diagram of the Sputtering Process.

A plasma is a fluid that contains a large number of mobile negatively and positively charged particles. A plasma can be initiated by applying a potential across parallel plate capacitor configuration, where the space between plates is filled with a dilute neutral gas (usually Ar). If the applied potential is large enough that one of the gas molecules can become ionized, the separated ion and electron will be accelerated towards opposite plates. These accelerating particles will collide with inert gas molecules at a rate determined by the mean free path in the gas, which is determined by the pressure and the scattering cross section of the gas species present. If the accelerating particles gain sufficient energy between scattering events, the scattering can lead to ionization of additional gas. This process can lead to an avalanche, such that a significant fraction of the gas becomes ionized. The current density i that results between two parallel plates is given by the Townsend equation[133]:

$$i = i_0 \frac{\exp\{\alpha d\}}{1 - \gamma_e(\exp\{\alpha d\} - 1)} \quad (3.1)$$

Here, i_0 is the initial current at the cathode, α is the coefficient of first ionization and it represents the probability per unit length that a collision between a gas atom and an electron will result in ionization, d is the distance between parallel plates, and γ_e is the Townsend secondary electron emission coefficient. When positively charged gas ions strike the negative electrode surface, they have a chance to cause the emission of electrons, known as secondary electrons. The Townsend secondary electron coefficient gives information about how many secondary electrons are created per ion incident on the cathode surface giving a contribute to the total current between the capacitor plates. The ionization coefficient depends on the ionization potential V_i of the gas species, the mean free path in the gas λ , and the electrical field E applied to the electrodes[134]:

$$\alpha = \frac{1}{\lambda} \exp\left\{\frac{-V_i}{qE\lambda}\right\} \quad (3.2)$$

The breakdown of a gas into a plasma is taken as the limit which the current goes to infinity, or equivalently, that the denominator of equation(3.1) goes to zero. Combining this condition with (3.2) and remembering the inverse relation between the pressure of the gas p and the mean free path λ ($p \propto (1/\lambda)$), we can get an expression for the voltage required to sustain a plasma given all of the relevant parameters, the breakdown voltage V_B

$$V_B = \frac{Apd}{\ln(pd) + B} \quad (3.3)$$

where A and B are fitting coefficients that account for the relationship between the mean free path λ and the pressure p as well as the effect of secondary electron yield at the cathode. The equation(3.3) represents Paschen's Law[135]. At low pressure (or if the distance d of plates is small), there are relatively few collisions between energetic electrons and gas molecules so the breakdown voltage rises. As pd is increased, V_B is reduced, until the mean free path in the gas makes it such that a greater electric field is required for electrons to gain enough energy to ionize gas molecules between scattering events. Thus V_B rises with increasing pd .

Once the breakdown voltage is reached the plasma becomes self-sustaining through impact ionization and secondary electron yield. The spark of the plasma is known as Townsend discharge. In this condition the gas begins to glow, the voltage drops, and the current rises abruptly. This mode of operation is called normal glow that does not cover the entire cathode. The spectrum emitted by the plasma is characteristic for the used gas species, because the ionized particles relax by photoemission. A small additional current increase leads to the coverage of all regions of the cathode. This mode of operation is called abnormal glow and it is the mode used for sputtering. Increasing the current leads to significant heating of the cathode, followed by a further avalanche of thermionic electrons in addition to secondary electrons. The output impedance of the current supply limits the voltage, and the low-voltage high-current arcing discharge develops[Fig.3.2].

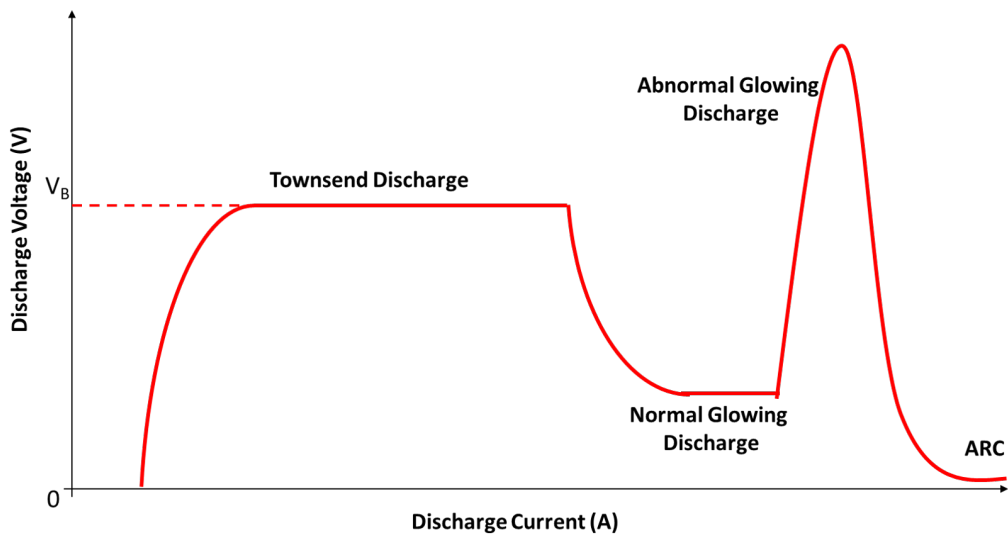


Figure 3.2: IV-Characteristics of a DC discharge[136]. The DC discharge is initiated by Townsend's avalanche. The range of the Townsend discharge is almost flat. This originates from the fact that a small increase in voltage leads to a higher electron multiplication in the gap, producing more electrons and ions, giving more secondary emission at the cathode, leading to even more electrons in the gap and a further multiplication of charges. This means that for a small increase in voltage, the current rises considerably. When it is self-sustaining, the gas begins to glow intensively. The mode most often used in thin-film technology is the abnormal glow. In the high-current regime the plasma shows an electrical breakdown (arc).

3.1.1 DC/RF Sputtering

The sputtering process is classified as DC or RF depending on the type of power supply used. DC sputtering is used to deposit metals. In case of insulators after the ions strike the surface, their charge will remain localized and with passage of time positive charge will build up on the target, making it unfeasible to further bombard the surface. This can be prevented by bombarding the insulator by both positive ions and electrons simultaneously. That is done by applying a RF potential to the target. The creation of a self-sustaining plasma is the first step of in a DC or RF sputtering process. Consider the same parallel plate arrangement as discussed above, but now replace the cathode with a plate of some metal, which we desire to deposit in a thin film. At the anode, we place a substrate onto which we will deposit the metallic film[Fig.3.3]. The sputtering chamber is filled with an inert gas. The plasma is established by applying the DC power to the electrodes during the sparking phase.

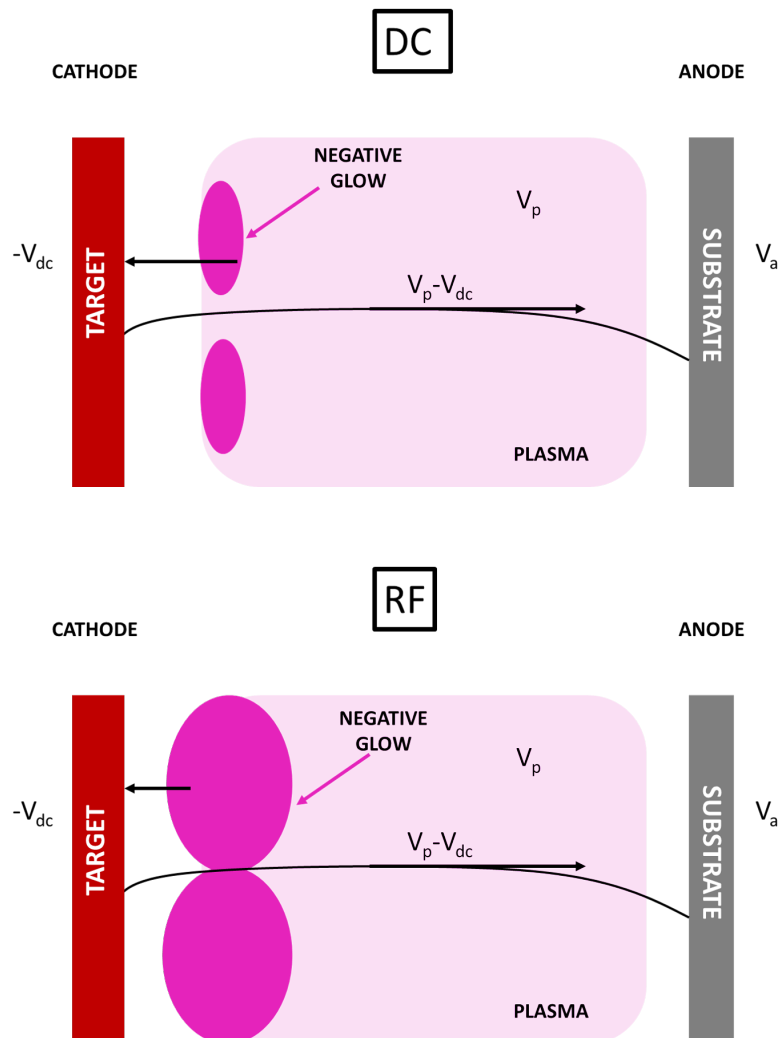


Figure 3.3: Schematic diagram of the plasma potential distribution of a DC and an RF discharge. The RF discharge has a relatively low plasma impedance (high negative glow) at a constant discharge power compared to the DC discharge[137].

The sputtering of the material from the cathode occurs in the following way: gas molecules in the glowing region of the plasma become ionized by colliding with high-energy electrons. When these ions encounter the transition region between the plasma and the powered cathode (defined by the negative glow region) they are accelerated towards the cathode. Ions start off in the plasma at some potential V_p , they are accelerated through the negative glow, and arrive at the cathode at potential V_{dc} (assumed to be negative), gaining energy $q(V_p - V_{dc})$. The ion impinging on the surface of the target will transfer some of this energy to target atoms at the surface. In this way some number of target atoms will be dislodged from the target surface and be sent flying into the chamber, where a portion of those atoms will deposit on the substrate and form the desired thin film. The sputtering yield is defined as the number of sputtered atoms per incident ion. In case of RF bias, below about 50 kHz, ions are sufficiently mobile to establish a complete discharge at each electrode on each half-cycle. DC sputtering conditions essentially prevail at both electrodes, which alternately behave as cathodes and anodes. Above 50 kHz two important effects occur: firstly, electrons oscillating in the glow region acquire enough energy to cause ionizing collisions, reducing the need for secondary electrons to sustain the discharge. Secondly, RF voltages can be coupled through any kind of impedance so that the electrodes need not be conductors[138]. This makes it possible to sputter any material irrespective of its resistivity. RF sputtering essentially works because the target self-biases to a negative potential. Once this happens, it behaves like a target in DC biased where positive ion bombardment sputter away atoms for subsequent deposition. Negative target bias is a consequence of the fact that electrons are considerably more mobile than ions and have little difficulty in following the periodic change in the electric field. In an RF sputtering system, the target is capacitively coupled to the RF generator. As the oscillating RF signal is applied to the target, a large initial electron current is drawn during the positive half of the cycle. However, only a small ion current flows during the second half of the cycle. This would enable a net current averaged over a complete cycle to be different from zero; but this cannot happen because no charge can be transferred through the capacitor. Therefore, the operating point on the characteristic shifts to a negative voltage – the target bias – and no net current flows.

3.1.2 Magnetron Sputtering

The use of magnetic fields confine the plasma close to the target and enhance the sputtering rate. In a magnetron sputtering system, a magnetic field is applied that is perpendicular to the electric field between the cathode and anode. Due to these perpendicular fields, electrons that would otherwise simply accelerate towards the anode execute cycloid motion, with the net motion perpendicular to both fields. This increases the likelihood of impact ionization by effectively trapping the electron near the cathode. The result is that at a given pressure and target voltage, greater current density flows between the electrodes. Alternatively, magnetron sputtering allows the same current to flow at lower gas pressures. DC magnetron sputtering at a few mTorr allows sputtered material to arrive at the substrate with more of its initial energy[Fig.3.4].

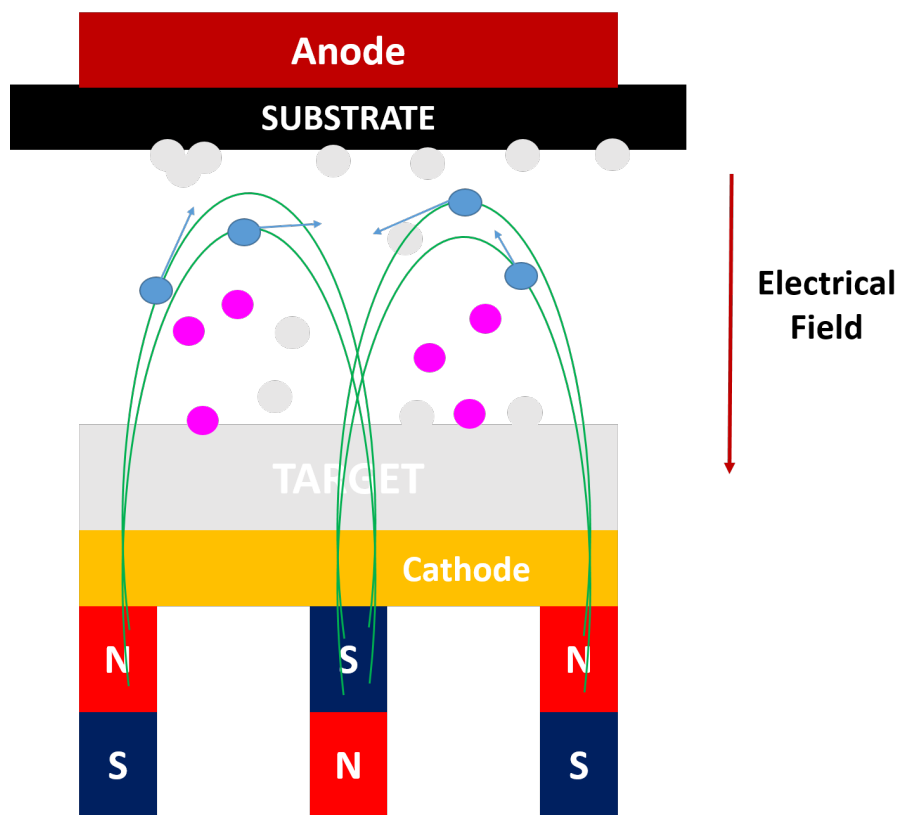


Figure 3.4: Scheme of magnetron sputtering process. The magnetic field (green lines) traps secondary electrons (blue) in the discharge for a longer duration, increasing the probability of ionising argon (magenta) during their travel from cathode (target) to anode (substrate).

The IV curve of a DC magnetron sputtering source has been proposed to have the following form[139]:

$$I = \beta(V - V_0)^2 \quad (3.4)$$

where β is a coefficient, while V_0 is the minimum voltage for maintaining the discharge. The value of β is correlated with the strength of the magnetic field of the magnetron and is roughly a measure of the magnetron efficiency. The coefficient β changes with pressure depending on the magnetic field strength and changes with secondary electron yield[139].

In order for the glow discharge to be self-sustaining, every electron emitted from the cathode must produce sufficient ions to create one additional electron at the cathode. This minimum voltage is given by the expression:

$$V_0 = \frac{kV_i}{\Gamma_e \epsilon_i \epsilon_e} \quad (3.5)$$

where k is a constant fit, V_i is the ionization energy of the sputtering gas, Γ_e is the effective secondary electron yield, ϵ_i is the ion collection efficiency and ϵ_e is the ion generation efficiency[140]. Due to the magnetron, the secondary electron yield from the target is effectively reduced, since secondary electrons captured in the magnetron have a pressure-dependent chance of being recaptured by the cathode[141], unlike without the magnetron. At sufficiently low pressure, the cycloid motion of a free electron that starts at the cathode surface with zero velocity will cause the electron to return to the cathode surface where it can be recaptured. Without the magnetron it would move towards the anode unambiguously. The reduced effective secondary electron yield is clearly compensated for by the increased number of ions produced per secondary, due to the increased plasma densities and deposition rates made possible by magnetrons. This result does suggest however that a sufficiently strong magnetic field could actually increase the plasma impedance. Magnetrons are commonly classified as 'balanced' or 'unbalanced'[Fig.3.5].

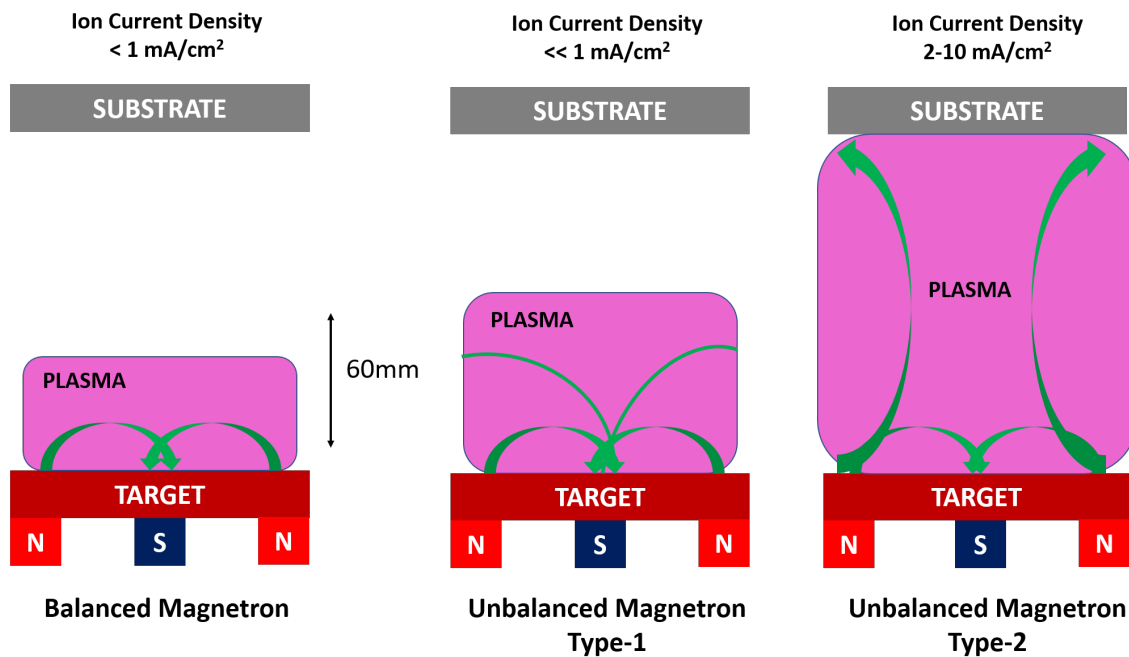


Figure 3.5: Schematic representation of the plasma confinement observed in conventional and unbalanced magnetrons[142].

In a balanced magnetron, the plasma is strongly confined to the target region. A region of dense plasma typically extends some 60 mm from the target surface. Films grown on substrates positioned within this region will be subjected to concurrent ion bombardment, which can strongly influence the structure and properties of the film. Substrates are placed outside of this region. Consequently, the ion current drawn at the substrate (typically less than 1 mA/cm^2) is generally insufficient to modify the structure of the film.

The energy of the bombarding ions can be increased by increasing the negative bias applied to the substrate. However, this can lead to defects in the film and increased film stress, and therefore, be detrimental to the overall film properties. Thus, it is difficult to deposit homogeneous and uniform films on large, or complex components using conventional magnetrons[143]. To deposit dense films without introducing excessive intrinsic stresses, a high flux ($>2 \text{ mA/cm}^2$) of relatively low energy ($<100 \text{ eV}$) ions is generally preferred[144]. These conditions are readily provided by unbalanced magnetrons. The unbalanced magnetron was described the first time by Window and Savvides and classified as type-1 and type-2[145, 146, 147]. In the type-1 case, the central pole was strengthened relative to the outer pole. In this case the field lines which do not close in on themselves are directed towards the chamber walls and the plasma density in the substrate region is low. In the type-2 the outer ring of magnets is strengthened relative to the central pole. In this case, not all the field lines are closed between the central and outer poles in the magnetron, but some are directed towards the substrate, and some secondary electrons are able to follow these field lines. Consequently, the plasma is no longer strongly confined to the target region, but is also allowed to flow out towards the substrate. Thus, high ion currents can be extracted from the plasma without the need to externally bias the substrate. Thus, in addition to providing a high flux of coating atoms (compared to a basic sputtering source), the type-2 also acts as a very effective ion source. Furthermore, the ion current drawn at the substrate is directly proportional to the target current. The deposition rate is also directly proportional to the target current. As a result, and unlike other ion-plating processes[148, 149], the ion-to-atom arrival ratio at the substrate remains constant with increasing deposition rate[150].

3.1.3 Reactive Sputtering

Sputter deposition of metallic and insulating compounds is of considerable technological interest. Sputter-deposited compounds commonly used in superconductor applications include nitrides like NbN, TiN, TaN and NbTiN. A reactive gas, such as nitrogen or oxygen, when introduced into a sputtering process, will react with the target surface as well as the sputter deposited metal atoms, and thus form a compound thin film at the substrate as well as at the part of the chamber walls that receives sputtered particles. This method, known as reactive sputtering, also has the advantage of providing more control over the stoichiometry of the deposited film by adjusting the gas flow. As the reactive gas flow is increased, the topmost layer of the target changes from metallic to compound, which often implies a change from conducting into non-conducting. Accordingly, the former sputtering condition is commonly referred to as metal mode and generally has a comparatively high rate, whilst the latter condition is referred to as compound mode. Target poisoning during reactive sputter deposition is an effect that significantly influences both the stoichiometry and the deposition rate. The central difficulty with reactive sputtering is balancing hysteretic IV behaviour, film stoichiometry, and deposition rates, which are all affected by the flow of reactive gas. Compounds that can be formed with reactive sputtering, generally have different secondary electron emission coefficients and different sputtering yields than their metallic constituents. The secondary electron yield has a dramatic effect on the plasma behaviour.

It is not hard to imagine that the current-voltage behaviour of a plasma can be very different based on the details of the reactive gas. Hysteresis in reactive sputtering can be understood in the following way[151, 152]: assume that there is no compound on the target surface, and it is established a plasma under the conditions of discharge voltage stabilization[Fig.3.6].

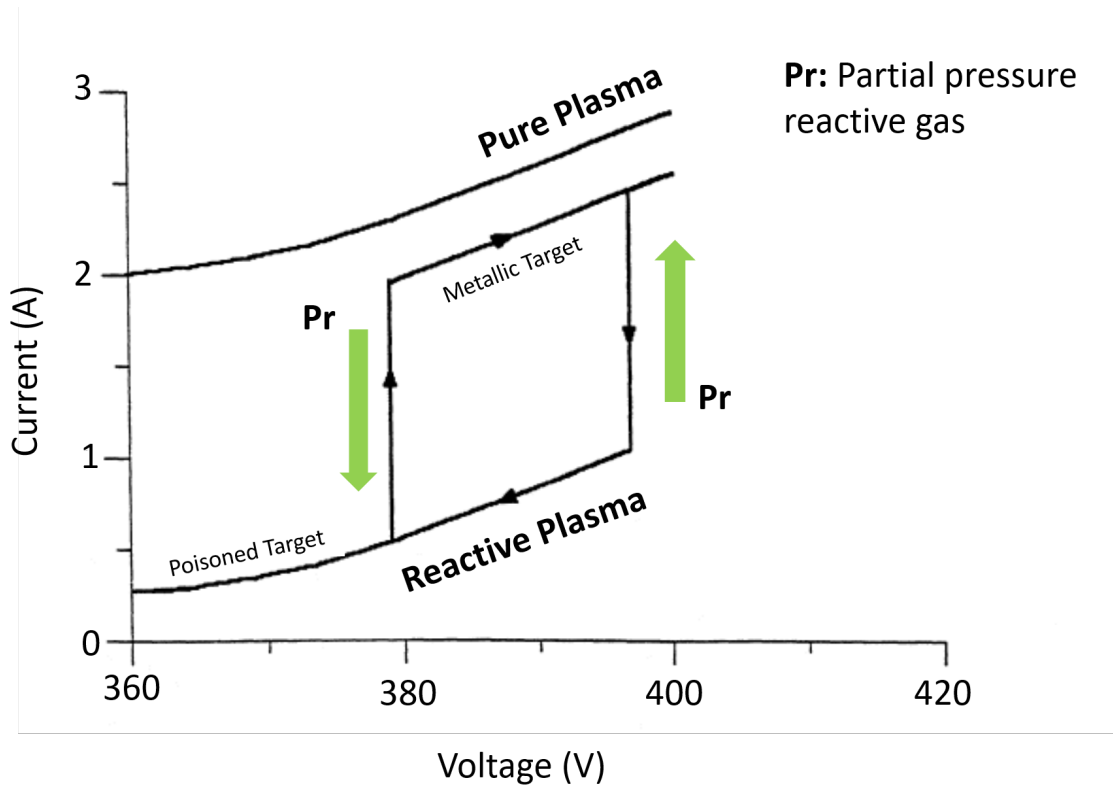


Figure 3.6: IV characteristic of the plasma during a reactive sputtering in the voltage stabilization condition[151].

As the flow of reactive gas is added to the plasma, the compound will form at the target surface. At low discharge voltages and when the sputtering rate is very low, the reactive gas mainly reacts with the target becoming covered with a compound and the target is poisoned. As discharge voltage gradually increases, the sputtering rate of increases and at a certain critical voltage, the sputtering rate of the target becomes higher than the rate of the poisoned target. The sputtered target atoms absorb reactive gas. The reactive gas partial pressure decreases and since the pure target has a larger secondary electron emission factor than the poisoned target surface, discharge current rises sharply. Then, if discharge voltage is afterwards gradually reduced, the reactive gas will still be almost completely absorbed by the target to form the compound on the substrate. However at a critical point, the target sputtering rate decreases such that fewer ions reach the surface. As a result, the reactive gas partial pressure increases and the current drops abruptly and the target is instantly poisoned. A different behaviour can be observed when the sputtering operates under the current stabilization condition.

The plot looks S-shaped[Fig.3.7], i.e. the hysteresis effect does not take place, because the current stabilization compensates for the change in the sputtering rate occurring at the transition from the metallic to the reactive mode.

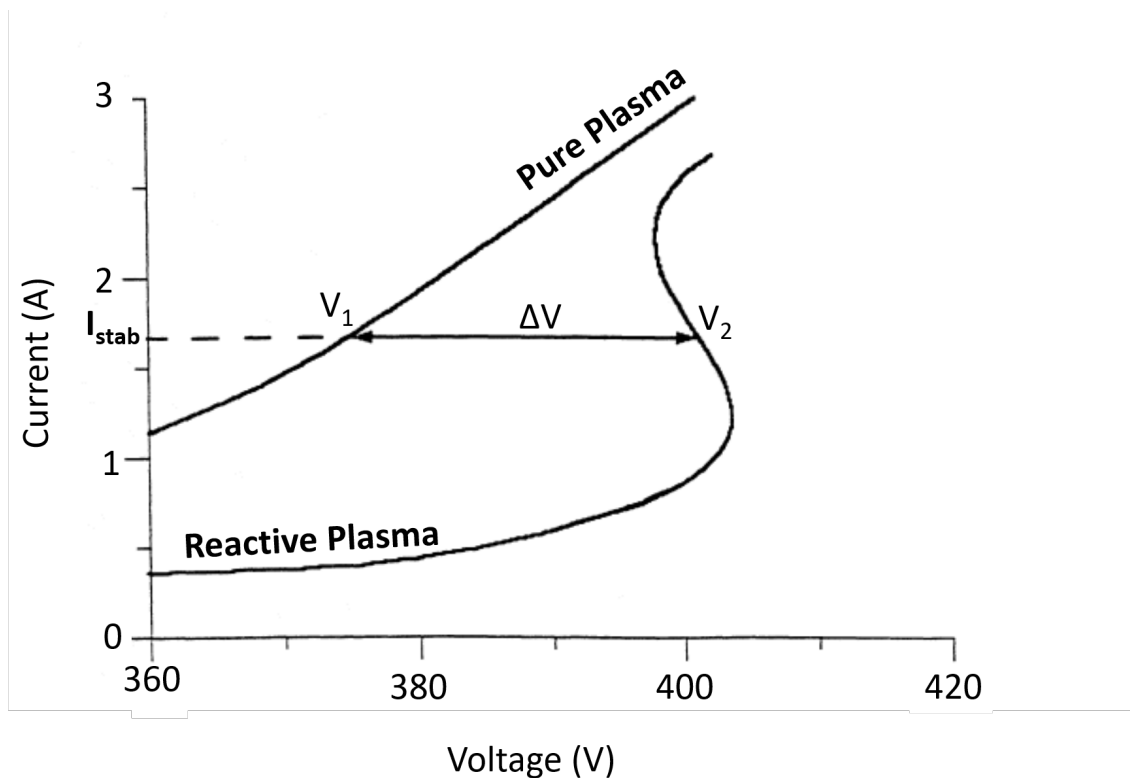


Figure 3.7: IV characteristic of the plasma during a reactive sputtering in the current stabilization condition[151].

For example, if the sputtering rate increases, the area of the target covered with the compound material gets smaller and the sputtering rate of metal increases. A higher proportion of the metallic atoms at the target surface absorb more reactive gas, so the partial pressure of the reactive gas decreases and the discharge voltage as well. The sputtering rate then returns to its initial value. If the sputtering rate decreases, the compound will form at the target surface and the discharge voltage rises, due to which fact the sputtering rate is restored. Therefore, there is a one-to-one correspondence between the discharge voltage and the reactive gas partial pressure in the discharge. This fact makes it possible to estimate the value of the reactive gas partial pressure in the discharge, using the quantity $\Delta V = V_2 - V_1$, which can be measured easily because V_1 is the discharge voltage in pure plasma for a given stabilized current and V_2 is the discharge voltage in a gas mixture for the same current.

3.2 The Magnetron Sputtering Equipment

The materials used for the fabrication of the SNSPD arrays characterized in this work of thesis are made by a DC/RF balanced magnetron sputtering tool (Plassys VI) installed in 2014 in the James Watt Nanofabrication Centre (JWNC) of the University of Glasgow[Fig.3.8].

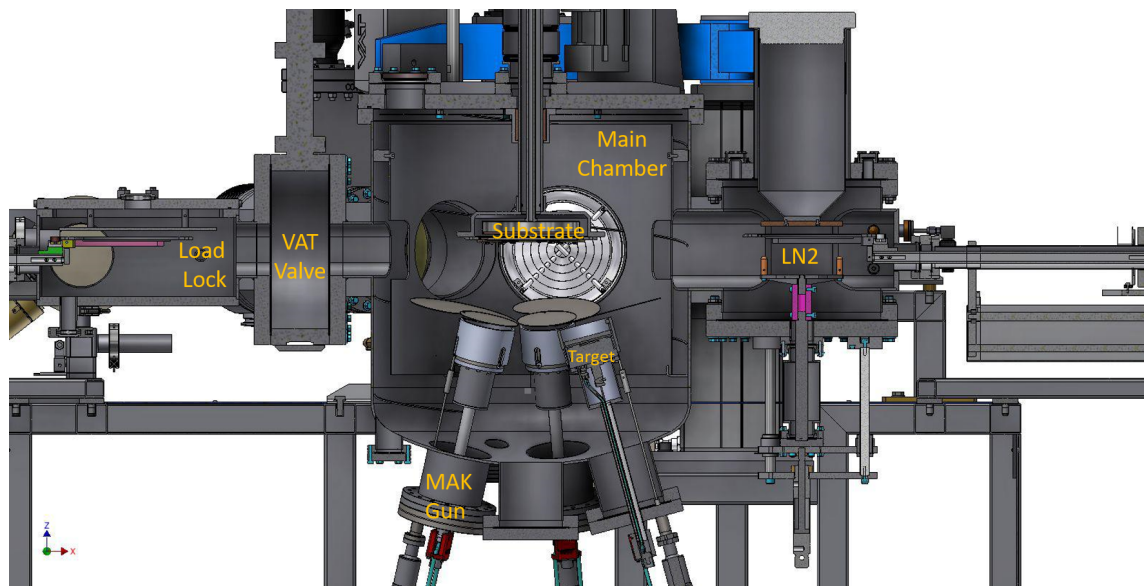
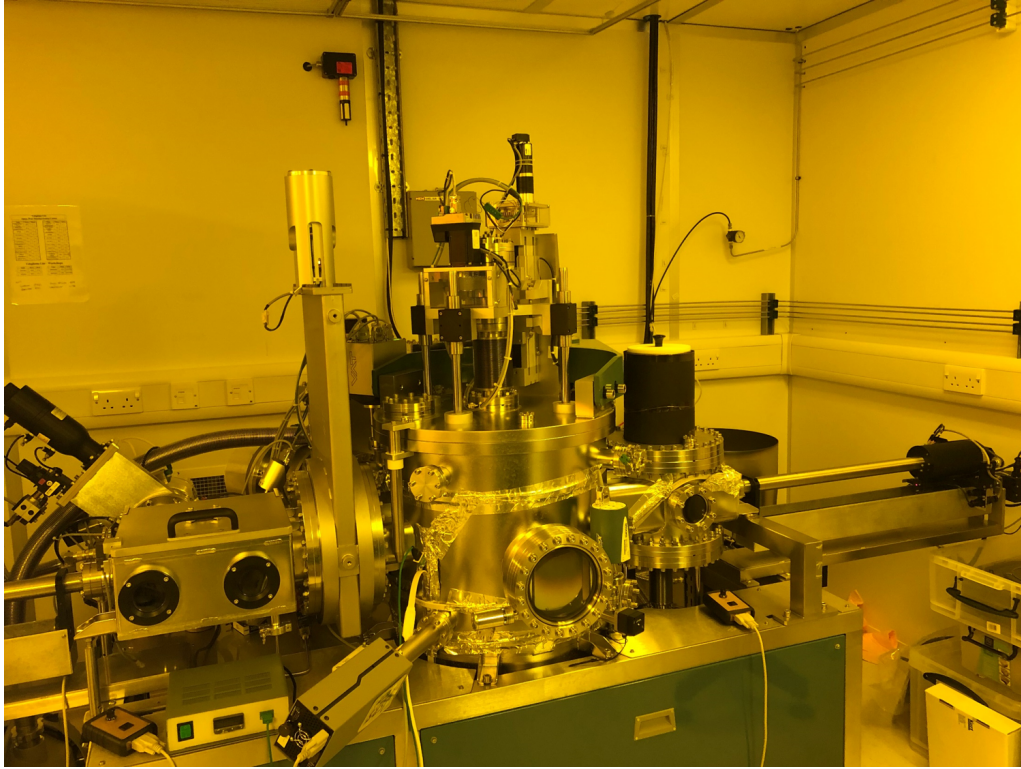


Figure 3.8: Plassys VI DC/RF Magnetron sputter deposition system installed in the JWNC (upper). CAD drawing of the sputtering tool (lower).

This equipment has been manufactured by the French company Plassys and it composed of a main sputtering chamber with 304 litre volume mounted on a careened frame with levelling feet, a control cabinet mounted on casters, a load lock separated from the main chamber by a valve and two automatic sample transfer arms. One transfer arm is designed to transfer the sample from the load lock to the main chamber while the other on transfers the sample from the main chamber to a nitrogen trap used to cool down the substrates before the sputtering process. This system is computer controlled. All movements are carried out via magnetic coupling (rotation) or bellows sealing (translation). Inside the main chamber are installed five MAK magnetron sputter guns manufactured by Meivac, USA[Fig.3.9].

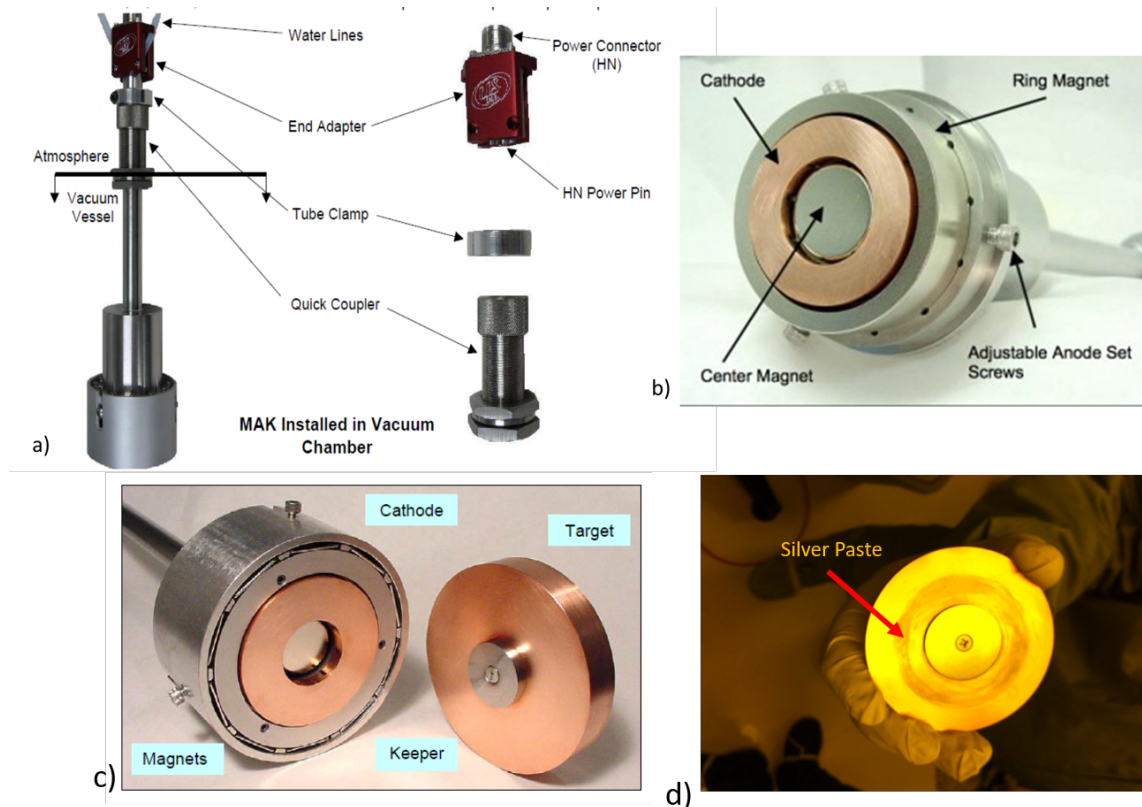


Figure 3.9: a) Scheme of the MAK sputtering gun (Meivac, USA) installed in the main chamber of the sputtering tool. b) Extremity of the MAK gun where the target is placed. c) The target is bonded to a Cu backing plate with a magnetic keeper attached. d) The bonding is made by a silver paste[153].

Each gun can hold a 76.2 mm diameter sputtering target with a thickness from 3.17 mm to 6.35 mm. Targets are protected by a shield and covered by a moveable shutter made of Al. All targets are connected to a power supply. The power supplies are configured to enable co-sputtering from two or more targets simultaneously. The table [3.1] shows targets installed in the sputtering tool, their power source, their manufacturers, their dimensions and purity. The substrate holder is mounted on a magnetically coupled feedthrough. Its distance from the magnetron cathodes can be adjusted by a motorised controller. The target-substrate distance can be adjusted over a range of 74 - 160 mm. The substrate holder can even rotate up to a speed of 200 rpm during thin film deposition to provide better uniformity. The configuration between the substrate and targets can be direct or confocal.

Table 3.1: List and properties of targets installed in the Plassys VI as of October 2019

Material	Purity	Diameter	Thickness	Power Source	Manufacturer
Nb	99.9%	3.00"	0.25"	DC	IAM
Ti	99.9%	3.00"	0.25"	DC	MMS
Si	99.9%	3.00"	0.25"	RF	IAM
Al	99.9%	3.00"	0.25"	DC	IAM
Mo ₈₀ Si ₂₀	99.9%	3.00"	0.25"	DC	KJLC

The confocal configuration is when multiple magnetron sputtering sources are arranged in a specific circular pattern and are aimed at a common focal point. When a substrate is placed in the vicinity of this focal point and rotated on its own axis, it is possible to deposit highly uniform single layers, multi-layers and co-deposited alloy films. The configuration installed in the sputtering equipment is a confocal configuration[Fig.3.10].

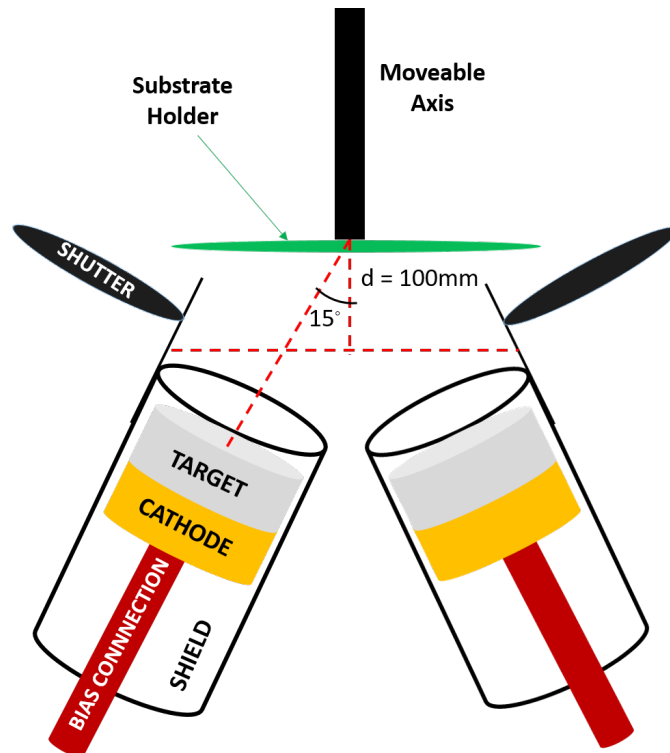


Figure 3.10: Diagram of the confocal configuration installed in the Plassys VI. The guns are oriented upwards at 15° to the vertical axis, whereas the substrate holder is on axis facing downwards. The substrate holder is placed at 100 mm from targets to get the most uniform film growth over a large area.

According to the specifications provided by the system manufacturer, at a distance of 100 mm the film growth is most uniform over a large area. There is a PID controlled resistive heater attached to the holder, which can heat the substrates up to 800 °C. The heater has a factory calibrated thermocouple to measure the substrate temperature. The sputtering system also has the capability of cooling substrates before film growth. The main chamber is connected to a liquid nitrogen (LN₂) trap mounted on a flange. This trap is manually filled by nitrogen liquid before the film deposition. The substrate carrier is transferred from the main chamber to an elevator mounted on the base plate. This motor driven elevator pushes the substrate carrier against the LN₂ trap to cool it down. Once the carrier has been cooled down, it is transferred to the substrate holder. A magnetically coupled transfer arm will move the substrate from the LN₂ position to the deposition position inside the main chamber. The sputtering chamber is connected to two high vacuum pumping assemblies: a turbomolecular pump model STP-A803/A1303 manufactured by Edwards Limited and a cryopump model cryo-plex 8LP of the American company Trillium. These pumps can generate in the main chamber a vacuum below 1×10^{-7} Torr. To improve the vacuum in the main chamber, a system to bake-out has been installed both inside and outside the main chamber. During a bake-out process the main chamber is exposed to high temperature in vacuum to remove gasses, water vapour and other contaminants. The bake-out inside the chamber is controlled by the software, while the external bake-out is controlled by a thermocouple[Fig.3.11].

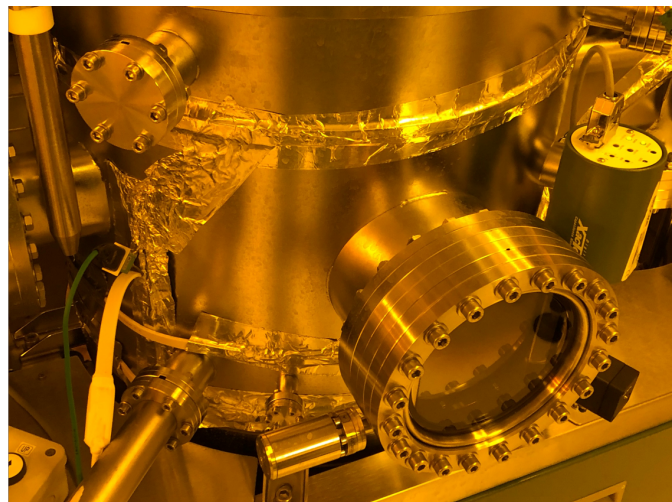
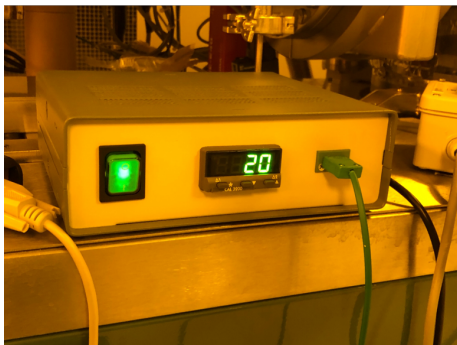


Figure 3.11: A heater tape is attached to the main chamber in order to bake-out the walls of the main chamber.

The vacuum can be improved by titanium sputtering. Since Ti ions are very reactive, components of the residual gas in the chamber which collide with the chamber wall (covered of Ti) are likely to react and to form a stable, solid product. This is known as gettering. Thus the gas pressure in the chamber is reduced. So after a bake-out and a Ti sputtering, the base pressure in the main chamber can reach a value below 5×10^{-9} Torr. The pressure in the main chamber is monitored by a Pfeiffer TPR 280 Pirani Gauge (from 3.75×10^{-4} Torr to 750 Torr range) and by an Ionization Gauge Transducer (from 3×10^{-10} to 5×10^{-2} Torr range) manufactured by the Kurt J. Lesker company.

The main chamber is connected to four gas lines (Ar, N₂, O₂ and CH₄). Each line is equipped with a digitally controlled mass flow controller and a pneumatic stop valve. During the execution of any process in the chamber, the cryopump line is closed with a gate valve (Mode CF-200) and the turbopump is throttled with a butterfly valve (VAT model 612). The position of this throttle valve, along with the flow rate of incoming gas, controls chamber pressure during any process. During sputtering processes, the pressure in the main chamber is monitored by a capacitance manometer manufactured by Brooks (100 mTorr range) as it is independent of by the type of gas present in the chamber. The substrates are then inserted into the system through a load lock mounted on the left side of the chamber. The load lock is a stainless steel chamber with a hinged top lid and viewport [Fig.3.12].

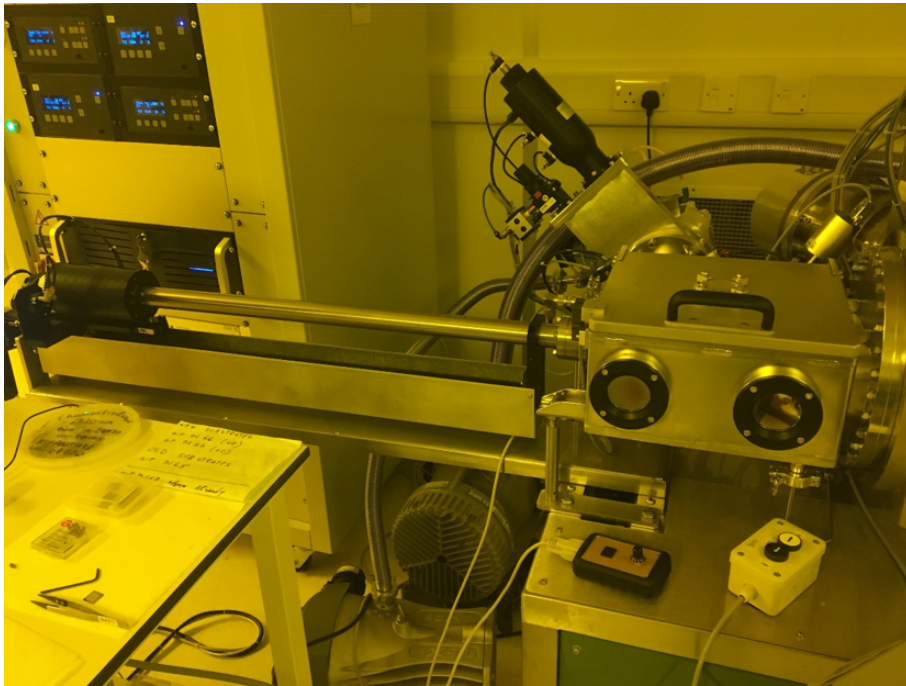


Figure 3.12: Load lock attached to the main chamber of the sputtering tool. The transfer arm (left) is used to move the sample from the load lock (right) into the main chamber (not show)

A transfer valve separates the main process chamber from the load lock, allowing the sputter chamber to be kept at high vacuum at all times and to prevent contamination. The load lock is connected to a turbomolecular pump model nEXT 400 that can achieve a vacuum state of about 3×10^{-8} Torr. Before being transferred to the main chamber, the substrate can be cleaned with argon plasma in the load lock. The plasma is generated by a RF power supply. A motor driven, magnetically coupled transfer arm (the same design as the arm serving the LN₂ trap) is used to insert the samples in the chamber and to transfer the samples back to the load lock at end of film growth. The substrate carrier has a set of adaptors to mount 6" wafer or lower and adaptors to install substrates 10 mm × 10 mm or 15 mm × 15 mm square. Adaptors are made of aluminium for room temperature or cooled deposition processes.

A specific substrate carrier made of molybdenum is to be used when substrates need to be heated[Fig.3.13].

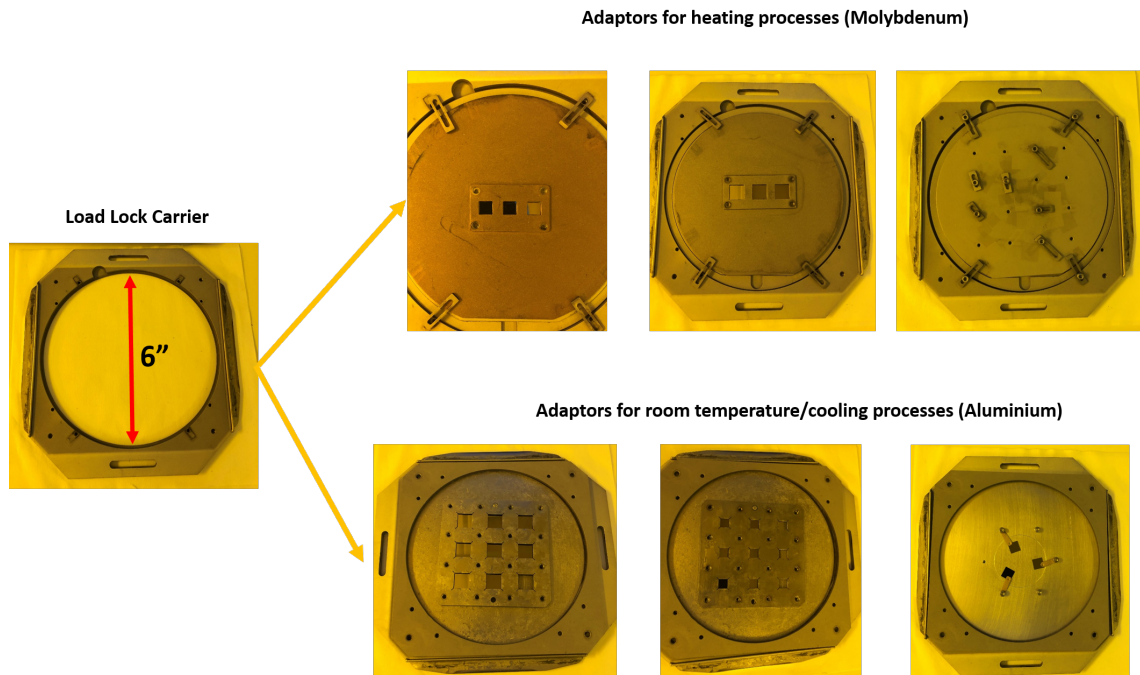


Figure 3.13: The substrate carrier. It has an adaptor mount to install 6 inches (152.4 mm) diameter wafers or eventually substrates diced in 10 mm × 10 mm or 15 mm × 15 mm squares. The Molybdenum adaptor is used when substrates need to be heated, the Al one when substrates need to be cooled.

3.3 Lithography

Following sputter deposition of the thin film, the next process is to define the geometry of the device. This process is called lithography and it consists of exposing the film (covered by a polymeric substance called resist) to an irradiation of high energy. After exposure, the sample is developed by an appropriate solvent to obtain the pattern desired. Resists are classified as positive and negative according to their exposure properties. The sample is then developed and if the resist is positive exposed parts are removed. If the resist is negative parts unexposed are removed[Fig.3.14]. The irradiation can be done either using photons or electrons. In case of photons the process is called photolithography, while in case of electrons is called electron beam (e-beam) lithography. The choice of the irradiation depends on the dimensions of the desired pattern. Usually the photolithography is used to realize patterns of the order of microns irradiating the sample by ultra-violet (UV) light wavelength (less than 400nm), while the e-beam is used to realize patterns of the order of nanometres.

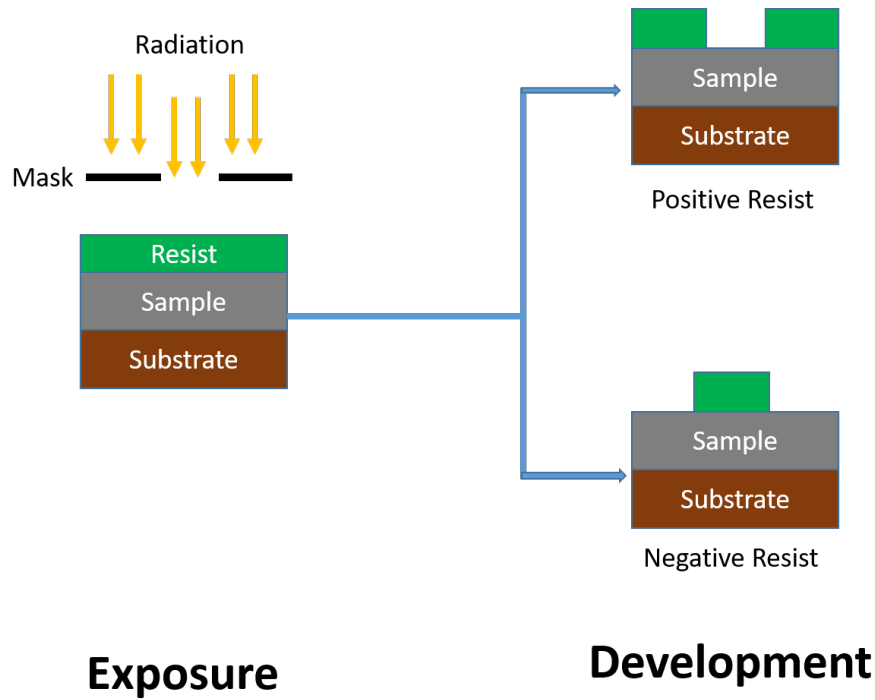


Figure 3.14: The fundamentals of lithography scheme process: the sample is deposited onto a substrate after the sputtering process. The sample is then covered by a polymeric substance called resist sensitive to the high energy irradiation. The geometry of the pattern desired is designed on the mask placed between the sample and the irradiation source. After the exposure, the sample is developed and if the resist is positive the part of the part exposed are removed. If the resist is negative the part unexposed are removed.

The reason is similar to the difference between the resolution of an optical microscope and a scanning electron microscope (SEM). As optical photon, the movement of high-speed electrons also has a wavelength given by the relation of Louis de Broglie:

$$\lambda = \frac{h}{mv} \quad (3.6)$$

where h is the Planck constant, m the mass the electron (see glossary) and v the velocity of the electron determined by the accelerating voltage, or electron potential, given by the equation

$$V = \frac{1}{2e}mv^2 \quad (3.7)$$

Combining these two equations

$$\lambda = \frac{h}{\sqrt{2meV}} \quad (3.8)$$

Since the typical accelerating voltage of a e-beam equipment is 100 keV, then the wavelength of electrons is calculated to be about 4 pm.

3.3.1 Photolithography

Photolithography is the standard process to realize structures of the order of microns. This process has been used in this work to realize three series of microwires of 200 μm length and width 2 μm , 5 μm and 10 μm . Each microwire is patterned in a four-probe structure used to measure the transport properties of the superconducting film. To transfer these patterns on a sample, a Cr photomask of 5" square has been fabricated via e-beam lithography in the JWNC. Before the exposure, the sample must be covered by the photoresist. First, the surface of the sample is cleaned of impurities via acetone and methanol in ultrasonic bath for 5 min and then rinsed in reverse osmosis (RO) water. The sample is then heated at 90 °C for three minutes to drive off any moisture that may be present on the surface. The sample is then covered with a uniform layer of resist applied via spin coating. The sample is mounted on a vacuum chuck and the resist is applied to the centre of the sample via a syringe, then the sample is spun using a calibrated recipe to achieve the desired resist thickness. The sample is then baked to evaporate the coating solvent and to harden the resist after the spin coating. The resist used in this work is a photoresist S1805 of the positive S1800 series[Fig.3.15].

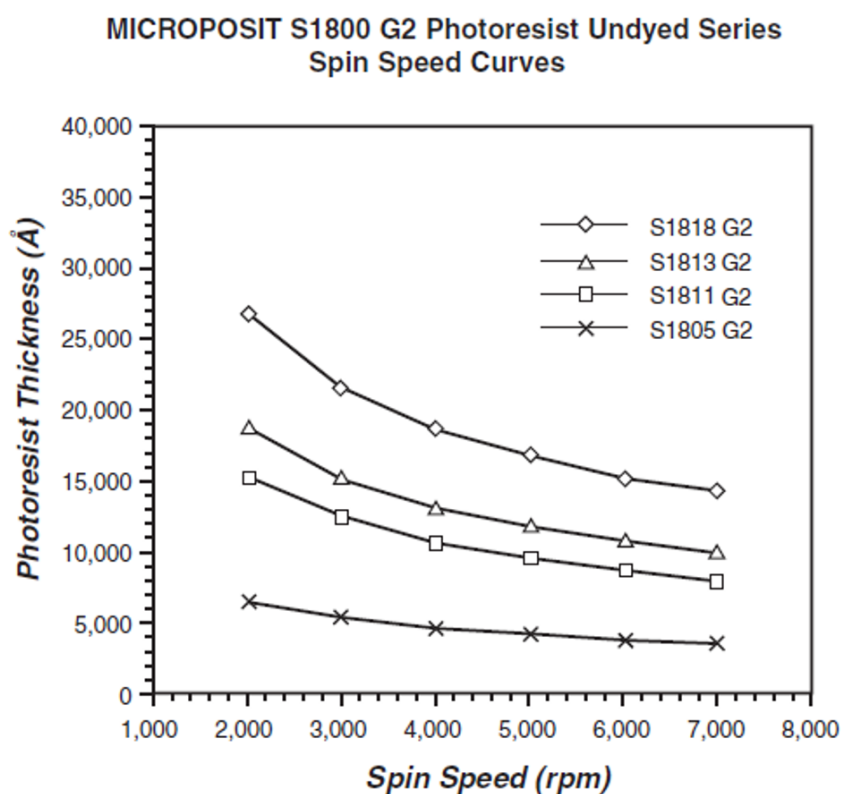


Figure 3.15: Thickness of main types S1800 positive photoresist as function of the speed of the spin coating. This graph is taken from S1800 microposit datasheet[154].

This resist has been spun at 4000 rpm for 30 sec (thickness 0.5 μm) and then heated on a hot-plate at 115 °C for 1 min. At this point, the sample is ready to be exposed to the light. The photolithography process is performed using the Karl Suss Mask Aligner MA6 installed in the JWNC[Fig.3.16].

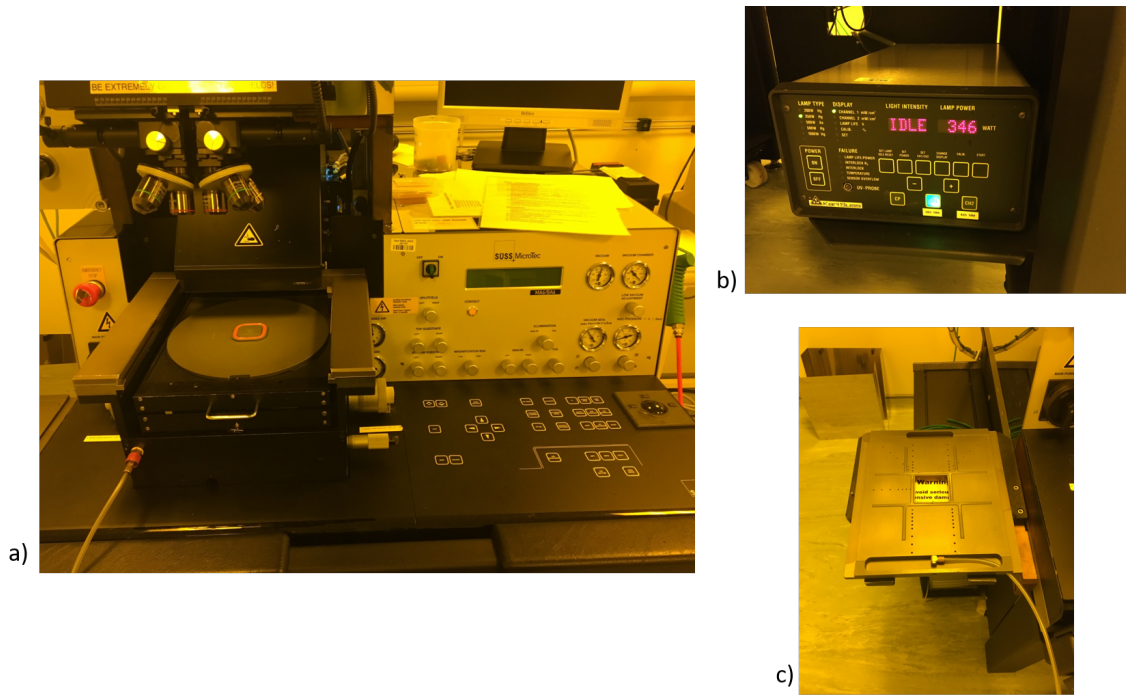


Figure 3.16: a) Mask Aligner MA6 manufactured by SÜSS MICROTEC SE installed in the JWNC[155]. b) Power source of the exposure lamp, in this case a 350 W UV365 mercury arc discharge lamp. c) Vacuum chuck where the photomask is placed.

The Karl Süss MA6 is a contact aligner used for optical lithography down to 1 μm as reported in the manual[155]. It can be used with 4-inch, 5-inch and 7-inch mask plates and is capable of samples up to 6 inch (150 mm) diameter wafer size substrates. Wafers and substrates up to 6 mm thickness can be processed. It is equipped with a 350 Watt, UV365 mercury arc lamp (350 nm – 450 nm wavelength range) capable of operating in constant power or constant intensity mode. The illuminating photons are generated by photoelectric effect. The MA6 is ideal for exposing broadband positive and negative resists and it can be used both for front side and back side alignment. The photomask is mounted on a vacuum chuck, while the sample is held on a support beneath the photomask. Accurate levelling and gap control of mask and wafer is essential to avoid parallax errors and to achieve higher resolution. The levelling and gap calibration system of the MA/BA6 is designed to fulfil highest demands with regards to accuracy and reliability. The MA6 offers various exposure modes to meet any requirements for a broad range of applications. Soft, hard and vacuum contact printing is used to achieve highest resolution down to submicron range. Proximity printing is applied to avoid any mask/wafer contact. The prevention of mask contamination directly translates into higher yield. For samples used in this thesis, the exposure mode was performed in hard contact mode, a gap of 40 μm between the sample and the photomask and the alignment of the photomask was made by the top side. The final exposure was carried out using light of 365 nm wavelength. After the exposure the sample is developed rinsing it in the microposit MF-319 developer for 75 sec and then in RO water to block the development process.

3.3.2 Electron Beam Lithography

Electron beam lithography (EBL) uses a beam of electrons to expose the resist and offers major advantages over the photolithography as the wavelength of the electrons is much shorter than that of UV light, an electron beam is capable of patterning at a far higher resolution, allowing features down to about 10 nm to be written, taking into account spherical and chromatic aberrations. The resist itself is sensitive to electrons and not electromagnetic radiation. Instead of using a physical mask to define the pattern, the electron beam is computer controlled and exposes regions as determined by an electronic computer-aided design (CAD) mask. Although the ability to create any pattern electronically without the need to fabricate expensive mask plates makes e-beam a highly flexible tool, the exposure process occurs serially, pixel-by-pixel, resulting in a significant writing time. This, together with the high equipment and maintenance costs are the main drawbacks of the technique. As well as being able to write single step jobs, electron beam writers are capable of aligning successive patterns on a substrate (registration) to within about 50 nm, allowing users to write multiple lithography steps for more complex samples. The EBL equipment used to fabricate SNSPD arrays of this thesis is a Vistec VB6 UHR EWF (ultra-high resolution - extended wide field) one of the most advanced EBL systems in the world providing direct writing in micro and nanometre patterns with a typical resolution of 25 nm, a stitching accuracy with a maximum error of 5 to 30 nm depending on the field size, a typical overlay accuracy of about 20 nm (maximum error)[Fig.3.17] .

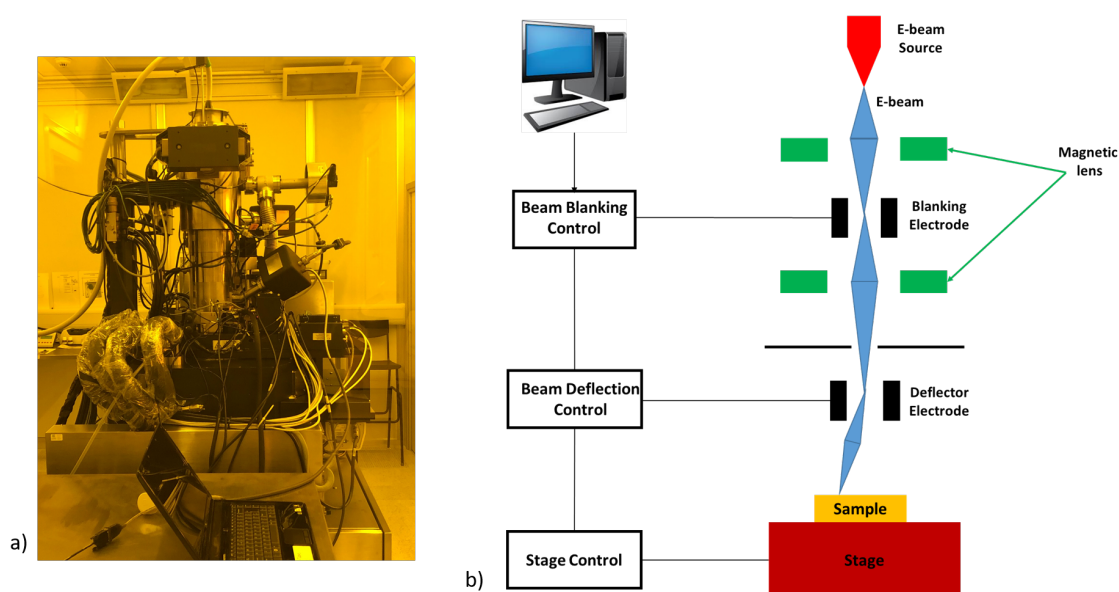


Figure 3.17: a) Vistec VB6 UHR EWF electron beam lithography equipment installed in the JWNC. b) Schematic illustrating the main principles of EBL system operation.

A beam of electrons is generated by an electron gun using a cathode emission. In Vistec VB6, the electron gun is a Schottky emitter equipped with a heated zirconium oxide (ZrO_2) coated tungsten (W) tip. Electrons are emitted by thermionic effect, are accelerated by a potential (fixed at 100 keV) and then focused onto the material through a system of apertures, electrodes and magnetic lens. The pattern data for lithography is stored in the hard disk of the computer used to control the system.

Subsequently, this data is transferred from the hard disk to the blanking control system and beam deflector control system through a high speed data processing system. The beam is switched on and off to draw the pattern by blanking circuit, and deflected to the designated position by operation of the deflector circuit. The desired pattern is drawn using a combination of this electron beam movement and the movement of the stage. In this work, the layout of an SNSPD array is designed by the software LayoutEditor and produced as a .gds file. Within the one file, LayoutEditor allows the creation of individual cells or structures which can be brought together to make up the final design. In addition, different layers can be specified if multiple lithography steps are required. However, the .gds file is not compatible with the beam writer system because the machine is only able to handle primitive shapes. Hence, additional processing steps are required to convert the file to a format compatible with the beam writer. The .gds file is then transferred to a computer employing a software named Beamer (product by the German company GeniSys GmbH). Once a series of input parameters are provided along with the .gds file, the software fractures the design to be exposed into trapezoids. The .gds file is then converted into a .vep file which is sent to both the beamwriter control computer and the job layout program BELLE (Beamwriter Exposure Layout for Lithographic Engineers) used in the next step of the conversion process. BELLE requires the .vep file complete with all of the patterning information to produce a final job layout (.bel) file. Finally, the layout file is sent to the control computer and together with the design file, is used by the beamwriter to pattern the resist. The interaction between the electron beam and the sample exposed generates scattering effects[Fig.3.18].

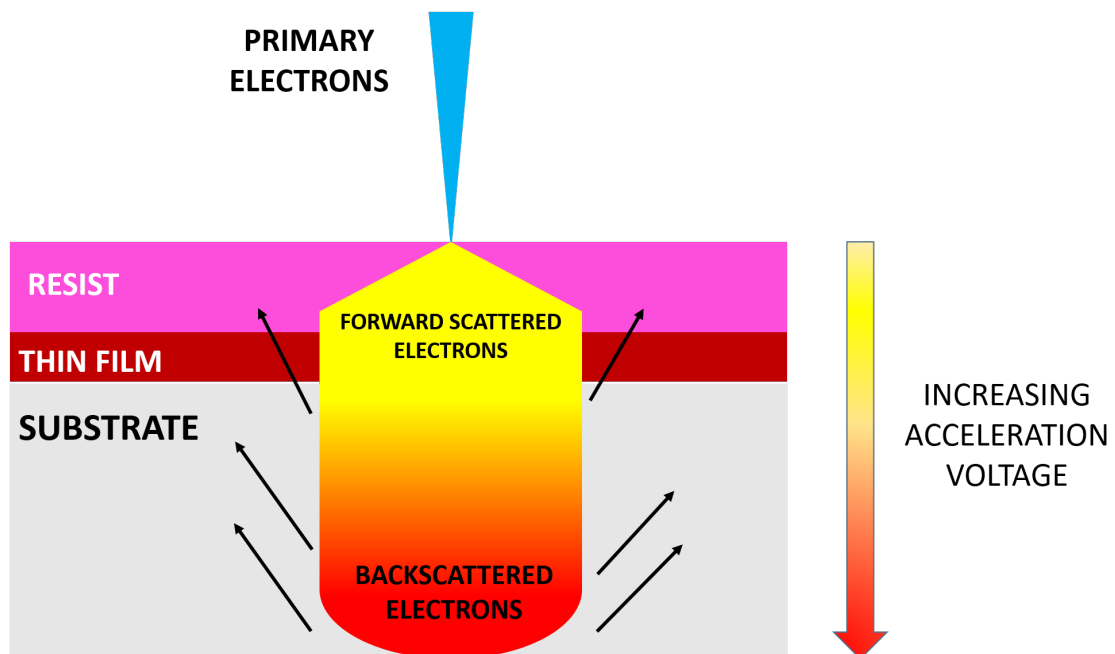


Figure 3.18: Interaction volume of e-beam exposure. As the primary electrons penetrate the resist and enter in the substrate, some of them undergo large-angle scattering events, leading to backscattering, in which these electrons return back to the resist in places far from the spot where the primary beam entered. The forward scattering arises from electron-electron interactions, which deflect the primary electrons by a typically small angle, thus statistically broadening the e-beam in the resist (and further in the substrate)

These effects are classified as forward and backward scattering. In forward scattering, the beam electrons collide with the orbital electron of an atom from resist and substrate to either excite or ionize the atom resulting in an inelastic scattering event while the backscattering electrons are due to the collision of an electron with the nucleus of an atom in the substrate resulting in an elastic scattering event. When electrons penetrate the resist and enter the substrate some of them undergo large-angle scattering events, leading to backscattering, in which these electrons return back to the resist in places far from the spot where the primary beam entered contributing to the exposure and causing subsequent inelastic scattering. This causes additional, usually undesirable, exposure in the resist and is known as the proximity effect. The electron energy influences the scattering angle: lower energy electrons scatter to a larger angle whereas higher energy electrons scatter to a smaller angle. In these terms, high-energy electrons (high accelerating voltage) help to minimize the proximity effect. In this thesis, two kinds of e-beam resist have been used: polymethyl methacrylate (PMMA) and ZEP-520. Both are positive tone resist. The PMMA is usually used for a metal lift-off process called "metalization". In this process gold pads are defined to bond the device to allow electronic characterization and the markers for alignment of the VB6. As in photolithography, the surface of sample is first cleaned ultrasonically by acetone and methanol, then rinsed in RO water. After 5 min of prebake in a 180 °C oven, a bi-layer of 12% 2010 PMMA (AR-P 632.12) and 4% 2041 PMMA (AR-P 649.04) are spun onto the substrate at 4000 rpm, which roughly gives a resist thickness of 0.78 μm for 12% PMMA and 0.15 μm for 4% PMMA respectively and then baked on vacuum hotplate for 5 minutes at 150 °C each. Then the samples are exposed by a dose of 750 $\mu\text{C}/\text{m}^2$ and a beam of 64 nA with a spot size of 33 nm. After exposure, the substrate developed in a solution of MIBK:IPA (1:1) for 60 seconds and rinsed in IPA for few seconds before being blown dry by nitrogen. At this point, the bond pads and the markers are defined depositing Ti-Au (5nm-100nm) on the sample by electron beam evaporation and then cleaned ultrasonically by acetone (lift-off). The ZEP-520 was used to define pixels of the SNSPD nanowire array and their connections with the gold pad. After the cleaning process, the sample was spun by 2:1 Anisole ZEP at 4000 rpm (thickness about 100nm) and then heated on a hot-plate 180 °C for 4 min. In this case, the exposure follows two steps: one by a dose of 270 $\mu\text{C}/\text{m}^2$ and a beam of 128 nA (50 nm spot size) to define the connections and the second by a dose of 300 $\mu\text{C}/\text{m}^2$ and a beam of 1 nA (4 nm spot size) to define the pixels.

3.4 Reactive Ion etching

After the lithography process, the geometry of the device is determined by the resist patterned on the top of the sample. At this point the sample is bombarded by a plasma (generated by a RF power source) that removes the part of the sample uncovered by the resist. This process is called in general dry etch. For the fabrication of SNSPD arrays, reactive ion etching (RIE) has been used. This process follows some basics of the RF sputtering process: the sample is placed in a vacuum chamber onto a cathode connected to a RF power supply. In this process, the substrate is the target (cathode) to be bombarded while the second electrode S_2 (anode) is formed by the walls of the chamber[Fig.3.19 a)].

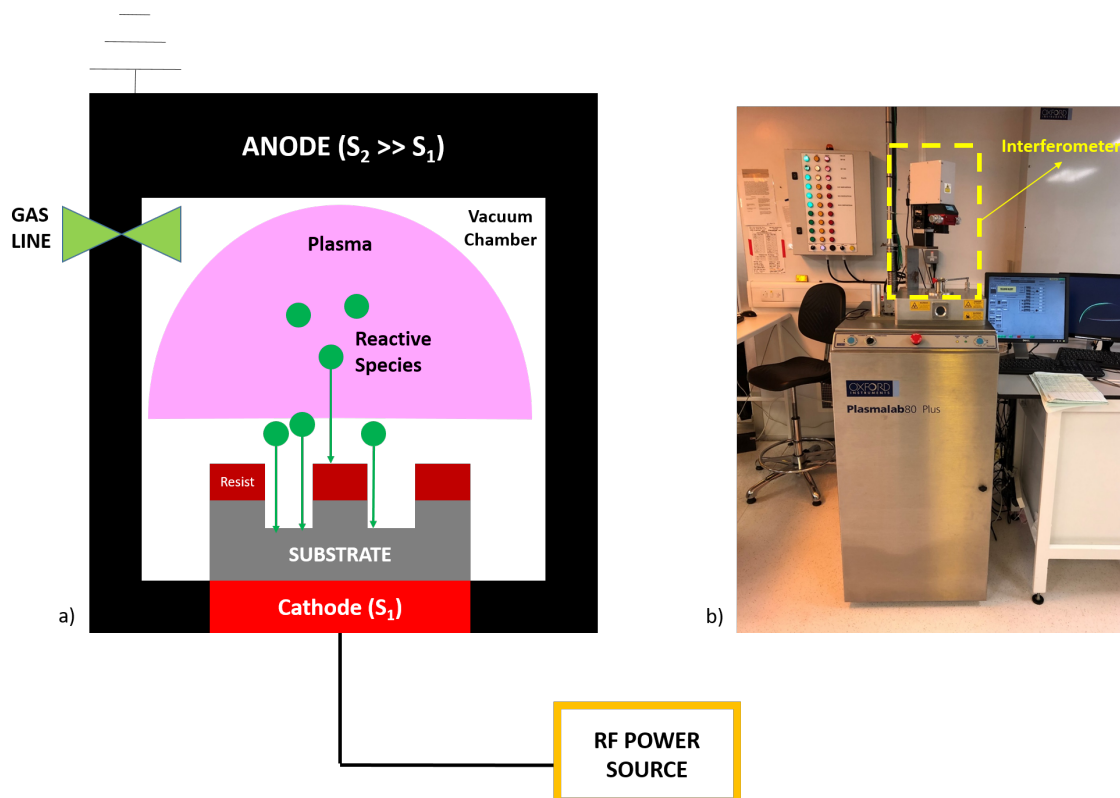


Figure 3.19: a)Diagram of a standard configuration for a reactive ion etch (RIE) chamber. b) Oxford Plasmalab 80 Plus Plasma Etcher installed in the JWNC. The tool is equipped by an interferometer to monitor the etch depth.

The relation between surfaces of the cathode S_1 and of the anode S_2 and their voltages is given by the following equation[158]:

$$\frac{V_1}{V_2} = \left(\frac{S_2}{S_1} \right)^4 \quad (3.9)$$

The magnitude of voltage induced at the electrodes is dependent on the ratio of the electrode surface areas. In other words, a higher voltage is induced at the electrode with a smaller surface area. In general, the electrode 2 that opposes the electrode 1 on which the wafer is placed has a much larger surface area in the dry etch system, so that an adequate voltage is achieved at the wafer. Because the chamber walls are normally held at the same electrical potential as electrode 2, the structure helps make S_2 larger than S_1 .

Because the V_2 induced at the chamber walls is small, the sputtering on the walls is suppressed, and as a result there is an added advantage of suppressing the release of impurities, such as heavy metals from the chamber walls. The equipment used for the fabrication of SNSPD arrays is the Oxford Plasmalab 80 Plus Plasma Etcher installed in the JWNC[Fig.3.19 b)]. The main difference between the sputtering and RIE is the use of reactive gas like CF_4 or SF_6 . RIE mechanism proceeds as follows: first, the reactive gas is introduced into the chamber, where it is broken down into chemically reactive species (radicals and ions) to form plasma. Reactive species diffuse to the surface to be etched and are then adsorbed on this surface. Once the reactive species reach the surface, they move around on the surface (surface diffusion) until they react with the exposed film. Afterwards, products of the reaction will desorb from the surface and diffuse away through the gas stream. An example of RIE process is explained in Fig.3.20 that shows the etching of a silicon substrate in CF_4 plasma.

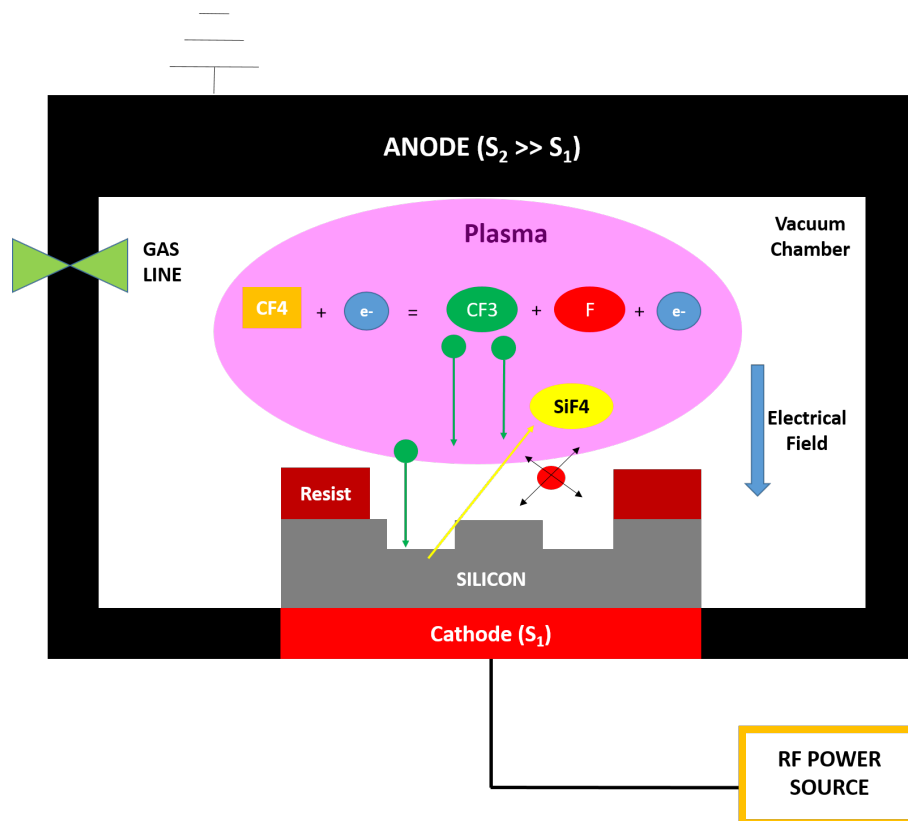


Figure 3.20: RIE process scheme of silicon in CF_4 plasma. Ions CF_3^+ follow the electric field direction while radicals F move randomly by Brownian motion.

Applying the electric field between the cathode (the silicon) and the anode (chamber walls), CF_4 molecules interact with electrons generating ions (CF_3^+) and fluorine radicals (F). Ions are accelerating towards the silicon. The interaction of reactive ions CF_3^+ (as radicals) with silicon generate volatile SiF_4 that diffuses in the chamber. Both ions and radicals interact with silicon to produce SiF_4 that diffuses in the chamber. The ion-assisted process enhances the probability to etch the target vertically that closely replicates the mask patterns (anisotropic etching[156, 159, 157]).

Table [3.2] shows the recipe of the dry etch process used in this thesis to realize the microbridge structures and SNSPD multipixel array.

Table 3.2: Dry Etch recipe used to realize SNSPD array and microbridges structure.

Gas	CF ₄
Flow	50 sccm
Pressure	30 mTorr
Power	80 W
Temperature	22 °C

3.5 Cryogenic systems

As explained before, SNSPDs work at temperature below their critical temperature that is a few degrees above absolute zero. Then they have to be installed in cryogenic systems. A historical way to cool down a superconductor is to immerse the device in liquid helium (4.2 K) but the evaporation of the cryogenic liquid that slowly boils away makes the use of liquid helium dewars very expensive and efficient gas recovery is challenging. Moreover, the liquid helium may lead to several safety hazards to require a serious safety training. A possible solution to these problems are refrigeration systems based on closed cycle cooling. These systems are known as cryocoolers[163]. Their working principle is based on compression and expansion of gases. Cryocoolers are classified as operating through recuperative cycles and regenerative cycles. In the recuperative cycles, there is a steady flow of gas in one direction with steady low and high pressures in the appropriate locations. Compression occurs at ambient temperature T_0 , with the heat of compression being dissipated to the ambient. Expansion occurs at the cold end at a temperature T_c , where the net refrigeration power \dot{Q}_c is absorbed. The heat exchanger for the recuperative cycles is known as a recuperator or recuperative heat exchanger. It has two separate flow channels: one for the high-pressure fluid and one for the low-pressure fluid. The low-temperature expansion can be by a valve as in the Joule-Thomson (J-T) cycle or by an expansion engine as in the Brayton cycle. The J-T cycle normally uses a working fluid that is liquefied at the cold end, such as nitrogen for 77 K, hydrogen for 20 K, and helium for 4.2 K. For higher temperatures, mixed refrigerants of nitrogen and various hydrocarbons are often used to provide higher efficiencies. The regenerative cycle operates with oscillating flows and oscillating pressures, and almost always use high-pressure helium as the working fluid. Frequencies vary from about 1 Hz for the Gifford–McMahon (GM) and some pulse tube cryocoolers to about 60 Hz for Stirling and some pulse tube cryocoolers. In these cryocoolers heating occurs as the pressure is increasing, and cooling occurs as the pressure is decreasing. The use of a displacer in the Stirling and GM cryocoolers moves most of the gas to the hot end during the compression process and to the cold end during the expansion process.

In the pulse tube cryocooler oscillating flow through the warm-end orifice (or a long capillary called an inertance tube) moves the gas with a similar phase relationship as provided by a displacer, but without a moving part. Thus, the pulse tube cryocooler has an inherent potential to be more reliable and have less vibration than either the Stirling or GM cryocoolers. The use of valves in the GM cryocooler or with pulse tubes driven with a GM-type compressor and rotary valve (known as GM-type pulse tubes) reduces their efficiency compared with valveless compressors (or pressure oscillators) as used in the Stirling or Stirling-type pulse tubes. However, the use of valves in the compression process provides a region of steady high pressure where an adsorber can be used in conjunction with a commercial oil-lubricated compressor in order to achieve high reliability at relatively low cost. The regenerative heat exchanger (regenerator) used for these cycles has only one flow channel, which is filled with a porous matrix with high surface area and heat capacity (packed screens or spheres). Heat is transferred from the ‘hot blow’ to the ‘cold blow’ via the matrix, where the heat is stored for a half cycle in the heat capacity of the matrix. Cryosystems used in this research are two GM cryocoolers and pulse tube refrigerator (PTR) installed in the laboratory of Quantum Sensor Group (QSG) based in the James Watt School of Engineering (Rankine Building) of the University of Glasgow. Gifford McMahan cryocoolers can reach 2.2 K base temperature. One has been used to measure superconducting properties of 8 nm NbN and 8 nm MoSi. The second one has been used to measure superconducting and optical properties at 1550 nm of the 8-pixel SNSPD array made via 8 nm NbN. Since the 8-pixel SNSPD array made via 8 nm MoSi exhibits 3.2 K mean critical temperature, it has been tested in the PTR with an additional ^3He sorbtion stage that can reach 300 mK base temperature.

3.5.1 The Gifford-McMahon (GM) cycle

Gifford–McMahon (GM) cryocoolers were first developed in 1960[164]. It consists in a cold head connected to a helium compressor. The cold head contains a compression and expansion space, a regenerator, and a displacer. Usually the regenerator and the displacer are combined in one body. The pressure variations in the cold head are obtained by connecting it periodically to the high- and low-pressure sides of a compressor by a rotating valve. Its position is synchronized with the motion of the displacer. During the opening and closing of the valves irreversible processes take place, so GM-coolers have intrinsic losses. The GM cooling cycle can be divided into four steps as follows[Fig.3.21]:

- The cycle starts with the rotary valve connecting the cold head to the high-pressure room temperature gas from the compressor. The gas, now in the hot end of the cold head, is compressed and heat is released to the surroundings.
- At the completion of the high-pressure filling phase, the displacer moves to the left and the gas passes through the regenerator entering the regenerator at ambient temperature and leaving it with temperature a lower temperature. Thus, the heat storage feature of the regenerator retains the temperature gradient between the warm and cold ends of the cold finger and smooths out the cyclic temperature variation of the gas.

- Next, the rotary valve connects the low pressure suction from the compressor return to the cold head, thus expanding and cooling the gas in the cold side.
- In the final portion of the cycle, the displacer moves to the right to reposition at the end of the coldfinger to ready it for the upcoming high-pressure gas filling phase. Again, during this part of the cycle, the gas passes through the regenerator, and the heat storage feature of the regenerator smooths out the cyclic temperature of the gas as it flows between the two ends of the regenerator.

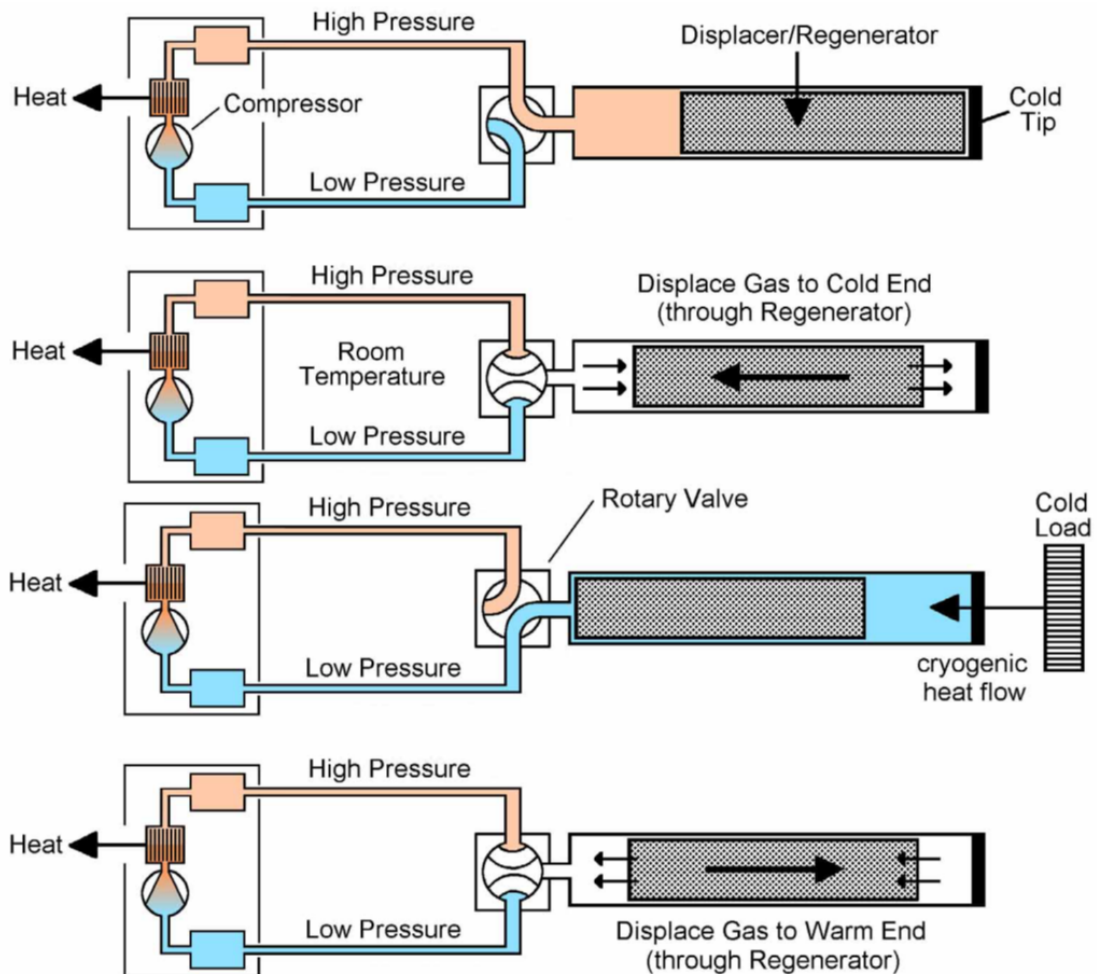


Figure 3.21: Schematic of Gifford McMahon refrigeration cycle[165].

GM cryocoolers installed in the QSG laboratory are model RDK101D cold-head manufactured by Sumitomo Heavy Industries, Ltd. This model is a two stage GM cryocooler. The coldest stage (second stage) can reach a temperature below 3 K. One of the cryocooler has been designed to measure the intrinsic properties of superconducting materials as the critical temperature, the critical current density and the sheet resistance, while the other one has been designed to measure electrical and the optical properties of SNSPDs. All the part of the cryocoolers (stages, shields, vacuum panels) have been manufactured by the James Watt School of Engineering Mechanical Workshop (Rankine Building).

Helium compressors are indoor air-cooled. One is a model CNA-11 (power consumption 1.2-1.3 kW at 50 Hz, 1.3-1.5 kW at 60 Hz) and the other is a model Zephyr (power consumption 3.0 kW at 50 Hz, 3.4 kW at 60 Hz). Before to start the cooling down process, the cryosystem is sealed by a metal vacuum can and then attached to a turbo pump to reach a pressure of about $7.5 \cdot 10^{-5}$ Torr before turning on the helium compressor.

The Ekinator

This system has been realized to measure the critical temperature of eight superconducting thin film samples concurrently and then updated by the author of this thesis to measure the critical current density of eight superconductors concurrently at different temperature. Devices are mounted on the second stage of the cryocooler. On this stage is placed a circular metal disc where there are eight rectangular holes with steps at their boundary to place four pogo pins. In each holder (made of Tufnol) are inserted four pogo pins by press fitting. On the top of this is placed another circular metal disc which has eight slots to accommodate eight samples $15 \text{ mm} \times 15 \text{ mm}$ square. This disc is to be placed on the metal stage with pogo pins in such a way that all the pogo pins can touch the samples. On the top of this disc has been installed a $1 \text{ k}\Omega$ resistor. Its function is to heat the cryogenic system to perform measurements at different stable temperatures. Near the resistor has been installed a first temperature sensor, a second under the pin holder and a third at the second stage of the cryostat [Fig.3.22].

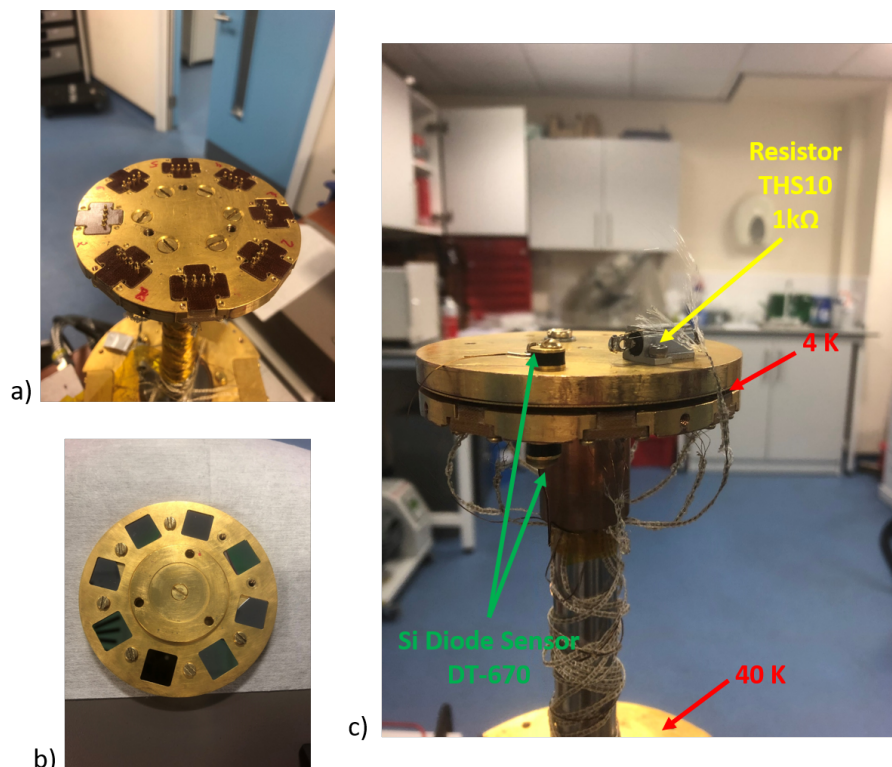


Figure 3.22: a) Gold-plated copper circular disc filled by pogo pin holders. Each holder is made by Tufnol. b) Sample holder for eight $15 \text{ mm} \times 15 \text{ mm}$ square samples. c) Samples are connected to pins by contact. On each holder is attached a calibrated temperature sensor silicon diode model DT-670. On the sample holder is installed a $1 \text{ k}\Omega$ resistor to act as heater of the system.

All temperature sensors are DT-670 silicon diodes each mounted in a gold-plated copper bobbin manufactured by Lakeshore Cryotronics. The thermometers installed on the second stage are DT-670-CU-1.4L model (calibrated 1.4 K to 325 K). Thermometers, pogo pins and the heater are connected to four 12-pin cryogenic connectors attached at the rectangular panels of the hexagonal base of the cryostat. Thermometers are connected via manganin wires (already installed in the copper bobbin) while pogo pins and the heater via polyester insulated constantan (copper-nickel alloy) twisted pairs provided by CMR-DIRECT. This wire has been chosen for its low thermal conductivity (3.5 W/m K at 10 K [166]) to reduce the heat loss that can affect low-temperature measurements. Another way to reduce the heat loss in the wires is to lag the wire from the second stage of the cryocooler wrapping the wire several times round the cryostat[Fig.3.23 a)]. The electrical set-up is installed in a large metal box for electromagnetic shielding[Fig.3.23 b)].

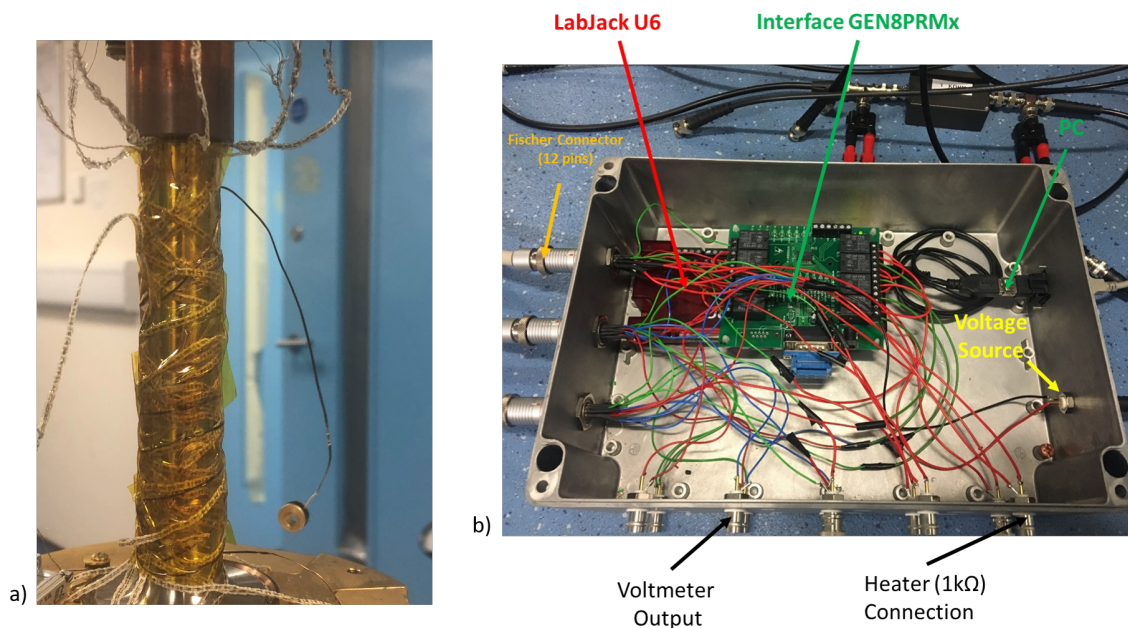


Figure 3.23: a) Thermal anchoring in the Ekinator. b) Ekinator electrical set-up. The set-up is built in a metallic box to prevent electrical noise pickup. Pogo pins and the heater are connected via Fischer connectors from the cryosystem to the interface GEN8PRMx and BNC connectors. The interface is connected to a PC via the interface Labjack U6 by USB port.

The set-up has been realized to measure the electrical resistance of a superconductor via the 4-point probe method[Fig.3.24 a)]. Two pogo pins are connected to isolated voltage source SIM928 and the other two are connected to a digital voltmeter SIM970 ($10 \text{ M}\Omega$ impedance) to measure the voltage drop across the device. To measure the bias current, a load resistor has been installed in series to the device and then connected to a Keithley 2000 Multimeter to measure its voltage drop. The ratio between this voltage drop and the load resistor gives the bias current in the device. In order to measure the resistance of eight devices at the same time, pogo pins are connected to the voltage source passing by eight relays installed on the interface GEN8PRMx provided by EasyDaq. This interface is connected to a Labjack U6 to communicate to the PC via USB interface. Other pogo pins are connected to voltmeters SIM970 via BNC connectors. In the same set-up, the heater is connected to a SIM960 Analog Proportional Integral Derivative (PID) controller across a high voltage linear amplifier P200 (FLC Electronics AB, Sweden, gain $\times 10$)[Fig.3.24 b)].

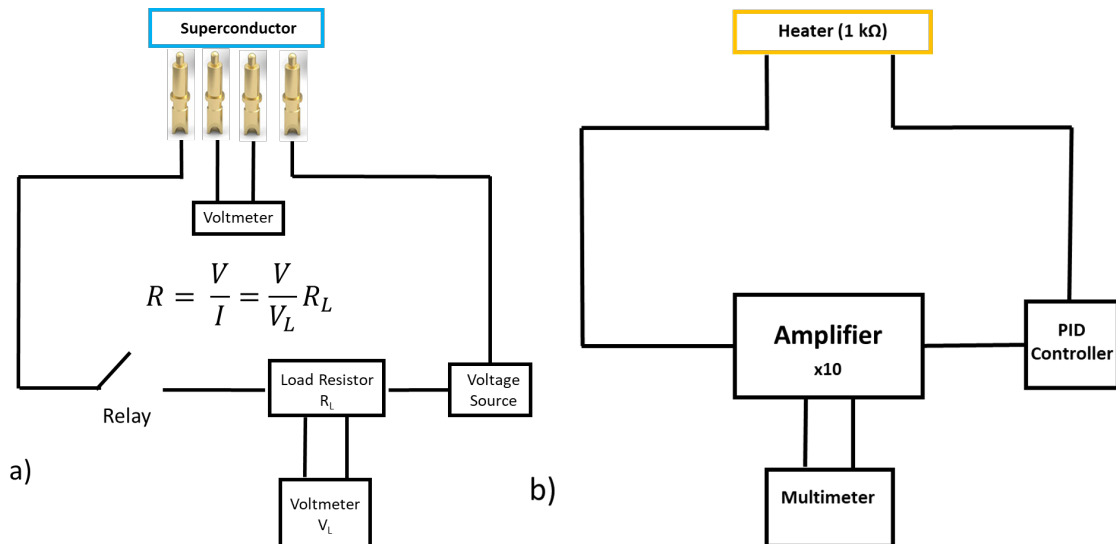


Figure 3.24: Ekinator electric set-up scheme. a) External pogo pins are connected to the voltage source across a relay onto the interface GEN8PRMx and a load resistor. Pins in the middle are connected to the voltmeter to measure the voltage drop. The bias current is given by the voltage drop across the load resistor measured by a voltmeter. b) The heater is connected to the PID controller across an amplifier (gain x10). The voltage across the heater is monitored by a multimeter in parallel to the amplifier.

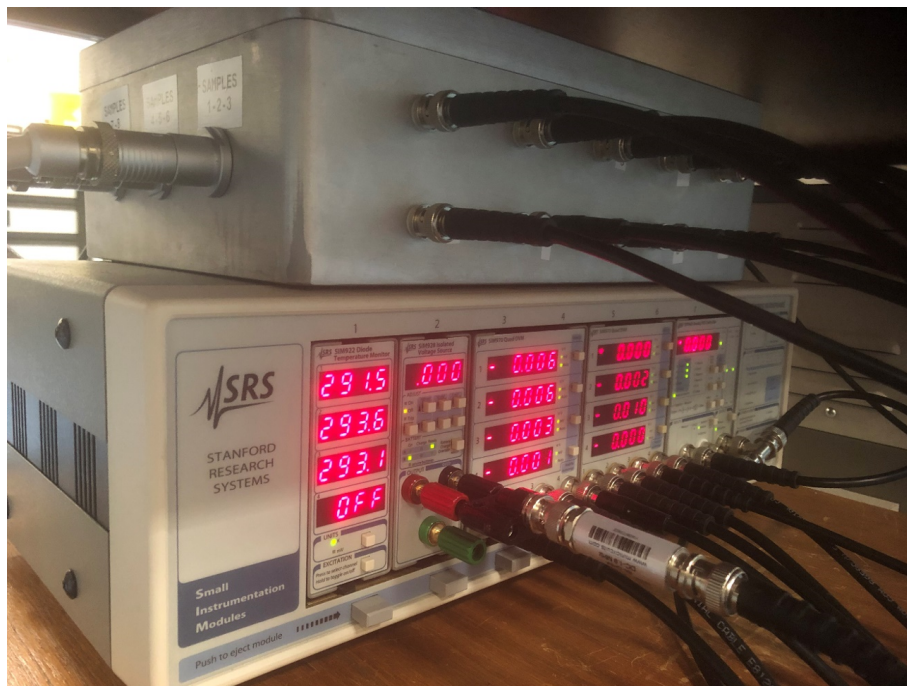


Figure 3.25: SRS SIM900 Mainframe. From the left: SIM922 Diode Temperature Monitor, isolated voltage source SIM928, two digital voltmeter SIM970, SIM960 PID controller.

Thermometer sensors are connected to the SIM922 Diode Temperature Monitor via a different metallic box. The isolated voltage source, digital voltmeters, the PID and temperature monitor are installed in an SRS SIM900 mainframe[Fig.3.25] which is connected to a computer through a RS-232 cable, while the Labjack is connected to the PC by USB 2.0.

These instruments are controlled by a Python program and by this is possible to monitor signals of the instruments (temperature and potential difference) to compute the bias current and the resistance of devices. The cooling down process of superconductors in the Ekinator system follows these steps:

- First, devices are installed on the sample holder[Fig.3.22 b)] and then screwed on the pogo pin holder[Fig.3.22 a)]. Devices are connected to pins by contact.
- The thermometer DT-670 (calibrated) and the heater (1 k Ω) are screwed near each other on the top of the sample holder[Fig.3.22 b)].
- The second stage is protected thermally by a custom designed gold-plated aluminium radiation thermal shield. The entire system is then sealed by a metal vacuum can and then attached to a turbo pump[Fig.3.26].
- Once the system reaches a pressure of about $7.5 \cdot 10^{-5}$ Torr the helium compressor is turned on and the system begins to cool down. The turbo is turned off and disconnected from the cryocooler when the cryosystem reaches about 200 K. After about 6h, the system reaches its base temperature (2.1 K at the second stage and about 36 K at the first stage.)

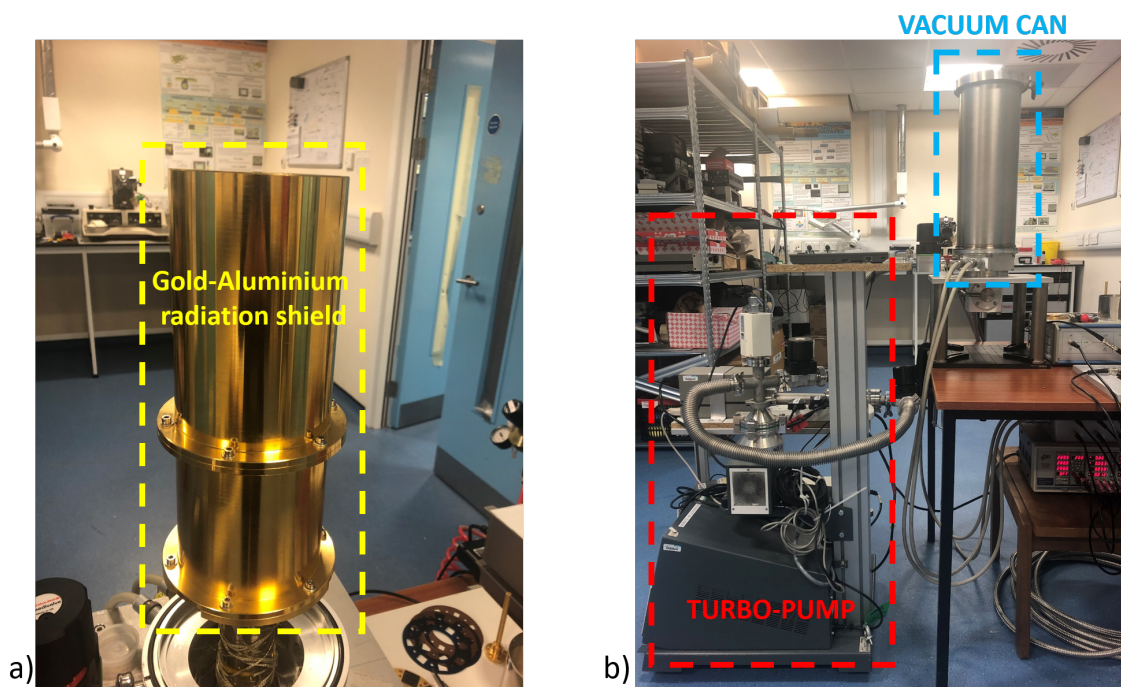


Figure 3.26: a) Gold-plated aluminium radiation shield machined in the workshop of School of Engineering Department of the University of Glasgow. b) Ekinator sealed by a vacuum can and connected to a turbopump (Adixen).

Once the Ekinator is at 2.1 K, the electric set-up is turned on by the Python program monitoring the temperature and the resistance of superconductors. The critical temperature of each pixels has been measured biasing the device with a low voltage input and recording the voltage drop V_s of the device (converted in resistance $R_s = V_s/I$ by Ohm's law) at different temperature starting from 2.1 K when the device is cold. Turning off the helium compressor, the cryocooler starts its warming up phase.

Registering temperature and resistance (data are converted in a .txt file by Python), is possible to plot the R-T characteristic of the superconductor.[Fig.3.27 a)]. The critical current is measured when the cryostat is kept at 2.1 K and the device is biased by a periodic voltage input. Monitoring the voltage of the device and the applied bias current, it is possible to plot the I-V characteristic of the device[Fig.3.27 b)].

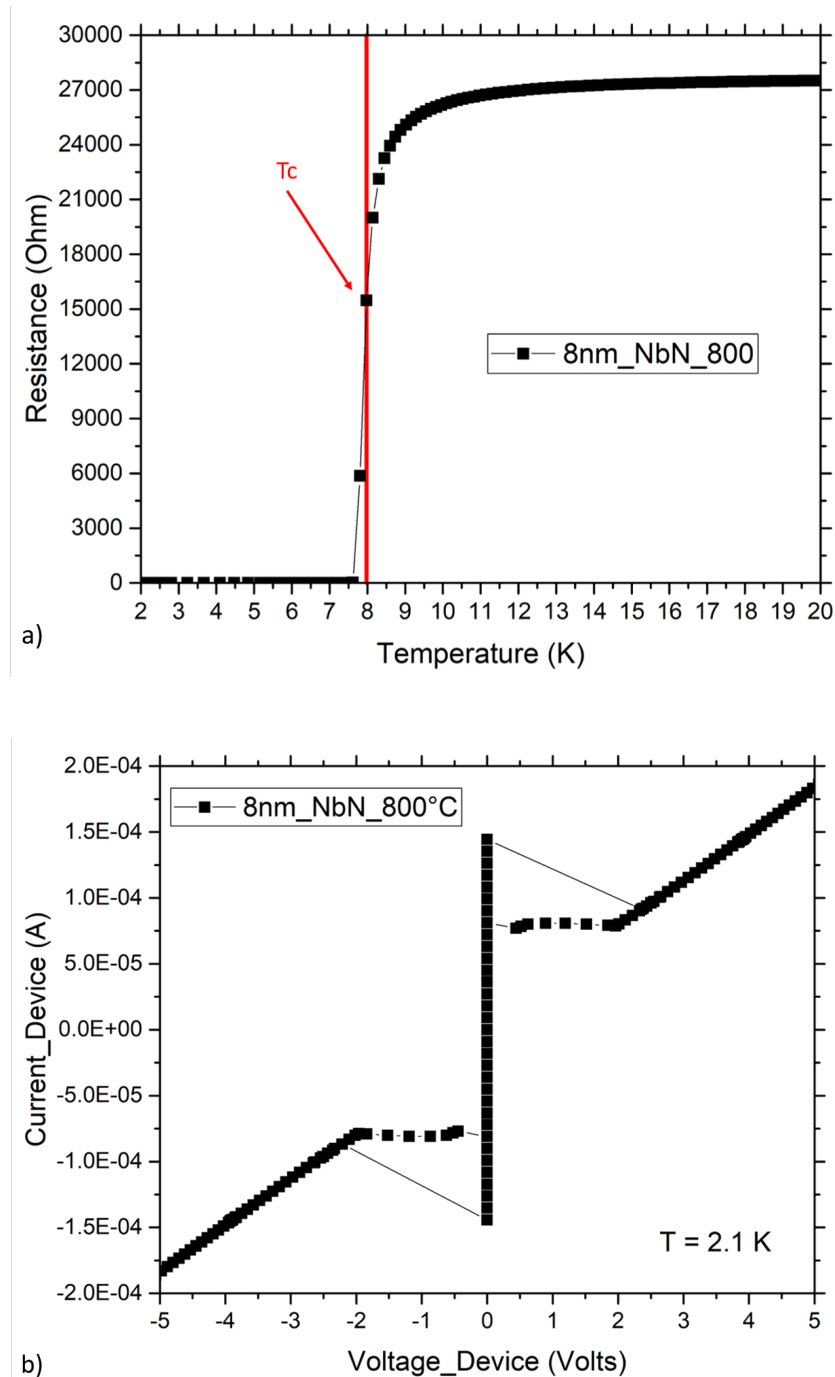


Figure 3.27: a) R-T characteristic of 8nm-thick NbN growth on HR Si substrate heated at 800 °C and patterned in a 2 μm x 200 μm microbridge. In this work, the critical temperature is taken in the middle point of the resistive transition. b) I-V characteristic at 2.1 K of 8 nm-thick NbN growth at 800 °C on HR Si and patterned in a 2 μm x 200 μm microbridge. The critical current $I_c(2.1K) = \pm 144.3\mu A$.

The x-axis is the voltage of the device measured by the voltmeter SIM970, while the y-axis is the bias current given by Ohm's law $I = V_s/(R_L + R_s)$. When the sample is in the superconducting state $R_s = 0$. When it switches to the normal state and $R_s \gg R_L$ then the current across the device under test drops. The hysteresis effect presents in the I-V plot is due to Joule heating of the device after its passage from the superconducting to the normal state. Reducing the bias current, the device does not become superconducting at the same value of critical current of before. When the helium compressor is on the lowest temperature of the cryostat is about 2.1 K. Biasing the heater (1 k Ω resistor) by the PID controller, the cryostat heats by Joule heating. Due to its low power performance (Output $\pm 10V$; 0.1mA), the PID SIM960 has been connected to a power amplifier P200 (Output $\pm 100V$; 1A) manufactured by FLC Electronics, Sweden. In this way, the cryocooler can be heated at temperature far from 2.1 K[Fig.3.28].

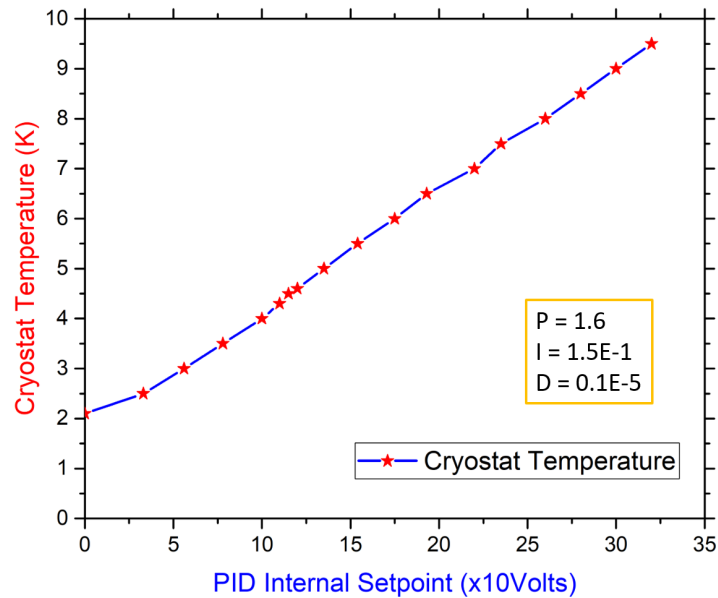


Figure 3.28: Cryocooler temperature when the heater is biased via PID. The PID internal setpoint is amplified by the P200 amplifier and the cryostat temperature grows for Joule heating. To stabilize the PID output, the instrument has been configured as follows: P = 1.6, I = 1.5E-1, D=0.1E-5 to stabilize the output signal. The PID output (amplified) is monitored by a Keithley 200 multimeter.

The amplified output signal has been connected in parallel to a multimeter to monitor the amplified output signal. The PID has been configured monitoring the amplified signal. The aim of the heater is to measure the critical current of a superconductor at different temperatures and to fit these data with the critical current density equation (2.12) to get information about the critical current density at 0 K and the critical temperature of the superconductor.

The Zephyrator

This system has been realized for low temperature electrical and optical characterization of SNSPD devices. The cryocooler model is the same of the one described in the previous section: a RDK101D cold-head manufactured by Sumitomo Heavy Industries, Ltd, two cooling stages and connected to a air-cooled HC-4A Zephyr (so it is named "Zephyrator").

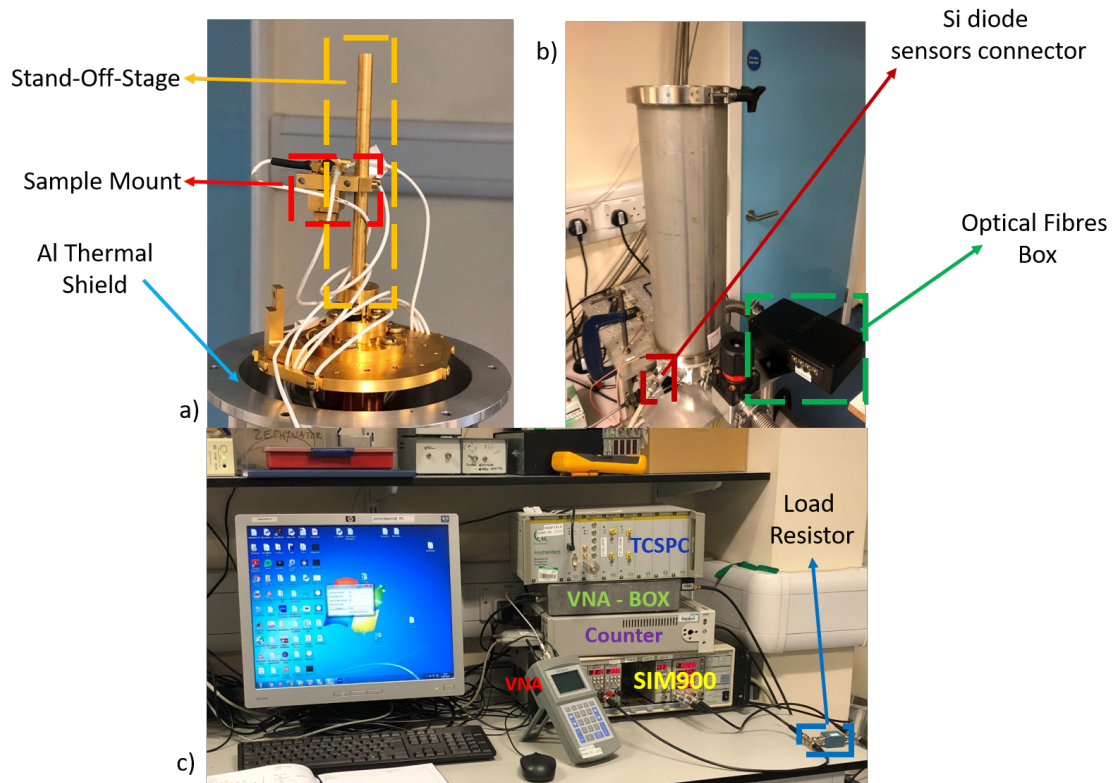


Figure 3.29: (a) Zephyrator second stage (4 K). The sample holder is mounted on a stand-off-stage attached to the 4 K stage of the cryocooler. The stage is then covered by an Al thermal shield. (b) Complete image of the Zephyrator with the vacuum can. The black box attached is the feed-through of optical fibres. (c) Zephyrator electronic set-up. From the top: the TCSPC module for timing jitter measurement, the metallic box connected to the VNA for kinetic inductance measurement, the universal counter for the count rate and the mainframe SIM900 where there are installed the temperature monitor, the voltage source connected to the sample across a load resistor and a quad voltmeter. All these instrument are connected to a PC desktop and controlled via Python codes.

Devices are installed on the second stage (4 K) of the cryocooler onto a stand-off-stage thermally linked with brass screws[Fig.3.29 a)]. Lakeshore DT-670 Si-diode thermometers are mounted on 4 K and 40 K stages to accurately monitor their respective temperatures. Thermometer sensors are connected to the SIM922 Diode Temperature Monitor via a 12-pin Fischer connector[Fig.3.29 b)] across a specific electric set-up embedded in a metallic box. Readout and biasing of SNSPDs is done with 50 Ω impedance matched hermetic SMA connectors fitted on the flange plate and soldered on the one side of a brass coaxial cable. Whereas, on the other side an SMP connector is crimped and connected on the sample mount. In the system are installed 8 RF coaxial cables. The optical link between the detectors and room temperature equipment (i.e. laser, attenuators, polarizers, ect.) occurs through a hermetically sealed fibre feed-through with 16 optical fibres that are spliced on the fibre-coupled SNSPD devices.

Fibres are then installed in a room temperature black box connected to the cryostat[Fig.3.29 b)]. Fibre is connected to a laser diode via two attenuators (JDS Uniphase HA9) and a polarizer[Fig.3.30].

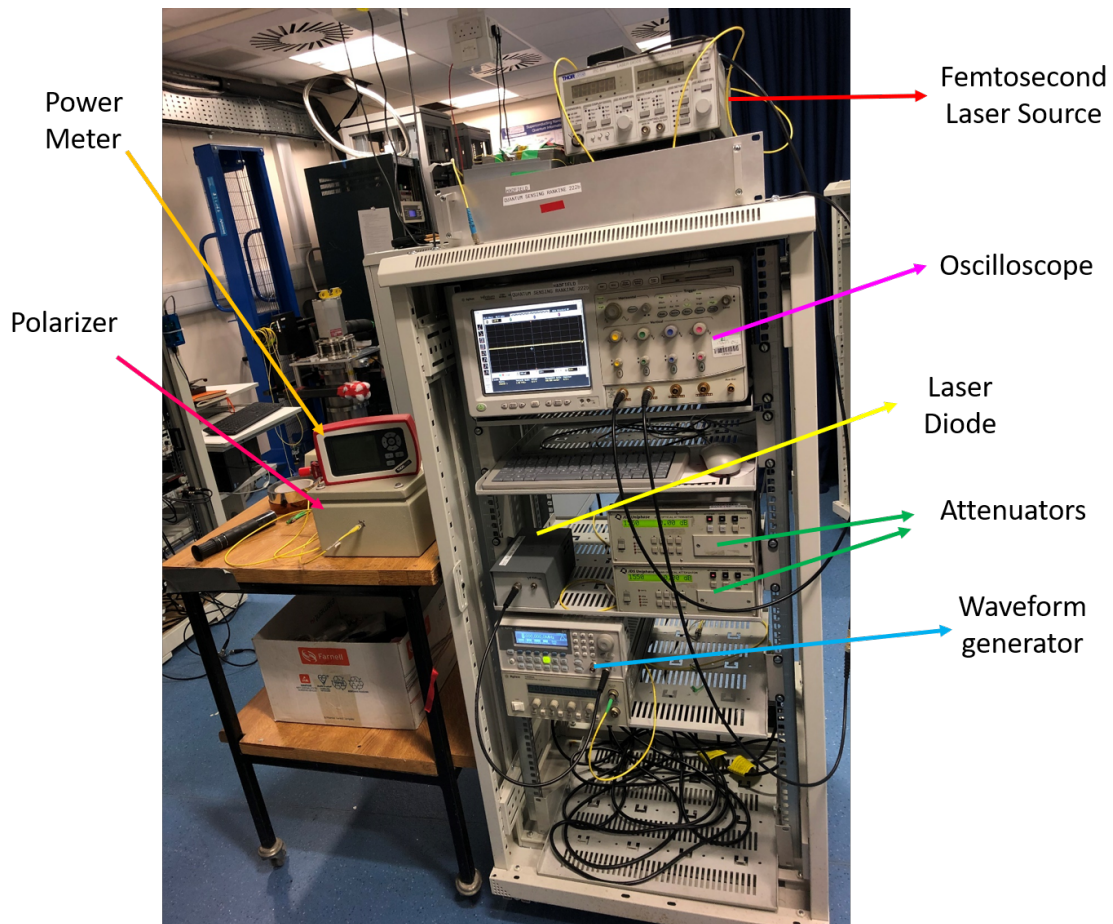


Figure 3.30: Optical set-up. All the instruments required for an optical measurement are collected in an instrumentation rack. From the top: the femtosecond mode-locked fibre Kphotonics CNT-1550-TK laser used for timing jitter measurement, oscilloscope Agilent Technologies 54845A, 8 GHz bandwidth, 1550nm laser diode source, two attenuators, a waveform generator connected to the laser source to generate pulsed laser of 5MHz frequency. Next to the drawer there is a manual polarizer. The laser power output is measured by a digital power meter. Optical fibres are checked by a FS200 fibre inspection scope (Thorlabs) before to be connected to instrument.

Custom designed aluminium radiation shields, flanges for optical/electrical feed-throughs and blank plates have been machined in the workshop of the James Watt School of Engineering of the University of Glasgow. As in the Ekinator, the whole fridge is thermally shielded from the environment by Al radiation shields and sealed by a vacuum can. The critical temperature and the critical current at 2.2 K of the SNSPD are measured by an isolated voltage source SIM928 and a digital voltmeter SIM970. The SIM922 Diode Temperature Monitor, the isolated voltage source SIM928 and the quad digital voltmeter SIM970 are installed in the SIM900 main-frame. A load resistor of 100 k Ω is connected in series to the SNSPD to measure the bias current. The resistance of the device is measured via two-probe method. The critical temperature and the critical current at 2.2 K are measured in the same way as described in the previous cryo-system. In addition this system permits measurement of the kinetic inductance of the SNSPD. This parameter gives information about the reset time of the detector.

The kinetic inductance is measured by a computer controlled Via Bravo vector network analyzer (VNA) with a frequency response from 0.1-50 MHz that simultaneously measures the phase and amplitude of the reflected signal. This instrument is connected to a custom-made metal box made to attenuate VNA power output to a safe region for the SNSPD and re-amplifies the returning signal[Fig.3.31]. The metal box is then connected to the device across a picosecond bias-tee (model PSPL5541A, from 80 kHz to 26 GHz).

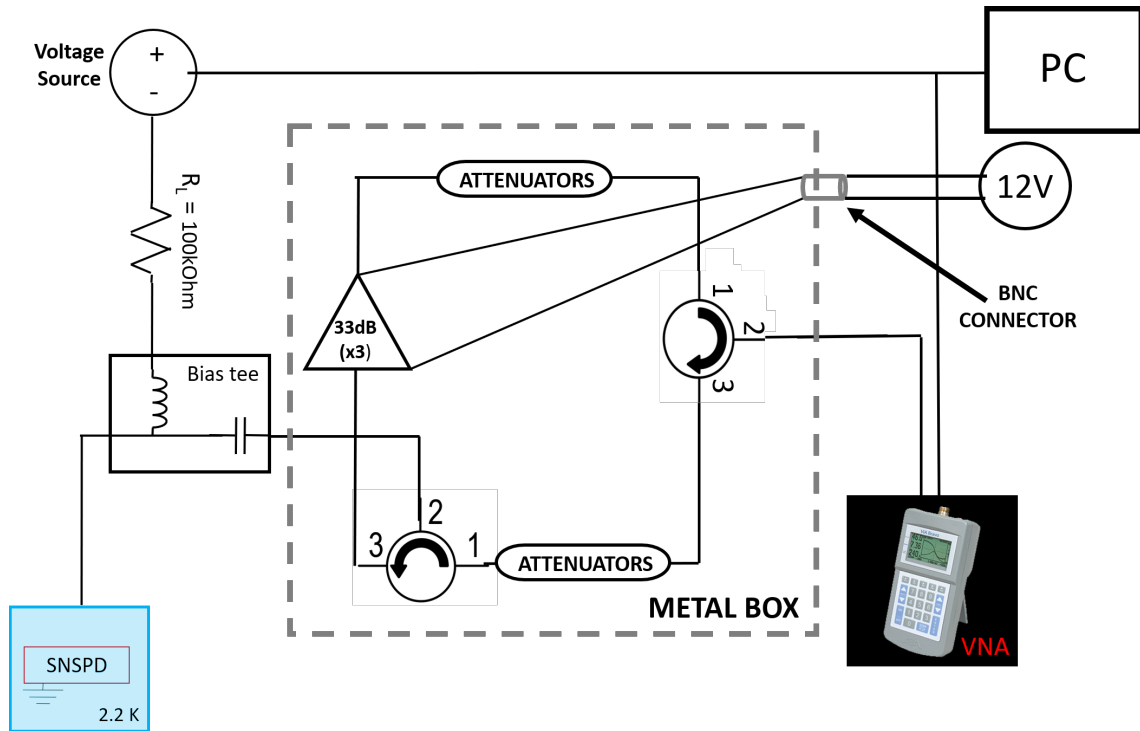


Figure 3.31: Electrical scheme for the SNSPD kinetic inductance measurement.

The basic of the VNA operation is simple: the VNA output signal is transmitted to the device under test (SNSPD). This signal is first attenuated by a series of variable attenuators (VATs) provided by Minicircuit company to attenuate the power output of the VNA (5dBm@50 Ohms in according to datasheet) that could damage the SNSPD. This signal is then reflected by the SNSPD and at same time, when the device is biased, the variation of the kinetic inductance of SNSPD produces a signal transmitted to the vector analyzer. So the reflected signal and the signal transmitted are amplified by a chain of three LNA-1000 amplifiers (total gain 99 dB), attenuated by two attenuator (10 dB and 6 dB) and then collected by the VNA that transmits information to the PC. The kinetic inductance as function of the bias current is achieved using an automated computer program written by Python that varies the bias current of the SNSPD in a range of bias currents from zero up to the critical current records the total inductance.

For the optical characterization, the SNSPD is biased by the voltage source (with a load resistor in series) while the output signal-pulse from the detector is amplified with a room temperature amplifier-chain (RF Bay Inc. LNA-580 and LNA-1000) with a total of 56dB amplification and can be monitored with high speed (8 GHz bandwidth) oscilloscope (Agilent Technologies 54845A). The rate of signals (count rate) is measured by an universal counter (Agilent 53131A) computer controlled. The device is connected to a laser diode source by a single mode fibre (SMF28e+) across a polarizer and a series of two attenuators. The laser source is controlled by waveform generator (Agilent 33220A) that can generate laser pulses of a frequency of max 5 MHz[Fig.3.32].

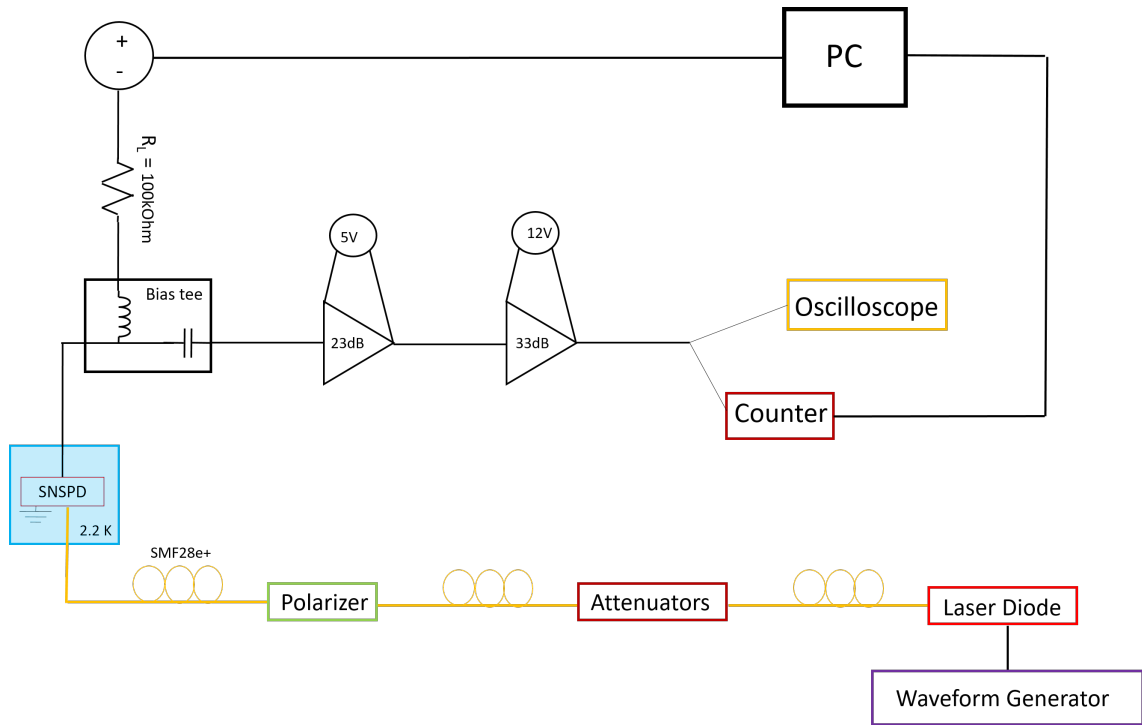


Figure 3.32: Electrical scheme for the SNSPD optical characterization.

The timing jitter of the SNSPD is measured connecting the device to the INPUT of a time correlated single-photon counting (TCSPC) card (PicoQuant PicoHarp 300) and using as laser source a femtosecond mode-locked fibre Kphotonics CNT-1550-TK laser (central wavelength $\lambda = 1560$ nm) with 50 MHz repetition rate that generates narrow optical pulses which are routed to a 90:10 beamsplitter[Fig.3.33]. The 90% output is connected to attenuators used to attenuate the pulses down to single-photon regime and then coupled to the SNSPD while the 10% is used as input for an InGaAs fast photodiode (Thorlabs DET08CFC InGaAs, $\lambda = 800$ -1700 nm, 70ps rise time) and is electrically connected into the Sync port of the TCSPC card. The time interval between a start (InGaAs fast photodiode) and a stop (SNSPD) signal are recorded by the software of the TCSPC and a histogram is formed. For a conventional SNSPD (single-wire meander), the response shape is Gaussian and the timing jitter is defined as the full-width at half-maximum (FWHM) of the Gaussian curve.

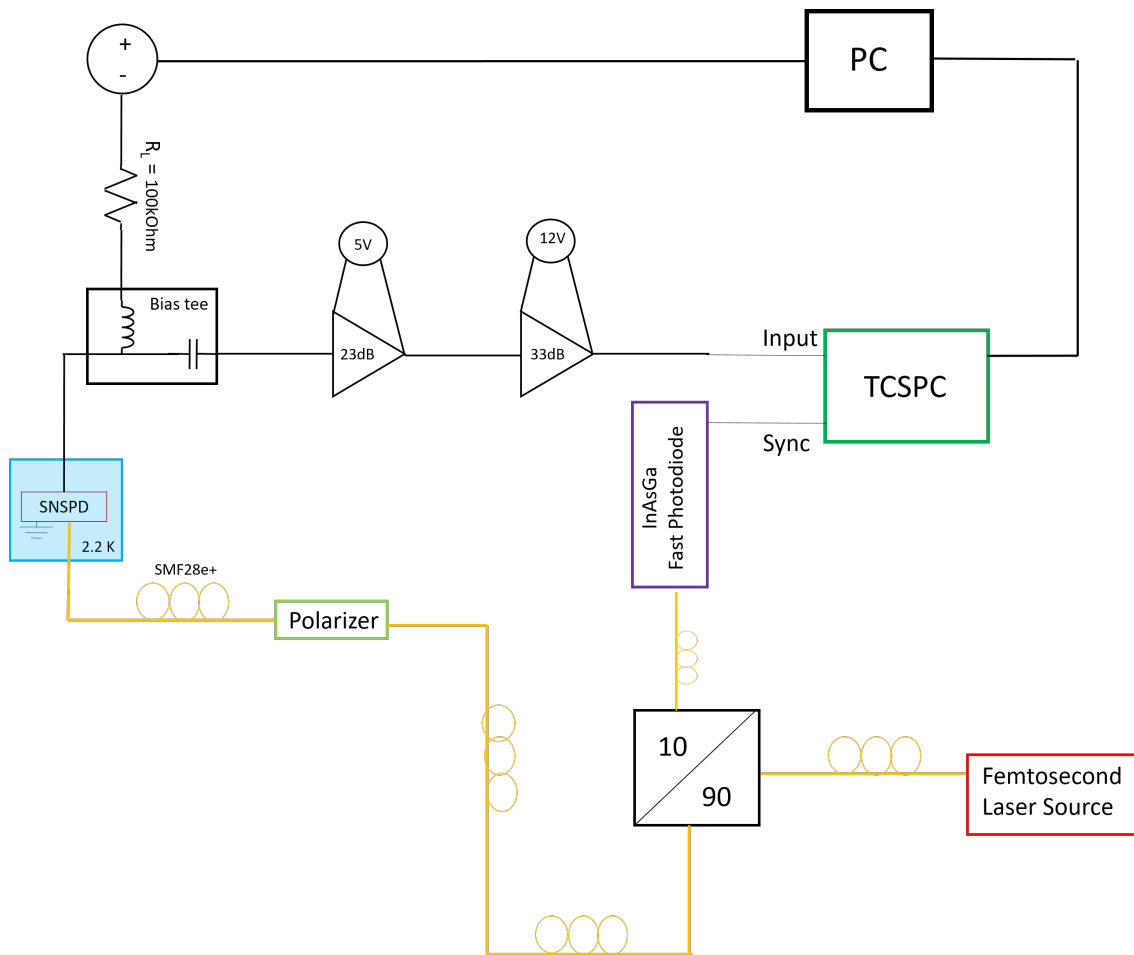


Figure 3.33: Electrical scheme for the SNSPD timing jitter measurement.

3.5.2 The Pulse Tube Refrigerator (PTR)

Modern PTRs have been realized by Radebaugh in 1986[167]. Like GM cryocoolers, PTR are classified in term of regenerative cycle: He gas in a closed tube that oscillates in pressure[Fig.3.34].

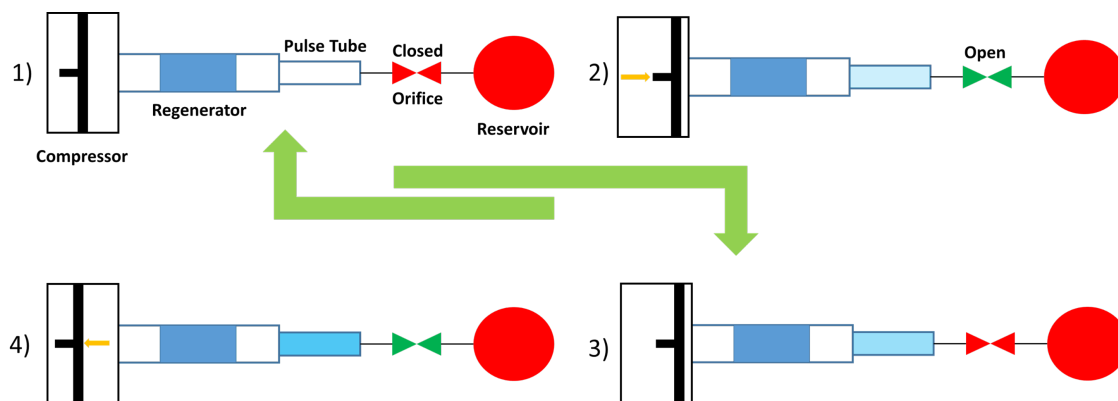


Figure 3.34: Schematic of Pulse Tube Refrigerator operation cycle.

The difference with GM cryocoolers is the absence of the displacer. While in GM cryocoolers the pressure of the cold gas moves the displacer, in PTR cryosystems the gas oscillates in the tube without moving any part hence lower mechanical vibration is achieved during cooling operation. In addition, PTRs have a remote rotary motor, which can be mounted away from the cryostat in order to avoid vibrations to the sample. PTRs are also equipped with a reservoir connected to the pulse tube by an orifice placed outside the heat exchanger. The basic process of PTR operation can be divided in four steps[Fig.3.34]:

1. The system is at rest and pressure equalised.
2. The piston compresses the gas. The gas pressure increases to a state higher than the reservoir. Gas from the hot end of the pulse tube moves through the orifice into the reservoir.
3. A short time later, the pressure becomes equalised and the orifice closes.
4. The piston moves back, expanding the gas. The flow of gas moves from the reservoir through the hot end. Low pressure gas in the pulse tube moves towards the cold end. The cold, low pressure gas moves through the cold stage, picking up heat from the objects attached to the stage.

Actually in the QSG laboratory there are installed three PTRs: one is a Cryomech PT403-RM coldhead composed of a two-stage cryostat that can reach a base temperature of 3.5 K. A second one is a Cryomech PT405-RM coldhead composed of two-stage with an additional ^3He stage that can reach a base temperature of about 350 mK. Recently a new PTR has been installed in the laboratory, manufactured by Sumitomo (model RP-082B2), composed of two-stage with a minimal temperature of about 1 K. Cryomech PTRs are connected to a water-cooled CP2800 compressor, while the Sumitomo PTR is connected to a water-cooled F-70LP/HP compressor.

The Rankinator

The PTR used in this work for the nano-optical test is the Cryomech PT4505-RM. This system has been named "Rankinator" since it is installed in the Rankine Building (James Watt School of Engineering - University of Glasgow). In this system a confocal microscope is attached to a stack of stepper and scanner motors (Attocube systems) that allows scanning across the device with sub-nanometre resolution. In this way is possible to made nano-map of SNSPDs. This PTR has been equipped with $^4\text{He}/^3\text{He}$ sorption pumps connected to the CP2800 water-cooled compressor that allows characterization of SNSPDs devices at 400 mK. These pumps consist of charcoal connected to the coldhead via a long tube for collecting the cryogenic liquid [Fig.3.35].

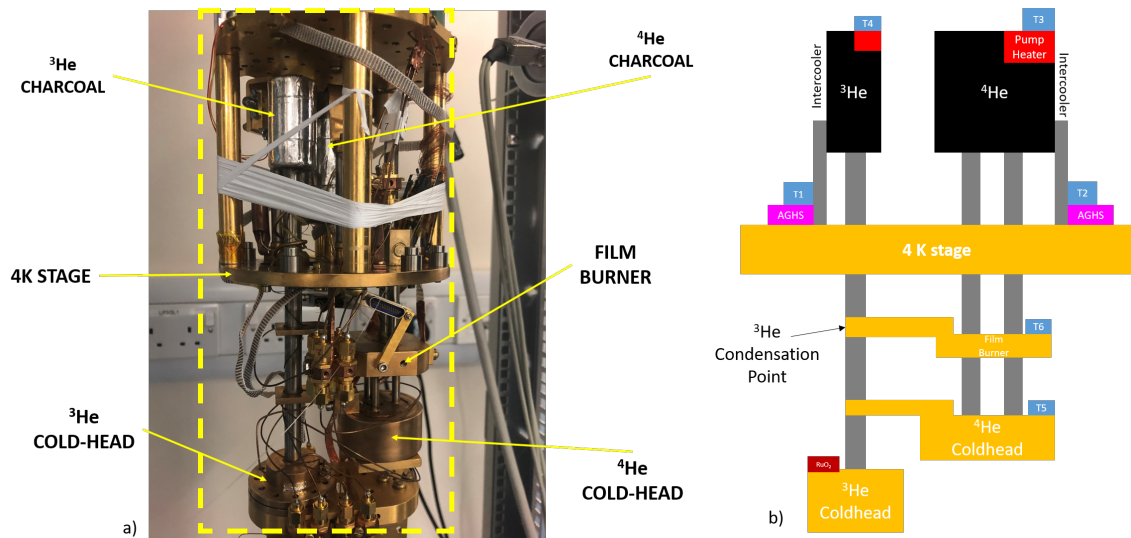


Figure 3.35: a) Picture of the sorption pumps installed in the Rankinator. b) Schematic of sorption pumps. Charcoals (black) are installed before the 4 K stage. Pump heaters (red) are biased (turned on) when the PTR reaches 40 K to ensure a major desorption of the He gas. When they are on, He gas flows into tubes (grey) to coldheads. Active Gas-Gap Heat Switches (AGHSs) (purple) dissipate heat into the ^4He and into the film burner to condense ^4He liquid (below 1 K). ^3He inside the tube is then liquefied since the tube is connected thermally to the film burner that is below 1 K. Under these conditions, the ^3He coldhead can reach a base temperature of 400 mK. Si diodes thermometers (blue) are connected on the pump heaters, heat switches and on ^4He coldhead. On ^3He coldhead is installed a RuO₂ thermometer diode (dark red).

The aim of sorption pumps is to liquefy ^3He using liquid ^4He . Below 5 K, the charcoal absorbs the enclosed $^4\text{He}/^3\text{He}$ gas. Around 16/19K and above, the gas is expelled into the tubes. The temperature of the charcoal is controlled by two pump heaters (300 Ω / 400 Ω). Pump heaters are usually biased (turned on) when the Rankinator is cooled down between 40-45 K to ensure a majority desorption of He gas. When pump heaters are on ^4He and ^3He gas begins condensing inside the tube. The liquid ^4He drips down into the film burner to the ^4He stage. The heat load generated in this process is dissipated by Active Gas-Gap Heat Switches (AGHSs) attached to each sorption pump. AGHSs are small sorption pumps with their own charcoal, He gas and pump heaters(10 k Ω). When AGHSs are on, they expel He and allow the flow of heat between the isolated sorption pump and the rest of the fridge. When off, the He is reabsorbed creating a vacuum and barring any thermal transfer. As the pump heater cools below 6K, the charcoal begins absorbing the remaining ^4He gas increasing the vacuum in the cryosystem. This reduces the vapour pressure on the liquid ^4He causing the film burner to cool down lower than 1 K.

Since the film burner is connected thermally to the ^3He tube, the gas inside (the ^3He pump is still on) starts to condense and the liquid ^4He in the film burner stage begins evaporating. Once the film burner begins warming ($> 1\text{ K}$), the ^3He pump heater is turned off and the ^3He AGHS is switched on dissipating any heat load. As the ^3He pump heater cools to 5 K , the charcoal begins absorbing the remaining ^3He gas, reducing the vapour pressure on the ^3He liquid and allowing the ^3He to reach a base temperature of about 400 mK . The Rankinator temperature is monitored by five Si diodes (DT-670) installed respectively on pump heaters, heat switches and the ^4He coldhead[Fig.3.35]. One RuO_2 diode is installed on ^3He coldhead for its accuracy at low temperature. Thermometers, pump heaters and switches are connected respectively to a Lakeshore 224 temperature monitor and two Keithley current supplies. The RuO_2 is connected to a SIM921 Resistance Bridge[Fig.3.36].

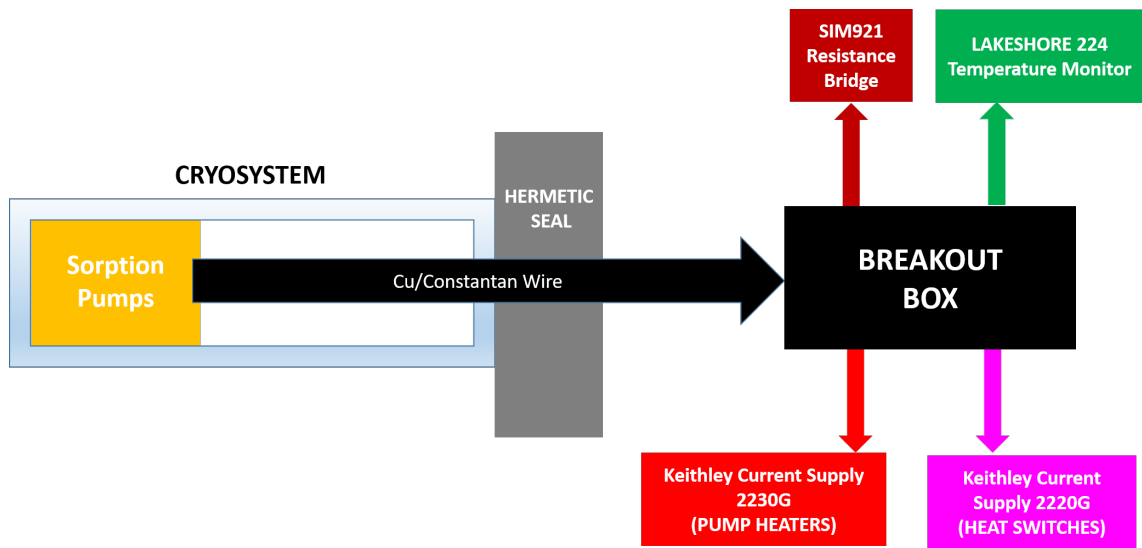


Figure 3.36: Sorption pump micro-pin wiring diagram. The hermetic seal is not placed on the outer can, but inside a T-piece outside the can. This creates the extra room needed for more wiring seals[168]. Wiring are then connected to a homemade breakout box connected to Keithley current supplies, Lakeshore 224 temperature monitor and SIM921 resistance bridge.

For the electrical characterization of SNSPDs, four rigid RF coax cables (SMA to SMP) have been installed at the ^3He coldhead. These cables are then connected to room temperature instrument via other four SMA rigid coax cables. For optical measurement, a hermetically sealed fibre feed-through, 16 optical fibres enter the fridge. The Rankinator has been equipped with a bespoke machined confocal microscope configuration setup composed of a single-mode fibre and a microscope lens tube setup for nano-optical measurements[168, 169, 170]. This confocal microscope configuration setup is mounted on a stack of three piezoelectric stepper motors (Attocube systems) that allows the confocal microscope system to move in x and y-axes over a large area ($5\text{ mm} \times 5\text{ mm}$). The third piezoelectric motor is used for the focus of the confocal microscope. Additionally, a stack of two independent scanning motors (Attocube systems) gives the ability for small area $30\text{ }\mu\text{m} \times 30\text{ }\mu\text{m}$ scanning across the device. The three stepper motors were controlled by an Attocube ANC300 piezo motion controller whereas, the two scanner motors were controlled by an Attocube ANC200 motion controller. The microscope is attached via a flexible thermal link to the ^3He coldhead.

Light delivered from the single-mode fibre to the microscope lens tube setup is firstly collimated by a Geltech 352280-C lens with numerical aperture (NA) = 0.15 and then focused by a Geltech 352330-C lens with NA = 0.68. Both these lenses come with an antireflection coating (ARC) designed for 1050 nm to 1700 nm[Fig.3.37].

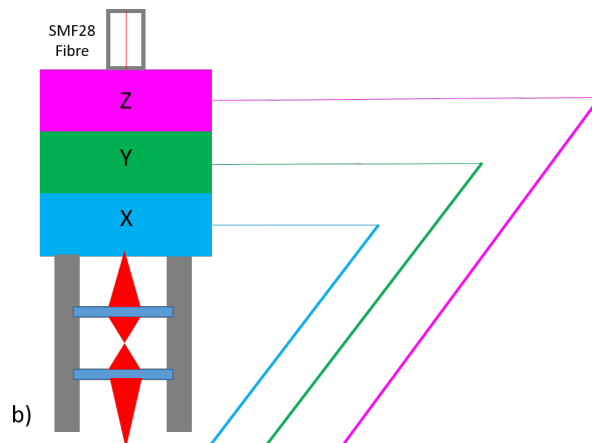
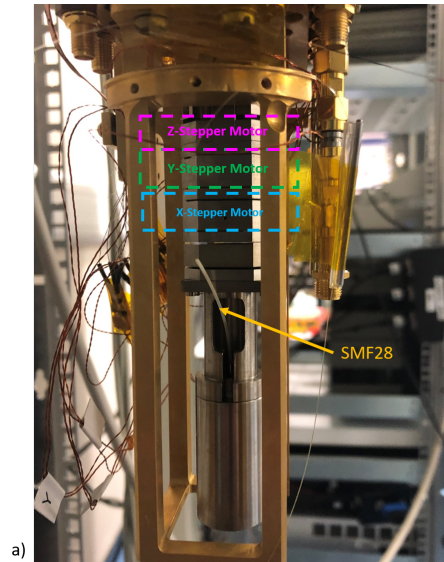


Figure 3.37: a) The confocal microscope is mounted on a stack of 4 attocubes: one to move the microscope both in the X and Y direction and the other two to move respectively the microscope along the length (X), the width (Y). The Z-stepper motor need to focus the optical fibre (SMF28) on the sample. b) Scheme of the confocal microscope. c) Attocube ANC300 piezo motion controller to control three attocubes.

Chapter 4

Thin Film Characterization

This chapter describes the process of optimization of NbN and MoSi thin film chosen for the fabrication of SNSPD arrays. Firstly, the choice of substrate is considered. The next section details the sputtering optimization process for NbN and MoSi. The chapter concludes reporting superconducting properties of 8nm thickness NbN and MoSi measured by the Ekinator (section 3.5.1)

4.1 Selection and preparation of substrates

The standard way to obtain high quality superconductivity thin films is by growth an appropriately selected substrate. In this case, the lattice structure of the film material should be well matched to that of the substrate. The table [4.1] shows the lattice constant of NbN, NbTiN, MgO sapphire and silicon.

Table 4.1: Lattice type of NbN, NbTiN, MgO, sapphire and Si at 300 K.

	Lattice Type	Lattice Constant	Reference
NbN	NaCl - cubic	0.439 nm	[171]
NbTiN	NaCl - cubic	0.440 nm	[171]
MgO	NaCl - cubic	0.421 nm	[171]
Sapphire(Al_2O_3)	Hexagonal	0.476 nm	[172]
Si	Diamond	0.543 nm	[173]

Since MgO and sapphire substrates have lattice parameters similar to crystalline films as NbN and NbTiN, they are a good choice. However, thin films grown on silicon substrates are an attractive choice for combining superconducting detectors with waveguide circuits or optical cavities. For this reason, 4-inch high-resistivity ($>10\text{ k}\Omega\text{cm}$) intrinsic Si wafers, orientation $\langle 100 \rangle$, double side polished have been chosen to be substrates for NbN and MoSi thin films. Wafers have been diced in 15 mm x 15 mm and 10 mm x 10 mm squares to be easily installed on sample mounts to match the sputtering tool^{3.2} and the test setup installed in the Ekinator (section 3.5.1).

Before the deposition, substrates are first cleaned ultrasonically by acetone and IPA, then mounted on the substrate carrier and installed in the load lock of the sputtering equipment. Before transferring the substrates into the main chamber, they are cleaned by argon plasma for 2 minutes to remove any impurities from the surface.

4.2 NbN thin film optimisation

Usually, high-quality NbN thin films are obtained when the conditions of deposition are optimized to obtain films with maximum T_c . NbN critical temperature depends strongly on the concentration of nitrogen in the total sputtering pressure. High concentration of nitrogen can modify the geometry of NbN reducing its superconducting properties[174, 175]. In order to find the highest critical temperature of NbN, several NbN bulk (large thickness) films have been made at different sputtering pressure varying the nitrogen pressure between 10% and 20% of the total pressure. Before any sputtering process, the surface of Nb target is cleaned by argon pre-sputtering for 5 min. After this, substrates are installed onto a Mo sample holder and transferred by the load lock to the main chamber and positioned at 100 mm distance from the target. When the pressure inside the main chamber is about 10^{-8} Torr, the sample holder starts to rotate at a speed of 50 rpm and N_2 gas flow is introduced. The throttling valve is fixed at 75° while the flow is manually settled to set the capacitance manometer at the desired pressure. After waiting for 1 minute to stabilize the Ar gas flow a stable sputtering pressure is achieved and the shutter on the target is opened. After 30 sec the target is biased by a constant current of 0.8 A for 20 min to ensure to obtain a large thickness (bulk) film. After 20 min, the bias is turned OFF and the main chamber is pumped again. Samples are then transferred from the main chamber to the load lock by the automatic transfer arm. At this point, the load lock is vented and samples are removed to be installed in the Ekinator to measure their critical temperature as described in the section 3.5.1. As shown in Fig.4.1, the sputtering process is started from the pressure of 1.5 mTorr to 1.8 mTorr varying the pressure of nitrogen on the total sputtering pressure. At each sputtering pressure, the critical temperature presents a maximum value for different nitrogen pressure that peaks at a pressure of 1.7 mTorr then decreases thereafter. Then the highest transition temperature T_c is obtained when the sputtering pressure is 1.7 mTorr and the nitrogen pressure is 0.18 mTorr (10.6% of the total pressure). Under these conditions, the critical temperature of a bulk NbN growth on a HR silicon substrate at room temperature is 14.6 K. Since this is the maximum value achieved for a NbN bulk film, then NbN thin film used for SNSPD array fabrication have been made following the sputtering recipe described before. Once settled sputtering parameters, next step is to know the sputtering rate to set the sputtering time to realize thin films. A fast way to measure the thickness of a sputtered film is to mark the substrate by a marker pen before the sputtering and then remove the marked area by immersing the sample in acetone (a primitive lift-off procedure). After this the shape of the marker is "printed" onto the substrate and the thickness can be measured by any profilometer. In this way, three NbN films have been realised with sputtering time respectively 20 min, 10 min and 1 min measuring respectively a thickness of about 180 nm, 89nm and 9 nm.

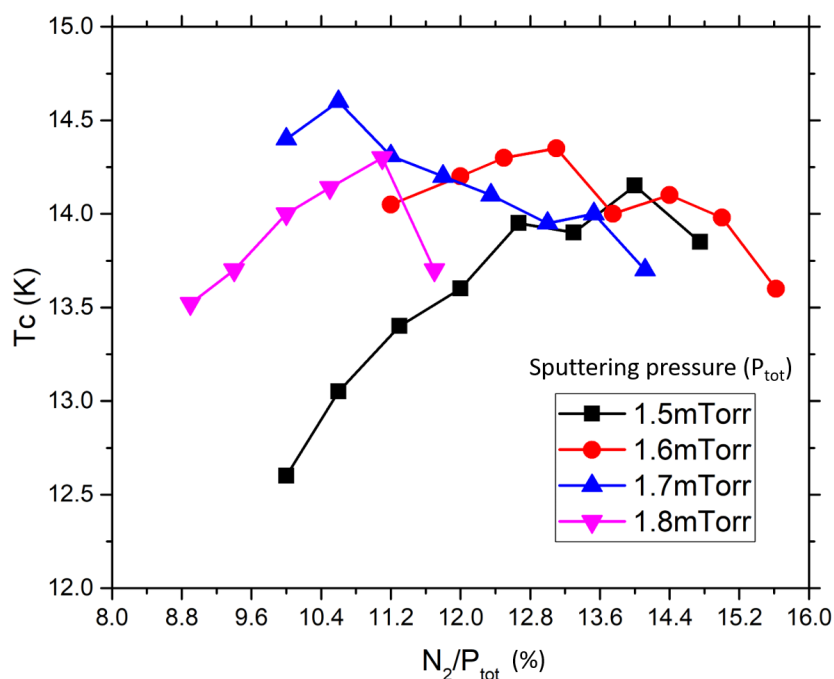


Figure 4.1: NbN critical temperature T_c versus nitrogen pressure on the total sputtering pressure expressed in percentage. NbN are grown on HR Si substrates at room temperature via DC magnetron sputtering process. The sputtering process has been run for 20 minutes to ensure the growth of large thickness film (roughly more than 100 nm). For a given total pressure P_{tot} , a maximum in the T_c can be found by varying the proportion of N_2 . This value increases with the total sputtering pressure till a maximum value. In this case the maximum value (14.6 K) corresponds to 1.7 mTorr total pressure with 10.6% nitrogen.

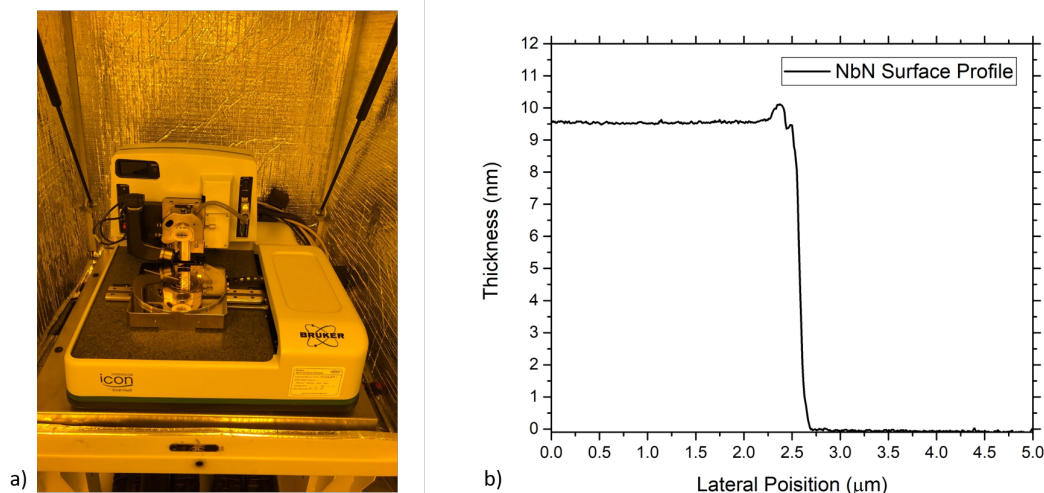


Figure 4.2: a) ICON AFM equipment installed in JWNC cleanroom. b) 1D profile plot of a NbN thin film growth on HR Si substrate and marked with a pen marker to enable a step to be created by a primitive lift off procedure. The edge bump is an artifact caused by the AFM when the scanning needle jumps from a low area to a high area (the scanning direction here is from the right to the left). The measure has been made on a range of 5 μm on the lateral position. Data have been extracted from the software Nanoscope Analysis as .txt file then plotted and translated to 0 by the software OriginPro. The vertical distance represents the thickness measured. The value measured is about $9.5 \text{ nm} \pm 0.01$ fitting between the two levels.

These thickness values have been measured by a DektakXT profilometer installed in the JWNC cleanroom. For a precise measurement of the sputtering rate, the thickness of the sample made in 1 min has been measured by the Icon AFM equipment[Fig.4.2]. From the linear fit of two levels, the thickness measured is about $9.5 \text{ nm} \pm 0.01$. The sputtering rate of NbN is then about 0.16 nm/sec . As a starting point for SNSPD fabrication, several NbN 8nm-thick films have been deposited on HR Si using a total sputtering pressure of 1.7 mTorr, 0.18 mTorr nitrogen pressure, 0.8 A bias current and a sputtering time of 50 sec. Some samples have been grown on 15 mm x 15 mm square and 10 x 10 mm square HR Si substrates. The 15 mm x 15 mm square has been used to test the critical temperature in the Ekinator cryo-system (section 3.5.2), while the 10 mm x 10 mm sample is used to fabricate the SNSPD array structure. A first set of samples has been grown at room temperature exhibiting 6 K a critical temperature. Other substrates have been heated at 800°C to increase the critical temperature. With heating under these conditions 8nm-thick NbN films show 8 K critical temperature[Fig.4.3].

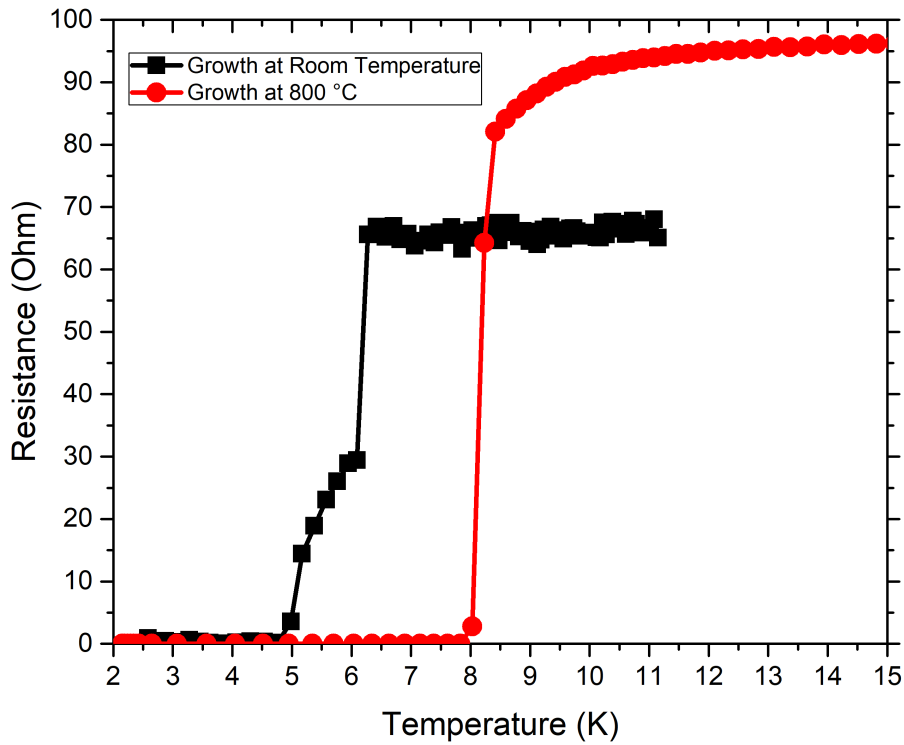


Figure 4.3: RT characteristic of two NbN 8nm-thick films deposited on HR Si at room temperature and heated at 800°C . The critical temperature is choose in the middle of the resistive transition. The critical temperature is enhanced and the width of the superconducting transition is decreased due to substrate heating. These data have been measured with the Ekinator (section 3.5.2).

4.3 MoSi thin film optimisation

In this work, MoSi thin films have been grown on HR Si substrates using a pure $\text{Mo}_{80}\text{Si}_{20}$ target (3.00" diameter \times 0.250" thickness) provided from Kurt J. Lesker Company. In this case, the growth of the amorphous MoSi does not require the use of a co-sputtering process made by Mo and Si target independently. The use of a co-sputtering process (as previously pursued in our group by Dr Archan Banerjee[176]) ensure the precise control of Mo and Si stoichiometry, but it requires the control of the sputtering pressure, the DC bias current for the Mo target and the RF bias power for the Si target lengthening time of fabrication. For this reason, in this thesis work, sputter growth using a MoSi alloy target has been pursued. Before the sputtering process, the MoSi target surface is pre-sputtered by argon plasma at 2 mTorr pressure and biasing the target with a constant current of 0.8 A for 6 min. Substrates are cleaned and transferred in the main chamber in the same way as before: ultrasonic bath in acetone and IPA, then argon etching in the load lock for 2 min and then transferred to the main chamber by the arm transfer. The distance between substrate and target is kept at 100 mm, the throttling valve is kept at 75° and the sample holder is settled to rotate with a speed of 50 rpm. After 1 min, argon gas is introduced in the main chamber keeping the flow at 30 sccm. Under these conditions, the pressure reading on the gauge is about 1.66 mTorr. After 1 min to stabilize the gas pressure at constant gas flow rate, target is biased at 0.3 A keeping the shutter closed for 5 min to stabilize plasma. As explained before, the sputtering rate is measured marking the substrate before the sputtering process and then analyzed by a profilometer after the lift-off. For this step, a series of MoSi thin films have been grown for sputtering times of 7.5 min, 5 min and 2 min. Analyzing these samples by the Icon AFM equipment, as described for the NbN films in the previous section, their respective thickness are 29.8 ± 0.03 nm, 20.2 ± 0.01 nm and 8 ± 0.01 nm confirming a sputtering rate of about 4 nm/min. Critical temperatures of these unpatterned films is showed in the [Fig.4.4]. The sample of 30 nm thickness exhibits a critical temperature of about 7 K that is comparable with the critical temperature of a bulk MoSi film that is 7.3 K in according to the literature[176, 177]. For this reason, the sputtering recipe described before has been used to realize a set of 8 nm thickness MoSi films on a set of 15 mm \times 15 mm HR Si substrates to measure the critical temperature in the Ekinator achieving a value of about 5 K. Amorphous properties of MoSi films can be improved by cooling the substrate[176] so before the sputtering, some substrates have been transferred from the main chamber to the LN_2 chamber and then cooled to -180°C adding liquid nitrogen. After this, substrates are transferred again into the main chamber immediately ready for the sputtering process. MoSi 8nm-thick films grown on cooled substrates show a slight increase of critical temperature and resistivity[Fig.4.5]. In summary, nine 8 nm thickness MoSi deposited on 10 mm \times 10 mm HR Si cooled to -180°C have been realized for the fabrication of SNSPD arrays.

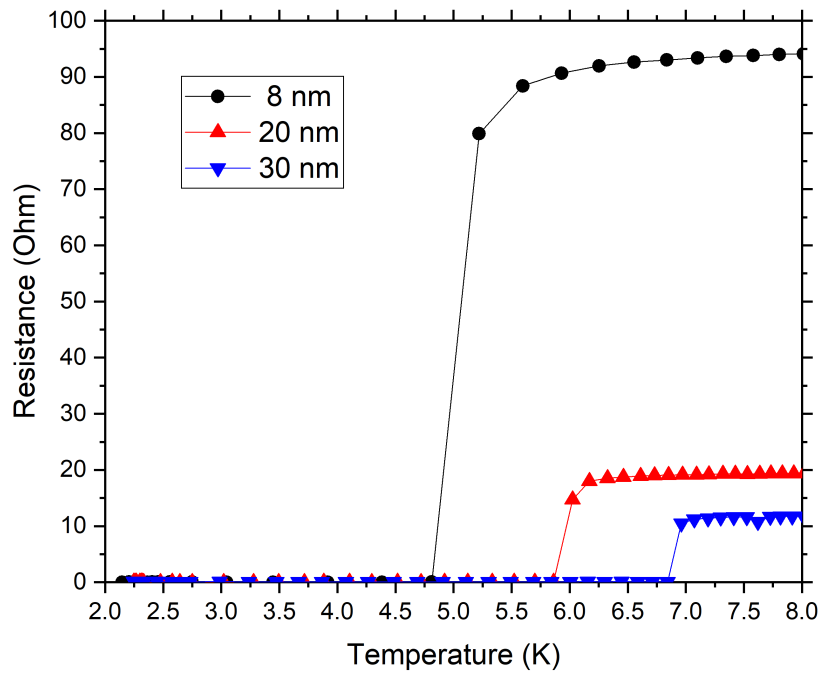


Figure 4.4: RT characteristic of three unpatterned MoSi of different thickness. The insert table shows the approximate values of the thickness measured by the Icon AFM equipment.

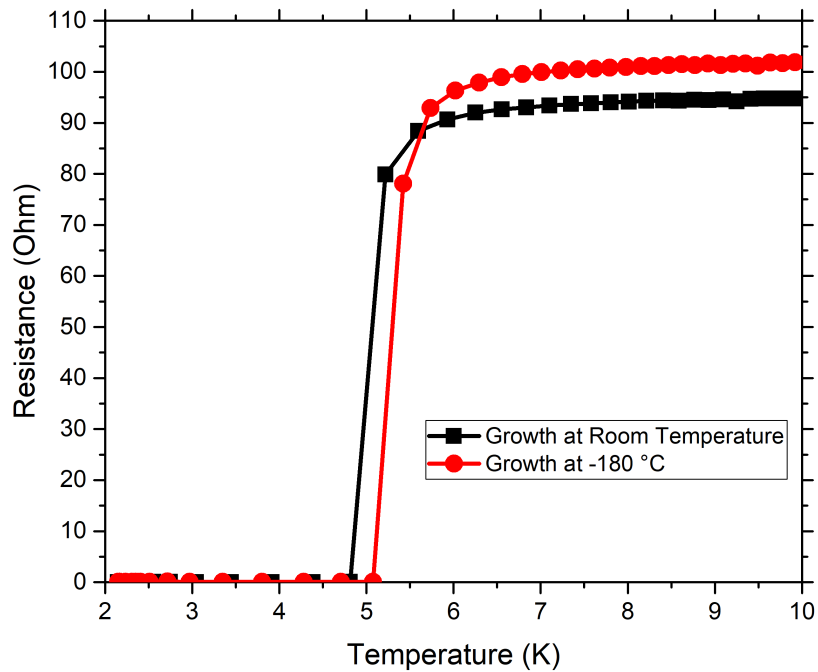


Figure 4.5: RT characteristic of two MoSi 8nm-thick films deposited on HR Si at room temperature and cooled at -180°C . The film growth on the cooled substrate shows a slight increase of the critical temperature. These data have been measured with the Ekinator (section 3.5.2)

4.4 Superconducting properties of patterned thin film test structures

Before commencing fabrication of SNSPD arrays, it is useful to understand as fully as possible the superconducting properties of the sputtered thin films. The critical temperature is one of the most important properties since it gives information about the energy gap and the critical current of the superconductor (section 2.2). High critical current is advantageous for SNSPDs as this will lead to larger output pulses, improving the signal-to-noise, increasing the efficiency and reducing the timing jitter, besides a large energy gap reduces the sensitivity of the detector at long wavelengths. Since the critical current is a geometric parameter, then it can be increased by modifying the dimension of the pattern chosen for the SNSPD fabrication. This information is provided by the critical current density J_c of the superconductor. This parameter is measured in the Ekinator (section 3.5.1). While the critical temperature can be measured using an unpatterned film, the measurement of the critical current density the superconductor thin film needs to be patterned in a microbridge structure. This structure has been designed by a software .gds editor (Layout Editor) to be compatible with the 4-point probe layout in the cryocooler. As explained in the section 3.5.1, this consists of a row of 4 pogo pins at a spacing of 2.7 mm. The microbridge structure realized for this set-up [Fig.4.6] consists of a microbridge 200 μm long connected to four large pads separated by a distance of 200 μm between each pin. The pads are large enough to make reliable contact with the corresponding pogo pins.

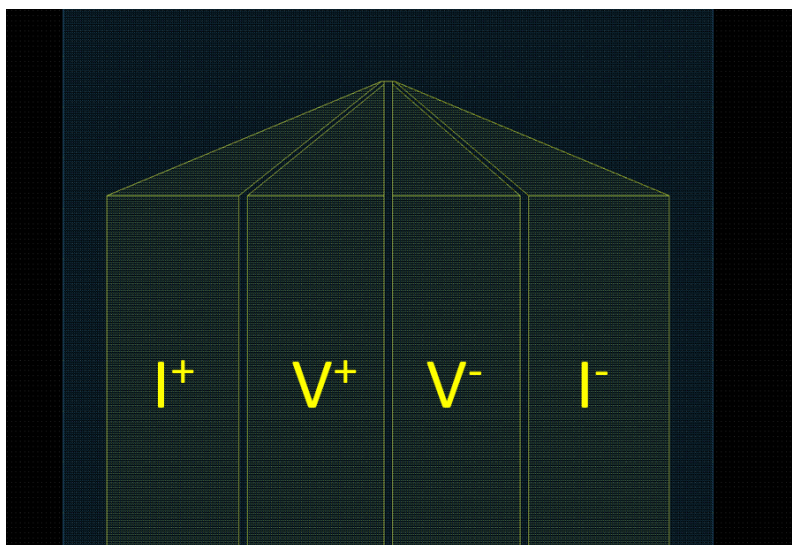


Figure 4.6: Layout of the 2 μm x 200 μm microbridge designed for the 4-point probe characterization (section 3.5.1). External pads (I^+ and I^-) are connected to the voltage source adding a load resistor in series. Internal pads (V^+ and V^-) are connected to a voltmeter

Three microwires in this configuration have been designed. Each is 200 μm long and the width is 2, 5 and 10 μm respectively. These patterns are created by photolithography from a Cr photomask. To measure their superconducting properties, NbN and MoSi 8nm-thick films grown on 15 mm x 15 mm HR Si substrates have been patterned respectively in 2 μm x 200 μm , 5 μm x 200 μm and 10 μm x 200 μm microbridges via photolithography using the positive-tone photoresist S1805 and a MF-319 developer [Fig.4.7].

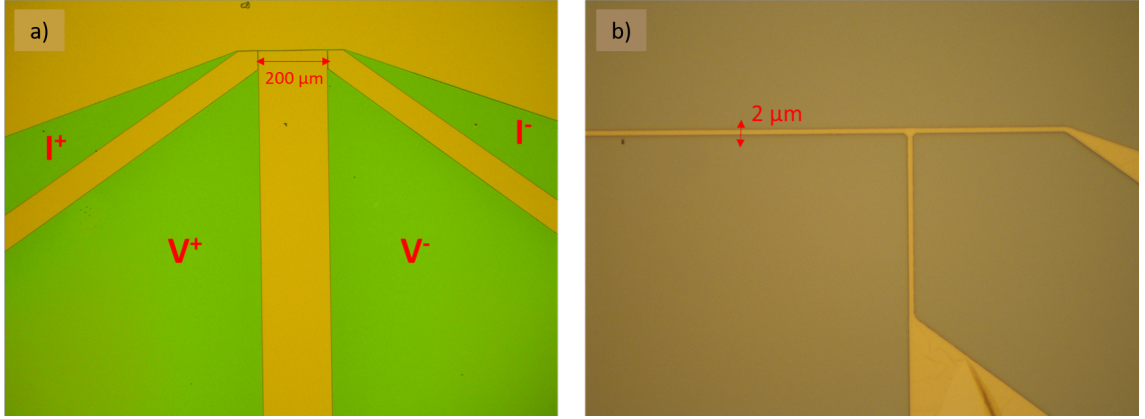


Figure 4.7: Images of 8nm-thickness NbN microbridge $2 \mu\text{m} \times 200 \mu\text{m}$ before the dry etch (a) and after the dry etch (b) taken by the Nikon Eclipse optical microscope installed in the JWNC. The microbridge is connected to four large pads. The outer pads are for passing bias current whilst the voltage drop is measured across the central pair.

The pattern is then transferred onto the thin film via CF_4 plasma [Table 3.2]. After stripping the resist in acetone bath warmed at 50°C for several hours, the device is installed in the cryocooler and cooled at 2.1 K. The heater installed in the cryocooler (section 3.5.1) permits measurement of the critical current of the microbridge over a range of temperatures between the base temperature (2.1 K) and the T_c . By definition [178], the critical current density $j_c = I_c/(S)$ where $S = \text{width} \cdot \text{thickness}$ is the cross-sectional area of the superconductor. Experimental data [Fig.4.8] are then fitted by the equation (2.12) introduced in the section 2.2.2.

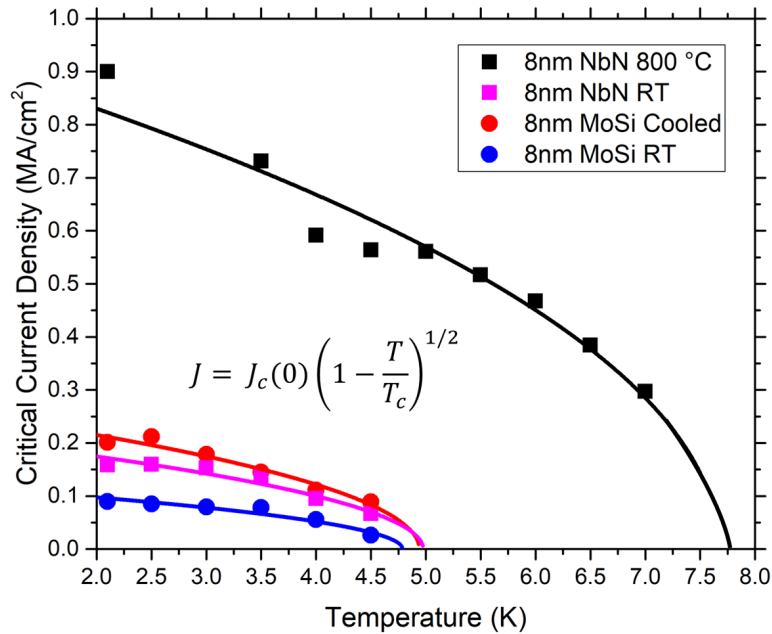


Figure 4.8: Critical current density versus temperature for $2 \mu\text{m} \times 200 \mu\text{m}$ NbN, $5 \mu\text{m} \times 200 \mu\text{m}$ MoSi (growth cooling substrate) and $10 \mu\text{m} \times 200 \mu\text{m}$ MoSi (growth at room temperature). All films are 8nm thickness. Experimental data are fitted using a Chi-squared nonlinear fit with the equation of BCS theory (2.12) to extract the critical current density at 0 K ($J_c(0)$) and the critical temperature T_c .

Critical current density is 0.22 MA/cm^2 for NbN grown on HR silicon substrate at room temperature. This value increases to 0.95 MA/cm^2 because the quality of the NbN crystalline film improves when it is deposited onto a heated substrate. This value is next to 1.2 MA/cm^2 for a high quality NbN film deposited onto a silicon substrate[179]. In the same way, critical current density of MoSi is 0.12 MA/cm^2 and then slightly increases to 0.28 MA/cm^2 when the silicon substrate is pre-cooled using the liquid nitrogen trap of the sputtering tool3.2. This value is next to 0.2 MA/cm^2 measured recently by our research group[176] for 10 nm thickness, 173 nm wide MoSi made via a co-sputtering process of Mo and Si. Critical current densities deviation from literature values can be explained by inhomogeneity caused during the microwire fabrication. The RT characteristic of devices is measured first cooling the device to the base temperature of 2.1 K and then warming up the cryocooler (turning off the helium compressor) recording the voltage of the device on the voltmeter and the temperature on the SIM922 monitor[Fig.4.9].

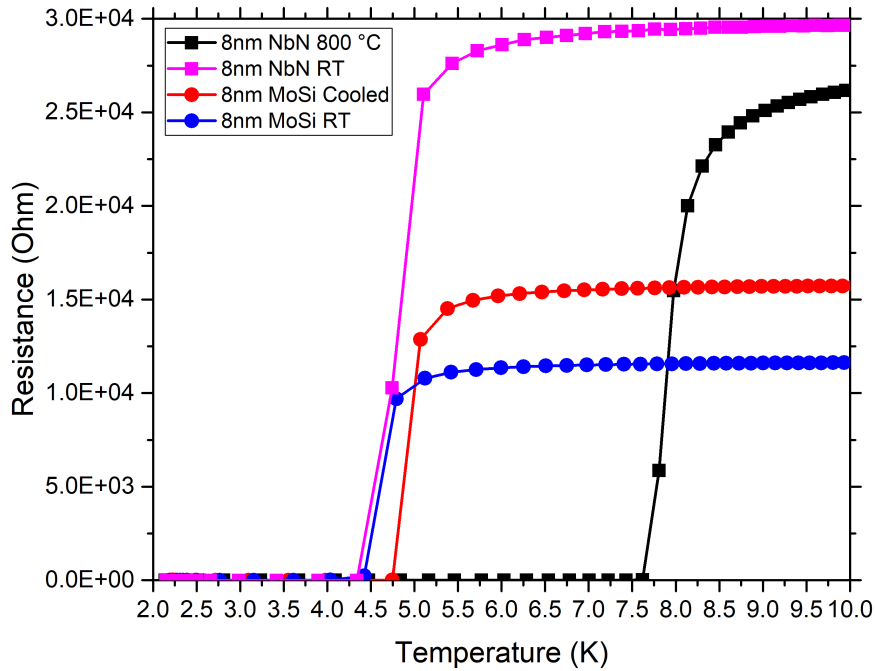


Figure 4.9: RT characteristic of two $2 \mu\text{m} \times 200 \mu\text{m}$ NbN test structures grown at room temperature (magenta) and heating the substrate at 800°C (black), $5 \mu\text{m} \times 200 \mu\text{m}$ MoSi (grown cooling substrate to -180°C) and $10 \mu\text{m} \times 200 \mu\text{m}$ MoSi (grown at room temperature). All films are 8nm-thick.

Another parameter useful for the superconducting thin film characterization is the residual resistance ratio (RRR) defined as the ratio of the resistivity of a material at room temperature and just above the superconducting transition temperature. Since defect prevalence increases the electron scattering in the material in the normal state, a large RRR is associated with a sample with few defects.

Since superconducting thin films have been grown on undoped high resistivity substrates ($>10\text{ k}\Omega\text{cm}$), the resistance measured at room temperature is affected by the parallel resistance of the silicon substrate[Fig.4.10]. Cooling the system, the silicon substrate becomes completely insulating and the NbN resistance acquires the expected value. In this work, RRR is calculated as the ratio of the resistivity $\rho(200\text{K})$ at 200 K and the resistivity $\rho(20\text{K})$ at 20 K. The resistivity $\rho(T)$ of a conductor for a given temperature T is expressed by the equation:

$$\rho(T) = t \cdot R(T) \cdot \frac{w}{L} = t \cdot R_{sheet} \quad (4.1)$$

where $R(T)$ is the resistance of the film for a given temperature T, t is the thickness of the superconducting thin film, w the width and L the length of the microbridge patterned onto the thin film. The quantity $R_{sheet} = R(T) \cdot \frac{w}{L}$ is the sheet resistance (square resistance) of the thin film.

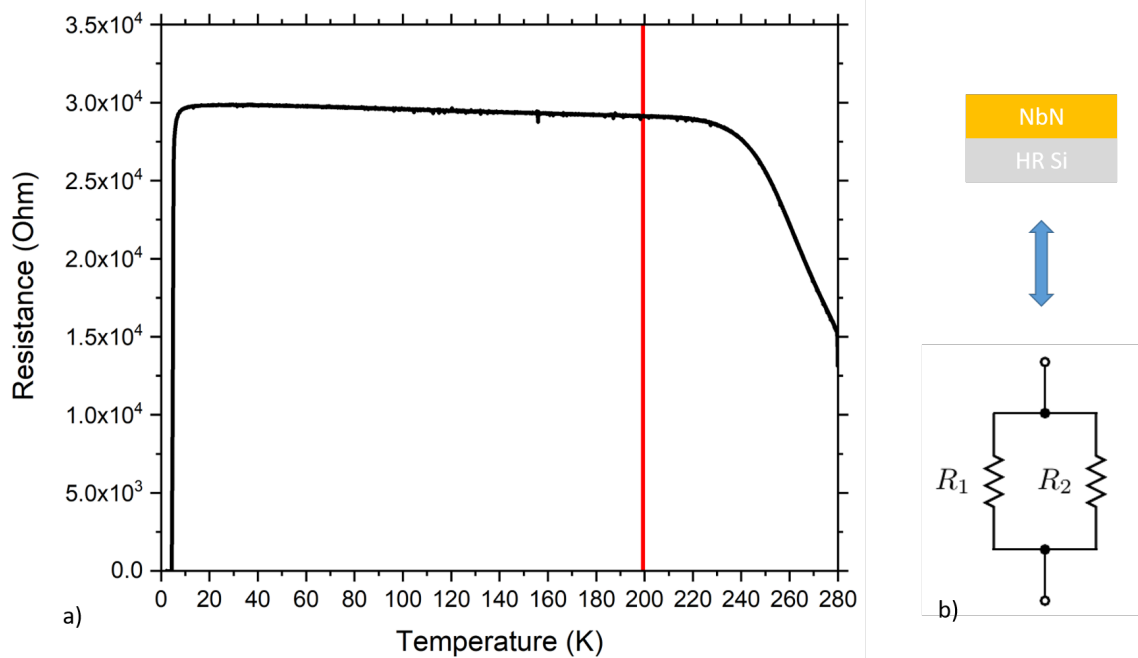


Figure 4.10: a) RT characteristic of $2\ \mu\text{m} \times 200\ \mu\text{m}$ microbridge NbN grown at room temperature on a HR Si substrate. b) The system superconductor/substrate can be considered like two resistors R_1 and R_2 in parallel. Since their resistance is similar, at room temperature the resistance of NbN is affected by substrate resistance and the result is a lower value expected.

Table 4.2 shows the critical temperature of samples before and after the photolithography highlighting how the lithography process can affect superconducting properties of thin films. This suppression of the critical temperature is due to a degradation of the film thickness possibly during the dry etch process. The proximity effect model explains the decrease in T_c , as the result of the existence of degradation layers between the thin film surface and the film-substrate interface[180, 181, 182].

Critical temperature of unpatterned films are in agreement with values of critical temperature of MoSi thin film and NbN thin film measured in some previous works[100, 179, 183].

Table 4.2: Critical temperature of 8nm-thick NbN and MoSi films grown at different temperature before and after the photolithography.

Sample_ID	Substrate Temperature	T_c Unpatterned	Microbridge Dimensions	T_c Microbridge
NbN RT	RT	5.5 K	2 μm x 200 μm	5 K
NbN 800 °C	800 °C	8.2 K	2 μm x 200 μm	8 K
MoSi RT	RT	5.1 K	10 μm x 200 μm	4.8 K
MoSi Cooled	-180 °C	5.4 K	5 μm x 200 μm	5.1 K

The table 4.3 shows superconducting intrinsic properties of 8 nm thickness NbN and MoSi. Resistivity ρ and sheet resistance R_{sheet} are calculated by the equation (4.1).

Table 4.3: Intrinsic superconducting properties of 8 nm thickness NbN and MoSi microbridges deposited on silicon substrate: critical temperature T_c , critical current density at 0 K $J_c(0K)$, resistivity at 20 K $\rho(20K)$, sheet resistance at 20 K

Sample_ID	Microbridge Dimensions	T_c (K) Fit	$J_c(0K)$ (MA/cm^2) Fit	$\rho(20K)$ ($\mu\Omega \cdot cm$)	$R_{sheet}(20K)$ (Ω/\square)	$\rho(200K)$ ($\mu\Omega \cdot cm$)	RRR
NbN RT	2 μm x 200 μm	5	0.22	238.6	298.25	232.96	0.98
NbN 800 °C	2 μm x 200 μm	7.8	0.95	220.1	275.12	211.13	0.96
MoSi RT	10 μm x 200 μm	4.8 K	0.12	466.84	583.55	449.94	0.98
MoSi Cooled	5 μm x 200 μm	4.9 K	0.28	316.1	395.12	304.63	0.96

Critical temperature values calculated from the fit of equation (2.12) are comparable with values measured from RT characteristics. NbN exhibits a larger value of critical temperature when the Si substrate is heated during the sputtering process, consequently it exhibits a large critical current density and a reduced resistivity in agreement with reference[179]. Thus means a reduction of the sheet resistance associated with the increase of the grain size in NbN increasing its crystalline structure that is relevant for NbN superconducting properties[174]. In according to the literature[184], MoSi samples present lower value of critical temperature than NbN. The critical temperature (and thus the critical current density) of the MoSi can be improved cooling the substrate by liquid nitrogen. Even the MoSi grown at room temperature exhibits a larger RRR than the MoSi grown cooling the Si substrate. In conclusion, there are not large discrepancies of RRR, thus all devices present minor defects.

The superconducting properties summarized in table 4.3 are a starting point for the fabrication of SNSPDs in general. First, the critical temperature gives information about the energy gap of the superconductor and then about the intrinsic detection efficiency of the detector. The critical current density is a reference for the critical current $I = Jtw$, where t is the thickness of the thin film and w is the width of nanowire. For a given thickness, the width can be chosen large to get a large critical current. Whereas, a large width can affect the hot-spot model explained in the section 2.3. For this reason SNSPD pixels of this work have been patterned with a width of 100 nm that is a standard value for any SNSPD. At least, the resistivity $\rho(20K)$ gives information about the inductance per square L_k^\square given by the equation[174, 185]

$$L_k^\square = \frac{\hbar}{1.75k_B\pi} \frac{\rho(20K)}{tT_c} \quad (4.2)$$

As result, for a given meander structure, it is possible to predict the kinetic inductance of the superconductor and so get information about the reset time of SNSPD signals. The table[4.4] summarizes the critical temperature, the energy gap and the square impedance of superconducting thin films chosen for the fabrication of SNSPD multipixel array.

Table 4.4: Critical temperature, energy gap, and the inductance per square of 8nm-thick NbN and MoSi growth on pure silicon substrates at different temperatures. Inductance per square values are calculated from eq.(4.2).

Sample ID	T_c	Energy Gap	Inductance per square
NbN RT	5 K	0.75 meV	83 pH/ \square
NbN 800 °C	7.8 K	1.2 meV	49 pH/ \square
MoSi RT	4.8 K	0.72 meV	170 pH/ \square
MoSi Cooled	4.9 K	0.72 meV	112 pH/ \square

NbN grown heating the substrate presents high value of critical temperature and critical current density, and low value of resistivity at low temperature and kinetic inductance per square. On the other hand, the NbN presents a low value in terms of the critical temperature and this means an energy gap of the same order of the MoSi samples and thus a large range in term of wavelength (ideally a range between the visible and the microwave range). For this reason, even the 8 nm thickness NbN grown at room temperature has been chosen to realize the 8-pixels array. In conclusion, MoSi samples exhibit similar critical temperature. To fabricate the 8-pixels structure, only the 8 nm thickness MoSi grown cooling the substrate has been chosen because of its large critical current density and its small resistivity at low temperature and kinetic inductance per square.

Chapter 5

SNSPD Array Characterization

This chapter reports the low temperature characterization of the prototype SNSPD arrays based on 8 nm thick NbN and MoSi films. First the layout of the multipixel structure and its fabrication steps are introduced. The next section describes sample mounts used and the optical set-up used to align the optical fibre. In the final section, single-photon response is investigated for 8-pixel arrays at 1550 nm wavelength.

5.1 Design and Fabrication

The array configuration realized for this work is based on the optoelectrical characterization of each single pixel to test the uniformity of the system in terms of their superconducting and optical properties. For this purpose an array configuration of 8 pixels has been designed[Fig.5.1].

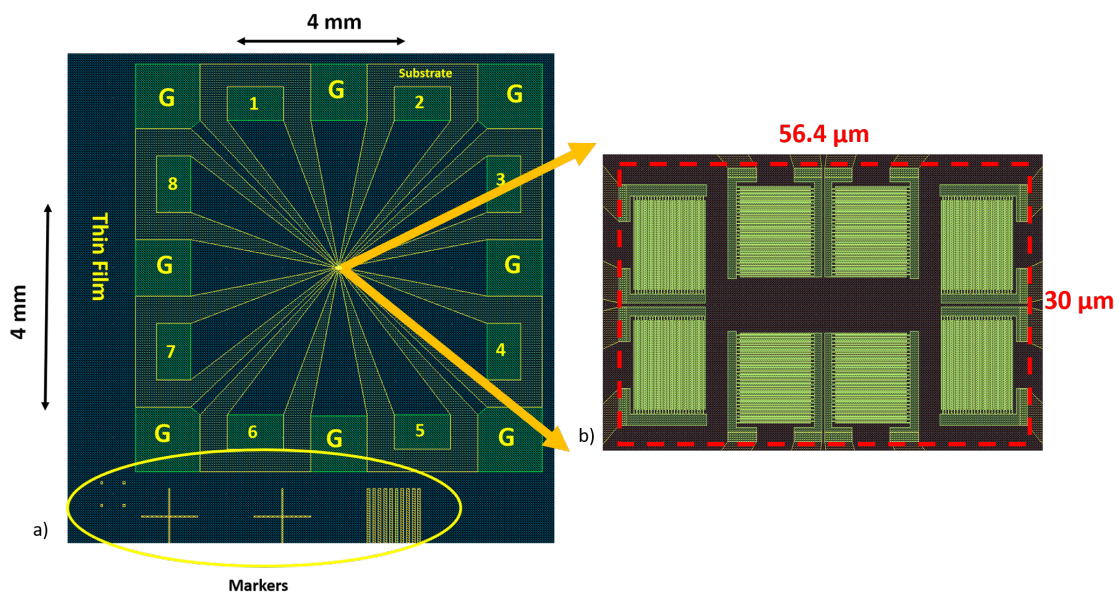


Figure 5.1: a) Layout of the multipixel array scheme designed for this work. The layout has been designed by LayoutEditor software. Pixels are installed in in 50 Ohm coplanar waveguides (CPWs). The structure is adapted to be printed on substrates covering a 4 mm × 4 mm die. Markers are required to align the e-beam tool (section 3.3.2) during the fabrication of nanowires and waveguides. The layout is designed for a positive-tone e-beam resist: the layers represent zones for exposure. b) Sketch of the 8-pixels structure. The structure covers 30 μm × 56.4 μm area (red rectangle). Each pixel is a meander square covering 10 μm × 10 μm area, the width of nanowires is 100 nm with 50% filling factor.

Each pixel is a nanowire of 100 nm width structured in a meander square $10\ \mu\text{m} \times 10\ \mu\text{m}$ with 50% filling factor implemented in a coplanar waveguide (CPW) that act as 50 Ohm impedance transmission lines delivering signals from the chip to the external electronics. Current bias is applied between the centre conductor and the group via the DC arm of an external bias tee. Pixels have one common ground contact (divided in 8 large pads) and separate contacts to be characterized independently. As explained in section 3.3.2, the multipixel array is fabricated via e-beam lithography in three steps[Fig.5.2]:

- **Metalization:** first gold pads and markers are defined by a preliminary e-beam procs. Positive-tone 200k PMMA e-beam resists AR-P 632.12 Anisole and AR-P 649.04 are spun on the sample at 4000 rpm and softbaked on a $150\ ^\circ\text{C}$ vacuum hot plate for 5 min. The sample is then exposed by $750\ \mu\text{C}/\text{m}^2$ dose, 64 nA beam (100 keV accelerating voltage) and 16 variable resolution unit (VRU). After the development for 60 sec in MIBK:IPA (1:1) solution, 5 nm / 100 nm of Ti/Au are deposited on the sample by e-beam evaporation. Parts covered by resist are removed ultrasonically whilst the sample is immersed in acetone
- **Nanostructure Design:** Nanowire and waveguides are realized spinning positive-tone ZEP520 at 4000 rpm (resulting in a resist thickness of approximately 100 nm) and softbaked on a $180\ ^\circ\text{C}$ vacuum hot plate for 4 min. The exposure of the samples consist of two steps: one by $270\ \mu\text{C}\ \text{m}^2$ dose, 128 nA beam and 40 VRU to define waveguides and the other by $300\ \mu\text{C}\ \text{m}^2$ dose, 1 nA beam and 3 VRU to define nanowires. Then the sample exposed is developed in O-xylene solution for 30sec and inspected by a SEM tool[Fig.5.3].
- **Dry etching:** The array structure is then defined by dry etch process at room temperature consisting of CF_4 plasma (50 sccm flow) at 30 mTorr pressure and 80 W power. Residual ZEP520 is removed immersing the sample in microposit remover 1165 for several hours, rinsing in IPA and cleaning by nitrogen gun.

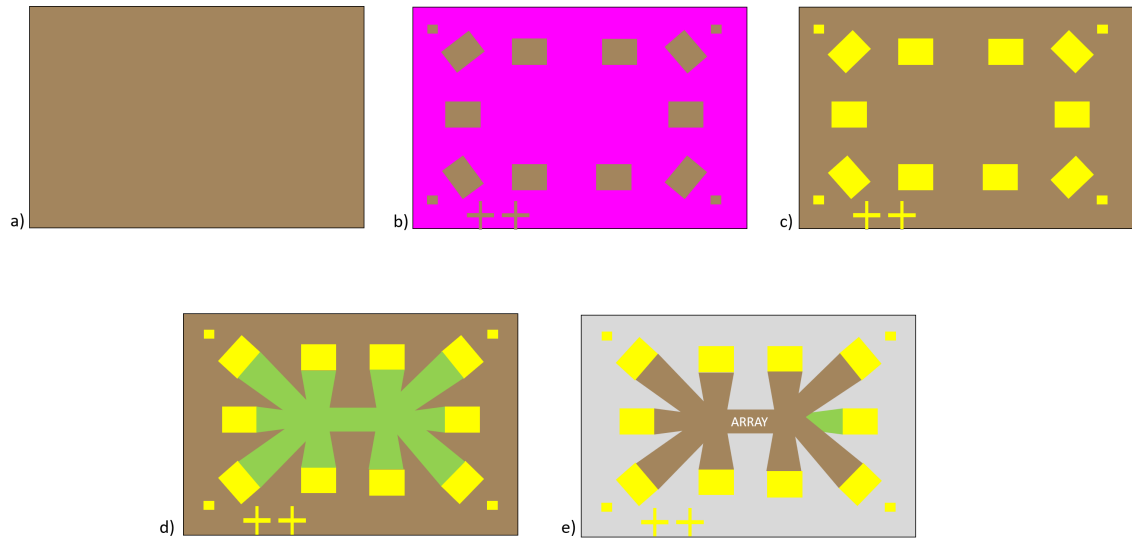


Figure 5.2: Diagram of the SNSPD 8-pixels structure fabrication steps. a)-c) Metalization step: The surface of the superconducting thin film sample (brown) is first cleaned of impurities via ultrasonic bath of acetone and methanol. Then a bilayer of positive-tone 200k PMMA e-beam resists AR-P 632.12 Anisole and AR-P 649.04 are spun on the sample (violet). Then gold contacts and markers are printed via e-beam process and O-xylene development. Au/Ti (yellow) is then deposited on the material. The lift-off process removes gold parts onto the resist. d) Nanostructure design step: positive-tone ZEP520 resist is spun onto the device and after the e-beam process and the development in O-xylene, waveguides and the array structure (green) are printed. The array structure is observed in detail via SEM analysis [Fig. 5.3]. e) Dry etching: the array structure is defined exposing the device with CF_4 plasma that removes material parts not necessary leaving the substrate (grey). The positive-tone ZEP520 is stripped via acetone.

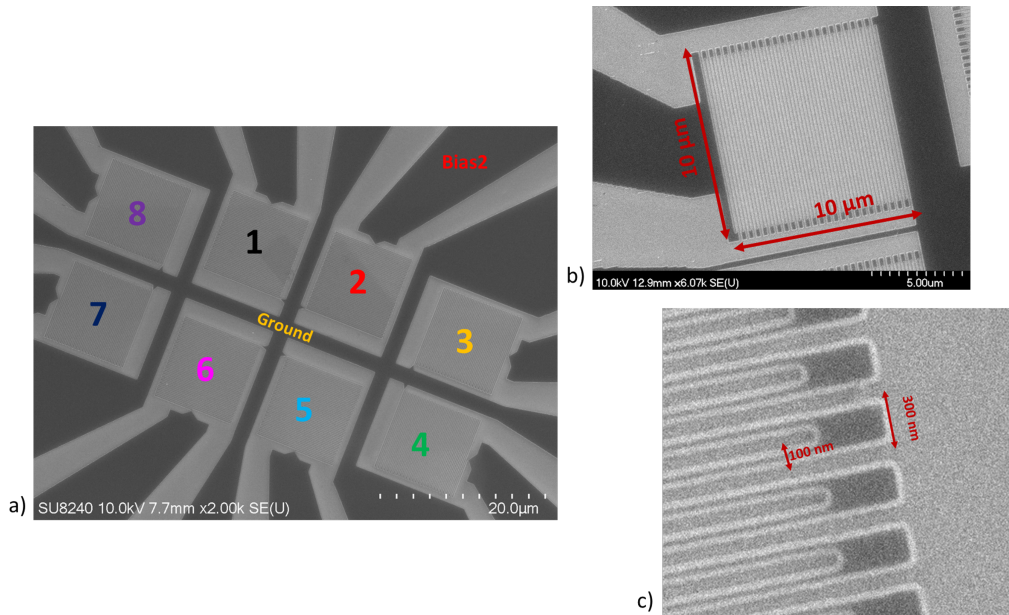


Figure 5.3: SEM images of the SNSPD array realized via 8 nm thickness NbN. a) The system is composed of 8 pixels. b)-c) Each pixel is a meander structure $10 \mu\text{m} \times 10 \mu\text{m}$ square, 100 nm width and 50% filling factor. Each pixel is configured to be biased independently. The ground is in common. Images are taken from scanning electron microscope systems a) SU8200 and b) S4700 both installed in the JWNC. The black zone represents the metal. The clear zone is the e-beam resist ZEP520.

5.2 Sample Mount and Fibre Alignment

For the fabrication process described before, superconducting thin films have been grown on $10\text{ mm} \times 10\text{ mm}$ square HR Si wafers $675\text{ }\mu\text{m}$ thick. The sample is then diced in $4\text{ mm} \times 4\text{ mm}$ squares to be mounted on a gold-plated oxygen-free high thermal conductivity (OFHC) copper sample mount and then aligned to a SMF28 single mode fibre (manufactured by Thorlabs) for the optical characterization at 1550 nm . In this work, sample mounts and alignment methods are different for each cryostat. As introduced in the chapter 3, the Zephyrator(3.5.1) and the Rankinator cryostat (3.5.2) are used for the characterization of the 8-pixel SNSPD array structure.

5.2.1 Zephyrator mount and alignment

The sample mount to be installed in the Zephyrator is shown in the [Fig.5.4 a)]. In this sample mount there are embedded four sections of high frequency laminated PCB connected by soldering to four SMP connectors. The device is attached on the sample mount by nail varnish and connected to SMP connectors by a Kulicke Soffa 4123 wedge wire bonder with the use of aluminium (Al) wire [Fig.5.4 b)].

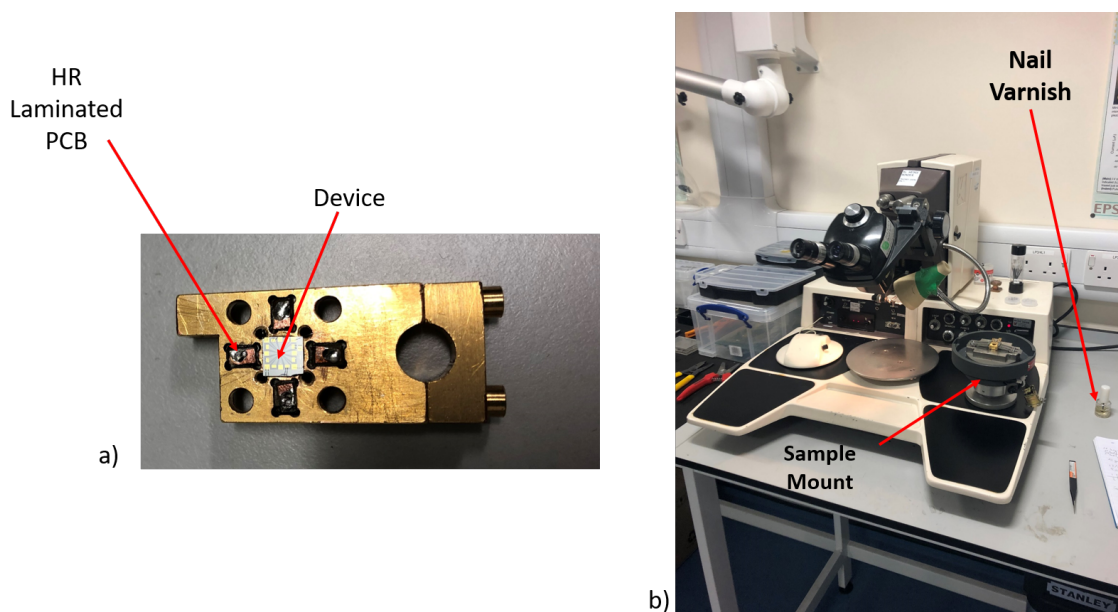


Figure 5.4: a) Gold-plated oxygen-free high thermal conductivity (OFHC) copper sample mount from its frontside. PCBs are connected to SMP connectors by soldering. The device is attached on the sample mount by nail varnish. b) Kulicke Soffa 4123 wedge wire bonder.

For the fibre coupling, an OFHC copper cap is installed onto the front side of the sample mount. The zirconia ferrule of the fibre pass in the middle of the cap and it is kept hold by a clamp screwed on the cap[Fig.5.5]. The optical alignment is achieved manually by the use of thin ($25\text{ }\mu\text{m}$ minimum shim thickness) steel shims and by of a confocal microscope integrated with an infrared InGaAs camera(X-Y axis). Steel shims control the distance of the ferrule from the device (Z-axis). In this work, the position Z of the fibre has been chosen to illuminate the entire area of the SNSPD array, then to cover all 8-pixels of the system. For this, a series of shims with a total of $900\text{ }\mu\text{m}$ thickness, have been installed in the OFHC cap.

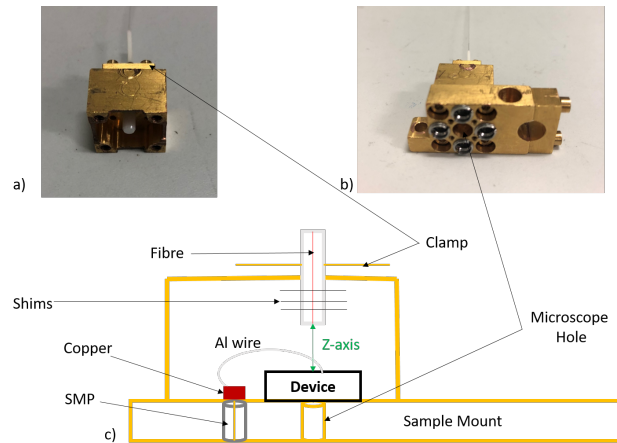


Figure 5.5: a) OFHC copper cap for optical coupling. b) Complete sample mount with optical coupling and c) its scheme. The fibre ferrule is inserted in the middle of the cap and kept hold by a clamp screwed on the top. The distance of the fibre from the device (Z-axis) is controlled by the use of thin steel shims.

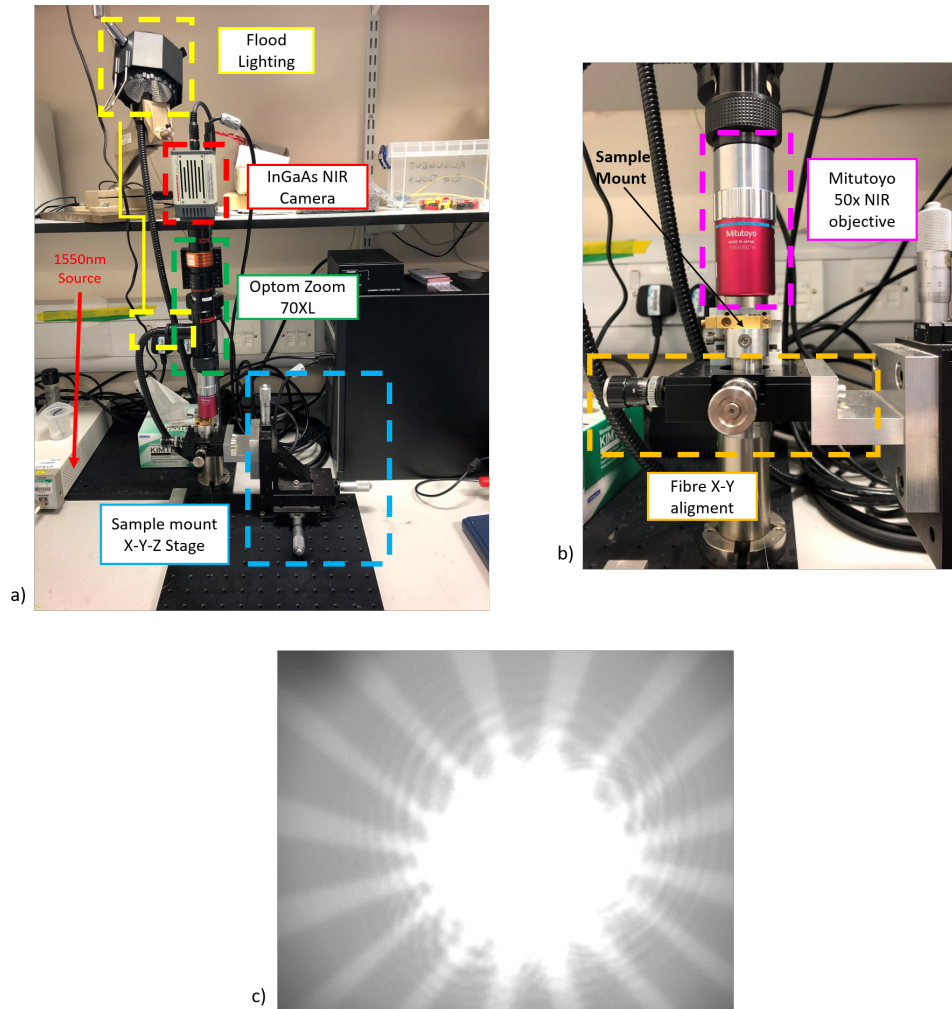


Figure 5.6: Set-up for the fibre alignment. a) The system is composed of a microscope integrated by a NIR InGaAs camera. A halogen lamp is needed to flood illuminate the sample. b) The sample mount is attached in the X-Y stage from the backside. c) Alignment of the optical fibre as observed by the NIR InGaAs camera. To cover entirely the area of the 8-pixels structure, the power output of a 1550 nm laser diode has been stabilized at $10 \mu\text{W}$.

The sample mount is then attached on the X-Y stage of the fibre alignment set-up[Fig.5.6]. The copper cap is loosened to move the fibre independent from the sample mount. The fibre is spliced to a 1550nm CW laser source. Turning on the laser, the device is viewed through the back side of the substrate by a microscope with an integrated camera near infrared (NIR) InGaAs. The distance between the ferrule and the device is measured through an optical coherence tomography (OCT) system. Basically, OCT is based on low-coherence interferometry[189]. It consists of splitting a low coherence light source in two beam paths: one path leads to the sample and one to a reference mirror. The two light beams reflect and interfere. The interference pattern contains information on the path length difference. The Fig.5.7 shows the OCT system used to measure the distance of the zirconia ferrule and fibre tip from the SNSPD.

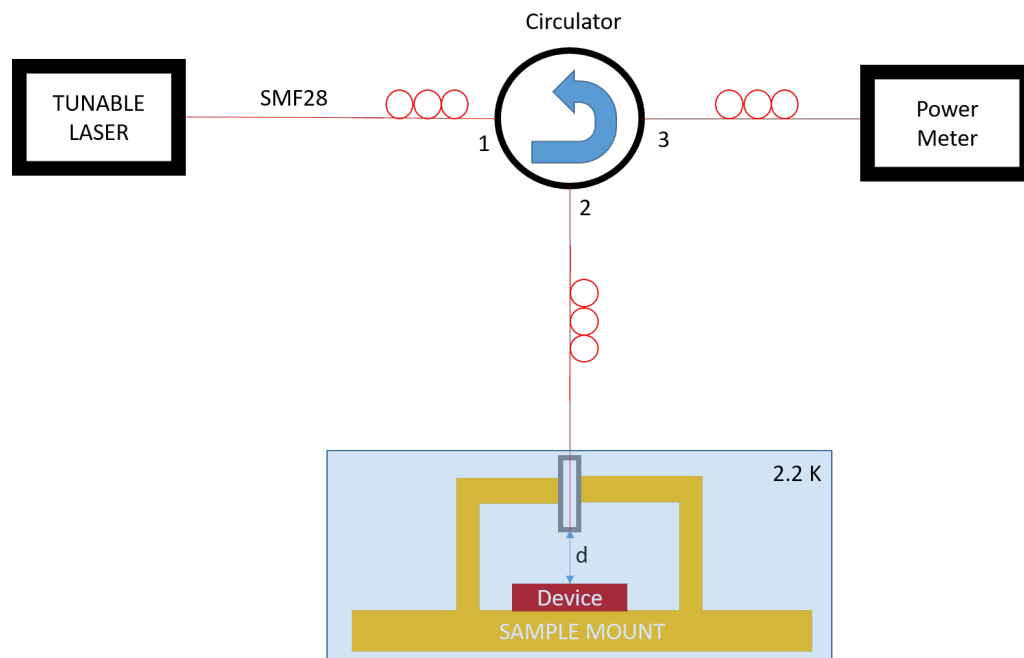


Figure 5.7: Optical coherence tomography set-up used to measure the distance d between the device and the fibre ferrule. In this work, the distance d is measured when the system is cooled down.

The system consist of a tunable laser source connected to the device and to a power meter by a circulator. In this system, the end of the fibre ferrule acts as a weak mirror: the path beam leads to the sample from the port 1 to the port 2 of the circulator. Reflected beams (one from the device and the other from the ferrule) back to the circulator and come out from the port 3 to the power meter. As a result, the path length difference information is contained in the interference spectrum of the average power fibre[Fig.5.8 a)]. A Fourier transform of this data, written by a Matlab program, returns the relative distance between the ferrule and the device[Fig.5.8 b)]. In this work, the distance has been measured when the sample was in the cryosystem, because during cooldown, the Z-axis is altered due to partial shrinkage of the sample mount and the fibre ferrule comes closer to the sample surface. At 2.2 K, the separation between the fibre end and the device measured is about $178 \mu\text{m}$.

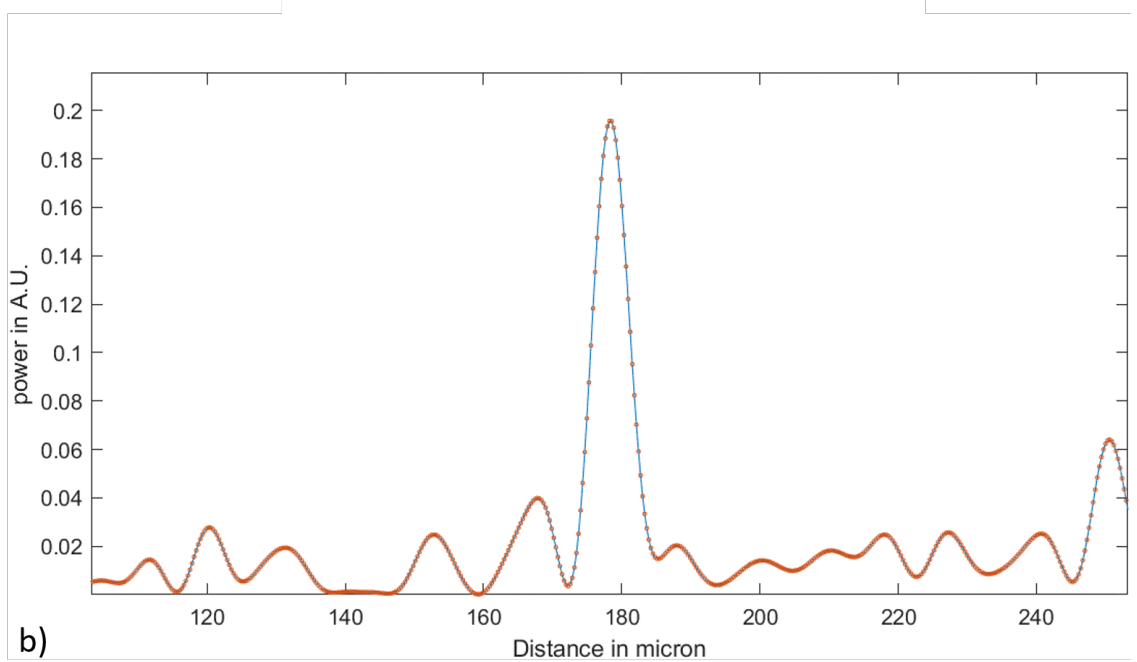
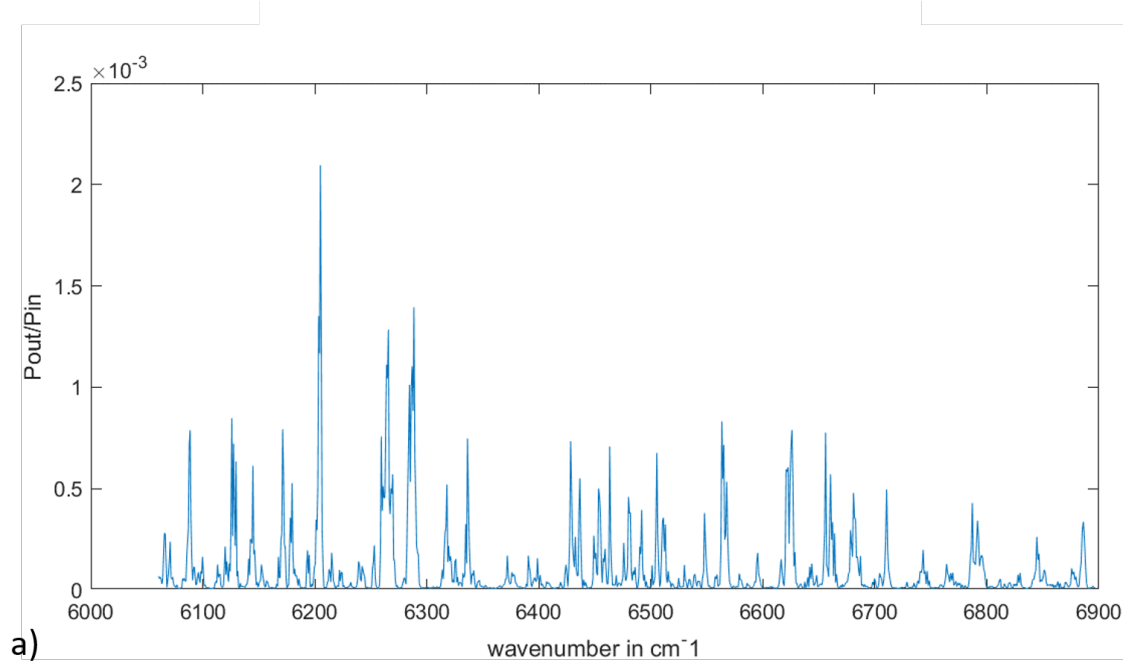


Figure 5.8: a) Average power fibre interference spectrum and its b) Fast Fourier Transform (FFT) processed result obtained by a Matlab program. The separation distance between the chip surface and the fibre ferrule is approximately $178 \mu\text{m}$ when the device is cooled to 2.2 K.

The Gaussian model of the laser beam is useful to evaluate the optical coupling efficiency of the device. A Gaussian beam is determined by two properties: its central intensity at the beam waist I_0 and by its width $w(z)$. The intensity distribution is given as[84]

$$I(x, y, z) = I_0 \left(\frac{w_0}{w(z)} \right)^2 \exp\left(-\frac{2(x^2 + y^2)}{w(z)^2} \right) \quad (5.1)$$

where z is the position along the optical axis, $x^2 + y^2$ is the distance perpendicular to z (expressed in cartesian coordinates) and $w(z)$ is the beam radius[Fig.5.9] gives as

$$w(z) = w_0 \sqrt{1 + \left(\frac{z}{z_0} \right)^2} \quad z_0 = \frac{\pi w_0^2}{\lambda} \quad (5.2)$$

where w_0 is the beam width at at Rayleigh length z_0 .

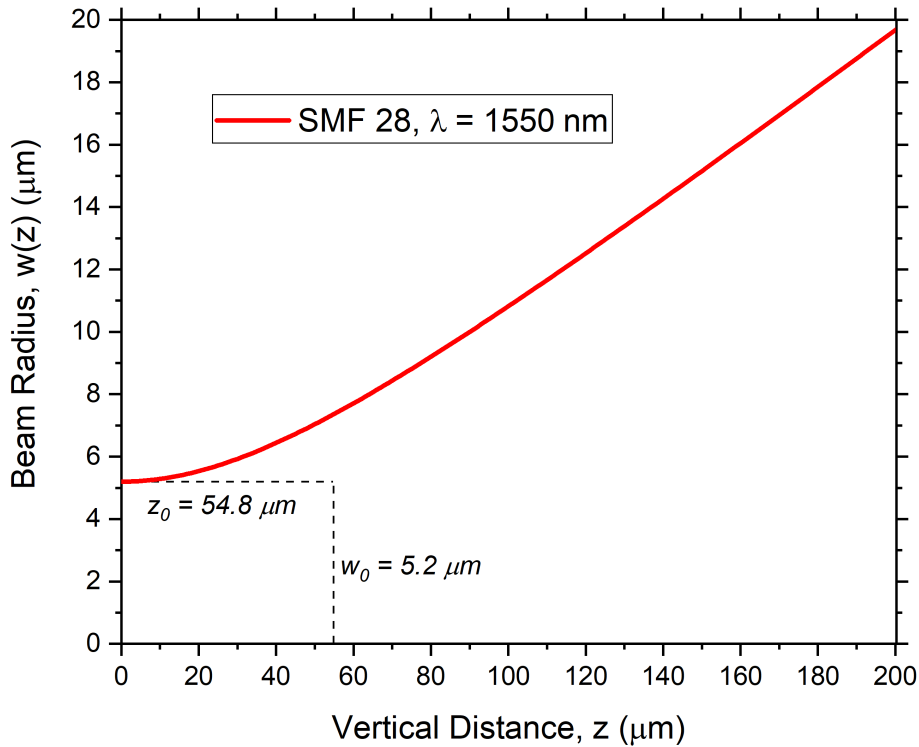


Figure 5.9: Graphical representation of eq.5.2 for the optical fibre SMF28, showing the initial beam width, $w_0 = 5.25\mu m$ and the Rayleigh length, $z_0 = 54.8\mu m$, for light with $\lambda = 1.55\mu m$.

In according to SMF28 datasheet[190], $w_0 = 5.2\mu m$ is the half of the mode-field diameter for $\lambda = 1.55\mu m$ wavelength, so the Rayleigh length $z_0 = 54.8\mu m$. At the distance of $z = 178\mu m$ the beam width is $w(z) = 17.7\mu m$, corresponding to a diameter beam of about $36\mu m$. Since the total area of the 8-pixels structure is a rectangle[Fig.5.1] of dimensions $x = 56.4\mu m$ and $y = 30\mu m$, then its diagonal is greater of the diameter beam, so at the distance of $z = 178\mu m$, the laser beam does not cover the entire area of the 8-pixels structure[Fig.5.10].

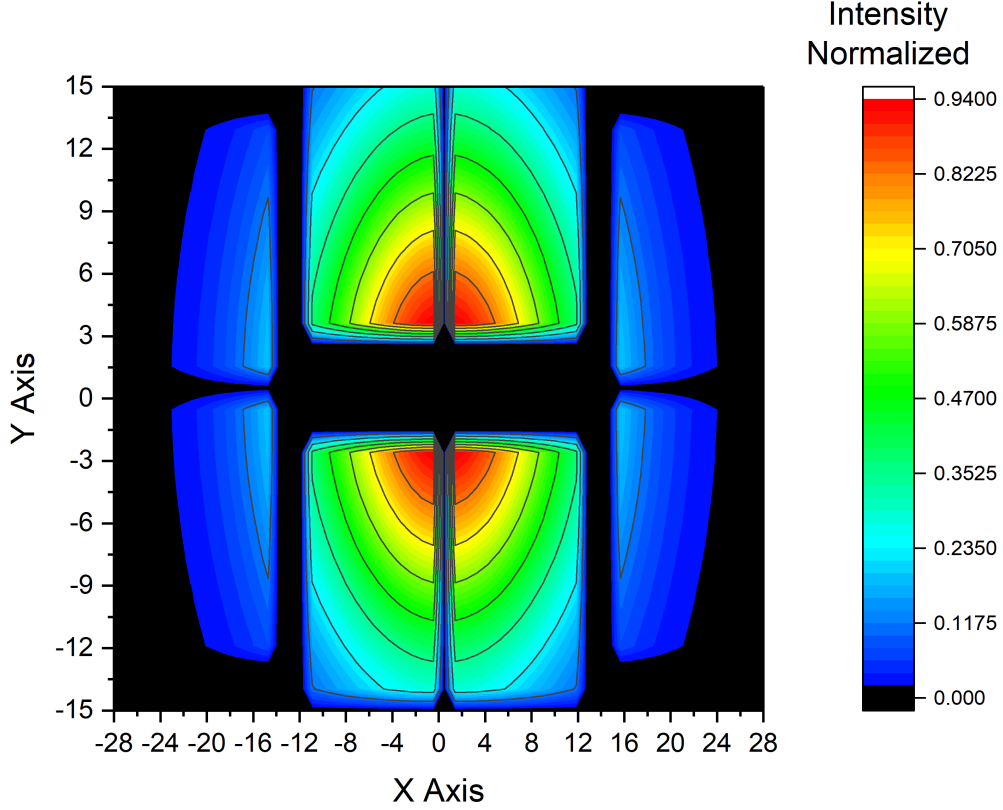


Figure 5.10: Map of the normalized intensity distribution of the coupling efficiency along the 8-pixels structure when the device is $178 \mu\text{m}$ far from the optical fibre. In this map, the intensity has been calculated only in the region of pixels, while external region are considered zero intensity. The position of pixels is fixed as designed in the .gds file[Fig.5.1]. Assuming precise alignment of the fibre axis on the centre of the SNSPD array structure, when the fibre is $178 \mu\text{m}$ far from the device, the beam covers mainly pixels in the middle (1, 2, 5 and 6).

Integrating the equation (5.1) over the area A of the detector we can obtain the power

$$P(z) = \int dA I(x, y, z) = I_0 \left(\frac{w_0}{w(z)} \right)^2 \int_{x_1}^{x_2} dx \int_{y_1}^{y_2} dy e^{-\frac{2(x^2+y^2)}{w(z)^2}} \quad (5.3)$$

Since the integral is Gaussian, we can also use the error function[191]

$$\text{erf} \left[\frac{\sqrt{2}}{w(z)} x \right]_{x_1}^{x_2} = \frac{2\sqrt{2}}{\sqrt{\pi}w(z)} \int_{x_1}^{x_2} dx e^{-a^2 x^2} \quad (5.4)$$

and write the equation (5.3) as:

$$P(z) = I_0 \frac{\pi w_0^2}{8} \left[\text{erf} \left(\frac{\sqrt{2}}{w(z)} x \right) \right]_{x_1}^{x_2} \left[\text{erf} \left(\frac{\sqrt{2}}{w(z)} y \right) \right]_{y_1}^{y_2} \quad (5.5)$$

To calculate the total power P_0 in the beam, we have to integrate over the whole area:

$$P_0 = I_0 \frac{\pi w_0^2}{8} \left[\text{erf} \left(\frac{\sqrt{2}}{w(z)} x \right) \right]_{-\infty}^{\infty} \left[\text{erf} \left(\frac{\sqrt{2}}{w(z)} y \right) \right]_{-\infty}^{\infty} = I_0 \frac{\pi w_0^2}{2} \quad (5.6)$$

In general[85] the coupling efficiency η_{coup} of a detector can be expressed as the ratio between the power $P(z)$ hitting the detector with the total power P_0 .

$$\eta_{coup}(z) = \frac{P(z)}{P_0} = \frac{1}{4} \left[\operatorname{erf} \left(\frac{\sqrt{2}}{w(z)} x \right) \right]_{x_1}^{x_2} \left[\operatorname{erf} \left(\frac{\sqrt{2}}{w(z)} y \right) \right]_{y_1}^{y_2} \quad (5.7)$$

The equation (5.7) is the coupling efficiency dependent by the distance z of the optical fibre from the detector. As shown in the [Fig.5.10] pixels do not cover the entire rectangle, so to measure the coupling efficiency of each pixels, we can assume the centre of the rectangle as the origin of axis ($x = y = 0$) and then find coordinates of each pixels[Fig.5.11].

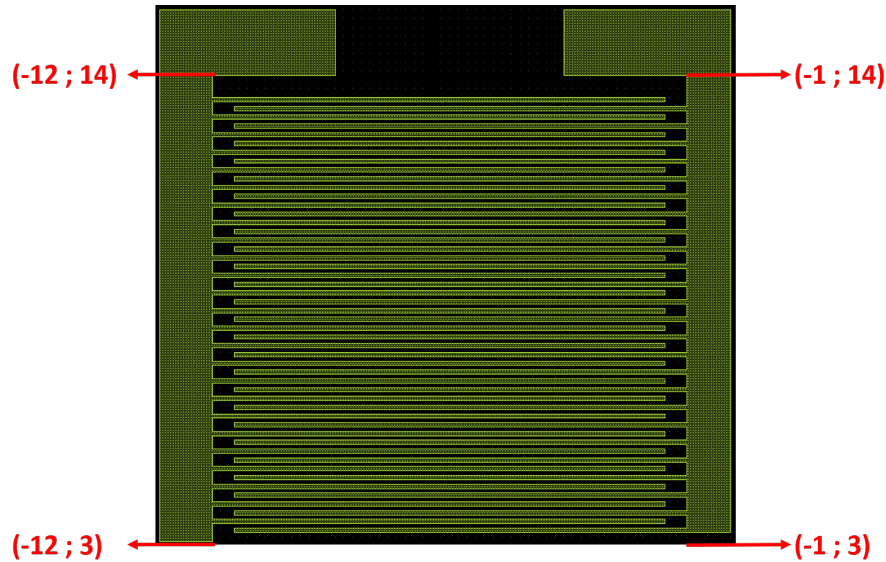
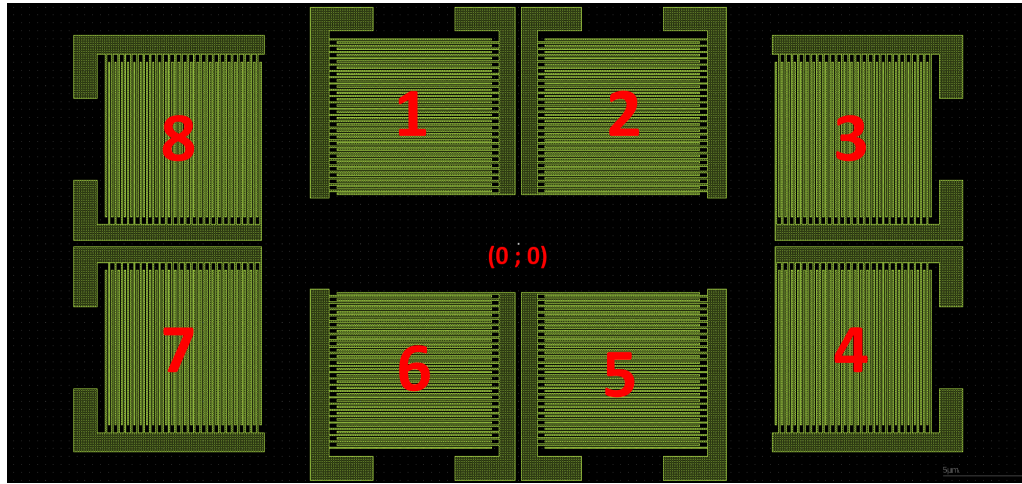


Figure 5.11: Upper: image of the .gds file representing the 8-pixels structure composed by 8 meander structure $10\mu m \times 10\mu m$ dimensions. By the software is possible to estimate coordinates of each point of the structure. In this case the origin ($x = y = 0$) is settled in the middle of the rectangle. Down: in this configuration, coordinates of the pixel 1 are respectively $x_1 = -1$, $x_2 = -12$, $y_1 = -3$ and $y_2 = 14$. These coordinates are taken from the beginning to the end of the meander structure (the black region is the nanowire). Coordinates of other pixels have been taken in the same way.

Once coordinates x_1 , x_2 , y_1 and y_2 are found, we can plot the equation (5.7) for each pixels[Fig.5.12]. Since the structure is symmetrical, the coupling efficiency of pixels 1, 2, 5 and 6 is the same. In the same way, the coupling efficiency curve of pixels 3, 4, 7 and 8 is the same.

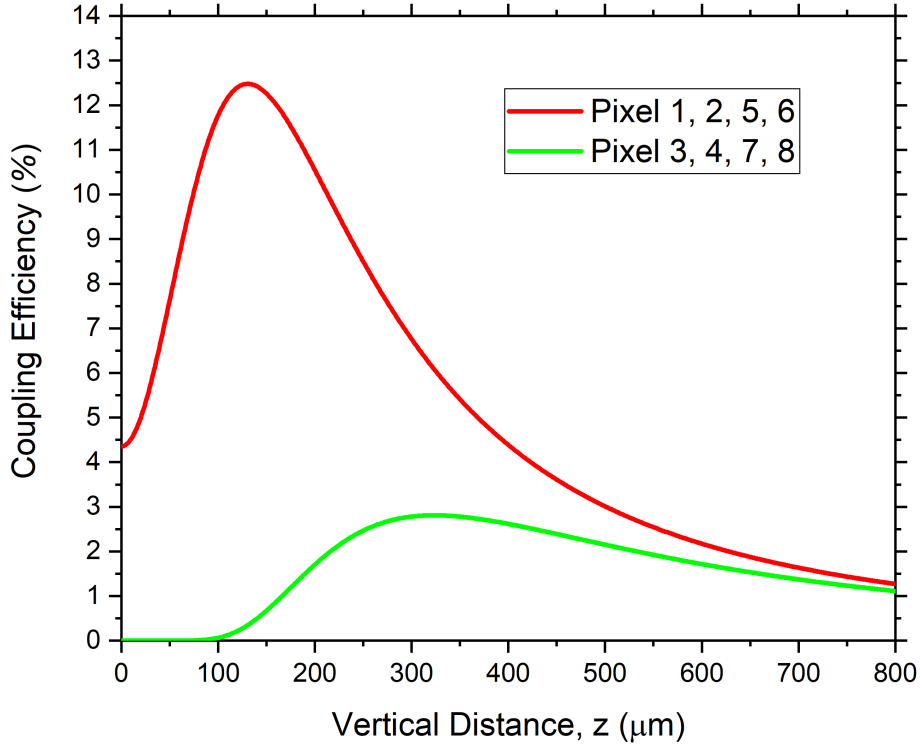


Figure 5.12: Calculated ratio of optical power plotted as a function of vertical distance z between the end of the fibre to the device.

The coupling efficiency reaches its maximum value when the fibre is settled far from the device. For short distance, the beam diameter is small and it can not cover pixels. Enhancing the distance, the beam diameter enhances covering pixels of the structure and so the power coupling $P(z)$ is increased. At the same time, increasing the distance of the fibre from the device, the efficiency tends to decrease as $P(z)$ decreases. In conclusion, the structure realized does not permit a good uniformity of the coupling efficiency. As expected from [Fig.5.10], the coupling efficiency of pixels 3, 4, 7 and 8 is smaller than other pixels since they are placed far from the beam spot origin[Fig.5.10]. At 2.2 K, the distance $z = 178\mu\text{m}$ corresponding to a coupling efficiency of about 11.42% for pixels 1, 2, 5 and 6 (pixels in the middle) and a coupling efficiency of about 1.25% for pixels 3, 4, 7 and 8 (external pixels). At last, the aligned packaged device is then mounted on the cold head of the Zephyrator, fibre spliced to SMF28 optical fibre feedthrough, electrically connected and cooled-down at 2.2 K.

5.2.2 Rankinator mount and alignment

In the Rankinator, optical measurements are done by the bespoke machined confocal microscope. The device is first installed on a larger sample mount and connected electrically to four SMP connections by wirebonding[Fig.5.13].

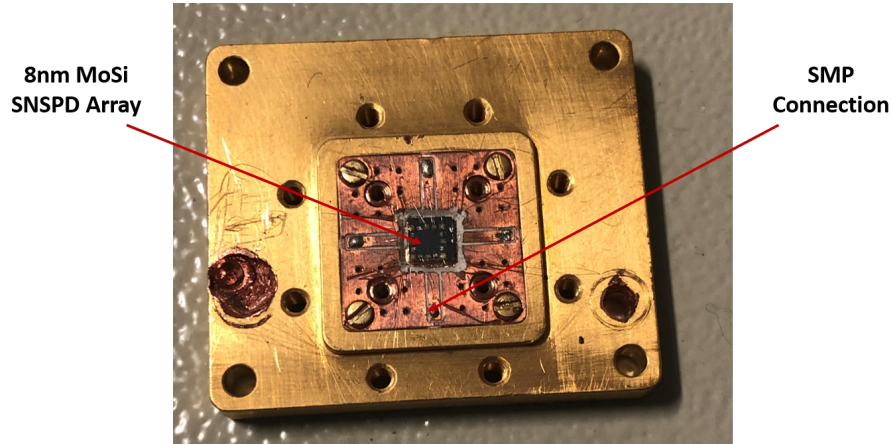


Figure 5.13: a) Sample mount made to be attached under the microscope under ^3He coldhead of the Rankinator

The sample mount is then attached to the ^3He stage under the microscope. Light delivered from the single-mode fibre is firstly collimated by a Geltech 352280-C lens and focused by a Geltech 352330-C to the device[Fig.5.14].

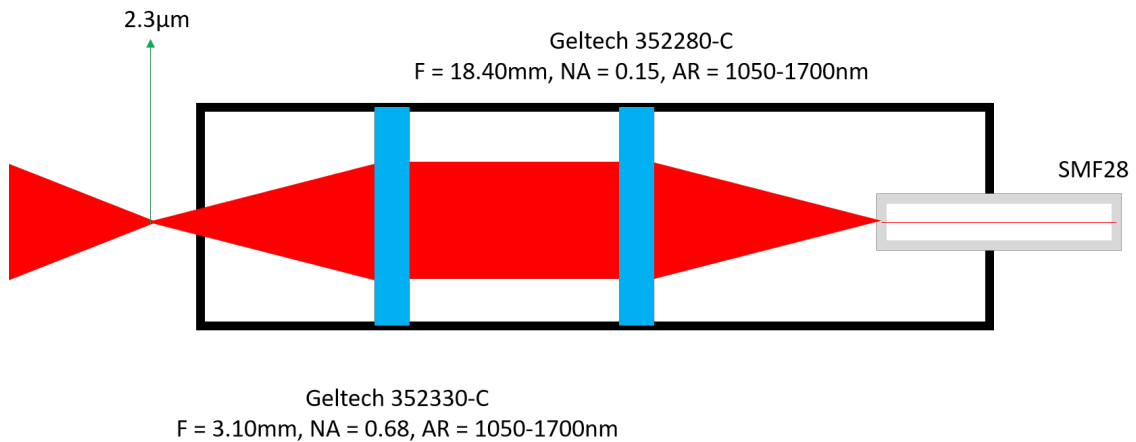


Figure 5.14: Cross section of the microscope lens set-up. Laser beam comes out from the optical fibre(right hand side), it is collimated by a Geltech 352280-C lens (focus length $F = 18.40$ mm, numerical aperture $NA = 0.15$) and then focused by a Geltech 352330-C lens ($F = 3.10$ mm, $NA = 0.68$). Both these lenses come with an anti-reflection coating (AR) designed for 1050 nm to 1700 nm as reported in their datasheet (Thorlabs website). From Sparrow's criterion, at 1550 nm wavelength, the expected beam waist in at the focus is $1.19 \mu\text{m}$. In the Rankinator setup with vibration damping, the best measured spot size is $2.3 \mu\text{m}$ (left hand side).

The focus spot generated can be calculated applying the Sparrow Criterion[192] if the optical instrument is only affected by diffraction. The criterion explains that two spots are still discernable if the combination of their functions creates a flat peak[Fig.5.15].

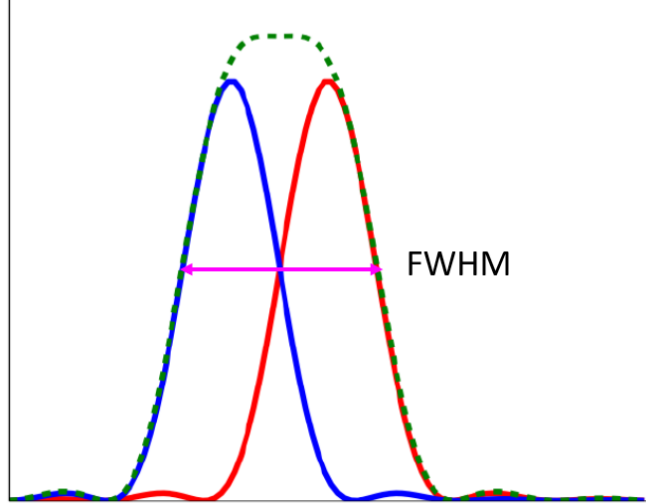


Figure 5.15: Sparrow criterion. Using the focusing lens with $NA = 0.68$, the minimum resolvable FWHM for 1550nm light is $1.19 \mu\text{m}$, but internal vibrations of the cryosystem generate a spot size of about $2.3 \mu\text{m}$ [168].

The FWHM of the total Gaussian shape is the focus spot of the light when comes out from the focus lens.

$$FWHM = 0.52\lambda/NA \quad (5.8)$$

where $NA = 0.68$ is the numerical aperture of the lens Geltech 352330-C. For $\lambda = 1550 \text{ nm}$, the focus spot is $FWHM = 1.19 \mu\text{m}$. This results represents the minimal resolution of the microscope. Due pulse tube vibration, laser spot size measured is $4.3 \mu\text{m}$ for the standard setup. Adding additional damping support underneath the outer shielding to reduced internal vibrations a better spot size of $2.3 \mu\text{m}$ is achieved. The alignment of the optical fibre installed on the top of the microscope, is carried out by X-Y-Z stepper motors by the ANC300 controller (section 3.5.2). First a reflection map of the device under test is created to find and illuminate the 8-pixels region. A light source (S5FC1550P-A2, 1550 nm) is connected through a fibre circulator (at room temperature) and then via a break out box and hermetic feed-through into the cryostat is connected to the miniature confocal microscope setup. Light is reflected from the device and guided through the focusing lens to the optical fibre and into the circulator located outside the cryostat and collected by an InGaAs fast photodiode. Based on the measured reflectance of the substrate, is possible to work out regions with different reflection[Fig.5.16]. This measurement is done at 5K (the base temperature of the pulse tube cooler without the ^3He stage activated) in order to avoid heating during the extended scanning of the piezoelectric motors. Once the device is mapped, a single-photon detector photoresponse mapping can be done disconnecting the photodiode and the circulator e connecting the laser source (connected to a pulse generator) to the device via a series of attenuators. The device is then biased and optical signal are measured by a counter as shown in [Fig.3.32] of section 3.5.1. In this configuration, the z -axis of the laser beam is not fixed as in the previous sample mount of the Zephyrator[Fig.5.5], so we can obtain the maximum coupling efficiency[102] of a SNSPD designed as a meander structure covering $10 \mu\text{m} \times 10 \mu\text{m}$ area using the equation (5.7) and assuming the active area of the SNSPD to be a square of width $l = 10\mu\text{m}$, centred at $x = y = 0$.

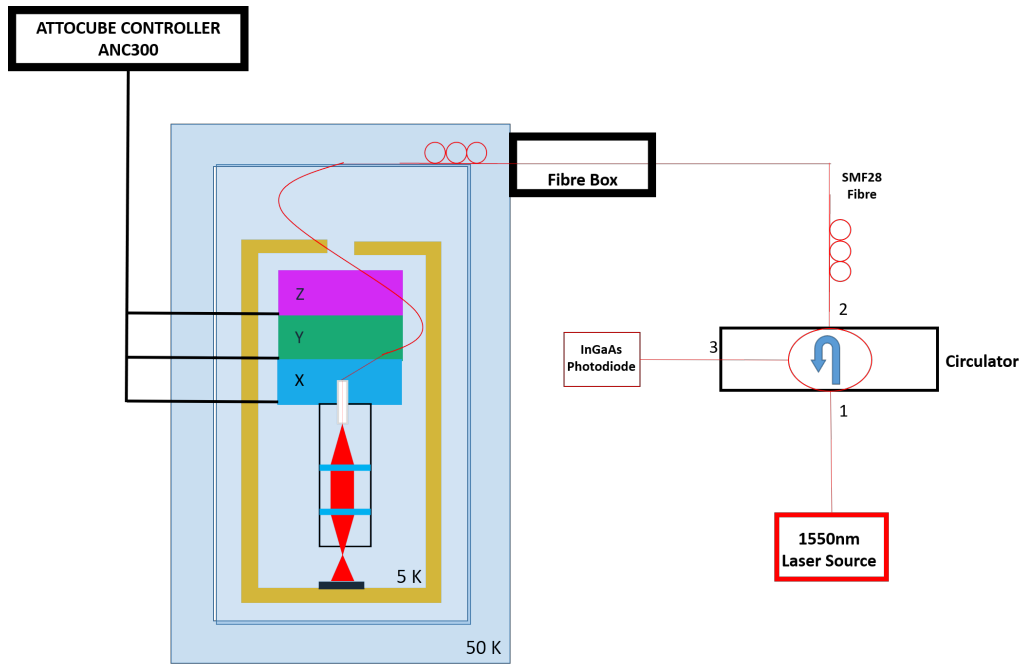


Figure 5.16: Experimental set-up to build a reflection map of the device under test in the Rankinator at 5 K to avoid heating of piezoelectric motors.

The graph [Fig.5.17] indicate a 90% coupling efficiency, when the distance z between fibre and the device is less than $30 \mu\text{m}$.

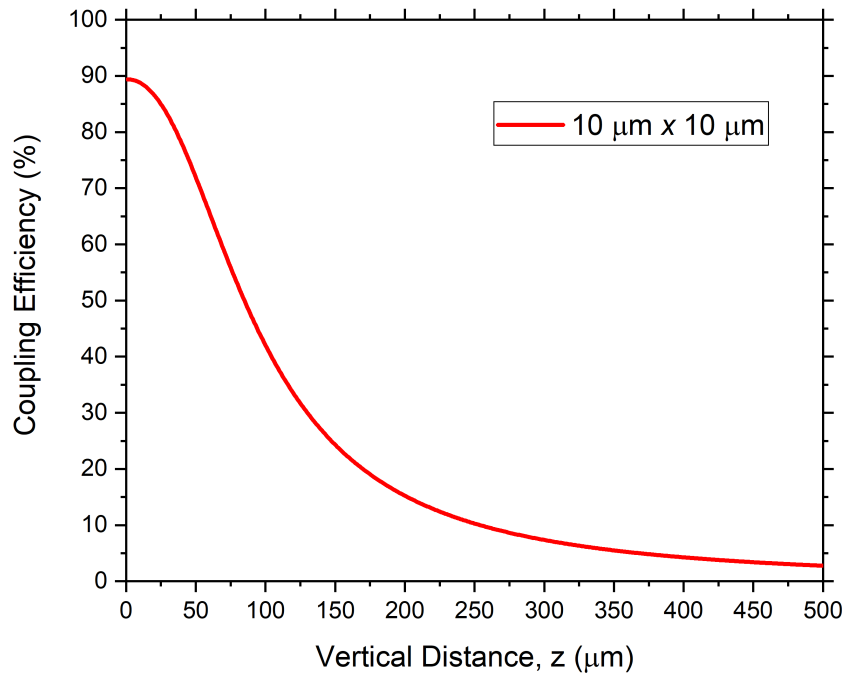


Figure 5.17: Coupling efficiency into $10 \mu\text{m} \times 10 \mu\text{m}$ SNSPD device plotted as a function of distance between the fibre end and the device in the Rankinator cryostat. The coupling efficiency is calculated by equation(5.7).

5.3 Low Temperature Electrical and Optical Characterization

Once devices are electrically connected and optically aligned, they are ready to be installed in cryocoolers. Since sample mounts are provided only of four SMP connections, the characterization of all 8 pixels requires two separate cooldowns.

5.3.1 NbN Array

The 8-pixels structure made via NbN have been tested in the Zephyrator. In the first cooldown odd numbered pixels (1, 3, 5, 7) have been connected electrically to SMP connectors, then device is optical aligned by the fibre alignment set-up[Fig.5.6] and then installed in the cryostat. To characterize even numbered pixels (2, 4, 6, 8), the device is removed from the cryostat (when it is at room temperature), the optical cap in unmounted[Fig.5.6 a)] to connect electrically the pixels to SMP connectors. Then the device is aligned again and cooled down in the cryocooler. The SMF has never been removed from the top of the cap[Fig.5.6 a)] keeping the distance $z = 178 \mu\text{m}$ at 2.2 K. Once the Zephyrator reached its base temperature (2.2 K), the first step of the characterization is to measure the critical current of pixels. The device is biased by an isolated voltage source V_s with a load resistor in series $R_L = 100k\Omega$. Biasing the device from the positive range to the negative range, a typical IV characteristic of a superconductor is achieved. The x-axis is the voltage drop of the device measured by the voltmeter, while the y-axis is the current inside the device $I = V_s/(R_L + R_s)$, where R_s is the resistance of the device[Fig.5.18].

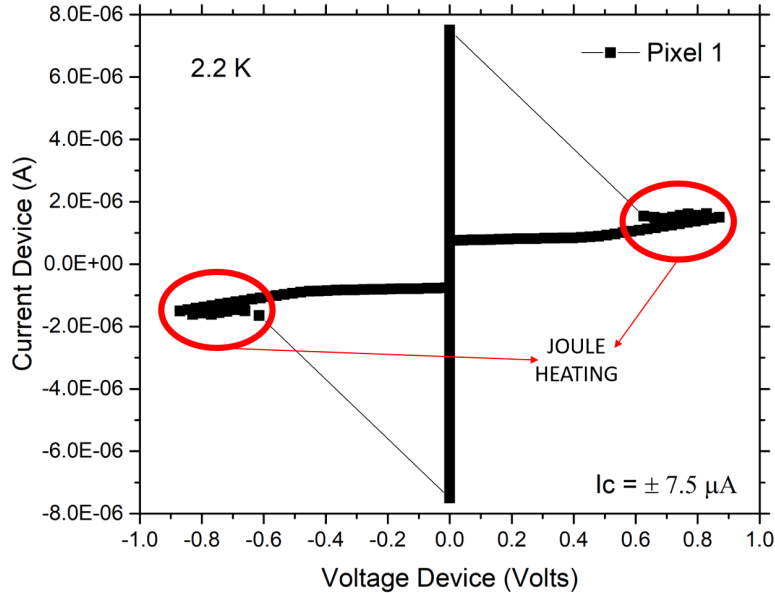


Figure 5.18: IV characteristic at 2.2 K of the pixel 1 of the SNSPD array structure made via 8nm-thick NbN grown on a HR Si substrate at room temperature. Due to the large normal state resistance, the current across the superconducting nanowire drops when it switches into the resistive state. Large normal state resistance produces large Joule heating generating hysteresis in the plot (red circle).

In this way, critical currents of the 8-pixel SNSPD array structure made via NbN have been measured. In the Zephyrator cryostat have been tested two NbN SNSPD deposited onto the HR silicon substrate: the first heating the substrate at 800 °C during the sputtering process, and the second keeping the substrate at room temperature (RT) during the sputtering process(as discussed in chapter4).

NbN onto Si 800 °C

In the first cooldown, pixels 1, 3, 5 and 7 have been bounded onto the sample mount of the Zephyrator cryostat[Fig.5.4]. As first step, critical currents of each pixel has been measured. The [Fig.5.19] shows the histogram of critical currents of pixel 1, 3, 5 and 7 of NbN device grown heating the Si substrate to 800 °C.

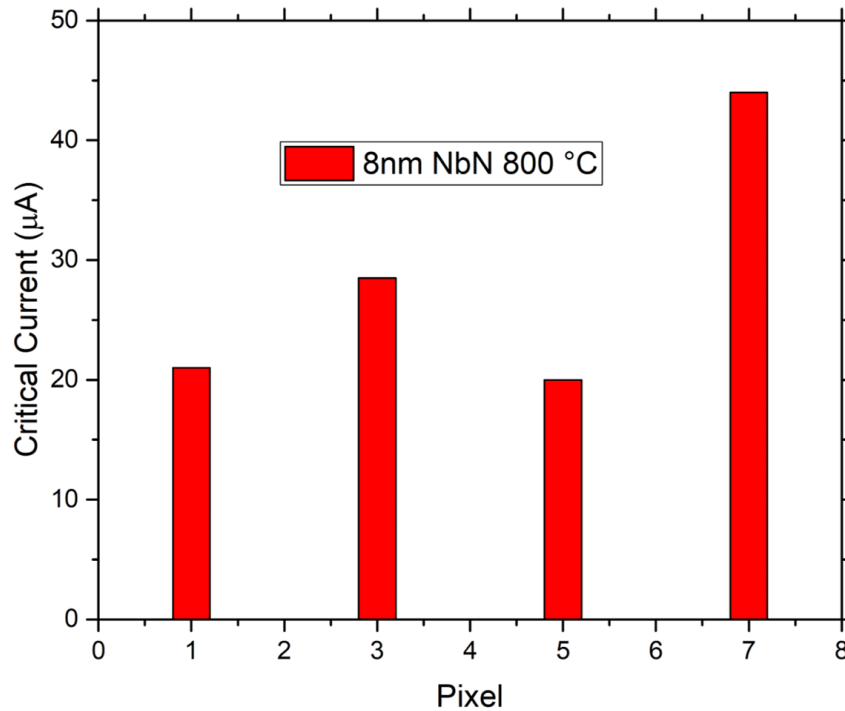


Figure 5.19: Histogram of critical currents measured at 2.2 K of 8 nm thickness NbN SNSPD 8-pixels array grown heating HR Si substrate to 800 °C.

For this device, pixels 1, 3, 5 and 7 exhibit respectively 21 μA , 28.5 μA , 20 μA and 44 μA critical current. For these pixels the mean and standard deviation are respectively $I_c^{mean} = 28.4 \mu\text{A}$ and $\sigma = 11.1 \mu\text{A}$. This device then presents a large discrepancy in term of critical current. Since the critical current is a geometric parameter, the critical temperature has been measured to test the uniformity of the device in term of its superconducting properties because as the critical temperature is does not depends by the geometric structure of the device. The critical temperature of each pixels has been measured as explained in section 3.5.1: the device is biased with a low bias current (typically 10 nA for these devices) and recording the voltage drop (converted in resistance by Ohm's law) at different temperature starting from 2.2 K when the device is cold. Turning off the helium compressor, the cryocooler starts its warming up phase.

Recording the resistance and the temperature, we achieve the R-T plot of each pixels[Fig.5.20].

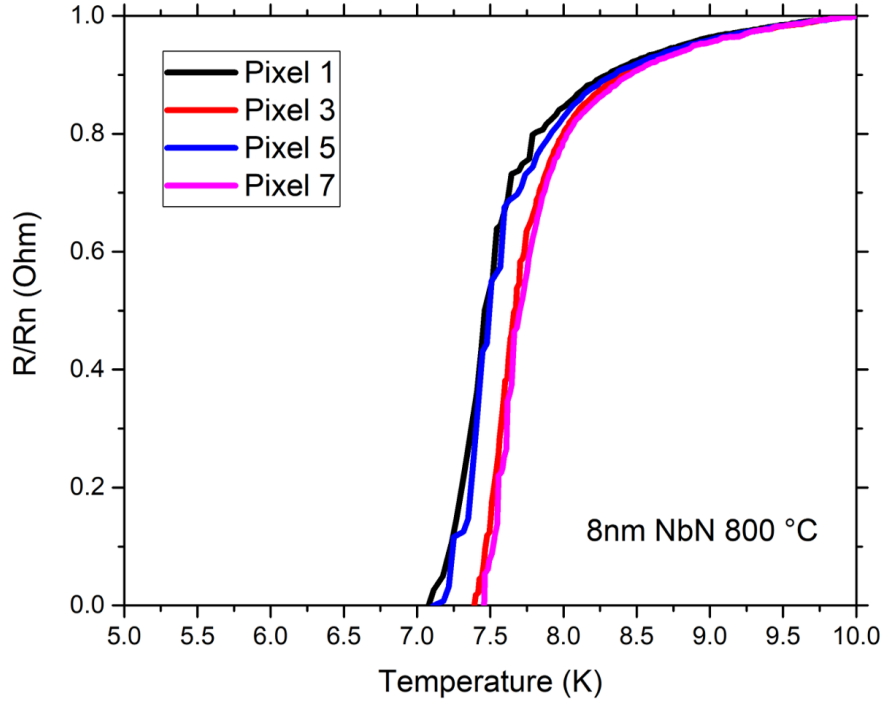


Figure 5.20: Normalised resistance versus temperature of odd numbered pixels of the 8nm thickness NbN SNSPD array grown heating HR Si substrate at 800 °C. The resistance of pixels is normalized respect to normal resistance R_n measured at 10 K.

Testing critical temperatures, of the NbN device grown on the heated substrate, the spread in the critical temperatures is shorter than the spread in critical currents ($T_c^{mean} = 7.4$ K, standard deviation $\sigma = 0.11$ K). We can conclude that intrinsic superconducting properties of this SNSPD are preserved because of the less spread of critical temperatures, while the large spread of critical currents is an evident sign that the device can be not uniform geometrically due probably to proximity effect lithography process. Due to large spread of critical currents for these pixels, the NbN device grown heating the substrate to 800 °C has not been studied further.

NbN onto Si room temperature

In the same way of before, critical currents and critical temperatures of the 8-pixels SNSPD made via 8 nm thickness NbN grown on HR silicon substrate at room temperature have been measured. The total critical current is defined as the mean value of critical current of each pixels[Fig.5.21] while the standard deviation represents the discrepancy of the mean value. The mean value and the standard deviation of the critical current of this system are respectively $I_c^{mean} = 7.94 \mu A$ and $\sigma = 1.59 \mu A$. The test of critical temperatures for this device[Fig.5.22] exhibit respectively $T_c^{mean} = 4.44$ K and $\sigma = 0.23$ K. Pixel 2 exhibits a normal resistance 10 times lower of other pixels[Fig.5.22].

The lowest value of the normal resistance associated with the highest value of the critical current means that nanowires of the pixel 2 are wider than other pixels due to the proximity effect of the e-beam lithography that can affect dimensions of pixels geometry.

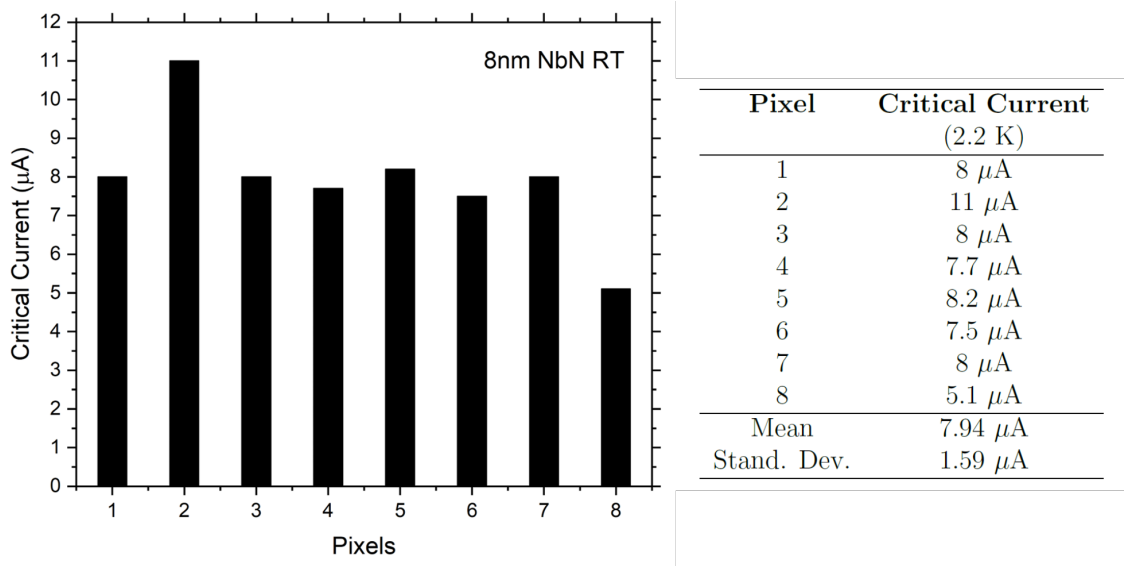


Figure 5.21: Histogram and table of critical currents measured at 2.2 K of all 8-pixels SNSPD array made via 8nm-thick NbN grown on Si substrate at room temperature (RT). The mean value of critical current and the discrepancy for this system are respectively $J_c^{mean} = 7.925 \mu\text{A}$ and $\sigma = 1.0912 \mu\text{A}$.

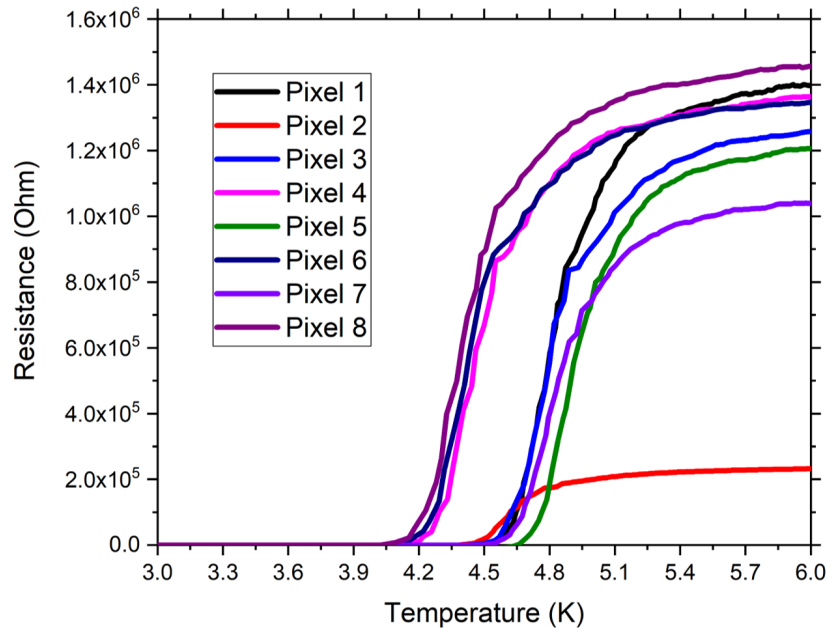


Figure 5.22: RT characteristic of the 8-pixels NbN SNSPD array grown at room temperature. The mean critical temperature is $T_c^{mean} = 4.44 \text{ K}$ and the standard deviation is $\sigma = 0.23 \text{ K}$. Large discrepancies of normal resistances (in particular of pixel 2) can be associated with the proximity effect of the e-beam lithography process that can affect dimensions of pixels.

Since this device exhibits minor discrepancies in terms of critical currents and critical temperatures, it represents a good candidate for the optical characterization at 1550 nm.

The optical characterization of a detector starts from the dark signals. These signals are as dark counts because they represent the signal of the detector when this one is not interacting with photons. This signal can be detected and analysed by the electrical set-up described in the section 3.5.1 [Fig.3.30]. A current bias is applied to the SNSPD pixel via the DC arm of a bias tee. The output pulses from the AC arm of the bias tee are amplified (56 dB total gain) and capture on a high speed (8 GHz bandwidth) oscilloscope. To detect the signal, the trigger of the oscilloscope is settled at 100 mV [Fig.5.23].

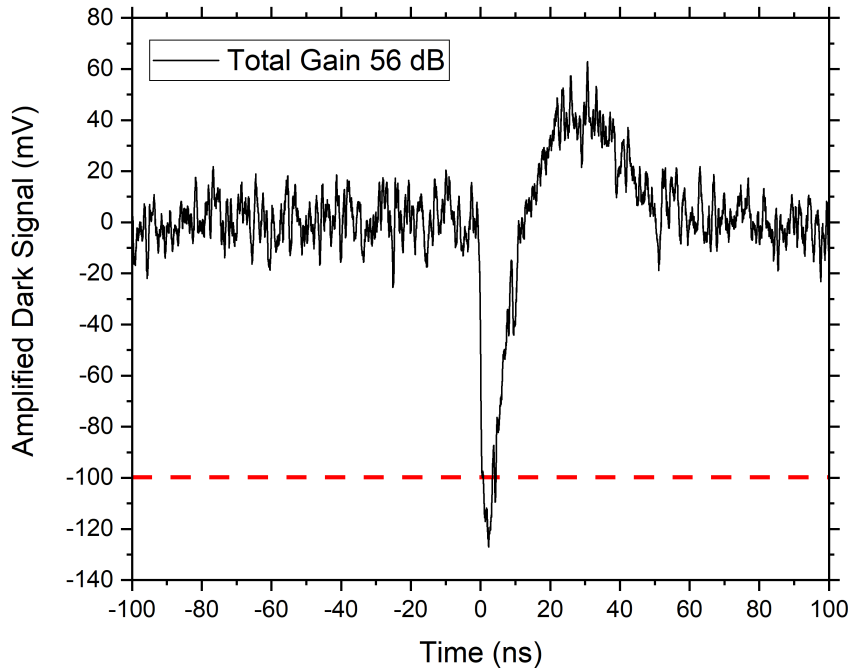


Figure 5.23: Amplified dark signal as measured by the oscilloscope at 2.2 K of the pixel 1 of the SNSPD array structure on 8nm-thick NbN grown on silicon substrate at room temperature. The total gain is 56 dB (amplifier-chain RF Bay Inc. LNA-580 23 dB gain and LNA-1000 33 dB). The pixel 1 is biased near its critical current ($8 \mu A$). The red line represents the trigger (100 mV) of the oscilloscope (8 GHz bandwidth). The peak of the amplified signal is about 127 mV.

The dark signal is an output pulse of the detector. The height of the output pulse is determined by the bias current and amplification gain. In accordance with the RL model introduced in section 2.7, the amplitude of the observed response is simply given by:

$$V_{pulse} = G \cdot I_b \cdot Z_0 \quad (5.9)$$

where $G = 56$ dB is the total gain of amplifiers chain, I_b the bias current flowing through the device and $Z_0 = 50 \Omega$ is the characteristic impedance of an output coaxial line. For the pixel 1 biased $I_b = 0.9 I_c$ with $I_c = 8 \mu A$, the voltage pulse $V_{pulse} = 20.2$ mV against 127 mV showed in the [Fig.5.23] due to the noise background of the measurement setup. In a conventional SSPD readout, when the device is connected directly to the output transmission line, the amplitude and the shape of the detected voltage pulse is simply determined by the bias current I_b and, irrespectively of the actual physics of photoresponse or dark-count mechanism [188].

Thus we expect a dark pulse and a true photon pulse at given bias current to have an identical height and shape, save for the effects of random electrical noise.

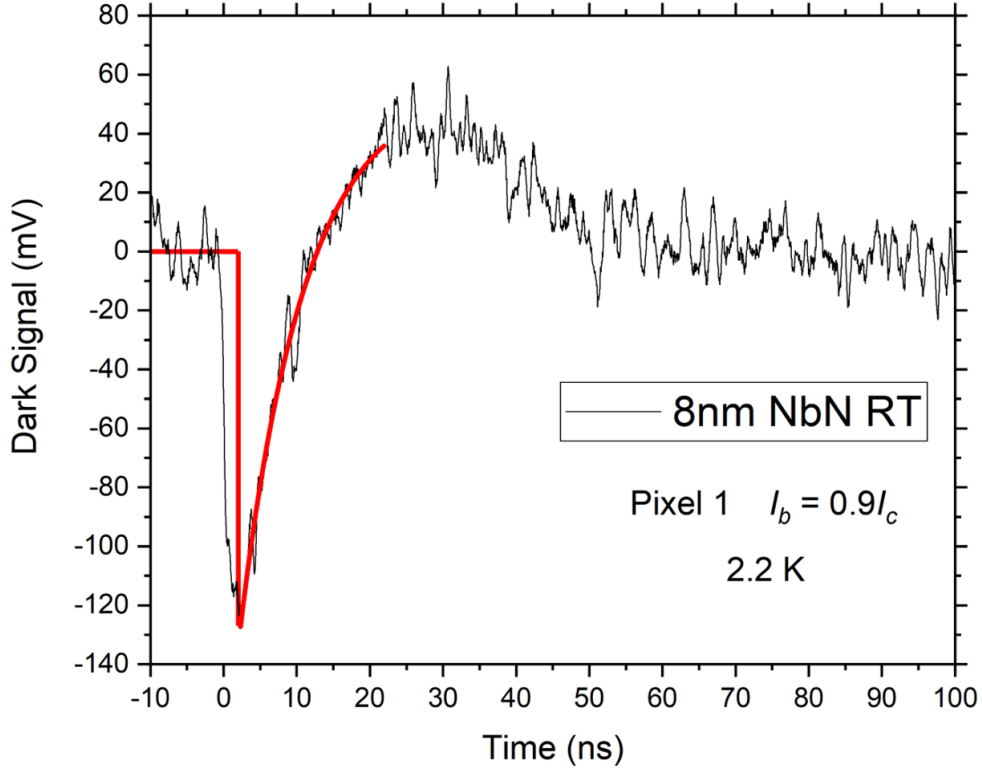


Figure 5.24: Enlargement plot of the dark signal (no amplified). The red line is the fitting equation 5.10. The rest time extracted from the fit is about $\tau = 9ns$. Negative voltages (below 0 V) is because the amplifier chain has a poor low frequency response (10 - 580 MHz for LNA-580 and 10 - 1000 MHz for LNA-1000). The amplifier chain acts as a high pass filter.

The dark signal can provide information about the reset time of the signal[Fig.5.24] fitting the output pulse with the equation[187]:

$$y = y_0 + Ae^{-\frac{t}{\tau}} \quad (5.10)$$

where y_0 is the offset of the pulse, A is the amplitude, t the time and τ is the reset time. , the reset time gives information about the kinetic inductance of the device. The pixel 1 of the 8-pixels structure made via 8 nm thickness NbN on HR silicon substrate (at room temperature) exhibits $\tau = 9ns$, so the kinetic inductance $L_k = \tau \cdot Z_0 = 0.45\mu H$, where $Z_0 = 50\Omega$ is the RF cable impedance. The oscillation in the output voltage pulse during recovery represents an afterpulsing effect of the detector due to the poor low frequency response of the RF Bay LNA-580 and LNA-1000 amplifiers used[186]. The oscilloscope is used to identify an appropriate trigger threshold (in this case 100 mV); this value is set as the trigger threshold for the counter to measure the count rate[Fig.5.25]. The dark count rate (DCR) is measured connecting the LNA amplifiers (56 dB total gain) to a universal counter. Biasing each pixel near its critical current, the counter starts to detect dark rate. The dark count rate increases rapidly as bias current is increased towards the critical current.

Once the critical current is reached, the device becomes normal (high resistance as shown in Fig.5.22) and signals disappear.

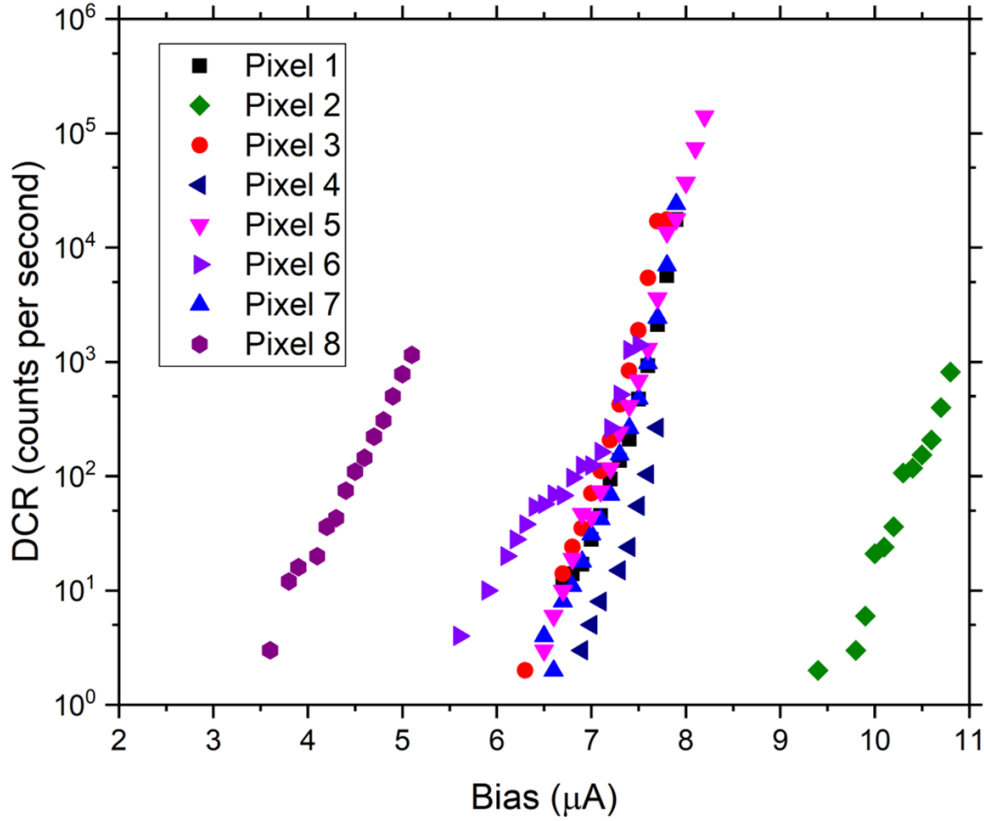


Figure 5.25: Dark count rate against bias current measured at 2.2 K of the 8-pixels SNSPD array structure on 8nm-thick NbN grown at room temperature.

As shown in [Fig.5.25] only pixels 2 and 8 exhibit different DCR, while other pixels exhibit similar DCR in according with the histogram of the critical currents[Fig.5.21] where results that pixel 2 has the highest critical current ($11 \mu\text{A}$), while pixel 8 has the lowest critical current ($5 \mu\text{A}$). At this point the system is ready for the analysis of the photon count rate (PCR). In this work, the laser source used is a laser diode 1550nm (LPS-1550-FC, Thorlabs) connected to a waveform generator to generate laser pulsed 1 MHz frequency. The laser diode is connected to the device by a SMF28 passing by two programmable optical attenuators in series and a polarizer[Fig.3.32]. The power output delivered into the optical fibre connected to the device under test in the cryostat is measured by a digital power meter. The generator has been adjusted to generate a power output of about $11 \mu\text{W}$ to cover the entire area of the 8-pixels structure[Fig.5.6]. The photon count rate is measured biasing the SNSPD near its critical current. Since the 8-pixels structure is not embedded in an optical microcavity, the SNSPD array has been illuminated by TE polarization to achieve the maximum photon count rate (section 2.4.1).

The polarizer has been adjusted manually to achieve the maximum count rate of the device[Fig.5.26].

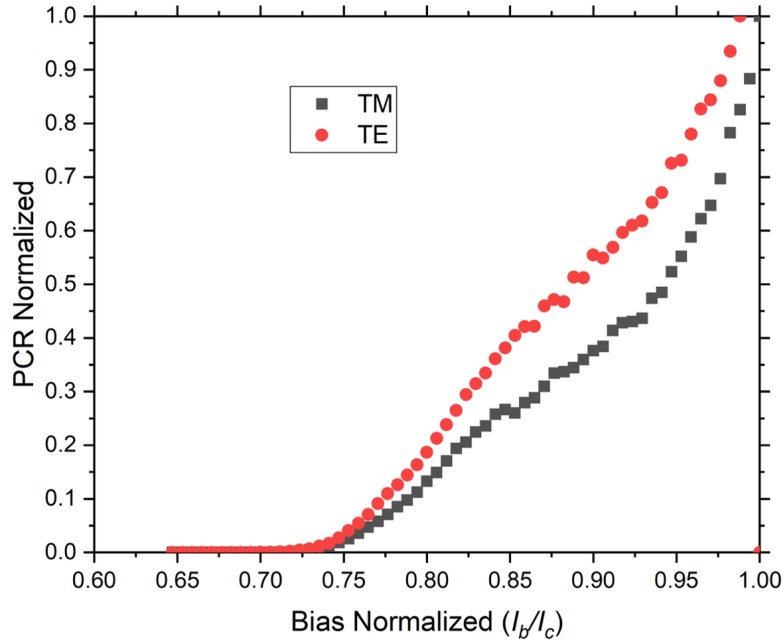


Figure 5.26: Normalized photon count rate against bias current (normalized to the critical current) of pixel 1. The photon count rate is higher when the device is illuminated in TE mode, that means that the absorption of the device increase when the incident light is TE polarized.

First, the photon count rate of pixel 1 has been measured over a range of attenuation[Fig.5.27]. The pixel 1, exhibits saturated response at high photon flux over a long bias range.

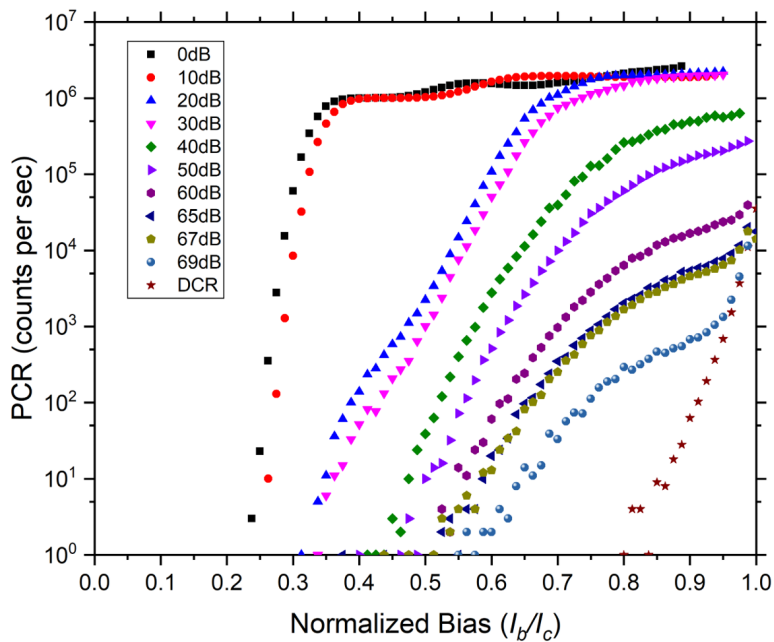


Figure 5.27: Photon count rate at different attenuation measured at 2.2 K of pixel 1 of the SNSPD array structure on 8nm-thick NbN grown on HR Si at room temperature. Bias current is normalized to the respective critical current ($I_c = 8\mu A$). The attenuation starts from 11 μW at 0 dB attenuation (10^7 photons per pulse) to 69 dB (10 photons per pulse).

This saturation effect falls away as the laser is attenuated and the photon flux is reduced. When the laser is attenuated to 69 dB, the photon rate is still far from the dark count rate, that means that the pixels is still sensitive to the light for high attenuation next to the single-photon regime. The number of photon per pulse (photon flux) is given by

$$\text{Photon per pulse} = \frac{E_{input}}{E_{photon}} = \frac{P\lambda}{hc\nu_{laser}} \quad (5.11)$$

where $E_{input} = P/\nu$ is the energy of the laser pulsed given by the product of the output power P and the frequency ν_{laser} of the laser, while $E_{photon} = hc/\lambda$ is the energy of the single photon. Adding the equation of power attenuation in optical fibres[84]

$$\text{Attenuation}(dB) = 10 \times \log_{10} \left(\frac{P}{P'} \right) \quad (5.12)$$

where P' is the attenuated power, the equation 5.11 becomes:

$$\text{Photon per pulse}(dB) = 10^{-\frac{dB}{10}} P \frac{\lambda}{hc\nu_{laser}} \quad (5.13)$$

thus the number of photons per pulse at different attenuation of the power output of the laser beam. When there is no attenuation ($dB = 0$), the equation 5.13 is reduced to equation (5.11). The number of photon per second (photon rate PR) is then given multiplying the photon per pulse by the frequency ν_{laser} .

$$PR(dB) = \frac{\text{number of photons}}{\text{second}} = 10^{-\frac{dB}{10}} \frac{P\lambda}{hc} \quad (5.14)$$

Using the equation (5.3) we are able to calculate number of photons per pulse incident on any pixels (with relative photon rate) at different attenuations[Table 5.1]. The total power P_0 incident on the 8-pixels structure is given by the equation power P passing through a circle of radius r in the transverse plane at position z according to Gaussian model[84]

$$P(z) = P_i \left(1 - e^{-\frac{2r^2}{w(z)^2}} \right) \quad (5.15)$$

Assuming $r = w(z)$, then $P(z) = P_0 = P_i(1 - e^{-2}) = 9.5\mu W$ where $P_i = 11\mu W$ is the laser beam power at the end of the fibre measured by power meter. As the intensity distributions is uniform across pixels[Fig.5.10], so incident power is distributed uniform for each pixels, so photon per pulse and photon rate are uniform for pixels 1, 2, 5 and 6 and for pixels 3, 4, 7 and 8. Since pixels 1, 2, 5 and 6 are totally inside the beam spot, their incident photon per pulse is larger than pixels 3, 4, 7 and 8 that are positioned almost outside from the beam spot.

The condition of single photon regime for the 8-pixels structure is when the incident power laser $11 \mu\text{W}$ is attenuated below 70 dB.

Table 5.1: Table of power attenuations, relative incident photon per pulse on pixels and relative photon rate per second calculated by eq.5.13 and eq.15.14. The laser wavelength is $\lambda = 1550\text{nm}$, pulsed with $\nu_{laser} = 1\text{MHz}$ and power P is calculated by equation (5.3) assuming $P_0 = 9.5\mu\text{W}$.

Power Attenuation (Pixels)	Incident Photon per Pulse (1,2,5,6)	Incident Photon Rate (PR) (1,2,5,6)	Incident Photon per Pulse (3,4,7,8)	Incident Photon Rate (PR) (3,4,7,8)
0 dB	$8.5 \cdot 10^6$	$8.5 \cdot 10^{12}$	$9.3 \cdot 10^5$	$9.3 \cdot 10^{11}$
10 dB	$8.5 \cdot 10^5$	$8.5 \cdot 10^{11}$	$9.3 \cdot 10^4$	$9.3 \cdot 10^{10}$
20 dB	$8.5 \cdot 10^4$	$8.5 \cdot 10^{10}$	$9.3 \cdot 10^3$	$9.3 \cdot 10^9$
30 dB	$8.5 \cdot 10^3$	$8.5 \cdot 10^9$	930	$9.3 \cdot 10^8$
40 dB	850	$8.5 \cdot 10^8$	93	$9.3 \cdot 10^7$
50 dB	85	$8.5 \cdot 10^7$	9.3	$9.3 \cdot 10^6$
60 dB	8.5	$8.5 \cdot 10^6$	0.93	$9.3 \cdot 10^5$
70 dB	0.85	$8.5 \cdot 10^5$	$9.3 \cdot 10^{-2}$	$9.3 \cdot 10^4$

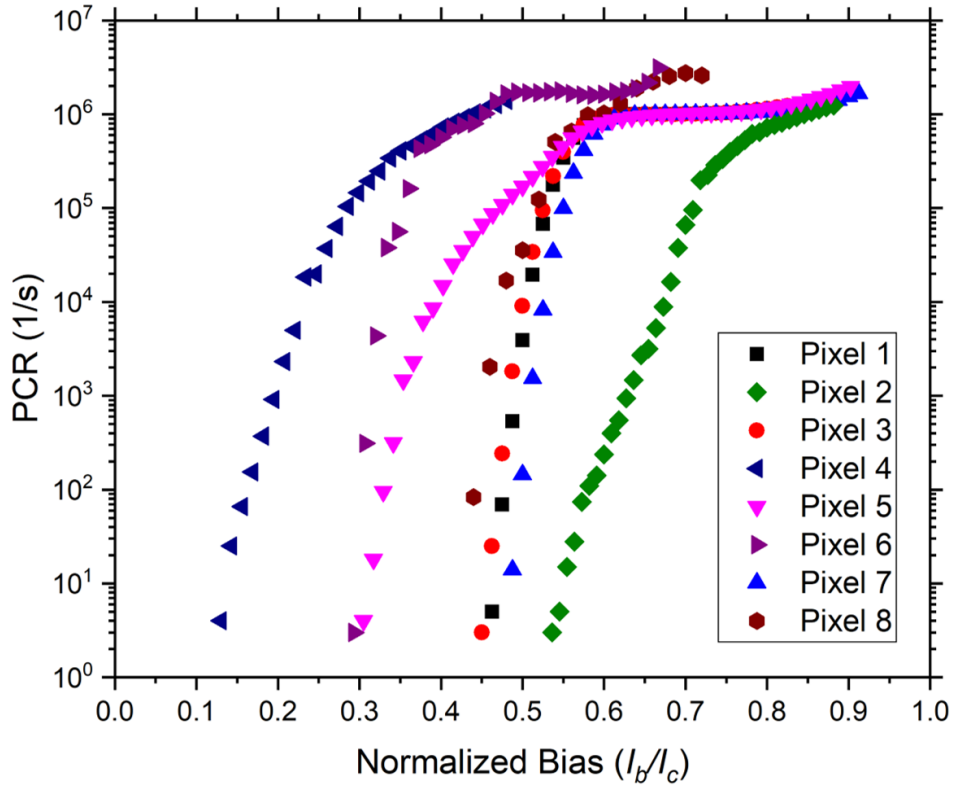


Figure 5.28: Photon count rate at 2.2 K for 8-pixel SNSPD array based on 8 nm thick NbN deposited on HR silicon at room temperature. Bias current is normalized to their respective critical current[Fig.5.21]. High photon flux, incident optical power $11 \mu\text{W}$, 1550 nm wavelength, repetition frequency 1 MHz.

It is interesting to measure the photon count rate of each pixel starting from the condition of 0 dB (no attenuation)[Fig.5.28] and then attenuate the laser beam to the single photon regime to see the behaviour of each pixel at different attenuations. Without attenuation, pixels 1, 3, 5 and 7 exhibit a saturated response over a bias range near their critical current, while pixels 4, 6 and 8 exhibit a saturation but it stops far from their critical current values. The pixel 2, that has the highest critical current, exhibits a short range saturation. All pixels are then sensitivity to the light and exhibit a saturation of the photon count rate when they are biased near their critical current. Since they illuminated, pixels enter to the normal state before they reach their critical current. Pixel 4, 6 and 8 become resistive when their bias current are respectively $I_b^{Pixel4} = 0.5I_c$, $I_b^{Pixel6} = 0.67I_c$, $I_b^{Pixel8} = 0.72I_c$, while other pixels become resistive approximately when their $I_b = 0.9I_c$. Then we can say that pixels 4 and 6 result more exposed to the light than other pixels, so it is expected that attenuating the laser beam to the single photon photon regime (70 dB), PCR of pixels 4 and 6 should result still far from their DCR. Attenuating the laser beam to 50 dB[Fig.5.29], all the pixels still show sensitivity to the laser illumination with the exception of pixels 2 an 8 that exhibit a rate similar to DCR[Fig.5.25].

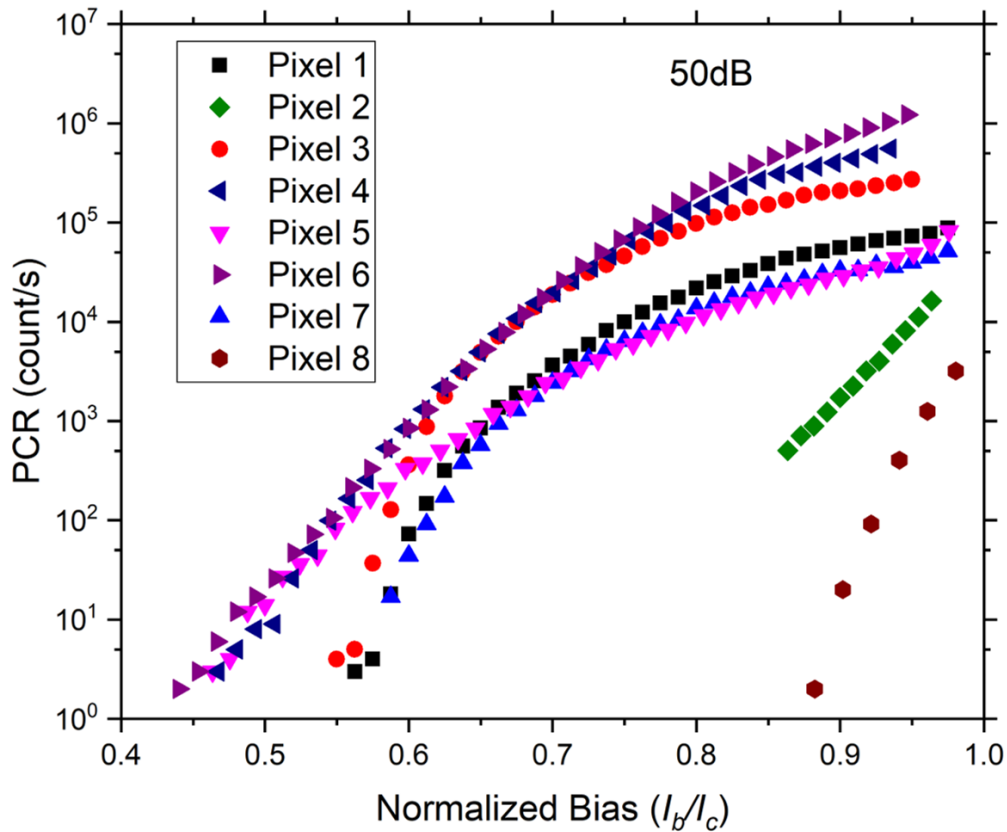


Figure 5.29: Photon count rate at 2.2 K for the 8-pixels NbN SNSPD array structure. Bias current is normalized to their respective critical currents. Laser is attenuated to 50 dB corresponding to 860 photons per pulse from the end of the fibre tip.

Attenuating the laser beam at 70 dB, only pixel 4 and 6 approach saturation near the critical current[Fig.5.30].

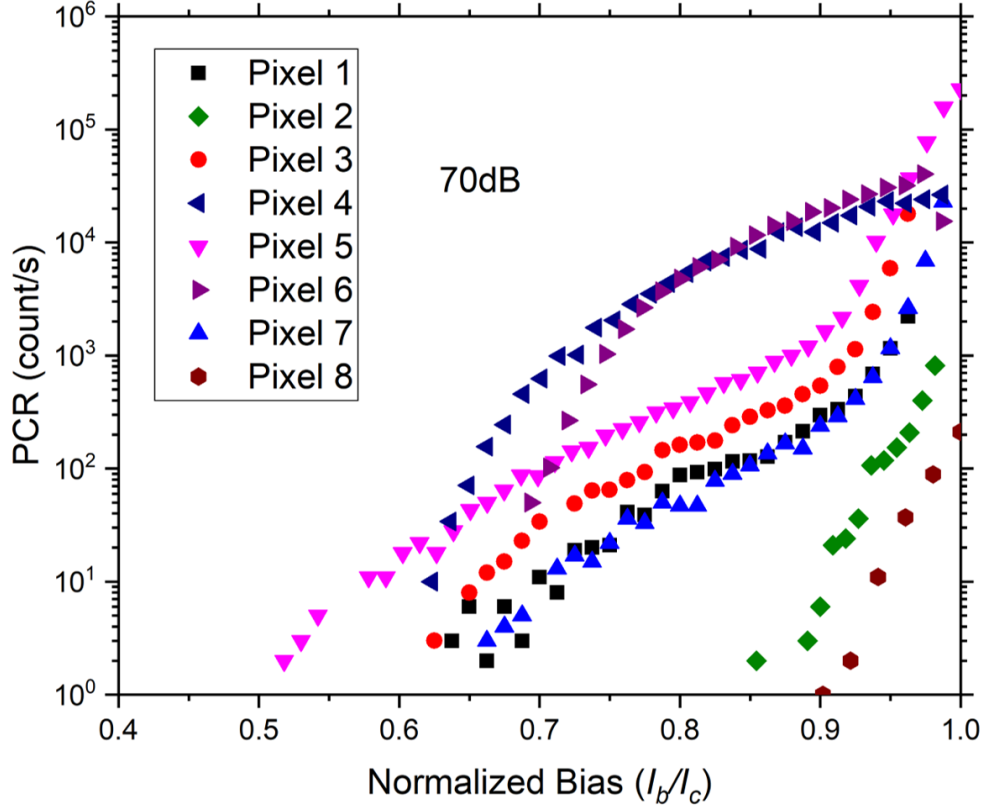


Figure 5.30: Photon count rate at 2.2 K for the 8-pixels NbN SNSPD array structure. Bias current is normalized to their respective critical currents. Laser is attenuated to 70 dB corresponding to 8.6 photons per pulse from the end of the fibre tip.

Pixel 1, 3 and 7 are still sensitive while pixel 2 and 8 exhibit dark counts. In according to [Table 5.1], attenuating the laser to 70 dB, we can consider the entire 8-pixels structure in the single photon regime (below 1 incident photon per pulse). The System Detection Efficiency (SDE) is defined as the ratio of the number of photons PCR as measured using the counter and the total photon rate PR input to the system[196]. Since this system is divided in 8 pixels, we can define the Pixel Detection Efficiency (PDE) as the system detection efficiency of each pixel and expressed by the equation[170, 196]:

$$PDE(\%) = 100 \cdot \frac{PCR - DCR}{PR} \quad (5.16)$$

Where PCR and DCR is respectively the photon count rate and the dark count rate of the pixel measured by the counter while PR is the photon rate incident on the pixel (see Table 5.1). PDE of has been calculated each pixels[Fig.5.31] assuming PCR and PR respectively the incident photon count rate and the incident photon rate onto the pixel when the laser beam is attenuated to 70 dB. In this regime, the photon rate of pixels 1, 2, 6 and 7 is $PR = 8.5 \cdot 10^5$ photons per second, while the photon rate of pixels 3, 4, 7 and 8 is $PR = 9.3 \cdot 10^4$ photons per second as shown in [Table 5.1].

Pixel 4 exhibits the largest pixel efficiency across the test SNSPD array with a value of 28.4% when it is biased very close its critical current. Following, pixel 6 exhibits PDE = 4.7% when it is biased very close its critical current. Other pixels exhibit PDE less than 1% in the single photon regime.

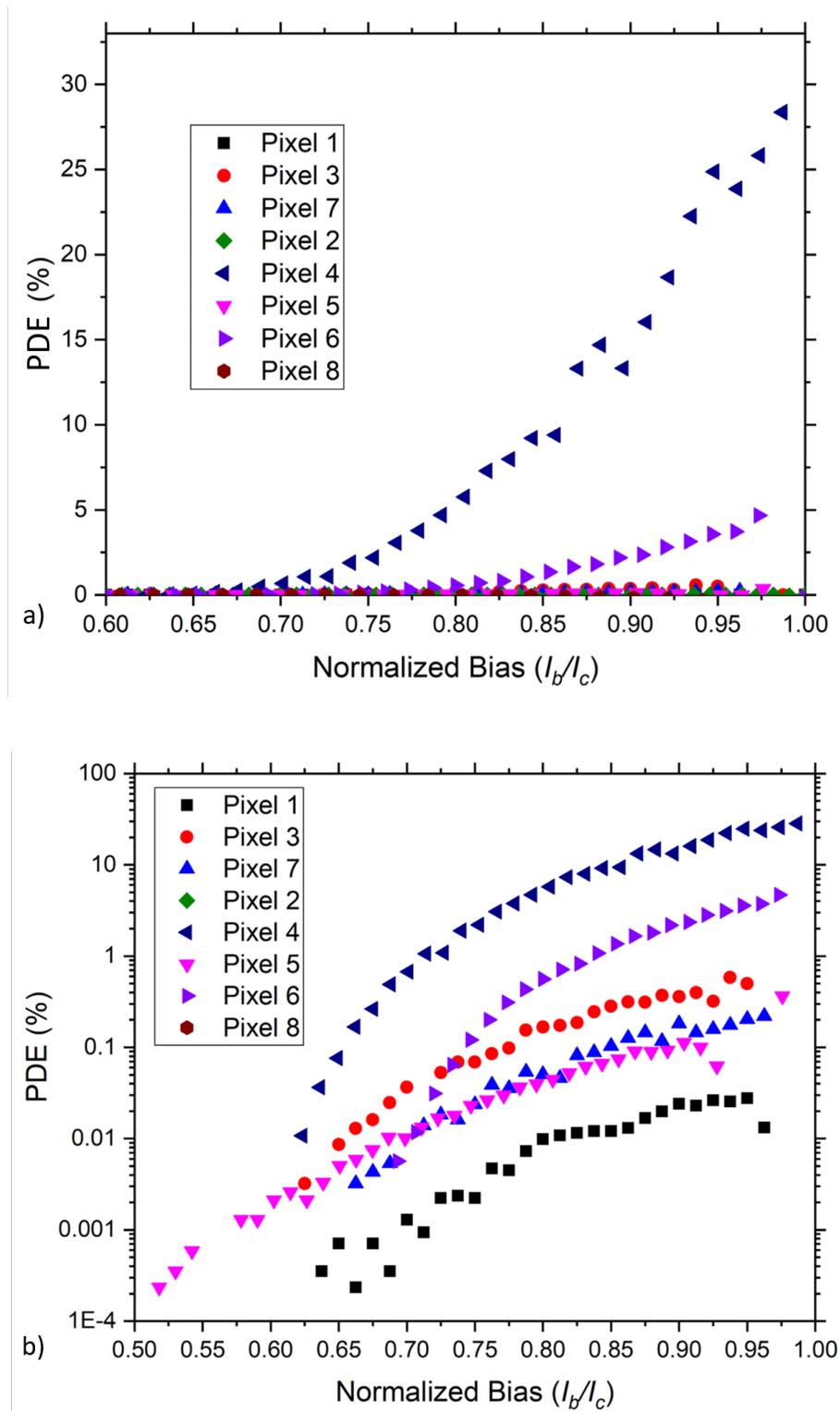


Figure 5.31: Pixel detection efficiency (PDE) in a) linear scale and b) logarithmic scale of each pixels using equation (5.16). Laser beam is attenuated to 70 dB to bring the 8-pixels structure in the single photon regime [Table 5.1]. Bias current is normalized to their respective critical currents.

Assuming that the fibre is perfectly aligned in the centre of the array structure [Fig.5.1], pixel 4 is positioned far from the laser beam centre and its coupling efficiency [Fig.5.12] is ten times lower than pixel 6 that is positioned near the beam centre. The discrepancy of their pixel detection efficiencies indicates that the fibre could be shifted from the centre of the array structure next to the pixel 4 due of the cooling down. By the way, pixel 6 exhibits a PDE larger than 4% and it is far from the pixel 4, so we can not assume that the laser beam is completely centred in the pixel 4 because a the Gaussian simulation [Fig.5.32] shows that the optical coupling efficiency of 6 is respectively 0.2% that is not compatible with the PDE of 4.7% measured for the pixel 6.

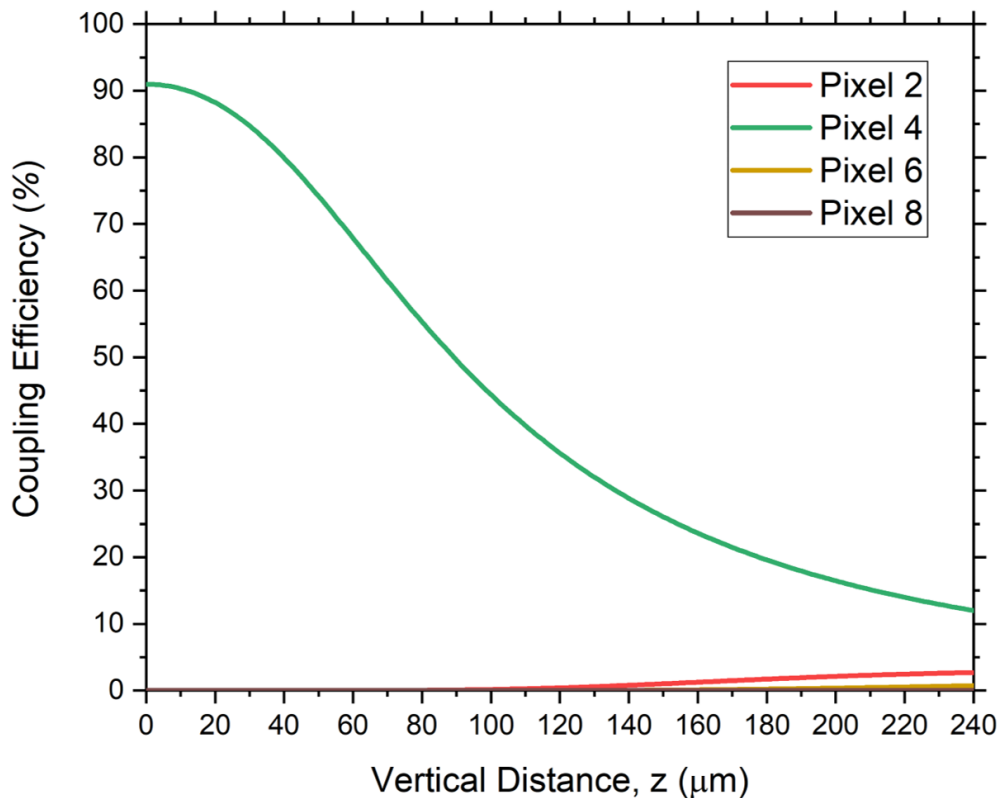


Figure 5.32: Optical coupling efficiency as function of vertical distance z between the end of the fibre to the device. The simulation has been made assuming the middle of the pixel 4 as the centre of the laser beam. Other pixels are discarded because they were not connected during the second cooldown.

It is worth noting that pixel 4 has a relatively low critical temperature (4 K as showed in the [Fig.5.22]) which perhaps enhances photon sensitivity at infrared and then its detection efficiency. To complete the characterization of the device at 2.2 K, the kinetic inductance and the timing jitter of each pixel have been tested.

Kinetic Inductance Measurement

The kinetic inductance of superconductor is a geometrical parameter associated with the reset time of a SNSPD (section 2.7. In the [Fig.5.24], we have calculated the reset time $\tau = 9ns$ fitting the equation 5.10 with the dark signal of pixel 1 estimating a kinetic inductance L_k of about $0.45 \mu H$. Due of the electrical noise and the after-pulsing, the calculation of the kinetic inductance is just an approximation. Thus the kinetic inductance is measured by the electrical set-up shown in the Fig.3.31.

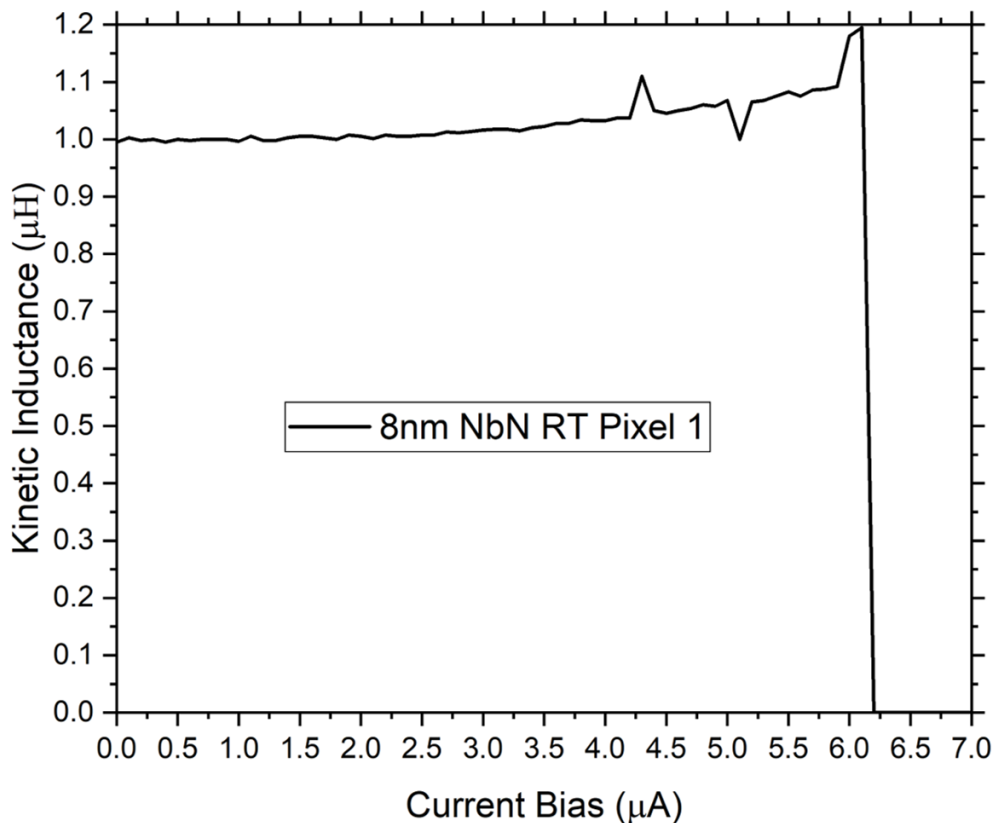


Figure 5.33: Plot of the kinetic inductance of pixel measured by the VNA at 2.2 K. The critical current of the pixel is reduced to the expected value ($8 \mu A$) due of the electrical noise of the electrical set-up built for the kinetic inductance. The kinetic inductance at $0 \mu A$ is about $1 \mu H$.

The AC arm of the bias tee is disconnected from the LNA amplifiers and the oscilloscope/counter and it is connected to the vector analyzer (VNA) (0.1 - 50 MHz bandwidth) across a built-up metallic box where there are installed attenuators to attenuate the VNA output signal to the SNSPD and amplifiers to amplify the reflected signal from the SNSPD and the signal of the variation the kinetic inductance (the SNSPD is biased) transmitted to the VNA. The vector network analyzer (VNA) Via Bravo is computer controlled by a Python program that measures the kinetic inductance of the device in a range of bias current from zero up to the critical current [Fig.5.33]. The Table 5.2 shows the kinetic inductance measured at zero bias for each pixel compared with their critical currents and the reset time calculated by the relation $\tau = L_k/50\Omega$, where 50Ω is the impedance of the RF cable.

As the critical current, the kinetic inductance is a geometrical parameter of an SNSPD, so their discrepancies are due to the proximity effect during the e-beam process that reduce the uniformity of pixels especially when e-beam writing is done over large area. Pixel 2 exhibits the largest critical current and the lowest normal resistance at low temperature[Fig.5.22] and its lowest value of the kinetic inductance confirms that nanowires of this pixel are wider than other pixels that does not exhibit large discrepancies. The reset time of pixel 2 is about 3.4 ns and this can explain the short PCR of the pixel when the laser beam is not attenuated[see the Fig.5.28].

Table 5.2: Kinetic inductance and critical current of each pixel of the 8-pixels NbN SNSPD array.

Pixel	Kinetic Inductance	Critical Current (2.2 K)	Reset Time
1	1 μH	8 μA	20 ns
2	0.17 μH	11 μA	3.4 ns
3	1.04 μH	8 μA	21 ns
4	1.9 μH	7.7 μA	40 ns
5	1.2 μH	8.2 μA	24 ns
6	1.1 μH	7.5 μA	22 ns
7	0.84 μH	8 μA	17 ns
8	1.13 μH	5 μA	22.6 ns
Mean	1.05 μH	7.84 μA	21.25 ns
Stand. Dev.	0.47 μH	1.59 μA	1 ns

Timing Jitter Measurement

The timing jitter is measured by electrical set-up showed in the [Fig.3.33]. The laser source is the the Kphotonics CNT-1550-TK, 50 MHz. Across the optical setup, the power output is about 27 μW . To measure the timing jitter of all pixel in the single photon regime(see Table 5.1), the laser beam has been attenuated to 60 dB (86 photon per pulse from the fibre tip) and each pixel is biased near the critical current ($I_b = 0.7I_c$). As explained in the section 3.5.1, the timing jitter measurement consists to measure the interval between the arrival of the photon and the corresponding electrical response of the detector. As a random variable, the jitter has a Gaussian distribution and it is identified as the FWHM of its distribution[Fig.5.34]. Timing jitter of each pixel is showed in the Table 5.3. The mean value is about 137 ps (standar deviation 10.3 ps). This value is larger than typical timing jitter values for a NbN SNSPD that typically is less than 100 ps[193, 194, 195]. This is due of the large distance of pixels and of the re-alignment of the optical fibre between two different cool downs that affects the uniformity of the coupling efficiency. Pixels 2 and 8 exhibit low PCR when the power laser is attenuated to 70 dB [Fig.5.30 b)] making impossible the measurement of their timing jitter. Assuming that the fibre is aligned near the pixel 4, then pixels 4 exhibits the largest PDE and this can even explain its low value of timing jitter than other pixels.

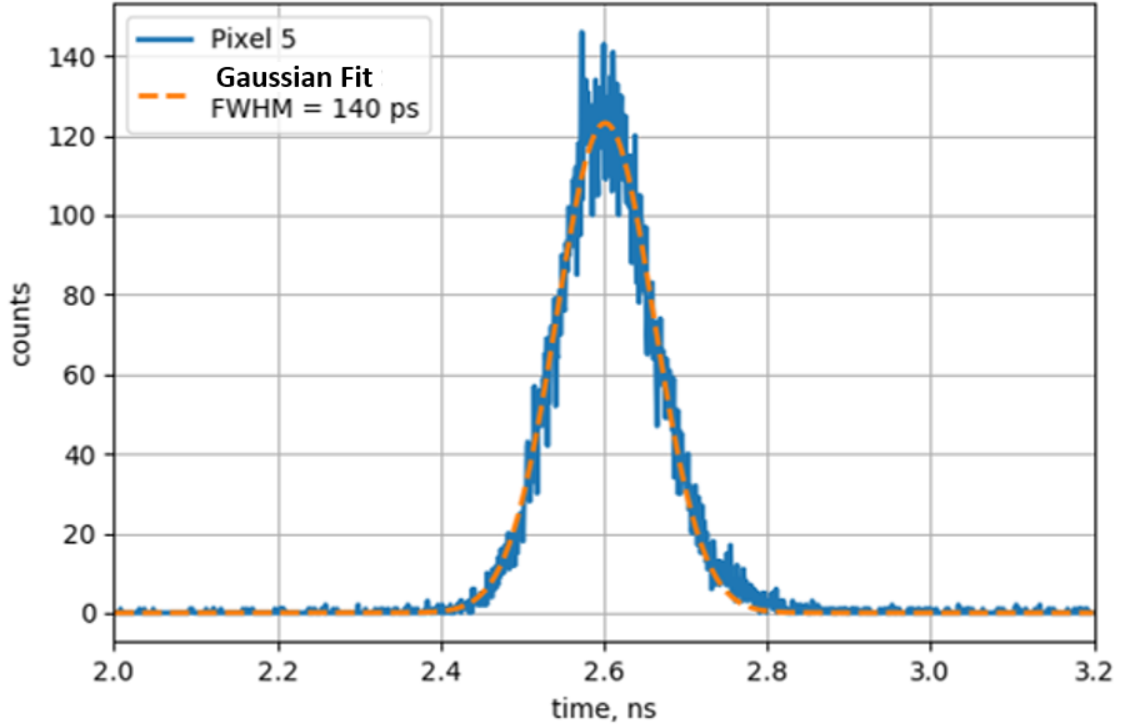


Figure 5.34: Timing jitter of the pixel 5 measured attenuating the laser beam at 60 dB. The plot is taken from the software HydraHarp. The FWHM of the Gaussian curve is calculated automatically by the software. The FWHM is 140 ps.

Table 5.3: Timing jitter of each pixel of the 8-pixels NbN SNSPD array measured at 60 dB.

Pixel	Timing Jitter
1	148 ps
2	x
3	144 ps
4	120 ps
5	140 ps
6	130 ps
7	140 ps
8	x
Mean	137 ps
Stand. Dev.	10.3 ps

The table 5.4 summarizes timing jitter measured at 60 dB, the kinetic inductance measured at zero bias, the critical current current at 2.2 K, the critical temperature a the pixel detection efficiency measured when the pixel is biased 95% of its critical current of each pixel of the SNSPD array made via 8nm thickness NbN grown at room temperature. Pixel 2 and 8 are not operative in the single-photon regime. Small discrepancies across pixels for each parameter confirms the uniformity of the 8-pixels structure in terms of its superconducting properties (small discrepancies in critical temperature, current and kinetic inductance).

Only pixels 4 and 6 are sensitive in the single photon regime exhibiting an efficiency of 28.4% and 4.7% respectively. Results illustrated in the Table 5.4 are discussed in the next chapter.

Table 5.4: Summary of the prototype SNSPD array properties: timing jitter, kinetic inductance, critical current, critical temperature, and pixel detection efficiency (PDE) measured when the pixel is biased 95% of its critical current.

Pixel	Timing Jitter	Kinetic Inductance	Critical Current (2.2 K)	Critical Temperature	PDE (0.95 I_c)
1	148 ps	1 μ H	8 μ A	4.5 K	0.03%
2	x	0.17 μ H	11 μ A	4.5 K	x
3	144 ps	1.04 μ H	8 μ A	4.5 K	0.5%
4	120 ps	1.9 μ H	7.7 μ A	4 K	28.4%
5	140 ps	1.2 μ H	8.2 μ A	4.8 K	0.36%
6	130 ps	1.1 μ H	7.5 μ A	4.4 K	4.7%
7	140 ps	0.84 μ H	8 μ A	4.5 K	0.22%
8	x	1.13 μ H	5 μ A	4.3 K	x

5.3.2 MoSi Array

Due its low critical temperature (on average 3.2 K), the 8nm MoSi SNSPD array has been tested in the Rankinator cryostat with a base temperature of 400 mK. As explained in 5.2.2, the device is attached on the ^3He coldhead under the attocube microscope. Due limitation of the sample mount[Fig.5.13], first have been tested odd pixels (1, 3, 5 and 7) and next pair pixels (2, 4, 6, 8). The cooling down of the Rankinator is done by two automatic programs written in Python code. The first one cools down the system from the room temperature to 5 K switching on pump heaters. As explained in the section 3.5.2, when pump heaters are switched on they desorb the $^4\text{He}/^3\text{H}$ gas from the charcoal and flows via tubes to coldheads reaching a temperature of about 5 K. To cool down the ^3He coldhead to 400 mK, a second Python code switch on and off Active Gas-Gap Heat Switches (AGSHs) in a cycling process that absorbs and expels He flow. In this cycling process, the base temperature of device varies between 0.4 K and 5 K. The software is written to cool down the equipment to 400 mK for about 3 hours after that the program switches off AGSHs bringing back the coldhead to 5 K. When the Rankinator is at 400 mK, the IV characteristics of each pixel tested are achieved by a similar equipment used for the Zephyrator to test the NbN SNSPD array. While in the Zephyrator, devices are biased by an isolated voltage source (SIM928), in the Rankinator devices are biased by a Keithley 238 High Current Source (DC current source). The [Fig.5.35] shows the IV characteristic of the pixel 1. All pixels exhibit similar IV characteristic. The critical current correspond to the value of the bias current when the pixel becomes normal. Of the 8 pixels, pixels 6 and 7 are respectively an open and a short circuit. In average[Fig.5.36], the mean critical current of the 8-pixels structure is 0.7 μ A with a deviation standard of 0.07 μ A.

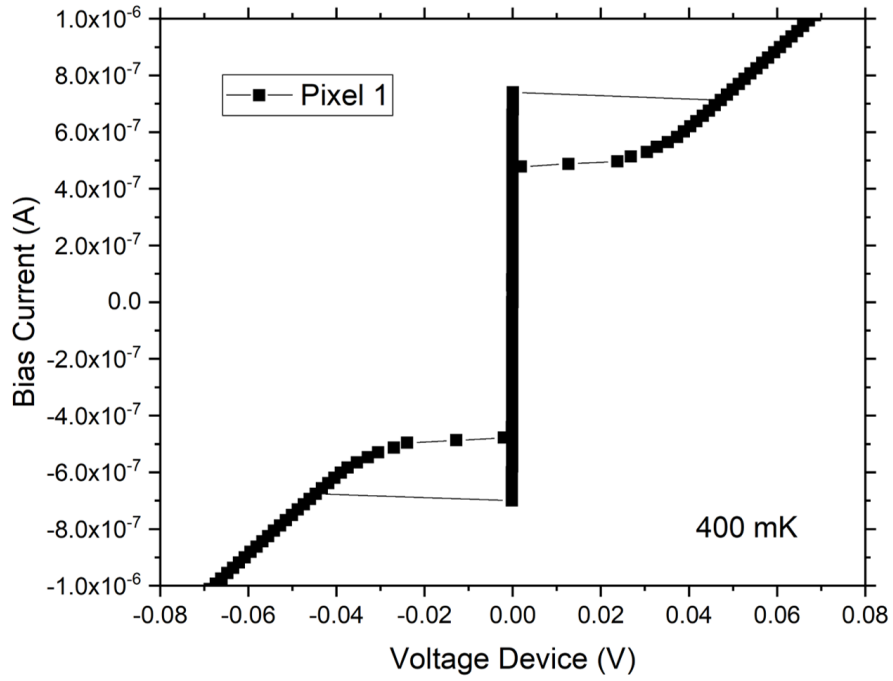


Figure 5.35: IV characteristic at 400 mK of the pixel 1 of the SNSPD array structure made via 8nm-thick MoSi. The y-axis is the bias current settled by the DC current source (the instrument is controlled by a Python code) and the x-axis is the voltage drop of the device. The pixels is biased between $\pm 1\mu A$. The device enter into the resistive state when $I_c = 0.74\mu A$. When the device is biased in the negative region $I_c = -0.7\mu A$. This offset is due to the electrical noise of the instrument since it does no work with battery as the voltage source SIM928.

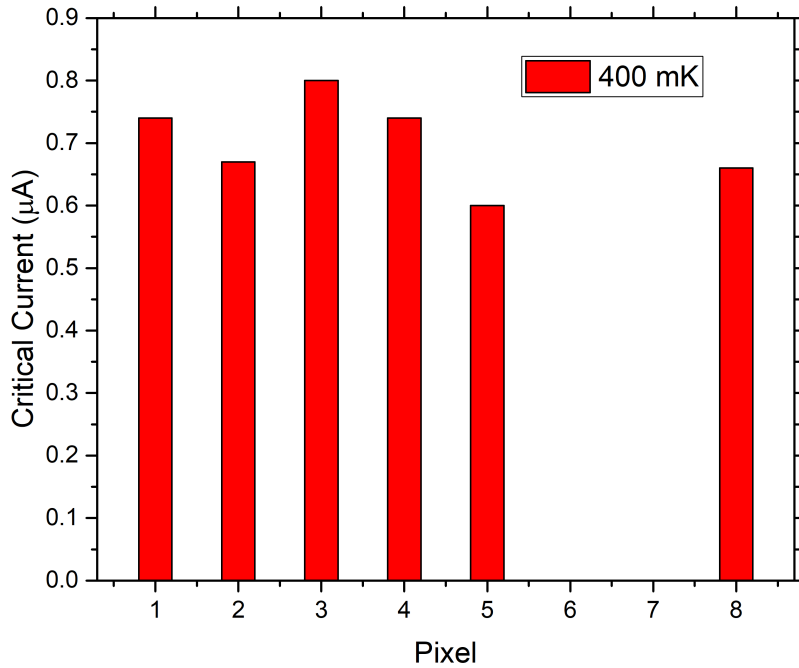


Figure 5.36: Histogram of critical currents measured at 400 mK of 8 nm thickness MoSi SNSPD 8-pixels array. Pixel 6 and 7 are respectively an open and a short circuit.

Turning off AGSHs, the heat load of sorption pumps brings the Rankinator again to 5 K. Turning on AGSHs heat load is dissipate and the coldhead where the device is installed can reach again 400 mK base temperature. The critical temperature of each pixel of the SNSPD array structure has been measured during this cycle (controlled in remote by a Python code). As shown in the [Fig.5.37], pixels 1, 2, 4 and 5 exhibit a value of about 4 K. Pixel 3 and 8 exhibits respectively 0.85 K and 2.3 K. Pixel 6 and 7 have not been measured because pixel 7 exhibited a short while pixel 6 is an open circuit.

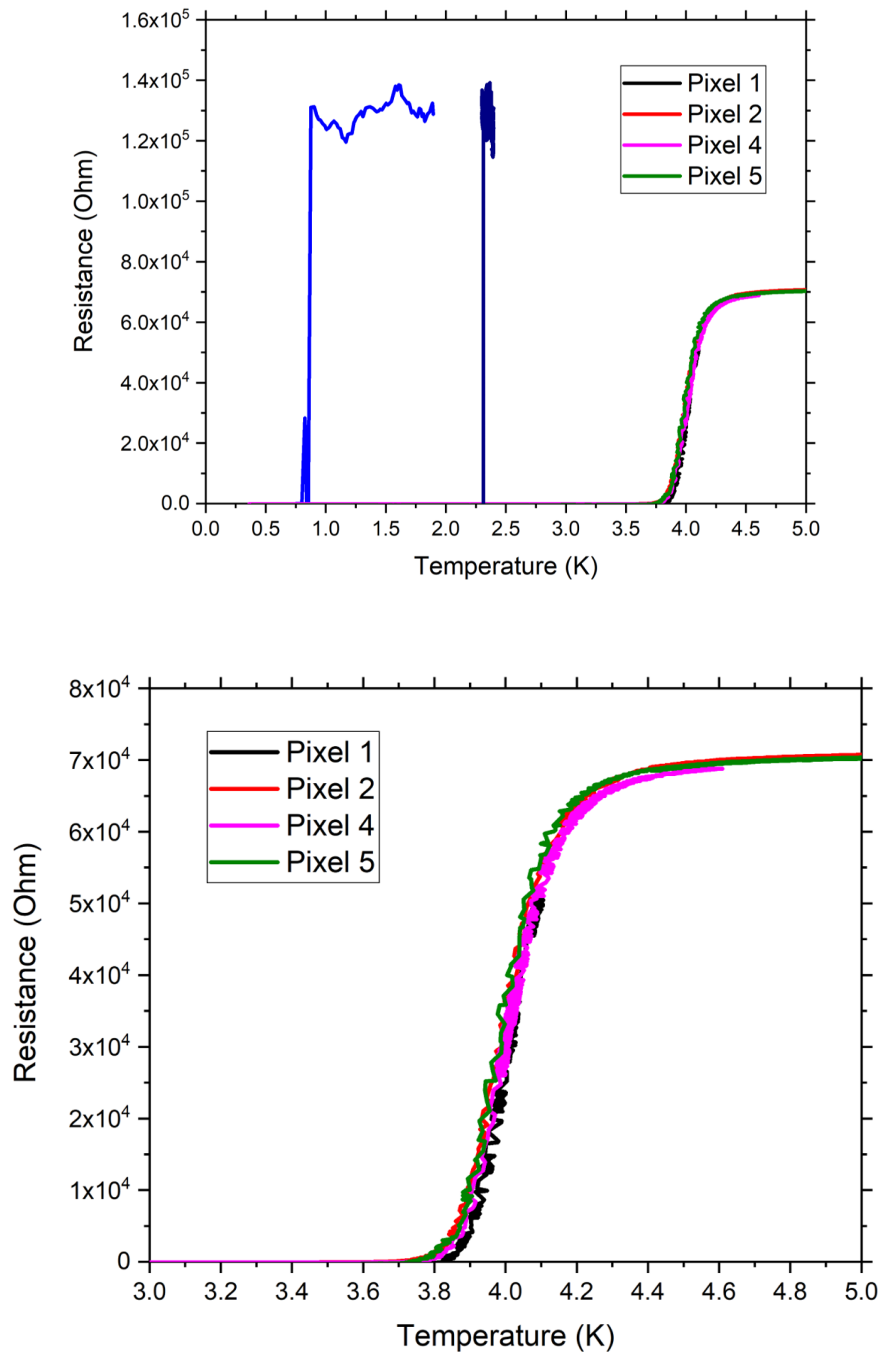


Figure 5.37: a) Resistance versus temperature measurement characteristic of 6 pixels of the 8nm thickness MoSi SNSPD array. Only pixel 1, 2, 4 and 5 exhibits similar curve shape while pixel 3 and 8 exhibit a comparable resistive state, but large spread of critical temperature. b) RT characteristic of pixels 1, 2, 4 and 5. Their critical temperature is 4 K

Superconducting properties of the 8 nm MoSi SNSPD array structure are listed in the Table 5.5.

Table 5.5: Critical current at 400 mK and critical temperature of each of pixel of the 8-pixels MoSi SNSPD array.

Pixel	Critical Current (400 mK)	Critical Temperature
1	0.74 μA	4 K
2	0.67 μA	4 K
3	0.8 μA	0.8 K
4	0.74 μA	4 K
5	0.6 μA	4 K
6	Open	Open
7	Short	Short
8	0.66 μA	2.3 K
Mean	0.7 μA	3.2 K
Stand. Dev.	0.07 μA	1.35 K

Mean values of critical current and critical temperature are respectively 0.7 μA and 3.2 K. Whereas, standard deviations are respectively 0.072 μA and 1.35 K. Except for pixels 3 and 8, the device does not present large difference between critical temperature and critical current proving a good uniformity in terms of superconducting properties. The dark count rate of pixels has been measured by the same equipment [Fig.3.30] used for the Zephyrator while the device is cooled down to 400 mK.

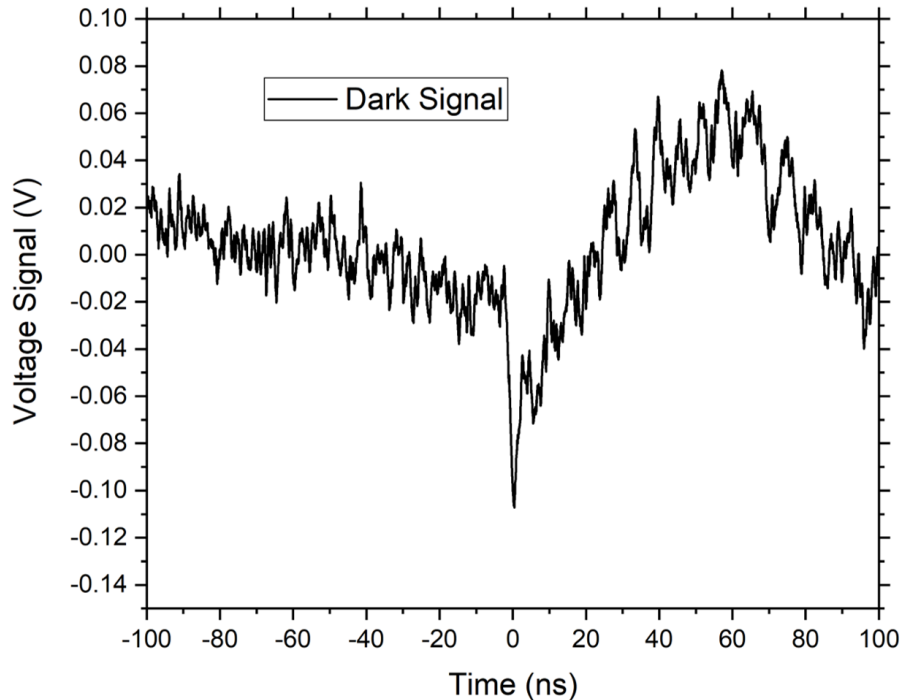


Figure 5.38: Dark signal of pixel 4 of 8 nm thickness MoSi grown cooling the substrate to -180°C (red). The peak of this dark signal is 107 mV for the MoSi. The dark signal of MoSi device appears in absence of bias. This effect is due to thermal effect of BeCu coax cables to connect the device to the room temperature electric set-up causing a voltage offset.

From the analysis of dark count rate of each pixels results a high background noise due to thermal effect of BeCu coax cables in the Rankinator used to connect the device to the room temperature electric set-up. This noise has produced dark signals[Fig.5.38] even in absence of bias. The dark count rate of pixels 2 and 4 shows the noise effect counting dark signals even at zero bias[Fig.5.39]. Due this noise and the small values of critical current do not permit a precise photoresponse analysis.

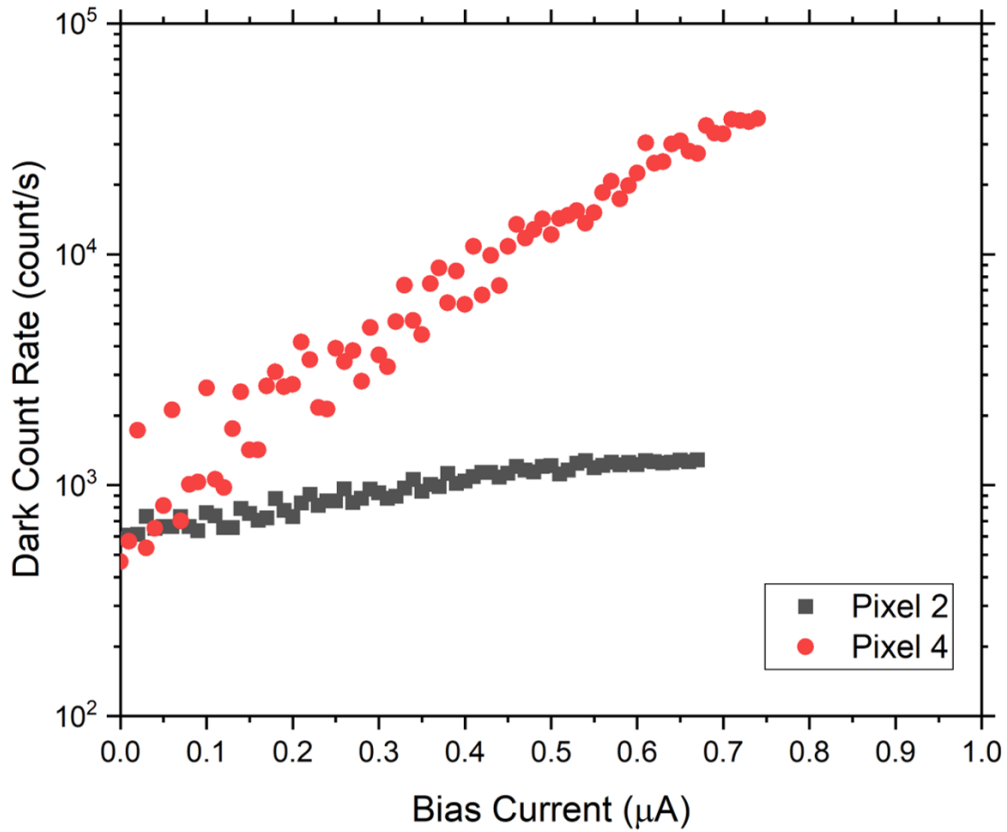


Figure 5.39: Dark Count Rate of pixels 2 and 4 of 8nm MoSi SNSPD array. Dark rate is present even when pixels are not biased due to thermal effect of coaxial cables that connect pixels to the room temperature instrument.

Chapter 6

Conclusions

To conclude the thesis, first a discussion of results described in the previous chapter comparing the superconducting properties of NbN and MoSi SNSPD array and a discussion about optical properties measured on the SNSPD array structure made via 8 nm thickness NbN grown on HR silicon substrate at room temperature. The chapter concludes with an outlook on promising avenues.

6.1 Discussion

In this thesis, we have fabricated SNSPDs configured in a multipixel structure composed of 8 pixels. Each pixel is a meander structure $10\ \mu\text{m} \times 10\ \mu\text{m}$ with 50% filling factor (the width of nanowires is 100 nm and they are separated 100 nm). Each pixel is connected to an independent contact pad, so each pixel is biased independently. The ground is in common [Fig.6.1].

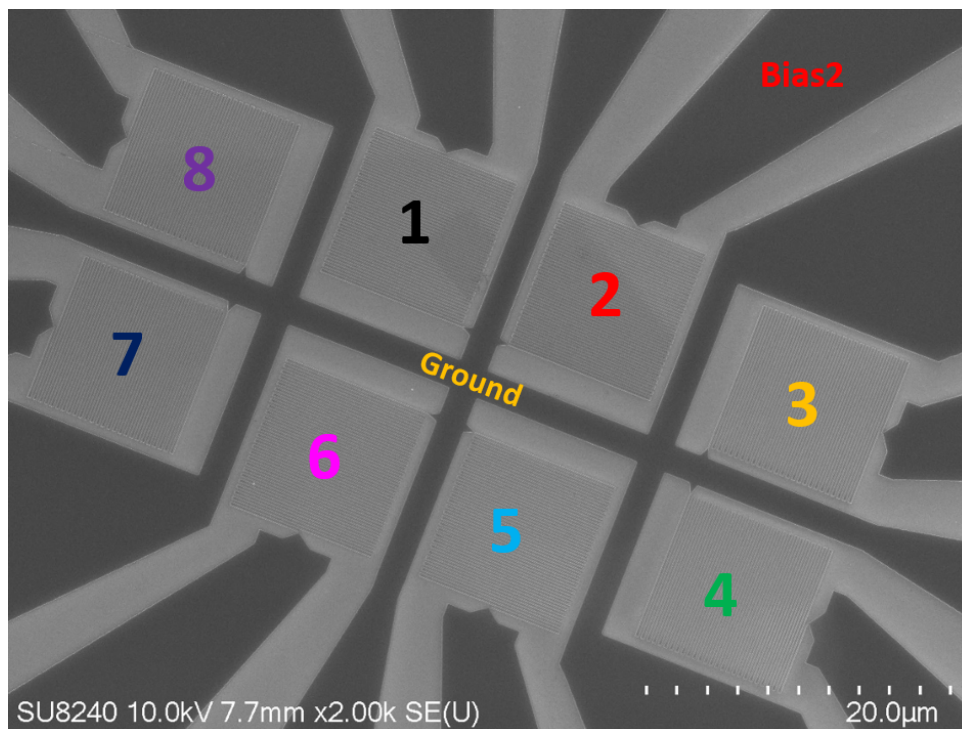


Figure 6.1: SEM images of the SNSPD array realized via 8 nm thickness NbN. The system is composed of 8 pixels embedded in a $50\ \Omega$ CPW. Ground is common and each pixel is biased independently.

Materials chosen to make these devices are NbN and MoSi. Advantages and disadvantages of these materials are listed in the [Table 6.1].

Table 6.1: Properties of NbN and MoSi useful for the fabrication of SNSPDs.

Materials	Properties	Advantages	Disadvantages
NbN	High critical temperature	Use of > 2 K cryocoolers	High superconducting energy gap
	Polycrystalline	Superconducting properties retained during processing	Lattice parameters must be compatible with the lattice parameters of the substrate
MoSi	Low critical temperature	Low superconducting energy gap	Cooling below 1K may be required (pulse tube plus ^3He sorption state)
	Amorphous	It can be deposited on any substrate without restriction	Susceptible to degradation during processing

Due to their amorphous nature, low energy superconducting gap and high absorption coefficient in the range of long wavelength[Fig.2.22], MoSi can be considered as a good choice in the fabrication of SNSPDs. So 8 nm thickness MoSi and NbN have been deposited on HR silicon substrate via DC magnetron sputtering. Before the fabrication of the 8-pixels structure, superconducting properties of these thin films have been measured and compared. As shown in [Table 4.3] and [Table 4.4], NbN thin film exhibits superconducting properties similar to MoSi thin films when it is deposited keeping the substrate at room temperature. After the electrical characterization, the 8-pixels structure has been printed on thin films via e-beam lithography and dry etch processes. Aim of this thesis is to compare the superconducting and the optical properties of 8-pixel SNSPD arrays made via 8 nm thickness NbN grown on HR Si substrate at room temperature and at 800°C , and via 8 nm thickness MoSi grown on HR Si substrate cooled at -180°C . Superconducting properties are given by two parameters: the critical temperature and the critical current. As explained in chapter 4, the critical temperature is an intrinsic parameter for a film of a given material and thickness, independent of the patterned geometry then the uniformity of the critical temperature across pixels proves the uniformity of the superconducting material. Table 6.2 summarizes the critical temperature of 8-pixels SNSPD array tested. Both the SNSPD arrays fabricated from NbN show relatively low spread in critical temperature in contrast to the SNSPD array fabricated in MoSi, which shows a larger standard deviation. Comparing these mean values with critical temperatures of unpatterned thin films [Table 4.2] we can highlight how critical temperatures of devices is decreased after the fabrication of SNSPDs.

Table 6.2: Critical temperature of 8-pixels SNSPD array made on 8 nm thickness NbN grown on HR Si at room temperature and at 800 °C and made on 8nm thickness MoSi grown on HR Si at -180°C .

Critical Temperature			
Pixel	NbN RT	NbN 800 °C	MoSi Cooled
1	4.5 K	7.3 K	4 K
2	4.5 K	x	4 K
3	4.5 K	7.5 K	0.8 K
4	4 K	x	4 K
5	4.8 K	7.3 K	4 K
6	4.4 K	x	Open
7	4.5 K	7.5 K	Short
8	4.3 K	x	2.3 K
Mean	4.44 K	7.4 K	3.2 K
Stand. Dev.	0.23 K	0.11 K	1.35 K

As shown in Table 6.3, critical temperatures for MoSi SNSPD devices are reduced significantly during processing relative to the unpatterned film, as compared to NbN SNSPD device.

Table 6.3: Critical temperature of 8nm-thick NbN and MoSi films grown at different temperature before and after the SNSPD fabrication.

Sample_ID	Substrate Temperature	T_c Unpatterned	T_c SNSPD	T_c Reduction
NbN RT	RT	5.5 K	4.44 K	19%
NbN 800 °C	800 °C	8.2 K	7.4 K	10%
MoSi Cooled	-180°C	5.4 K	3.2 K	40%

In terms of the critical current measured at fixed temperature, all SNSPD arrays exhibit some discrepancies between pixels. This parameter depends strongly upon the geometry of the device. Results for any devices tested are summarized in the Table 6.4 The SNSPD array made via NbN grown heating the substrate at 800 °C exhibits large discrepancy between pixels than the SNSPD made via NbN grown at room temperature. Compared to the NbN device grown at room temperature, the SNSPD made via MoSi does not show large spread in the critical current. In summary, small discrepancies of critical temperatures and critical currents proves the uniformity of the NbN device grown at room temperature and of the MoSi device. For the SNSPD array based on NbN grown at 800 °C, small difference of critical temperature prove the uniformity of the material, but large spread of critical current are due to a non uniformity of the geometry of pixels. These discrepancies are present even in the pixels 2 and 8 of the NbN device grown at room temperature.

Table 6.4: Critical current of 8-pixels SNSPD array made on 8 nm thickness NbN grown on HR Si at room temperature and at 800 °C measured at 2.2 K and made on 8nm thickness MoSi grown on HR Si at -180 °C measured at 400 mK.

Critical Current			
Pixel	NbN RT (2.2 K)	NbN 800 °C (2.2 K)	MoSi Cooled (0.4 K)
1	8 μ A	21 μ A	0.74 μ A
2	11 μ A	x	0.67 μ A
3	8 μ A	28.5 μ A	0.8 μ A
4	7.7 μ A	x	0.74 μ A
5	8.2 μ A	20 μ A	0.6 μ A
6	7.5 μ A	x	Open
7	8 μ A	44 μ A	Short
8	5.1 μ A	x	0.66 μ A
Mean	7.94 μ A	28.37 μ A	0.70 μ A
Stand. Dev.	1.59 μ A	11.08 μ A	0.072 μ A

These discrepancies are a consequence of the proximity effect in the e-beam lithography. During this process, the proximity effect can modify the geometrical structure of pixels. As mentioned in the section (3.3.2), all devices are made at the same conditions (same dosage). Observing pixels 2 and 8 of the NbN array grown at room temperature, we can note that the width of the pixel 2 is enhanced (high critical current) while the width of the pixel 8 is decreased (low critical current). Proximity effect is clearly evident in the NbN device grown heating the silicon substrate to 800 °C that exhibit the largest standard deviation of critical currents. A way to reduce this proximity effect during the e-beam process is the optimization of the exposure dose[187]. As explained in the (section 3.3.2), the e-beam dose represents the number of electrons per unit area of exposure. As explained in the reference [187], the width of nanowires of a large multipixels structure (in this case 16 pixels) is not uniform for high dosage and they can vary from the "ideal" value a maximum value w_{MAX} and a minimum w_{MIN} . To define an appropriate dosage, they defined the deviation factor

$$DF_{min} = \left(\frac{w_{MAX} - w_{MIN}}{w_{MIN}} \right) \quad (6.1)$$

that represent the factor of difference between the maximum w_{MAX} and the minimum w_{MIN} width at a specific exposure voltage. The uniformity of the width across pixels is confirmed when DF_{min} is minimized.

The decreasing of critical temperature showed in the [Table 6.3] explains the decrease of superconducting properties of devices during fabrication process. In particular MoSi device looks more deteriorated than NbN. A possible explanation is the absence of the silicon cap on the top of the device. Due of its amorphous nature, MoSi is easy-oxidizable and it can degrade rapidly than polycrystalline materials as NbN. For this reason, the surface of MoSi is usually covered by a thin silicon layer to prevent any oxidation[176]. By the way, the presence of the silicon cap reduce optical properties of the material[100], for this reason in this works the 8-pixels SNSPD has been pattern on 8 nm thickness MoSi not covered by a silicon layer. The decrease of superconducting properties and the not optimized e-beam dosage are demonstrated by low values of critical current. Pixels 6 and 7 are respectively an open circuit and a short circuit.

About optical properties, only the 8 nm thickness NbN grown on silicon substrate at room temperature has been characterized because the 8 nm thickness NbN grown on silicon substrate at 800 °C exhibits large discrepancies in term of the critical current demonstrating a non uniformity of geometrical structure and the 8 nm thickness MoSi grown on silicon substrate at -180 °C exhibits low values of critical current and a high background noise that does not permit a clear analysis of optical signals when the device is illuminated by the laser. As explained in the (section 5.2.1), the 8 nm thickness NbN grown on silicon substrate at room temperature has been mounted on an optical mount and the fibre is positioned far from the device to illuminate the entire area of the device. Since pixels are positioned very far between them, the optical coupling efficiency is not uniform across pixels. When the device is illuminated without attenuation, pixels exhibit a saturation of the photon count rate, in particular pixels 1, 3, 5 and 7 exhibit a saturation of the rate over a long bias range. Attenuating the laser beam to the single photon regime (70 dB) only pixel 4 and 6 look to be still sensitive to the laser exhibiting a pixel detection efficiency 28.4% and 4.7% respectively. Assuming that the pixel detection efficiency (PDE) is the system detection efficiency of a single pixel, then PDE can be express as(section 2.4):

$$PDE = OCE \times ABS \times IDE \quad (6.2)$$

where OCE is the optical coupling efficiency, ABS is the absorptance and IDE the intrinsic efficiency. In according to the Gaussian model explained in the (section 5.2.1) and assuming that the fibre is perfectly aligned, pixels 1, 2, 5 and 6 $OCE = 11.42\%$, while for pixels 3, 4, 7 and 8 $OCE = 1.25\%$ when the SMF28 (1550nm wavelength) is positioned $178 \mu\text{m}$ away from the device. The absorptance ABS can be calculated from equation (2.28) introduced in the section 2.4.2:

$$ABS = \frac{4Z_0 R_{sheet}}{(Z_0 + (n + 1)R_{sheet})^2} \quad (6.3)$$

where $Z_0 = \sqrt{\frac{\mu_0}{\epsilon_0}} = 376.73\Omega$ is impedance of vacuum, R_{sheet} is the sheet resistance of thin metal film and n the refractory index of the film. Using the sheet resistance at 20 K reported in the Table [4.3] then $R_{sheet} = 298.25\Omega/square$ and the refractory index $n = 4, 3$ at 1550 nm as reported by the reference [100] and showed in the [Fig.2.22], we can estimate the absorptance at 1550 nm of the 8 nm thickness NbN grown at room temperature as $ABS = 11.73\%$.

The intrinsic detection efficiency IDE depends by superconducting properties of the detector. The calculation of the IDE of pixels 4 and 6 gives respectively 1.94% and 0.03%. The pixel 4 exhibits the highest IDE as exhibits the lowest critical temperature of other pixels. Since as explained in the (section 2.2.2), low critical temperature means low energy gap that increase the sensitivity of the material to generate non equilibrium process compatible with the hot-spot model after the absorption of low energy (long wavelength photons). We need to remember that pixels have been tested in two separated cooldowns due of limitations of sample mount[Fig.6.2] that can connect electrically only 4 pixels.

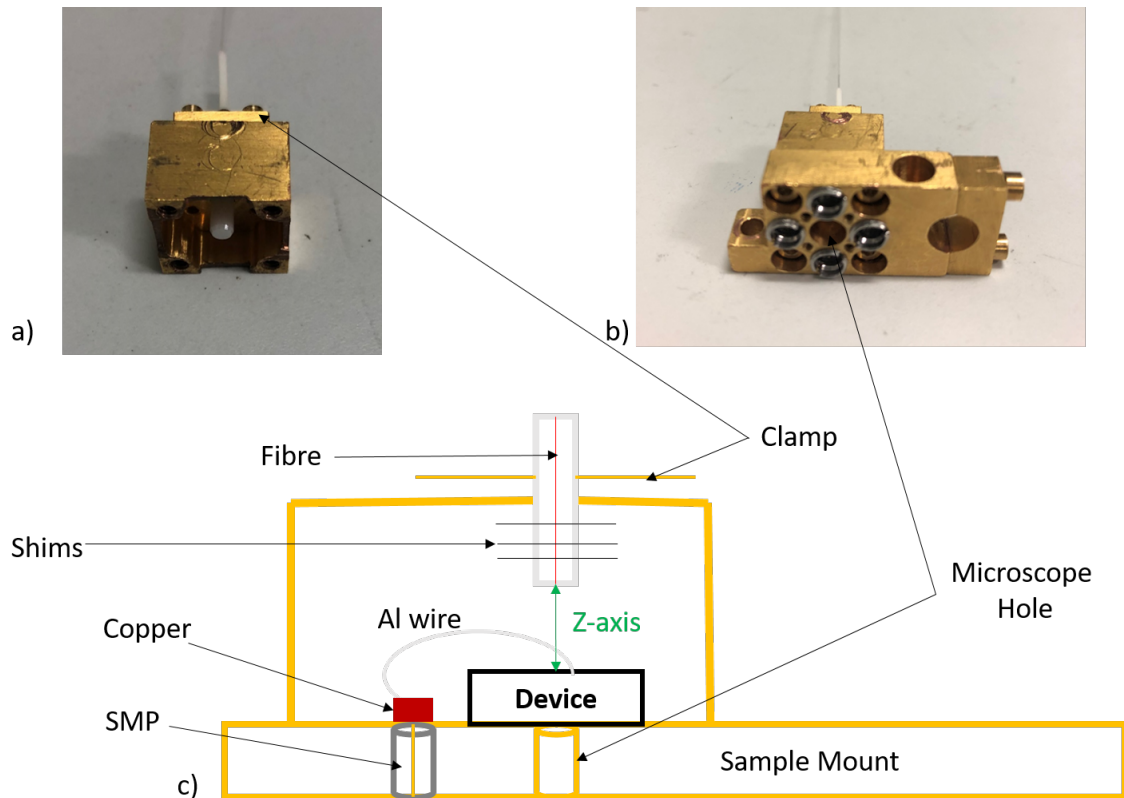


Figure 6.2: a) OFHC copper cap for optical coupling. b) Complete sample mount with optical coupling and c) its scheme. The fibre ferrule is inserted in the middle of the cap and kept hold by a clamp screwed on the top. The distance of the fibre from the device (Z-axis) is controlled by the use of thin steel shims.

The electrical connection of different pixels require the re-alignment of the fibre without remove the fibre from the optical cap so we can assume that the vertical distance ($178 \mu\text{m}$ at 2.2 K) is not changed. In the second cooldown, pixels 2, 4, 6 and 8 have been connected and assuming that the laser beam is centred in the pixel 4, the Gaussian simulation gives respectively 20% optical coupling efficiency for pixel 4 and 0.2% for pixel 6. In this conditions, IDE is respectively 0.12% for pixel 4 and 2% for pixel 6 and these results are incompatible with their respective critical temperature [Table 6.3].

In conclusion, the small discrepancies of the critical temperature for all SNSPD array confirm the uniformity of superconducting properties of the material. The SNSPD array made via NbN grown at room temperature has demonstrated a high uniformity that the SNSPD array made via NbN grown at 800 °C. The SNSPD array made via MoSi has demonstrated a small discrepancies in term of critical current and critical temperature, but the small value of critical current and the high background noise does not permit any optical characterization. Future MoSi SNSPD arrays should be based on thicker films or wider nanowires (to improve the critical current I_c) and should be protected with a thin Si cap layer to protect the superconducting properties of MoSi during patterning[197].

6.2 Outlook

Results achieved in this research are a good starting point to continue the fabrication of multipixel SNSPD arrays. The uniformity of the superconducting properties of NbN and MoSi material have demonstrated to be good candidate for a future fabrication, but it is necessary to improve the optimization process of the fabrication to avoid constrictions in the geometry. In particular, the thickness and the width should be carefully chosen to get high values of critical current in order to read high voltage output signals. The geometry of the device depends strongly by the e-beam dosage exposure as proved in the the reference[187] and showed in the [Table 6.3] where the NbN grown heating the substrate exhibits the highest standard deviation of the critical current due of the proximity effect that modifies geometrical structure of pixels. The fabrication of large area multipixel SNSPDs requires then an optimization of the dosage to reduce the proximity effect during the e-beam process.

In these trial devices, the single photon detection efficiency is modest, because the optical fibre has been positioned far from the device to illuminate the entire pixels area. In addition, the pixels are relative spread out and this does not permit a uniform optical coupling efficiency across pixels. A way to improve the optical coupling efficiency is the use of Multi Mode Fibres (MMF) because of their large core diameter that permits illumination of large active areas[198]. An alternative approach would be to employ a fibre collimator to mitigate beam divergence.

The detection efficiency of SNSPDs array can be improved even by implementation of an optical cavity structure such as the distributed Bragg reflectors (DBRs) tailored to the wavelength of the measurement. Another way is to realize a multilayer structure known as supercontinuum SNSPD A recent work[101], shows the simulation of the absorptance of single layer SNSPD compared with a bilayer SNSPD exhibiting an absorption greater than 70% over the spectral range from 400 to 2500 nm while for a single layer SNSPD the spectral range is from 600 to 1600 nm. The same simulation in a three-layer structure exhibits an absorption greater than 70% over the spectral range from 400 to 3000nm. Experimentally, a supercontinuum SNSPD made by 6.5-nm-thick NbN divided in two layers divided by 3-nm-thick SiO₂ and using Al as metal mirror separated from the SNSPD by 190-nm-thick SiO₂, exhibits detection efficiencies greater than 60% from 950 to 1650 nm.

The optical characterization results of the NbN SNSPD array grown at room temperature permit the characterization of the device at longer wavelength. Actually our research group has realized a set-up for LIDAR experiment that permits to characterize SNSPD at $2.3 \mu\text{m}$ wavelength using an optical parametric oscillator (OPO) source[199].

In this work, each pixel of the array structure is biased independently. Increasing number of pixels, increase the number of coaxial cables inside the cryocooler enhancing the heat load of the system. The real challenge of the SNSPD array is still the implementation of a scalable electronic readout. One of the most exciting recent results reported is the 64-channel event-driven encoder based on single flux quantum (SFQ) circuits[201]. The designed circuit consists of 64 magnetically coupled DC/SFQ (MC-DC/SFQ) converters which convert the electrical output signal from the SNSPD to SFQ pulses, a pulse number converter, an internal clock generator, a 7-bit binary pulse counter, an 8-bit shift register, and a voltage driver. Integrating this circuit with 64-pixels NbTiN SNSPD array installed in a GM cryocooler, it has demonstrated high time resolved readout operation. Recently, Jet Propulsion Laboratory (JPL) tested a kilopixel SNSPD array (1024 pixels) made via the amorphous WSi using 32×32 row-column readout measuring a system detection efficiency up to 8% at 1550 nm[202].

Concerning SNSPD made via the amorphous MoSi, a recent work demonstrated that the efficiency of an SNSPD made via MoSi embedded in a DBR microcavity exhibits a detection efficiency exceeding 95% in the communication wavelength[203]. Actually MoSi SNSPD with a detection efficiency over 80% are available commercially from the Swiss company ID Quantique[204]. A first prototype of large area SNSPD made via MoSi shows saturated detection efficiency at 1550 nm wavelength[205]. This detector cover an active area of $400 \mu\text{m} \times 400 \mu\text{m}$ and the width of wires is of the order of microns. The saturation of the detection efficiency proves the possibility to realize large microwire detectors, thus to overcome the drawbacks due to the e-beam lithography that can affect dimensions of the detector.

Bibliography

- [1] G.N. Gol'tsman et al., *Appl. Phys. Lett.*, vol.79, no.6, pp.705, 2001.
- [2] A. Engel, *Supercond. Sci. Technol.* 28 114003, 2015.
- [3] J. J. Renema, *The physics of nanowire superconducting*
- [4] C. M. Natarajan et al., *Super. Sci. and Tech.*, Vol. 25, 063001, 2012.
- [5] K. Inderbitzin et al., *App. Super., IEEE Trans.*, Vol. 23, No. 3, 2013.
- [6] G. Gol'tsman et al., *App. Super., IEEE Trans.* , Vol. 17, 246 –251, 2007.
- [7] K. Suzuki et al., *Physica C: Superconductivity*, 468, 2001 – 2003, 2008.
- [8] H. Shibata et al., *Optics Letters*, Vol. 40, No. 14, 2015.
- [9] B. A. Korzh et al., *Nat. Photonics* 14 (4), 250, 2020.
- [10] N. R. Gemmell et al., *Supercond. Sci. Technol.* Vol. 30, 11LT01, 2017.
- [11] T. Yamashita et al., *IEICE Trans. Electron.*, Vol. E100–C, No. 3, 2017.
- [12] A. Rochas et al., *IEEE Photonics Technology Letters* 15, 963-965, 2003.
- [13] S. Verghese et al., *IEEE Journal of Selected Topics in Quantum Electronics* 13, 870-886, 2007.
- [14] J. G. Timothy and R. L. Bybee, *Review of Scientific Instruments* 46, 1615-1623, 1975.
- [15] R. Bellazzini et al., *Nuclear Instruments and Methods in Physics Research Section a-Accelerators Spectrometers Detectors and Associated Equipment*, 591, 125-128, 2008.
- [16] J. A. Chervenak et al., *Applied Physics Letters* 74, 4043-4045, 1999.
- [17] K. D. Irwin et al., *Nuclear Instruments and Methods in Physics Research Section a-Accelerators Spectrometers Detectors and Associated Equipment* 520, 544-547, 2004.
- [18] L. A. Jiang et al., *Physical Review A*, Vol. 75, 062325, 2007.
- [19] A. Sharma, and J. G. Walker, *Review of Scientific Instruments*, Vol. 63, 5784-5793, 1992.

- [20] P. Cavalier et al. AIP Advances 1, 042120, 2011.
- [21] S. Miki et al., Opt. Express 23, 33729, 2015.
- [22] V. B. Verma et al., Appl. Phys. Lett. 101, 251114, 2012.
- [23] K. Onnes, Comm. Phys. Lab. Univ. Leiden, 29, 1911.
- [24] P. J. Ray, Master Thesis, Niels Bohr Institute, Faculty of Science, University of Copenhagen, 2015.
- [25] B. T. Matthias et al., Rev. Mod. Phys. 35, 1, 1963.
- [26] J. Nagamatsu et al., Nature 410, 63, 2001.
- [27] J. G. Bednorz and K. A. Müller, Z. Phys. B. 64, 189, 1986.
- [28] M. K. Wu et al., Phys. Rev. Lett. 58, 908, 1987.
- [29] A. Schilling et al., Nature 363, 56, 1993.
- [30] S. I. Cherednichenko et al., Proceedings of the Eighth International Symposium on Space Terahertz Technology(pp. 245–252), Harvard University, Cambridge, MA, 1997.
- [31] L. Zhang et al., App. Phys. Lett. 107, 122603, 2015.
- [32] Z. Wang et al., Journal of Applied Physics 79, 7837, 1996.
- [33] K. Smirnov et al., Supercond. Sci. Technol. 31, 035011, 2018.
- [34] Y. M. Shy et al., Journ. App. Phys. 44, 5539, 1973.
- [35] V. B. Verma et al., Appl. Phys. Lett. 105, 022602, 2014.
- [36] M. Planck, Annalen der Physik, vol. 309, Issue 3, pp.553-563, 1901.
- [37] A. Einstein, Annalen der Physik, vol. 322, Issue 6, pp.132-148, 1905.
- [38] J. A. O' Connor, Nano-Optical Studies of Superconducting Nanowire Single-Photon Detectors, Ph.D. Thesis, Heriot-Watt University, 2011.
- [39] G.A. Morton: RCA Rev., 10, 529, 1949.
- [40] G.A. Morton: IRE Trans. Nucl. Sci., 3, 122, 1956.
- [41] Photomultiplier Tubes Basics and Applications, Third Edition, Hamamatsu, 2007.
- [42] R H. Hadfield, Nature Photonics 3, 696-705, 2009.
- [43] J. R. Hook, H. E. Hall, Solid State Physics, 2nd Edition, 2001.
- [44] X. Meng et al., R. Soc. Open Sci 3, 150584, 2016.
- [45] P. Vines et al., Nat Commun. 2019; 10: 1086, 2019.

- [46] D. H. Andrews et al., *Rev. Sci. Instrum.*, 13, 281, 1942.
- [47] A. Lamas-Linares et al., *Appl. Phys. Lett.*, 102(23):1-5, 2013.
- [48] H. Kraus et al., *Europhys. Lett.*, vol. 1, no. 4, pp.161–166, 1986.
- [49] A. Peacock et al., *Nature*, vol. 381, no. 6578, pp. 135–137, 1996.
- [50] P. K. Day et al., *Nature* 425 (6960): 817–821, 2003.
- [51] B.Mazin et al., *Proc. SPIE 7735, Ground-based and Airborne Instrumentation for Astronomy III*, 773518, 2010.
- [52] M. Dobbs et al., *Rev. Sci. Instrum.* 83, 073113, 2012.
- [53] P. R. Maloney et al., *Proc. SPIE 7741, 77410F*, 2010.
- [54] S. Heyminck et al., *Proc. Twenty-First International Symposium on Space Terahertz Technology*, 2010
- [55] B. Mazin et al., *Proc. SPIE. Ground-based and Airborne Instrumentation for Astronomy III*, 773518, 2010.
- [56] Lita et al., *Optics Express* Vol. 16, No. 5, 2008.
- [57] Y. Takeuchi, *Epochal Tsukuba*, 2016.
- [58] Gao, *APL* 101 141602, 2012.
- [59] F. Marsili et al., *Nature Photonics* 7, 210, 2013.
- [60] H. K. Onnes, *Comm. Leiden* No. 1206, 1911.
- [61] W. Meissner, R. Ochsenfeld, *Die Naturwissenschaften*, 21, 787, 1933.
- [62] F. London, H. London, *Proc. Roy. Soc. A*, 49, 71, 1935.
- [63] A. B. Pippard, *Proc Roy Soc London A*216, 547, 1953.
- [64] M. Tinkham, *Introduction to Superconductivity*, Second Edition. New York, NY: McGraw-Hill. ISBN 0486435032, 1996.
- [65] A. A. Abrikosov, *J. Phys. Chem. Solids*, 2, 199, 1957.
- [66] L.N. Cooper, J.R. Schrieffer, J. Bardeen, *Phys. Rev.*, 108, 5, 1957.
- [67] J. J. Quinn, K. Yi, *Solid State Physics Principles and Modern Applications*, Springer, 2009.
- [68] L. N. Cooper, *Physical Review*. 104 (4): 1189–1190, 1956.
- [69] R.G. Sharma, *Superconductivity basics and application to magnets*, Springer, Vol.214, 2015.
- [70] N. W. Ashcroft, N. D. Mermin, *Solid State Physics*. Holt, Rinehart and Winston, 1976.

- [71] B. Matthias et al., *Rev. Mod. Phys.*, 35, 1, 1963.
- [72] P. L. Richards and M. Tinkham, *Phys Rev.*, 119, 575, 1960.
- [73] S. B. Kaplan, C. C. Chi, D. N. Langenberg, J. J. Chang, S. Jafarey, and D. J. Scalapino, *Phys. Rev. B* 14, 4854, 1976.
- [74] A. Rothwarf and B. N. Taylor, *Phys. Rev. Lett.*, 19, 27, 1967.
- [75] R. Sobolewski, *Superconducting and Related Oxides: Physics and Nanoengineering III*, Proc. SPIE. 3481, 480-491, 1998.
- [76] E.M. Baeva et al., *Phys. Rev. App.*, Vol. 10, 064063, 2018.
- [77] D. Pan, *Time-Resolved Photoresponse Studies of Ferromagnet/Superconductor NanoBilayers and Nanostructures*, Ph.D. Thesis, University of Rochester, 2010.
- [78] Semenov A D, Gol'tsman G N and Korneev, *Physica C*, 351, 349–56, 2001.
- [79] I. Charaev, *Improving the Spectral Bandwidth of Superconducting Nanowire Single-Photon Detectors (SNSPDs)*, KIT Scientific Publishing, 2018.
- [80] A. Semenov, A. Engel, H. W. Hubers, K. Il'in and M. Siegel, *Euro. Phys. J. B*, vol. 47, no. 4, 495-501, 2005.
- [81] M. Lindgren et al., *Appl. Phys. Lett.*, 74, 853, 1999.
- [82] W. Slysz et al., *Journal of Modern Optics* 54, 315-326, 2007.
- [83] R. H. Hadfield et al., *Optics Express* 13, 10846-10853, 2005.
- [84] Saleh and Teich, *Fundamentals of Photonics*, John Wiley Sons, 1991.
- [85] C. Natarajan, *Next generation superconducting nanowire single-photon detectors*, Ph.D. Thesis, Heriot-Watt University, 2011.
- [86] A. J. Kerma et al., *Appl. Phys. Lett.* 88, 111116, 2006.
- [87] A. J. Miller et al., *Optics Express* 19, 9102-9110, 2011.
- [88] S. Miki et al, *Appl. Phys. Lett.* 92, 61116, 2008.
- [89] A. Verevkin et al., *Appl. Phys. Lett.* 80, 4687, 2002.
- [90] X. Hu et al., *Opt. Lett.* 34, 3607-3609, 2009.
- [91] C. R. Fitzpatrick, *Single-photon metrology with superconducting nanowire single-photon detectors*, Ph.D. Thesis, Heriot-Watt University, 2013.
- [92] V. Anant et al., *Optics Express*, Vol. 16, No. 14, 10750, 2008.
- [93] V. Anant, *Engineering the optical properties of subwavelength devices and materials*, Ph.D. Thesis, Massachusetts Institute of Technology, 2007.

- [94] A. J. Kerman et al., Appl. Phys. Lett. 90, 101110, 2007.
- [95] R. H. Hadfield et al., Appl. Phys. Lett. 91, 241108, 2007.
- [96] F. Mattioli et al., J. Vac. Sci. Technol. B 30, 031204, 2012.
- [97] D. Rosenberg et al., Opt. Express 21, 1440-1447, 2013.
- [98] K. M. Rosfjord et al., Opt. Express 14, 527, 2006.
- [99] K. Erotokritu et al., Supercond. Sci. Technol. 31, 125912, 2018.
- [100] A. Banerjee et al., Opt. Mat. Exp., Vol. 9, No. 8, 2072-2088, 2018.
- [101] H. Li et al., Photonics Research, Vol.7, No.12, December 2019.
- [102] F. Zheng et al., Scientific Reports, Vol. 6, 22710, 2016.
- [103] Q. Guo et al., Scientific Reports, Vol. 5, 9616, 2015.
- [104] A. Semenov et al., Phys. Rev. B 80, 054510, 2009.
- [105] A. Korneev et al., Quant. Elect., 35, 698-700, 2005.
- [106] W. Zhang et al., Phys. Rev. App. 12, 044040, 2019
- [107] A. Korneev et al., App. Phys. Lett., 84, 5338-5340, 2004.
- [108] J. R. Clem, K. K. Berggren, Phys. Rev. B, Vol. 84, 174510, 2011.
- [109] A. Engel et al., Physica C, 444, pp. 12-18, 2006.
- [110] J. Kitaygorsky et al., App. Super., IEEE Trans., Vol. 17, No. 2, 275–278, 2007.
- [111] V. L. Berezinskii, Sov. Phys. JETP, 34, 610, 1972.
- [112] J. M. Kosterlitz and D. J. Thouless, J. Phys. C, 6, 1181, 1973.
- [113] Bulaevskii, L. et al., Phys. Rev. B, 83, 144526, 2011.
- [114] N. Marrocco et al., Appl. Phys. Lett., 97, 092504, 2010.
- [115] T. Taneda et al., Phys. Rev. B, 75, 174507, 2007.
- [116] J. J. Renema et al., Phys. Rev. B, 87, 174526, 2013.
- [117] U. Nasti et al., Phys. Rev. B, 92, 014501, 2015.
- [118] B. A. Korzh et al., Nat. Photonics, 2020.
- [119] M. Ejrnaes et al., Appl. Phys. Lett. 91, 262509, 2007.
- [120] F. Marsili et al., New J. Phys., Vol. 11, 045022, 2009.
- [121] A. Divochiy et al., Nat. Photonics 2(5), 302–306, 2008.

- [122] S. Jahanmirinejad and A. Fiore, *Opt. Express* 20(5), 5017–5028, 2012.
- [123] S. Jahanmirinejad et al., *Appl. Phys. Lett.* 101(7), 072602, 2012.
- [124] F. Mattioli et al., *Opt. Express*, 24, 9076, (2016).
- [125] M. S. Allman et al., *Appl. Phys. Lett.* 106(19), 192601, 2015.
- [126] H. Terai et al. *IEEE Trans. Appl. Supercond.* 19, 350, 2009.
- [127] S. Miyajima et al., *Opt Express* 26, 29045, 2018.
- [128] H. Terai et al., *Opt. Express* 20, 20115, 2012.
- [129] J. P. Allmaras et al., *OSA Technical Digest (online) (Optical Society of America)*, paper JTh3E.7, 2017.
- [130] S. Doerner et al., *IEEE Trans. on App. Super.*, Vol. 26, No. 3, 2016.
- [131] S. Doerner et al., *Appl. Phys. Lett.* 111, 032603, 2017.
- [132] E. Alfonso, J. Olaya, and G. Cubillos, *InTech*, 2012, pp. 397-432.
- [133] Townsend, *Electricity in Gases*, Chaps. Chap. 8, 9.
- [134] A.A. Kruithof, *Phys.*, 7(6), 519–540, 1940.
- [135] M. A. Lieberman, A. J. Lichtenberg, *Principles of Plasma discharges and materials processing*, 2nd Ed., 2005.
- [136] H. Bartolf, *Fluctuations Mechanism in Superconductors*, Springer Fachmedien Wiesbaden, 2016.
- [137] S. E. Park, J. C. Lee, J. Lee and P. K. Song, *Journal of the Korean Physical Society*, Vol. 54, No. 3, pp. 1283-1287, 2009.
- [138] M. Ohring, *The Materials Science of Thin Films*, Academic Press, New York (1992).
- [139] D. Depla, G. Buyle, J. Haemers, R. De Gryse, *Surface and Coatings Technology*, 200(14-15), 4329–4338, 2006.
- [140] J. Thornton, *Journal of Vacuum Science and Technology*, 15(2), 171, 1978.
- [141] G. Buyle, W. De Bosscher, D. Depla, K. Eufinger, J. Haemers, R. De Gryse, *Vacuum*, 70(1), 29–35, 2003.
- [142] P.J. Kelly, R.D. Arnell, *Vacuum* 56, 159-172, 2000.
- [143] J. Musil, S. Kadlec. *Vacuum* 40, 435-44, 1999.
- [144] F. Adibi, I. Petrov, J.E. Greene, L. Hultman, J.E. Sundgren, *J Appl Phys*, 73(12), 85809, 1993.
- [145] Window B, Savvides N. *J Vac Sci Technol A* 1986;4(2):196-202.

- [146] Window B, Savvides N. *J Vac Sci Technol A* 1986;4(2):453-6.
- [147] Savvides N, Window B. *J Vac Sci Technol A* 1986;4(2):504-8.
- [148] Bunshah RF, Juntz RS. *J Vac Sci Technol* 1972;9:1404.
- [149] Hecht RJ, Mullaly JR. *J Vac Sci Technol* 1975;12:836.
- [150] Kelly PJ, Arnell RD. *Surf Coat Technol* 1997;97:595602.
- [151] P. Yagoubov, G. Gol'tsman, B. Voronov, L. Seidman, V. Siomash, and S. Cherednichenko, Proc. of the 7th Int. Symp. on Space Terahertz Tech, pp. 290–302, March 1996.
- [152] B. Abdo, E. Arbel-Segev, O. Shtempluck and E. Buks, *IEEE Trans. on App. Super.*, VOL. 16, No. 4, 2006.
- [153] MAK Sputter Source Owners Manual (<http://www.meivac.com>)
- [154] Microposit™ S1800™ G2 Series Photoresists, Technical Datasheet, Electronics Materials, Microelectronic Technologies
- [155] Mask Aligners MA6/MA8 User Manual, SUSS MicroTec. (www.suss.com)
- [156] M. M. Mirza, Nanofabrication of silicon nanowires and nanoelectronic transistors. PhD thesis, 2015.
- [157] K. Nojiri, *Dry Etching Technology for Semiconductors*, Springer International Publishing Switzerland 11, 2015.
- [158] H. R. Koenig and L. I. Maissel: *IBM J. Res. and Dev.* 14, p.168 (1970).
- [159] H. Horiike, Proc. 19th Semiconductor Technology Seminar, p.193, 1981.
- [160] S. Miki et al., *IEEE Tran. on App. Super.*, Vol. 17, No. 2, 2007.
- [161] K.V. Smirmov et al., Proc. of SPIE Vol. 7138, 2008.
- [162] N. R. Romanov et al., *J. Phys.: Conf. Series* 1124, 051032, 2018.
- [163] R. Radebaugh, *J. Phys.: Condens. Matter* 21, 164219, 2009.
- [164] H. O. McMahon and W. E. Gifford, *Adv. Cryog. Eng.*, 5, 354, 1960.
- [165] Chapter 6 of *Low Temperature Materials and Mechanisms*, Ed. by Yoseph Bar-Cohen, CRC Press, Boca Raton, FL, pp. 109-1819, 2016.
- [166] S.W. Van Sciver, *Helium Cryogenics*, International Cryogenics Monograph Series, Springer Science+Business Media, LLC 2012.
- [167] R. Radebaugh et al., *Adv. Cryogen. Eng.* 31, 779, 1986.
- [168] L. J. Baker, Superconducting nanowire devices for optical quantum information processing, PhD thesis, University of Glasgow, 2018.
- [169] Robert M. H. et al., *App. Phys. Lett.*, 104(6), 063503, 2014.

- [170] K. Erotokritou, Next generation superconducting nanowire single-photon detectors, PhD thesis, University of Glasgow, 2019.
- [171] T. Shiino et al., Super. Sci. and Tech. 23, 045004, 2010.
- [172] Sapphire for Research and Development, CryStec Kristalltechnologie.
- [173] Semiconductor NSM (<http://www.ioffe.ru/SVA/NSM/Semicond/>)
- [174] M. Wen et al., Journal of Applied Physics 42, 035304, 2009.
- [175] G. Reithmaier et al., Journal of Applied Physics 113, 143507, 2013.
- [176] A. Banerjee et al., Super. Sci. and Tech. 30, 084010, 2017.
- [177] D. Bosworth et al., AIP Advances 5, 087106, 2015.
- [178] T. Matsushita, Flux Pinning in Superconductors, Springer Berlin Heidelberg, 2007.
- [179] S. Krause et al, Supercond. Sci. Technol. 27 065009, 2014.
- [180] L. N. Cooper, Phys. Rev. Lett. 6, 689, 1961.
- [181] L. Kang et al., J. Appl. Phys. 109, 033908, 2011.
- [182] J.J. Zhang et al., Supercond. Sci. Technol. 26, 045010, 2013.
- [183] A. Stockhausen, Karlsruhe, Germany: Karlsruhe Inst. Technol. (KIT), KIT Sci. Pub., 2013
- [184] J. S. Lehtinen et al., Supercond. Sci. Technol. 31 015002, 2018.
- [185] D. Niepce et al., Phys. Rev. App. 11, 044014, 2019.
- [186] V. Burenkov et al., J App. Phys. 113, 213102, 2013.
- [187] Q. Chen et al., IEEE Photonics Journal, Vol.12, No.1, 2020.
- [188] J. Kitaygorsky et al., App. Super., IEEE Trans., Vol. 19, No. 3, 2009.
- [189] M. Born, E. Wolf, Principles of Optics: Electromagnetic Theory of Propagation, Interference, and Diffraction of Light. Cambridge University Press. ISBN 978-0-521-78449-8, 2000.
- [190] SMF28 Datasheet Thorlabs(<https://www.thorlabs.com/drawings/2f86f9495895f8b4-16EF9D2D-90E8-AB4F-245661D0CDDDC022/SMF-28-100-SpecSheet.pdf>)
- [191] Larry C. Andrews, Special functions of mathematics for engineers, SPIE Press, p.110, 1998.
- [192] C. M. Sparrow, The Astrophysical Journal. 44, 76, 1916.
- [193] J. Wu et al., Appl. Opt. 56, 2195, 2017.

- [194] L. You et al., AIP Advances 3, 072135, 2013.
- [195] V. Shcheslavskiy et al., Review of Scientific Instruments 87, 053117, 2016.
- [196] H. Li et al., AIP Advances 8, 115022, 2018.
- [197] Y. P. Korneeva et al., Superconductor Science and Technology, Volume 27, Number 9, 2014.
- [198] L. Zhang et al., IEEE Photonics Journal, Vol.6, No.5, 2014.
- [199] G. G. Taylor et al., Conference on Lasers and Electro-Optics, OSA Technical Digest (Optical Society of America), paper JTh2A.93, 2019.
- [200] E. Knehr et al., Nanowire single-photon detectors made of atomic layer-deposited niobium nitride, arXiv:1906.05214v1, 12 Jun 2019.
- [201] R. Cheng et al., Niobium nitride thin films prepared by atomic layer deposition for efficient superconducting nanowire single-photon detectors, arXiv:1910.07010v1, 15 Oct 2019.
- [202] E. E. Wollman et al., Optics Express 35279, Vol. 27, No. 24, 2019.
- [203] D. V. Reddy et al., Conference on Lasers and Electro-Optics, OSA Technical Digest (Optical Society of America, 2019), paper FF1A.3.
- [204] <https://www.idquantique.com/single-photon-systems-july-2017/>
- [205] I. Charaev et al., Large-area microwire MoSi single-photon detectors at 1550 nm wavelength, <https://arxiv.org/abs/2002.09088>.